

# **Ab initio quantum-chemistry database for $\text{N}_2(v, J) + \text{N}$ in a state-to-state implementation of the DSMC method**

A thesis accepted by the Faculty of Aerospace Engineering and Geodesy of the University of Stuttgart in partial fulfillment of the requirements for the degree of Doctor of Engineering Sciences (Dr.-Ing.)

by

**Erik Torres**

born in Leipzig, Germany

Main referee: Prof. Dr.-Ing. Stefanos Fasoulas  
Co-referee: Prof. Dr. rer. nat. Claus-Dieter Munz  
Co-referee: Prof. Dr. Thierry Magin  
Date of defense: 12 September 2017

Institute of Space Systems  
University of Stuttgart  
2017



# Contents

<b>Abstract</b>	<b>5</b>
<b>Kurzfassung</b>	<b>7</b>
<b>Nomenclature</b>	<b>10</b>
<b>1. Introduction</b>	<b>15</b>
1.1. Motivation . . . . .	15
1.2. Thesis objectives . . . . .	19
1.3. Thesis outline and main contributions . . . . .	21
<b>2. Theoretical Background</b>	<b>25</b>
2.1. Rarefied gas dynamics: Relevant parameters and computational methods . . . . .	25
2.2. Use of DSMC in Aerospace applications . . . . .	29
2.3. State-to-state models for internal energy excitation and molecular dissociation in nitrogen . . . . .	33
2.4. High-fidelity model for $N_2$ : Rovibrational levels derived from the modified Le Roy potential . . . . .	34
2.5. NASA Ames N3 ab initio database . . . . .	38
2.6. Uniform rovibrational collisional (URVC) energy bin model . . . . .	46
2.7. Arrhenius fitting of binned rate coefficients . . . . .	52
<b>3. Implementation of URVC bin model in VKI DSMC code</b>	<b>55</b>
3.1. Analytical inversion of URVC rate coefficients . . . . .	55
3.2. Comparison of directly binned and analytically inverted cross sections . . . . .	59
3.3. Integration of state-specific cross sections into DSMC collision algorithm . . . . .	62
3.3.1. State-specific total cross section for $N_2(k)+N$ -pair . . . . .	62
3.3.2. State-specific reaction probabilities for $N_2(k)+N$ -pair . . . . .	64
3.3.3. Collision acceptance probability of $N_2(k)+N$ -pair . . . . .	64
3.3.4. Determination of post-collision state of $N_2(k)+N$ -pair . . . . .	65
3.4. Effect of URVC binning on thermodynamic properties of $N_2$ . . . . .	69
<b>4. Verification of URVC bin model in VKI DSMC code</b>	<b>83</b>
4.1. Internal energy excitation and dissociation in adiabatic reactor . . . . .	84
4.2. Internal energy excitation and dissociation across normal shock wave . . . . .	90

<b>5. Application of URVC bin model to atmospheric entry flows</b>	<b>103</b>
5.1. Integration of state-to-state bin model into RGDAS . . . . .	104
5.1.1. Conventional framework for chemistry and internal energy exchange in RGDAS . . . . .	104
5.1.2. Adaptation of URVC bin model to RGDAS chemistry framework . . . . .	106
5.1.3. Shortcomings of the current RGDAS integration . . . . .	108
5.2. 2D case: Cylinder of infinite length in hypersonic cross flow . . . . .	113
5.3. 3D case: IXV in atmospheric entry configuration . . . . .	140
<b>6. Conclusions and perspectives</b>	<b>167</b>
<b>Bibliography</b>	<b>173</b>
<b>A. Bin model-related definitions</b>	<b>I</b>
A.1. Generalized Boltzmann equation for $N_2(k)+N$ -mixture . . . . .	I
A.2. Mass production terms for macroscopic balance equations in bin model . . . . .	VI
A.3. Definition of the state-to-state internal temperature out of thermal equilibrium . . . . .	VII

# Abstract

In this work, the implementation within DSMC of a coarse-grain model for nitrogen is presented. The main contribution of this thesis is the development of a methodology by which a detailed state-to-state reaction mechanism for internal energy exchange and molecular dissociation can be reduced to a manageable size and incorporated into a DSMC code. The feasibility of using this model to simulate problems with realistic 2D/3D geometries and conditions relevant for atmospheric entry applications is demonstrated.

More specifically, the work performed consisted of several tasks. First, the detailed reaction-kinetic data for internal energy exchange and dissociation in  $N_2+N$ -collisions, which were extracted from an ab initio database developed at NASA Ames Research Center, had to be adapted to a form suitable for use by DSMC collision routines. It was found that the “raw” cross sections directly extracted from the database were affected by significant statistical noise, due to the relatively coarse sampling of impact parameters employed in the quasi-classical trajectory (QCT) method during their generation. As a consequence, the cross sections in their original form were considered unsuitable for direct use with DSMC. Instead, thermally averaged rate coefficients, obtained by integrating the original cross sections over all collision energies, were used as a starting point. This reduced the stochastic noise significantly, and in a subsequent step these temperature-dependent rate coefficients were converted back into collision energy-dependent cross sections. This inversion problem was tackled by an analytical technique, inspired by the cross section functional form used in Bird’s classical total collision energy method. Alternative inversion techniques for obtaining the cross sections numerically, such as Tikhonov regularization, or non-linear optimization via the downhill-simplex method were deemed too time-consuming to be practical. Second, in order to reduce the computational cost of the state-to-state model to reasonable levels, the number of discrete rovibrational states of  $N_2$  (and the associated mechanism for the internal energy exchange and dissociation reactions) had to be reduced considerably. For this purpose, an already existing coarse grain model known as the uniform rovibrational (URVC) bin model was adapted for its use with DSMC. In order to determine the most convenient distribution of rovibrational levels among a given number of bins and to determine the minimum number of bins necessary to reproduce the behavior of the full system by means of the URVC model, a parametric study was conducted. This study helped determine the “binning strategy” to best approximate the thermodynamic behavior of the full set of levels. Using bins with fewer rovibrational levels

at lower energies allows for a much better representation of the internal energy content in the gas at low temperatures. This is a desirable feature in atmospheric-entry flows, where the free stream is usually cold. The final choice used 10 variably-sized bins, which were able to reproduce the thermodynamic properties of the full set of levels over a wide range of temperatures.

For purposes of model testing, a dedicated DSMC code capable of simulating the detailed chemical dynamics of the state-to-state mechanism in unsteady 0D- and steady 1D flows was written at VKI. With the help of this code, the DSMC implementation of the URVC bin model was verified against equivalent master equation calculations in adiabatic reservoir-type simulations. The sensitivity of the internal energy relaxation- and dissociation rates to the choice of bins was examined, and the 10 variably-sized bins were again found to produce results which closely approximate those of the full set of levels. Subsequently, the URVC bin model was used to study internal energy excitation and dissociation in nitrogen, as it is compressed across a normal shock. This test case revealed that the bin model based on the NASA Ames cross sections predicts extremely high kinetic temperatures in the shock, with relatively slow excitation of the rovibrational energy modes and a delay in the onset of dissociation. Finally, the bin model was adapted for use with an external production-level DSMC tool. In this case, the RGDAS code developed at the Institute for Theoretical and Applied Mechanics (ITAM) in Novosibirsk, Russia was used. This integration was done in order to demonstrate the feasibility of using the state-to-state model two large-scale 2D and 3D DSMC simulations. As examples, two test cases roughly representative of Earth atmospheric entry of blunt bodies were used. The behavior of the bin model was studied by comparing it to calculations which made use of the conventional Larsen-Borgnakke and total collision energy models. It was found that the bin model predicts a much lower degree of internal energy excitation and slower dissociation across the bow shock than the conventional models.

There are several ways in which continued research into such high-fidelity models will still provide beneficial for future applications. One of its main uses will be to verify, or challenge some of the core assumptions inherent to the much less costly models currently in general use (i.e. Larsen-Borgnakke+TCE models in DSMC, or multi-temperature models in CFD), and help to propose improvements, or alternatives to these conventional models. Furthermore, since the QCT-derived chemistry data are essentially parameter-free, they are of special use to study the detailed chemical behavior of gas mixtures in situations where experimental data is scarce, or nonexistent.

# Kurzfassung

Diese Arbeit befasst sich mit der DSMC-Implementierung eines reduzierten *state-to-state*-Modells für Stickstoff. Der Hauptbeitrag der Arbeit ist die Entwicklung einer Methode, die es ermöglicht einen detaillierten *state-to-state* Reaktionsmechanismus für den Austausch innerer Freiheitsgrade und molekularer Dissoziation auf einen handhabbaren Umfang zu reduzieren und ihn in die DSMC-Methode zu integrieren. Im Anschluss wird die praktische Anwendbarkeit dieses Modells für die Simulation von Wiedereintrittszenarien anhand von zwei Beispielen mit 2D- und 3D-Geometrien veranschaulicht.

Die Arbeit kann in mehrere Abschnitte unterteilt werden. Zuerst mussten die Reaktionsquerschnitte für  $N_2+N$ -Stöße, die aus einer *ab initio*-Datenbank des NASA Ames Research Center stammen, in eine Form gebracht werden die ihre Weiterverwendung innerhalb der DSMC-Stoßalgorithmen ermöglicht. Dabei stellte sich heraus, dass die ursprünglichen Querschnitte mit beträchtlichem statistischem Rauschen behaftet waren. Dieses Rauschen kann unmittelbar auf die relativ kleinen Stichprobengrößen, die in der zugrundeliegenden *Quasi-Classical Trajectory* (QCT)-Methode verwendet wurden, zurückgeführt werden. Aus diesem Grund wurden die ursprünglichen Querschnitte als nicht geeignet für ihre direkte Anwendung in der DSMC-Methode erachtet. Stattdessen wurden aus ihnen zuerst Maxwell-gemittelte Reaktionsgeschwindigkeitskoeffizienten bestimmt, indem die Querschnitte über die Stoßenergie integriert wurden. Dadurch konnte das Rauschen erheblich reduziert werden. Im darauf folgenden Schritt wurden diese temperaturabhängigen Reaktionsgeschwindigkeitskoeffizienten zurück in energieabhängige Reaktionsquerschnitte umgewandelt. Dieses "Inversionproblem" wurde mithilfe eines analytischen Verfahrens, das sich stark an Bird's Vorgehen in der *Total Collision Energy*-Methode anlehnt, gelöst. Andere Methoden für die numerische Lösung solcher sog. schlecht gestellten (*ill-posed*) Probleme, z.B. Tikhonov-Regularisierung, oder nichtlineare Optimierung mittels der *Downhill-Simplex* Methode wurden als zu zeitaufwendig erachtet, um praktisch anwendbar zu sein. Zweitens, um den Rechenaufwand des *state-to-state*-Modells auf ein handhabbares Maß zu senken, musste die Anzahl der diskreten rotatorisch-vibratorischen Zustände des  $N_2$ -Moleküls (und die Komplexität des damit verbundenen Reaktionsmechanismus) erheblich reduziert werden. Um dies zu erreichen, wurde das vorhandene grobkörnige *Uniform RoVibrational Collisional* (URVC) *bin*-Modell für seinen Einsatz innerhalb der DSMC-Methode angepasst. Eine parametrische Studie zur Bestimmung der optimalen Verteilung der einzelnen Energieniveaus auf eine erheblich geringere

Anzahl von “bins”, bzw. “Klassen” und die maximal nötige Anzahl dieser Klassen wurde durchgeführt. Daraus konnte ein Klasseneinteilungsverfahren entwickelt werden, das eine sehr gute Approximation der thermodynamischen Eigenschaften der vollständigen Energieniveaus ermöglicht. Es stellte sich heraus, dass es vorteilhaft ist eine geringere Anzahl der Energieniveaus in die energetisch niedrigst gelegenen Klassen zu gruppieren. Dadurch ist eine bessere Nachbildung der thermodynamischen Eigenschaften bei niedrigen Temperaturen möglich. Dies ist besonders wünschenswert in Wiedereintrittsimulationen, da das Gas in der ungestörten Anströmung üblicherweise verhältnismäßig kalt ist.

Ein eigens am VKI geschriebener DSMC-Code wurde verwendet, um das Verhalten dieses Modells zu untersuchen. Dieser Code erlaubt es instationäre Reservoir-Simulationen und stationäre 1D-Strömungen mitsamt dem detaillierten *state-to-state* Mechanismus durchzuführen. Die DSMC-Implementierung des URVC *bin*-Modells wurde anhand Simulationen eines adiabatischen Reservoirs verifiziert. Dabei wurde die Abhängigkeit der charakteristischen Relaxations- und Dissoziationsraten von der Anzahl und Verteilung der Klassen untersucht. Hier stellte sich erneut heraus, dass 10 Klassen mit variabler Größe die thermodynamischen und reaktionskinetischen Eigenschaften des vollständigen Modells zufriedenstellend nachbilden können. Im Anschluss wurde das URVC-*bin*-Modell verwendet, um die Anregung innerer Freiheitsgrade und Dissoziation von Stickstoff innerhalb eines senkrechten Verdichtungsstoßes zu untersuchen. Bei diesen Rechnungen stellte sich heraus, dass das *bin*-Modell basierend auf den NASA Ames-Querschnitten außergewöhnlich hohe Translationstemperaturen in der Stoßfront vorhersagt, gefolgt von verhältnismäßig langsamer Relaxation der rotatorisch-vibratorischen Freiheitsgrade und verzögertem Einsetzen der Dissoziation. Zuletzt wurde das *bin*-Modell für seine Anwendung innerhalb eines etablierten DSMC-Codes angepasst. Im konkreten Fall wurde RGDAS verwendet, ein Code der am *Institute for Theoretical and Applied Mechanics* (ITAM) in Novosibirsk, Russland entwickelt wurde. Mithilfe dieser Software konnte die praktische Anwendbarkeit des *state-to-state*-Modells für 2D- und 3D DSMC-Simulationen größeren Umfangs bewiesen werden. Als Beispiele dienten zwei Testfälle, die annähernd den Wiedereintritt eines stumpfen Körpers in die Erdatmosphäre simulieren. In diesen Simulationen wurde das Verhalten des *bin*-Modells mit den in DSMC üblichen Borgnakke-Larsen, bzw. *Total Collision Energy*-Modellen verglichen. Hier wurde festgestellt, dass das *bin*-Modell deutlich geringere Anregung der inneren Freiheitsgrade und wesentlich langsamere Dissoziation im Verdichtungsstoß vorhersagt, als die herkömmlichen Modelle.

In Zukunft könnte sich die weiterführende Entwicklung der hier behandelten hochauflösenden Chemie-Modelle in zweierlei Hinsicht als nützlich erweisen. Einerseits könnten sie dazu dienen einige der Annahmen, die den heutzutage standardmäßig verwendeten Modellen (Larsen-Borgnakke+*Total Collision Energy* in der DSMC-Methode, oder *Multi-Temperature*-Modelle in CFD) zugrunde liegen, zu hinterfragen. Dies könnte dann zur Entwicklung von Verbesserungen, oder Alternativen zu den vorhandenen Modellen führen. Andererseits, besteht ein wesentlicher

Vorteil der Reaktionsraten, bzw. Querschnitte, die mittels der QCT-Methode generiert werden, in der Tatsache dass sie one zusätzliche, experimentell bestimmte Parameter auskommen. Dies wiederum bedeutet, dass sie besonders geeignet sind um die Reaktionskinetik des Gasgemisches unter Bedingungen zu untersuchen, wo experimentell bestimmte Ratenkoeffizienten unvollständig, oder gar nicht vorhanden sind.



# Nomenclature

## Acronyms

AHO	AnHarmonic Oscillator
BRVC	Boltzmann RoVibrational Collisional
CFD	Computational Fluid Dynamics
CTC	Classical Trajectory Calculations
DAC	DSMC Analysis Code
DSMC	Direct Simulation Monte Carlo
FHO	Forced Harmonic Oscillator
GHS	Generalized Hard Sphere
GSS	Generalized Soft Sphere
HyBVC	Hybrid Vibrational Collisional
ITAM	Institute for Theoretical and Applied Mechanics
IXV	Intermediate eXperimental Vehicle
LB	Larsen-Borgnakke
LD	Low Diffusion
LEO	Low Earth Orbit
MCF	Majorant Collision Frequency
MD	Molecular Dynamics
NTC	No Time Counter
PES	Potential Energy Surface
QCT	Quasi-Classical Trajectory
QK	Quantum-Kinetic
RGDAS	Rarefied Gas Dynamics Analysis System
RR	Rigid Rotor
RT	Rotation-Translation
SPARTA	Stochastic PArallel Rarefied-gas Time-accurate Analyzer
TCE	Total Collision Energy
TPS	Thermal Protection System
URVC	Uniform RoVibrational Collisional

VC	Vibrational-specific Collisional
VHS	Variable Hard Sphere
VKI	von Karman Institute for Fluid Dynamics
VSS	Variable Soft Sphere
VT	Vibration-Translation

### Greek Symbols

$\alpha_{\text{int}}$	Rovibrational energy surface accommodation coefficient [-]
$\alpha_{\text{rot}}$	Rotational energy surface accommodation coefficient [-]
$\alpha_{\text{vib}}$	Vibrational energy surface accommodation coefficient [-]
$\bar{\sigma}_k^{\text{el}}$	Elastic cross section for bin $k$ [ $\text{m}^2$ ]
$\bar{\sigma}_k^D$	Dissociation cross section from bin $k$ [ $\text{m}^2$ ]
$\bar{\sigma}_{k \rightarrow k'}^E$	Excitation/deexcitation cross section from bin $k$ to bin $k'$ [ $\text{m}^2$ ]
$\bar{\sigma}_k^T$	Total cross section for bin $k$ [ $\text{m}^2$ ]
$\Delta E_R$	Heat of reaction for chemical reaction $R$ [J]
$\Delta E_{(v=0, J=0)}^D$	Heat of dissociation of molecular nitrogen from ground rovibrational state [J]
$\Delta t$	Time step size [s]
$\eta_R$	Centrifugal distortion parameter [-]
$\eta_V$	Vibrational anharmonicity parameter [-]
$\mu_{\text{N}_2-\text{N}}$	Reduced mass of $\text{N}_2$ -N collision pair: $1.55 \times 10^{-26}$ kg
$\omega$	VHS viscosity exponent [-]
$\rho$	Mass density [ $\text{kg} \cdot \text{m}^{-3}$ ]
$\sigma_R$	Integrated cross section for chemical reaction $R$ [ $\text{m}^2$ ]
$\tau_w$	Surface shear stress [ $\text{N} \cdot \text{m}^{-2}$ ]
$\theta_R$	Characteristic temperature of rotation [K]
$\theta_V$	Characteristic temperature of vibrational [K]
$E_{a,R}$	Activation energy for chemical reaction $R$ [J]

### Physical constants

$h_P$	Planck's constant: $h_P = 6.62607 \times 10^{-34} \text{m}^2 \cdot \text{kg} \cdot \text{s}^{-1}$
$k_B$	Boltzmann constant: $1.38065 \times 10^{-23} \text{J} \cdot \text{K}^{-1}$

### Roman Symbols

$\bar{a}_k$	Degeneracy of rovibrational bin $k$ [-]
$\bar{E}_k$	Average energy of rovibrational bin $k$ [J]
$\bar{k}_{k \rightarrow k'}^E$	Excitation rate coefficient from bin $k$ to $k'$ [ $\text{m}^3 \cdot \text{s}^{-1}$ ]
$\bar{K}_{k \rightleftharpoons 2\text{N}}^{\text{eq}}$	Dissociation equilibrium constant between bin $k$ and atomic nitrogen [ $\text{m}^{-3}$ ]
$\bar{K}_{k' \rightleftharpoons k}^{\text{eq}}$	Equilibrium constant between bin $k$ and $k'$ [-]
$\bar{k}_k^{\text{el}}$	Elastic rate coefficient of bin $k$ [ $\text{m}^3 \cdot \text{s}^{-1}$ ]

$\bar{k}_k^D$	Dissociation rate coefficient from bin $k$ [ $\text{m}^3 \cdot \text{s}^{-1}$ ]
$\bar{k}_k^R$	Recombination rate coefficient to bin $k$ [ $\text{m}^6 \cdot \text{s}^{-1}$ ]
$\bar{n}_k$	Number density of rovibrational bin $k$ [ $\text{m}^{-3}$ ]
$\dot{Q}$	Heating per unit length [ $\text{kW} \cdot \text{m}^{-1}$ ]
$\mathcal{I}_{\text{N}_2}$	Set of rovibrational level indices of $\text{N}_2$
$\mathcal{I}_k$	Set of rovibrational level indices $i$ contained within bin $k$
$\mathcal{K}_B$	Set of bin indices containing truly bound rovibrational levels
$\mathcal{K}_{\text{N}_2}$	Set of rovibrational bin indices of $\text{N}_2$
$\mathcal{K}_P$	Set of bin indices containing pre-dissociated rovibrational levels
$\text{Kn}$	Knudsen number [-]
$\text{Kn}_{\text{GLL},\rho}$	Density gradient length-based local Knudsen number [-]
$A$	Coefficient in pre-exponential Arrhenius factor
$a_{\text{N}}$	Degeneracy of atomic nitrogen: $a_{\text{N}} = 12$ [-]
$a_i$	Degeneracy of rovibrational level $i$ of $\text{N}_2$ [-]
$a_{v,J}$	Degeneracy of rovibrational level $v, J$ [-]
$b$	Temperature exponent in pre-exponential Arrhenius factor
$c_{v,\text{N}_2}$	Specific constant-volume heat capacity at constant volume of $\text{N}_2$ [ $\text{kJ} \cdot \text{kg}^{-1} \cdot \text{K}^{-1}$ ]
$c_f$	Local surface skin friction coefficient [-]
$c_h$	Local surface heat transfer coefficient [-]
$c_p$	Local surface pressure coefficient [-]
$D$	Cylinder diameter [m]
$d_{\text{ref}}$	VHS reference diameter [ $\text{\AA}$ ]
$E$	Relative translational energy of collision pair [J]
$E'$	Post-collision relative translational energy [J]
$e_{\text{N}_2}$	Specific thermal energy of molecular nitrogen [ $\text{MJ} \cdot \text{kg}^{-1}$ ]
$E_{\text{N}}$	Energy of formation of atomic nitrogen [J]
$E_i$	Energy of rovibrational level $i$ of $\text{N}_2$ [J]
$E_{\text{N}_2(v=0,J=0)}$	Energy of ground rovibrational state of molecular nitrogen [J]
$F_D$	Drag per unit length [ $\text{N} \cdot \text{m}^{-1}$ ]
$g$	Magnitude of relative velocity of collision pair [ $\text{m} \cdot \text{s}^{-1}$ ]
$k_{\text{eq}}^D$	Thermally-averaged dissociation rate coefficient over all rovibrational levels of $\text{N}_2$ [ $\text{s}^{-1} \cdot \text{m}^{-3}$ ]
$k_R$	Rate coefficient for chemical reaction $R$
$k_i^D$	Dissociation rate coefficient of rovibrational level $i$ of $\text{N}_2$ [ $\text{m}^3 \cdot \text{s}^{-1}$ ]
$L_{\text{ref}}$	Reference length [m]
$n$	Number density [ $\text{m}^{-3}$ ]

## Nomenclature

---

$N_{\text{pairs}}$	Number of collision pairs to be tested [-]
$n_i$	Number density of rovibrational level $i$ [ $\text{m}^{-3}$ ]
$N_P$	Number of particles in cell [-]
$p$	Pressure [ $\text{N} \cdot \text{m}^{-2}$ ]
$P_{k \rightarrow k'}^E$	Excitation probability from bin $k$ to bin $k'$ [-]
$P_k^{\text{Sum}}$	Cumulative probability from bin $k$ [-]
$P_k^D$	Dissociation probability from bin $k$ [-]
$q_w$	Surface heat flux [ $\text{kW} \cdot \text{m}^{-2}$ ]
$S_{\text{ref}}$	Reference area [ $\text{m}^2$ ]
$T$	Temperature [K]
$T_{\text{int}}$	Temperature of the rovibrational modes of $\text{N}_2$ [K]
$T_{\text{ref}}$	VHS reference temperature [K]
$T_{\text{rot}}$	Temperature of the rotational mode of $\text{N}_2$ [K]
$T_{\text{vib}}$	Temperature of the vibrational mode of $\text{N}_2$ [K]
$V$	Velocity magnitude [ $\text{m} \cdot \text{s}^{-1}$ ]
$V_{\text{cell}}$	Collision cell volume [ $\text{m}^3$ ]
$W_P$	DSMC particle weight [-]
$x_{\text{N}}$	Mole fraction of atomic nitrogen [-]
$x_{\text{N}_2(k)}$	Mole fraction of bin $k$ belonging to molecular nitrogen [-]
$y_{\text{N}}$	Mass fraction of atomic nitrogen [-]
$Z^{\text{tra},*}$	Partition function of translational mode (per unit volume) [ $\text{m}^{-3}$ ]
$Z_{\text{N}_2}^{\text{int}}$	Internal partition function over rovibrational levels of $\text{N}_2$ [-]

### Super/subscripts

$\infty$	Index, denotes free stream conditions
$i$	Rovibrational level index
$J$	Rotational quantum number
$k$	Rovibrational bin index of $\text{N}_2$
$v$	Vibrational quantum number

# 1. Introduction

## 1.1. Motivation

The work presented in this thesis lies within the overlapping fields of hypersonic aerothermodynamics and rarefied gas dynamics. From an aerospace engineer's perspective, these two disciplines are of concern during the design of spacecraft which must survive atmospheric entry, or of vehicles intended for sustained high-speed, high-altitude atmospheric flight. Take for example the Apollo command module, whose main purpose was to protect NASA astronauts during descent through Earth's atmosphere in the final stages of their mission. During this phase, the capsules were exposed to high temperatures and extreme stresses caused by deceleration and simultaneous compression of the atmospheric gas impinging on the vehicle. Given lunar return speeds of about 11 km/sec (See Fig. 1.1, which shows the altitude-velocity map for a variety of Earth reentry vehicles) the free stream flow, when viewed in the vehicle's frame of reference, contains an enormous amount of kinetic energy. A significant part of this energy is absorbed by the translational mode of the gas in the bow shock ahead of the craft and subsequently transferred to its rotational, vibrational and electronic modes. Furthermore, high-energy collisions between gas particles may lead to the dissociation of molecular species such as  $O_2$  and  $N_2$ , subsequent formation of nitric oxide and to partial ionization of some gas constituents.

During its descent through Earth's atmosphere, a reentry vehicle is exposed to free-stream gas of ever-increasing particle density. At near-vacuum at the outer edges of the atmosphere, it first encounters the free-molecular regime. This regime is characterized by incoming free-stream gas impacting directly on the vehicle surface with barely any prior collisions between incident and reflected molecules. As a consequence, the gas-phase chemistry and internal energy exchange processes in the diffuse compression region ahead of the vehicle are said to be "frozen". Once the vehicle has descended to altitudes of approximately 100 km and lower, the free-stream density becomes high enough to raise the molecular collision rate to levels where some chemical activity can be observed in the gas phase. However, in this transitional region between the rarefied- and continuum regimes, the translational and internal energy modes of the gas are not yet in equilibrium. This is reflected in the strong departure between the translational, rotational and vibrational (and electronic) mode temperature profiles across the bow shock, as well as in a marked delay in the onset of molecular dissociation behind the shock front. Continuing its descent, the vehicle

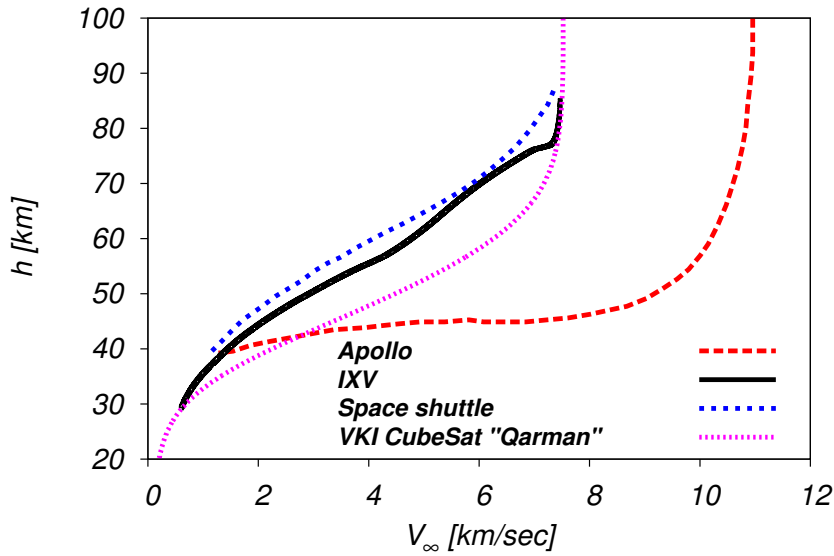


Figure 1.1.: Altitude-velocity map for Earth atmospheric re-entry. Red dashed line: Apollo lunar return, Black solid line: Intermediate eXperimental Vehicle (IXV) Low Earth Orbit return (LEO), Blue dotted line: Space shuttle LEO return, Purple dotted line: VKI Cubesat “Qarman” LEO return

reaches the high-density portion of the atmosphere at altitudes of about 70 km and lower. At this point, the collision rate in the gas is high enough for the incoming flow to remain near thermal equilibrium and the bow shock to become sharply focused. It is usually at these comparatively low altitudes that the vehicle becomes exposed to the highest heat transfer rates (commonly referred to as peak heating<sup>1</sup>). These flow regimes are encountered by all reentry vehicles, whether they follow the ballistic, semi-ballistic (e.g. Soyuz, or Apollo capsules), or lifting-body return trajectories (e.g. the Space Shuttle, IXV). Fig. 1.2 reviews these gas-dynamical flow regimes in a diagram of characteristic length scale vs. density ratio. The “reentry path” of Apollo has been traced in this figure to highlight the vast ranges of free-stream densities (and accompanying free-stream Knudsen numbers<sup>2</sup>) the vehicle is exposed to. However, the altitudes at which the different regimes are experienced by each type of vehicle depend very much on its size: Vehicles with characteristic dimensions much smaller than Apollo, where  $L_{\text{ref}} = 3.9 \text{ m}$  was used, will experience rarefied gas effects at much lower altitudes than the ones mentioned here.

From a computational modeling point of view, the combination of high-temperature gas phenomena and rarefied gas effects in atmospheric-entry flows pose significant challenges. At present, no single numerical method is able to deliver both accurate and fast predictions of the flow behavior throughout the entire range of conditions encountered during reentry. On one extreme exist the classical CFD methods based on solving the Navier-Stokes- or Euler equations. These are

<sup>1</sup>For Apollo, this occurs at 60 km.

<sup>2</sup>Its most straightforward definition is  $\text{Kn}_{\infty, L_{\text{ref}}} = \lambda_{\infty} / L_{\text{ref}}$ , where  $\lambda_{\infty}$  is the mean free path at free-stream conditions and  $L_{\text{ref}}$  is a macroscopic length scale characteristic of the particular flow problem.

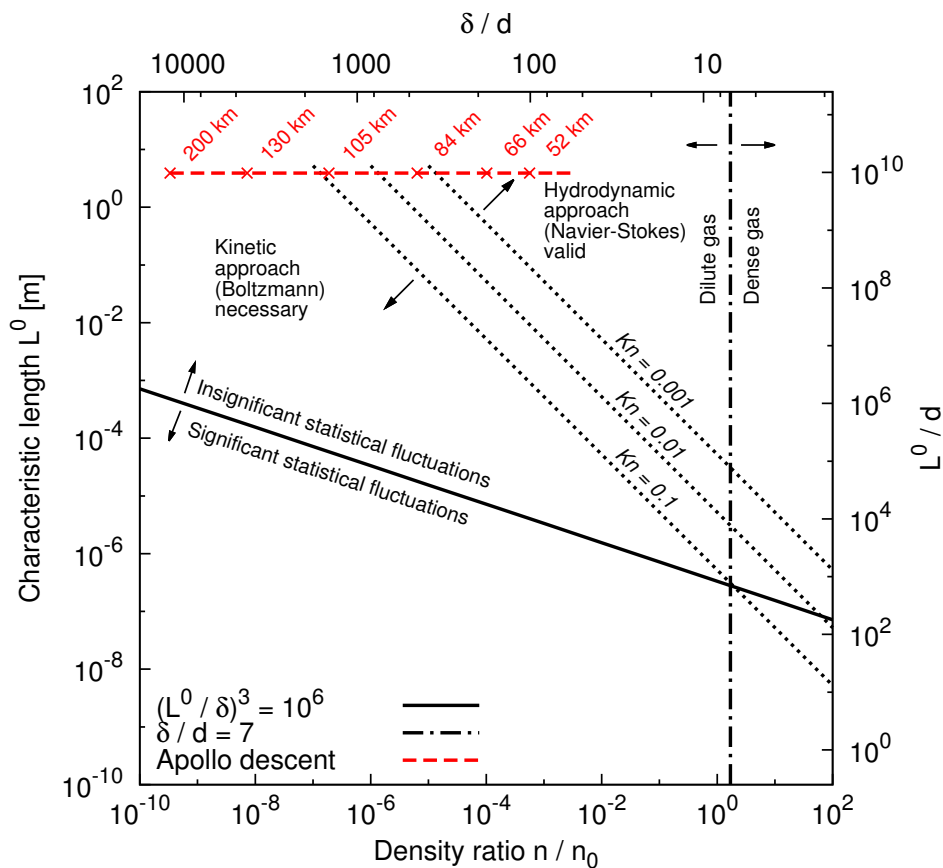


Figure 1.2.: Overview of Gas-dynamical flow regimes traversed by atmospheric entry vehicles (Adapted from Bird [1]). On one set of axes, characteristic length scale of the space craft  $L^0$  is plotted vs. normalized free-stream gas density  $n/n_0$ . Lines of constant Knudsen number are represented by dotted lines, roughly separating the continuum- or hydrodynamic region in the top right corner of the diagram from the rarefied-flow region to the upper left of the graph. Using a rough approximation for the gases in Earth's atmosphere, alternative axes can be defined in terms of the mean molecular spacing  $\delta = \sqrt[3]{1/n}$  and the average diameter for collision cross sections  $d$ . Setting the limit between dilute- and dense gas at  $\delta/d = 7$  defines the vertical dot-dashed line on the right. Beyond this curve, the atmosphere no longer behaves as a dilute gas and multi-body collisions become frequent. An additional line marks the region where the number of molecules contained in a cube with side-length  $L^0$  drops below one million. With such a small number particles, statistical fluctuations in the gas properties become so severe that the definition of spatially-averaged macroparameters is no longer practical. The reentry of Apollo is indicated by the red dashed horizontal line, along with corresponding estimated altitudes along its descent path

accurate at comparatively low altitudes, where the free-stream Knudsen numbers are small and the continuum regime prevails (i.e. the triangular region in the upper right corner of Fig. 1.2, roughly delimited by the diagonal line for  $Kn = 0.001$  and the dilute/dense gas boundary to the right). In this approach, the high-temperature effects causing thermo-chemical nonequilibrium

are taken into account by solving additional balance equations for the internal energy modes, while production terms in the mixture's individual species balance equations account for the effect of finite-rate chemistry [2]. However, the assumptions behind the Navier-Stokes equations break down at higher free-stream Knudsen numbers, where the collision rate in the gas is no longer high enough to maintain near-equilibrium molecular velocity distributions throughout the flow field. The consequence is that classical CFD codes will deliver inaccurate predictions, or outright fail to reach a solution. For simulations at these higher Knudsen numbers, alternative methods, which directly, or indirectly solve the governing Boltzmann equation [3], have to be used (this region is roughly located below and to the right of the line for  $Kn = 0.1$  in Fig. 1.2). Several competing methods have been devised over the years (see the discussion in Sec. 2.1), but by far the most widely used one by aerospace engineers nowadays is the direct simulation Monte Carlo method (DSMC) [1]. This stochastic, particle-based method has been especially successful in the simulation of hypersonic flows, due to its high efficiency compared to competing direct Boltzmann solvers and the relative ease with which high-temperature effects, such as internal energy exchange in poly-atomic gases and chemical reactions can be incorporated.

For engineers tasked with designing vehicles to survive Earth atmospheric entry, the issues related to high-temperature vs. rarefied gas effects become most relevant at two distinct stages of the reentry process. Peak heating, which is arguably the most important issue for designing the thermal protection system (TPS), usually does not occur in the transitional- but well within the continuum regime. At these conditions the heat loads the vehicle is exposed to are strongly influenced by the composition of the gas and the thermo-chemical processes occurring in the flow behind the bow shock. Thus, classical CFD tools based on the Navier-Stokes equations, which incorporate accurate thermo-chemical nonequilibrium models, coupled with suitable radiation modeling will be necessary to predict the critical heat loads. By contrast, in the transitional regime prevalent at higher altitudes, the thermal loads on the vehicle are comparatively low. The main quantities of interest at these early stages of reentry are the aerodynamic coefficients for drag, lift and roll/pitch/yaw moments. They are needed to plan the reentry trajectory and to predict the stability characteristics of the craft during descent. Here, the rarefied nature of the flow must be taken into account, since at such extreme conditions the linear relations between transport fluxes and flow field gradients in the Navier-Stokes equations<sup>3</sup> become invalid, and the surface stress and heat flux distributions can only be accurately predicted using gas-kinetic methods such as DSMC. Although in the rarefied regime the forces and moments acting on the vehicle mainly depend on the molecular scattering properties of its surface material, internal energy exchange- and reactive processes in the gas phase will also have an indirect influence, because they affect the surrounding flow field.

With these considerations in mind, a major motivation for this thesis is to take advantage of the growing body of high-fidelity chemical rate data, which over the last years has been -and is still

---

<sup>3</sup>i.e. Newton's law for viscous stresses, Fourier's law for the conductive heat flux, etc.

being- compiled for the major molecular and atomic constituents of Earth's atmosphere [4, 5, 6]. Such detailed rates are of particular interest, because they are derived from first-principles quantum-chemistry calculations and therefore provide an alternative to data obtained experimentally. Ab initio rates for the  $N_2(v, J)+N$ -system (frequently referred to in this thesis as the Ames N3 database) have been applied in the past in the framework of CFD codes, yielding new insight into the processes of rovibrational energy excitation and molecular dissociation characteristic of high-temperature reentry flows. In the process, these simulations called into question some of the assumptions made by existing multi-temperature models [7]. Thus, this thesis represents part of a similar effort to integrate such high-fidelity data into the DSMC world.

It is true that many successful reentry vehicles in the past have been designed without resorting to the sophisticated numerical tools and detailed chemistry models available today. However, the ever-increasing need to optimize the performance of these craft by minimizing the weight of their heat shield and the desire to gain a refined understanding of the thermo-chemical processes in reentry flows, will continue to force the aerospace community to improve their physical modeling capabilities. For future reentry craft, such as the ones that would potentially bring back astronauts from a Mars mission, engineers will likely have to rely to a large extent on numerical simulations for their design work, because performing large-scale ground-based experiments at full reentry conditions will be prohibitively expensive, or impractical. In a related application, when improved high fidelity chemistry models are used in simulations of ground-based wind tunnel tests, they can prove particularly useful for diagnosing the phenomena observed in such experiments. For example, detailed knowledge of rovibrational level populations can help experimenters better calibrate their optical measurements and to characterize more accurately the flow field within the test chamber.

It should be noted that the physico-chemical phenomena discussed in this work only represent a sub-set of the complete picture. In reality, gas-phase internal energy exchange and chemistry constitute only one of several competing phenomena affecting hypersonic reentry flows. Most likely, the influence of radiation, or plasma effects on the overall flow are much greater than the precise populations of rotational and vibrational levels. We are aware of the fact that by limiting ourselves to the just mentioned database, we will neglect some very important physical phenomena, i.e. electronic excitation, plasma effects due ionization, surface catalysis and gas-phase radiation effects.

## 1.2. Thesis objectives

The objectives of this thesis can be summarized in several key points. The primary goal is to take advantage of the large set of detailed chemical-kinetic data contained within the NASA Ames N3 database and apply it to DSMC simulations in the transitional regime. The purpose of this

effort is to extend the application of the N3 rate data beyond classical CFD methods used in the hydrodynamic regime, where they have already been applied extensively. It will be of special interest to observe the dynamics of internal energy excitation and molecular dissociation across the strong shocks which typically form ahead of blunt bodies exposed to hypersonic free-stream conditions. Such a study requires the use of DSMC, or equivalent gas-kinetic simulation schemes, since classical Euler-, or Navier-Stokes-based CFD solvers are not able to accurately resolve the shock region at upstream Mach numbers greater than  $Ma_\infty \approx 2$ .

During this procedure, care must be taken to implement the detailed chemistry mechanism in such a way as to ensure consistent behavior between the kinetic and hydrodynamic description. The availability of the Ames database provides a unique opportunity for this, because it essentially demands the use of the same state-to-state model for internal energy exchange and dissociation in both DSMC and CFD. In this manner, one is able to avoid many of the inconsistencies between the standard phenomenological models (Larsen-Borgnakke + TCE in DSMC vs. multi-temperature models in classical CFD), which were originally derived independently and on the basis of different assumptions for the two simulation approaches. Based on reported CFD results, where the Ames database has been used by other authors, it is expected that the state-to-state model implemented in this thesis will challenge some of the assumptions traditionally made in the conventional models in DSMC.

Along with integrating the ab initio rate data of the Ames database into DSMC, a complementary goal will be to make use of a so-called coarse-grain model to reduce the size (and with it the computational expense) of the detailed chemistry mechanism. Among the existing coarse-grain models originally proposed in the context of CFD, their merits and their compatibility with the kinetic description must be evaluated. In addition to this, the selected variant must be fine-tuned to produce simulation results, which match the behavior of the full chemical mechanism as closely as possible.

In order to accomplish these objectives, the work is divided into several sub-tasks.

- The first effort is to manipulate the Ames N3 database, to analyze its contents and to devise a suitable method for extracting easily usable state-specific cross sections from its “raw” format. Given the sheer size of the database, this process has to be conducted in an automated manner, requiring as little user input as possible.
- With the eventual application in mind, and given that a coarse-grain model is used all throughout this work, the detailed rate coefficient data taken from the database are “binned” before actual cross sections are extracted from them.
- In addition to generating the cross section data suitable for DSMC, a complementary task consists in writing a dedicated code with which to study the behavior of the model in simplified flow configurations. As an added benefit, this allows one to gain insight into the

basics of the DSMC method and to maintain control over all aspects of the implementation.

- Although the stand-alone DSMC code written as part of this thesis is useful for model verification purposes, it is not suited to performing large-scale simulations of atmospheric entry flows. It lacks both the capability of handling complex 2D/3D geometries and the ability to make use of parallel computer architectures. Thus, in order to apply the model to such flows, the external RGDAS code is used. This in turn, requires several adaptations of the state-to-state model

### 1.3. Thesis outline and main contributions

This thesis is structured as follows: The necessary theoretical background is condensed into **Ch. 2**. It begins by recalling some basic concepts from the field of rarefied gas dynamics specifically relevant for this work. This includes a short review of the state of the art concerning the direct simulation Monte Carlo method, as applied to atmospheric entry flows. In order to give context to the new developments discussed in later chapters, first the concept of a state-to-state description for the treatment of the rovibrational energy modes of a diatomic gas is recalled. Since this thesis deals exclusively with the integration of the NASA Ames quantum chemistry model for nitrogen into DSMC, the high-fidelity potential used by the NASA chemists is briefly discussed. Here, the purpose is to highlight the existence of the two distinct types of energy levels (truly bound vs. quasi-bound), and the differences in their behavior. In addition to this, the main contents of the ab initio database itself are presented. The intention is to give an overview of the detailed chemistry processes contained in the database and to present a small sample of the raw data it contains. Finally, the coarse grain model (in this case the URVC bin model) used to reduce the size of the full mechanism is recalled. This model is crucial to compress the information of the database into a manageable size for large-scale DSMC simulations.

Details about the implementation of the state-to-state mechanism in conjunction with the URVC bin model in DSMC are discussed in **Ch. 3**. First, a procedure for obtaining analytical expressions for the state-specific reaction cross sections is discussed. Then, these analytical cross sections are compared to binned cross sections derived from “raw” data extracted directly from the Ames database. This serves as a sanity check on the analytical forms, which are the ones ultimately used in the actual DSMC computations. Following this, details on adapting the DSMC collision algorithm to properly handle the state-to-state mechanism are discussed at length. To conclude this chapter, the influence of different URVC binning “strategies” on the thermodynamic properties of the nitrogen mixture is examined. Here, the goal is to obtain a good match with the behavior of the full set of levels, while maintaining the number of bins as small as possible.

The two test cases discussed in **Ch. 4** serve both to verify the implementation of the bin model

in the special-purpose VKI DSMC code, as well as to study the behavior of the chemical-kinetic data extracted from the Ames database. In the first case, unsteady internal energy excitation and dissociation of  $N_2$ -molecules in an adiabatic 0D-reactor is simulated using DSMC. The results are compared to equivalent master equation results, and excellent agreement between the two methods is found. Following this, a steady, normal shock wave in nitrogen is simulated using the same bin model. This test case highlights the advantages of fine-tuning the distribution of rovibrational levels, in order to match the low-temperature behavior of the full set of levels with only 10 bins.

**Ch. 5** presents the use of the state-to-state bin model in conjunction with RGDAS, an established, production-level DSMC code. To begin with, several adaptations to be taken into account for using the bin model in RGDAS are discussed. Following this, the bin model is used in the simulation of a hypersonic flow impinging on a cylinder of infinite length. This simplified 2D flow configuration is intended to mimic the conditions encountered by a blunt body entering the atmosphere near lunar return speeds. The resulting flow features and surface parameters obtained with the bin model are examined and compared to those obtained from reference calculations using conventional models. These cylinder simulations are carried out at two different values of the free-stream density in order to observe the effect of the degree of rarefaction on the chemical activity in the bow shock region. As a final test case, a full three-dimensional geometry is used to apply the state-to-state model to simulate atmospheric entry of an actual return vehicle, in this case ESA's Intermediate eXperimental Vehicle (IXV). Rather than expecting accurate predictions of aerodynamic coefficients and surface heat flux distributions, this test case is intended to demonstrate the feasibility of using the bin model in large-scale DSMC simulations.

Finally, concluding remarks and some suggestions for future work are presented in **Ch. 6**.

The main contributions of this thesis are thus covered in **Ch. 3** to **Ch. 5**. They include the development of a simple methodology for extracting cross sections from state-to-state rate coefficients. This technique should make it possible to “digest” a chemical mechanism as large as the one of the NASA Ames N3 database and to derive useful cross section data from it with a reasonable amount of effort. Although the mathematics behind the analytical inversion technique are not new, applying the method to such a large system and ensuring that the resulting detailed chemistry cross sections comply with detailed balance relations constitute an approach not commonly followed in the DSMC community. To this day it is still commonplace to rely on phenomenological models for treating chemistry and internal energy exchange. The analytical inversion technique used in this thesis should prove especially powerful when coupled with a coarse-grain model (in this case the URVC bin model) to reduce the size of the original detailed chemistry mechanism. Only the significant size reduction achieved with the help of this coarse-grain bin model will make large-scale multi-dimensional DSMC simulations feasible in reasonable times. Although it must be stressed that the uniform bin model was well-established before being used in this work, its

integration within the DSMC method has never been attempted before. As part of this integration, a new “binning strategy” involving bins of variably-sized energy intervals will be proposed. This new approach should prove to be superior to the previous equally-spaced bins in matching the gas thermodynamic properties of the full set of rovibrational levels, requiring only about ten bins in total. This, in turn should make it possible to apply the resulting model to large-scale DSMC simulations. Finally, a particularly useful side-effect of the analytical inversion technique followed in this thesis is the relative ease with which the detailed chemistry state-to-state model could potentially be integrated into the collision routines of an existing production-level DSMC code. By making clever use of the already implemented framework for chemistry based on the classical TCE model, changes to the source code of this external DSMC code could hopefully be avoided.



## 2. Theoretical Background

### 2.1. Rarefied gas dynamics: Relevant parameters and computational methods

One may approach the numerical simulation of gas flows with the help of several different methods, depending on the required level of detail (see Tab. 2.1). At the smallest scales, the gas may be described as a collection of molecules and atoms. Each one of these particles has a distinct position and velocity at any given instant. Individual molecules interact with each other via attractive and repulsive intermolecular forces, which will affect their trajectories in space. In order to determine the behavior of the gas as a whole, one must then track the individual trajectories of all particles over time. The motion of every individual particle is governed by Newton's laws (when classical mechanics is applicable), or the Schrödinger equation (when quantum-mechanical effects have to be taken into account). Computer simulation techniques for gases at this microscopic scale, nowadays referred to as Molecular Dynamics (MD), were introduced quite a long time ago by Alder and Wainwright [8, 9]. However, although this microscopic description is the most detailed, it becomes impractical for most real-life applications due to the enormous number of particles involved. For example, the number of molecules present in a cubic meter of air at standard atmospheric conditions is approximately  $2.7 \times 10^{25}$ . Tracking the trajectories of such a large number of particles is clearly impossible, even with the most powerful computers available today and will remain so for the foreseeable future. Therefore, when it comes to dilute gas flows, MD has been used throughout the last decades to study only very specific small-scale problems, mostly of an academic nature.

By contrast, the classical approach in fluid dynamics is to view the gas as a continuous medium. Here, the state of the gas is expressed by means of macroscopic (i.e. hydrodynamic) field variables (e.g. mass density, average fluid velocity, temperature, etc.) which are functions of physical location and time. The evolution of these field variables is governed by sets of partial differential equations, which express the principles of mass, momentum and energy conservation at this so-called hydrodynamic scale. The best-known examples are the Euler equations for inviscid- or the Navier-Stokes equations for viscous flows. Compared to the microscopic description at the molecular level, this approach has the advantage of being much less costly in terms of computa-

tional effort and has thus found widespread application in many areas of engineering.

Table 2.1.: Classification of mathematical descriptions of gas flows based on the physical scale

Physical scale:	<b>Microscopic</b>	<b>Mesoscopic</b>	<b>Macroscopic</b>
Description:	Molecular	Kinetic	Hydrodynamic
Governing equations:	<ul style="list-style-type: none"> <li>• Newton's equation</li> <li>• Schrödinger equation</li> </ul>	<ul style="list-style-type: none"> <li>• Boltzmann equation</li> </ul>	<ul style="list-style-type: none"> <li>• Euler / Navier-Stokes equations</li> <li>• Boltzmann moment systems</li> </ul>
Numerical methods:	<ul style="list-style-type: none"> <li>• Molecular dynamics (MD)</li> </ul>	<ul style="list-style-type: none"> <li>• direct Boltzmann solvers</li> <li>• Direct Simulation Monte Carlo (DSMC)</li> </ul>	<ul style="list-style-type: none"> <li>• classical CFD, e.g. Riemann solvers</li> </ul>

As was implied by the discussion in Sec. 1.1, accurate description of the flow in terms of classical fluid-dynamical equations is limited to collision-dominated flows, whose molecular velocity distributions exhibit only small deviations from thermodynamic equilibrium. Although this is the case for the majority of flow problems of engineering interest, it does not apply to transitional and rarefied flows, such as the ones encountered in high-altitude atmospheric entry. Although the gas at these conditions can still be considered as a continuous medium, the fundamental assumptions behind the conventional hydrodynamic closure for the transport fluxes (Fourier's law, Newton's law, Fick's law, etc.) break down at these conditions, and more precise information about the microscopic state of the gas particles is needed. In general, even when dealing with such rarefied flows, it is not necessary to know the precise state of every individual molecule or atom at every instant. Instead, one may resort to a statistical description in terms of a probability density function, which specifies the instantaneous distribution of molecular velocities  $\mathbf{c}$  at every point  $\mathbf{x}$  in the flow field. This is the so-called kinetic description, where the state of the gas is specified entirely in terms of the local velocity distribution functions  $f_p(\mathbf{x}, \mathbf{c}, t)$ ,  $p \in \mathcal{S}$ , where  $p$  denotes a particular chemical species out of the set  $\mathcal{S}$ . The evolution of the (set of) velocity distribution function(s) is governed by the (set of) Boltzmann equation(s) [3]. The Boltzmann equation is an integro-differential equation, which due to the complexity of its collision term must almost always be solved numerically. Among the most prominent solution methods are direct Boltzmann solvers, relying either on Monte-Carlo integration of the collision operators [10, 11], or deterministic spectral methods [12, 13]. Alternatively, so-called Boltzmann moment methods based on higher-order closures of the macroscopic balance equations [14, 15, 16, 17] make it possible to

apply classical CFD techniques in the transitional regime. However, when it comes to engineering applications, currently the most successful method for solving the Boltzmann equation is the particle-based direct simulation Monte Carlo method (DSMC) method [18, 1].

In order to determine at which flow conditions one must resort to gas-kinetic- as opposed classical CFD simulation methods, it is useful to have an estimate of the relative magnitudes of the relevant reference quantities. From Tab. 2.2 one can see that for the kinetic- and hydrodynamic descriptions two different sets of characteristic length- and time scales are relevant.

Table 2.2.: Characteristic scales for the kinetic and hydrodynamic descriptions

	Kinetic		Hydrodynamic	
Particle mass		$m^0$		-
Collision cross section		$\sigma^0$		-
Particle density		$f^0$		$n^0$
Temperature		-		$T^0$
Length	$\lambda^0 \propto$	$1/(n^0 \sigma^0)$		$L^0$
Velocity	$U^0 \propto$	$\sqrt{k_B T^0/m^0}$		$u^0$
Time	$\tau^0 \propto$	$1/\nu^0 = \lambda^0/U^0$	$t^0 \propto$	$L^0/u_0$
Viscosity		-	$\eta^0 \propto$	$U^0 m^0/\sigma^0$

On the kinetic side, the mean free path  $\lambda^0$  is defined as the average distance a given gas particle travels between successive collisions. It is linked to the mean collision time  $\tau^0$  via the characteristic thermal velocity  $U^0$ , which in turn directly depends on the particle's mass and the gas temperature. On the hydrodynamic side, the macroscopic length scale  $L^0$  is usually linked to the size of the solid objects immersed in the flow, or of the domain under consideration. The macroscopic time  $t^0$  represents a characteristic “residence time” of the flow in the domain. Particular ratios of the reference quantities in Tab. 2.2 yield three well-known non-dimensional numbers of special significance in gas dynamics:

$$\text{Kn} = \frac{\lambda^0}{L^0}, \quad \text{Ma} = \frac{u^0}{U^0} \quad \text{Re} \propto \frac{m^0 n^0 u^0 L^0}{\eta^0} = \frac{u^0 L^0}{U^0 \lambda^0} = \frac{\text{Ma}}{\text{Kn}} \quad (2.1)$$

Here,  $\text{Kn}$  is the Knudsen number, which quantifies the degree of departure from translational equilibrium in the flow. Large values of  $\text{Kn}$  represent highly rarefied conditions, which demand use of gas-kinetic methods. By contrast, small values of  $\text{Kn}$  indicate highly collisional near-continuum behavior, which can be treated with classical CFD methods. The Mach number  $\text{Ma}$  quantifies the relative importance of gas compressibility. Such effects are the result of tight coupling between the thermodynamic state of the gas and the flow field, and they become more and more severe with increasing Mach number. By contrast, when  $\text{Ma} \rightarrow 0$ , the incompressible limit is reached. At these conditions, momentum- and energy transfer in the gas are only weakly coupled. These two non-dimensional numbers can be combined further to yield the Reynolds number  $\text{Re}$ , which quantifies the relative importance of inertial to viscous forces in the fluid. At

## 2. Theoretical Background

high Reynolds numbers, the flow is dominated by large-scale vortical structures and transport of mass, momentum and energy occurs primarily via turbulent mixing. On the opposite end of the scale, small Reynolds numbers imply dominance of viscous transport processes and so-called laminar flow.

The path of the Apollo capsule, shown previously in Fig. 1.2, can be visualized in an alternative manner, using these three non-dimensional numbers. The diagram in Fig. 2.1 roughly shows the descent trajectory of the capsule as a function of global reference-length-based free-stream Reynolds and Knudsen numbers, along with free-stream Mach number contours. From the range of Reynolds numbers shown, one can estimate that the “rarefied” portion of the reentry path occurs in the laminar flow regime. For comparison, typical conditions for commercial airliners are indicated, where  $L_{\text{ref}}$  is the length of the fuselage.

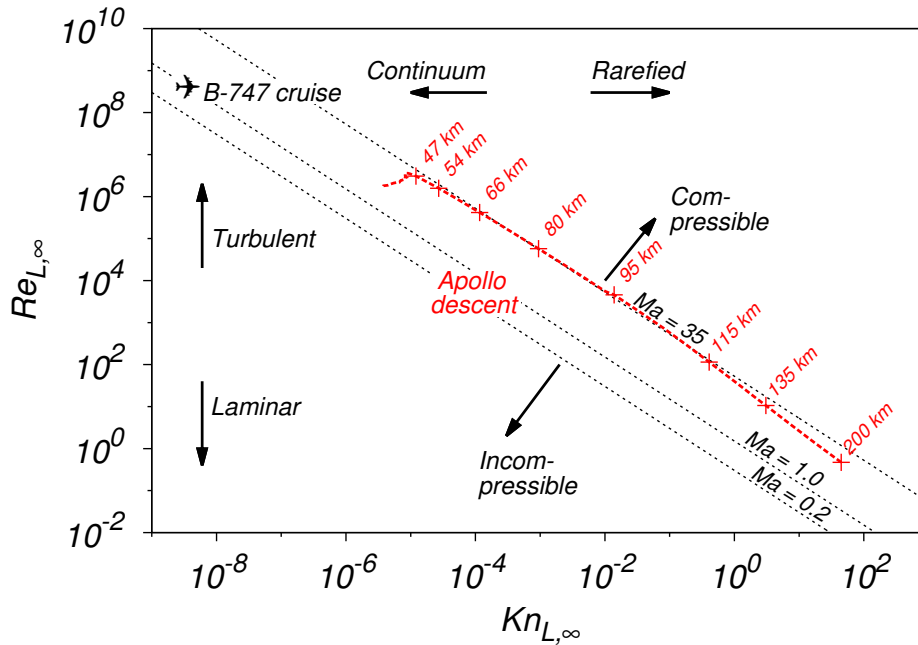


Figure 2.1.: Apollo descent in terms of free-stream Knudsen-, Reynolds- and Mach numbers

Since the Boltzmann equation describes the behavior of dilute gases at the kinetic scale, it essentially remains valid at all densities encountered during descent. This means that, at least in principle, the DSMC method could be applied over the entire range of free-stream conditions encountered by the reentry vehicle (as implied by Fig. 2.2). However, the computational cost of DSMC is directly tied to the requirement of resolving the local mean free path and collision frequency everywhere in the flow field. As the Knudsen is reduced, these resolution requirements make its use prohibitively costly. Thus, for simulating the full range of flow conditions along the reentry path, one will always depend on a combination of gas-kinetic and classical continuum-based numerical methods tailored to these particular flow regimes.

In Sec. A.1, a particular form of the generalized Boltzmann equation, which governs the evolution

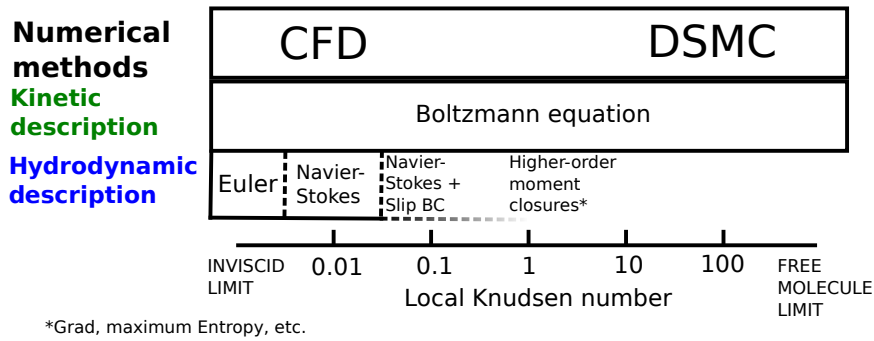


Figure 2.2.: Flow regimes and applicability of numerical models

of the nitrogen mixture discussed in this thesis is presented. It is only included for reference purposes, since this system of equations will be solved indirectly by means of the DSMC method. The DSMC method itself has been documented extensively elsewhere [18, 1] and will not be explained here. However, in the following section, a short overview over the main developments of this method is given, concentrating on its application to atmospheric entry flows.

## 2.2. Use of DSMC in Aerospace applications

Since the model developed as part of this thesis is intended for use with the DSMC method, this section contains a short overview of the developments in this technique over the last decades. This review is limited to aerospace-related applications, especially those concerning atmospheric entry flows. Significant contributions to the broader field of DSMC (e.g. the work of the Milan group [19, 20], or Garcia's work [21, 22, 23] ) can thus not be discussed at length here.

As the original proponent of the DSMC method, it was G.A. Bird who initially worked extensively on aerospace applications. He introduced the total collision energy (TCE) method [24], which for many years thereafter became the standard approach for modeling chemical reactions in DSMC. With his variable hard sphere (VHS) model [25], he proposed a simple phenomenological model for elastic collision cross sections. This made it possible to reproduce macroscopic transport properties in the gas, while simultaneously reducing the execution time of the collision algorithms, as compared to the previously used potential-based cross section models. Together, these two developments allowed for a much more realistic treatment of physico-chemical processes in atmospheric-entry-related problems [26]. Although not exclusive to aerospace applications, another major contribution to the development of DSMC was his no time counter (NTC) scheme, which allows for efficient particle selection routines [27] and is still in use in many current DSMC codes. More recently, he also proposed an alternative to the classical chemistry routines [28], which among other things, links the rates of vibrational excitation to the dissociation rates in air [29]. This is what eventually came to be known as the Quantum-Kinetic (QK) model [30, 31].

Certainly, a major portion of the DSMC development for aerospace applications has been conducted over the years by various groups in the United States. Among these, the one at NC State University was especially active in the early 1990's: Hassan and Hash introduced the generalized model (GHS) [32, 33] as a logical extension to the VHS model, which would include the effects of attractive forces in particle collisions. A major focus of their work was the modeling and coupling of inelastic collision processes, such as vibrational excitation with the dissociation reactions in air [34]. This work was being conducted at roughly the same time as Lumpkin [35] worked on similar applications. Especially, his contributions to the early implementation of the Larsen-Borgnakke (LB) [36] model and his efforts to make it consistent with the macroscopically observed relaxation behavior [37] are noteworthy, as initially there was some confusion in the DSMC community about the correct definition of the rotational and vibrational collision numbers [38].

During the mid-90's at NASA Johnson Research Center, the group of Le Beau developed the NASA DAC code for atmospheric entry applications [39, 40]. The DAC code was one of the first large-scale DSMC codes to make use of nearest-neighbor search algorithms inside collision cells [41]. Another one of its distinguishing features was the grid definition scheme based on an "immersed boundary"-approach [42], which made it simpler to simulate flows around bodies with complex three-dimensional shapes while maintaining a cartesian mesh for particle tracking. Among other applications, it was used by Moss to perform aerodynamic calculations to support the Mars pathfinder mission [43, 44], and to determine the aerodynamic coefficients of the Apollo [45] and Orion [46] capsules in the transitional regime. More recently the "Stochastic PARallel Rarefied-gas Time-accurate Analyzer" (SPARTA) of Sandia Laboratories [47], as well as the DSMC code developed by the group of Schwartzentruber [48] also use this immersed boundary approach. Apart from developing the SPARTA code, the group at Sandia Labs has been active in the development of the DSMC method itself [49, 50], with some direct contributions to atmospheric entry applications [51].

Another researcher who has contributed extensively to the development of DSMC for aerospace-related applications is Boyd. Since the beginning of the 1990's while at NASA Ames, he made several contributions to what has become the conventional approach to modeling of internal energy exchange and chemistry in DSMC. His first investigations were limited to nitrogen [52, 53, 54, 55, 56]. He continued refining the model for rotational-translational energy exchange by including temperature-dependence of the rotational relaxation numbers [57] and introducing discrete rotational levels for DSMC [58]. He compared the behavior of the chemistry models in DSMC to those of classical CFD solutions [59]. He also is one of the few researchers who have studied the effect of recombination reactions in DSMC chemistry modeling [60, 61]. In later work, he investigated the effect of vibration-dissociation coupling in strongly compressing flows [62, 63]. At the University of Michigan, Boyd's group has used the MONACO DSMC code [64] as a tool to determine the limitations of classical hydrodynamic models applied to

atmospheric entry flows in the transitional regime. They investigated continuum breakdown in hypersonic flows [65] and the range of validity of velocity slip and temperature jump boundary conditions to extend the range of applicability of Navier-Stokes solvers [66]. In addition to this, they have made important contributions to the development of so-called hybrid CFD-DSMC solvers. A strong coupling strategy between a Finite-Volume Navier-Stokes solver and a DSMC code was first implemented for the steady 1D normal shock problem [67]. One problem, which arises when using DSMC solutions as a boundary condition for the CFD solver is the statistical noise in the instantaneous flow macroparameters. It can cause stability issues in the Navier-Stokes solution, and strategies for reducing it were investigated by Boyd and co-workers [68]. In later work the hybrid strategy was adapted to 2D geometries, more representative of atmospheric entry flows [69, 70]. In addition to coupling DSMC with classical CFD codes, they also investigated hybrid schemes, where both the rarefied and continuum regions were solved using a particle method. Their so-called low-diffusion (LD) method was first applied to normal and oblique shock wave problems [71]. Later, the LD model was extended to include viscous effects, in order to simulate the expansion in nozzles [72] and 2D atmospheric entry problems including rotational and vibrational nonequilibrium [73]. On the topic of high-fidelity modeling of air chemistry, Boyd et al. [74] have proposed a vibrational state-resolved model based on the forced harmonic oscillator (FHO) model of Adamovich [75, 76], and later also performed Monte Carlo simulations of nitrogen dissociation based on state-resolved cross sections [77].

More recently, at the University of Minnesota the group of Schwartzenuber has worked on optimization of the DSMC method for massively parallel multi-processor clusters [78]. Their DSMC code is based on an immersed-boundary type approach to geometry representation and a multi-level cell approach [79, 48] and automatic mesh refinement [80]. The group is also active in integrating physical models, originally based on molecular dynamics [81] into the DSMC method [82]. The resulting DSMC scheme computes all steps of the algorithm as usual, except for the determination of the post-collision particle velocities, which in each instance are obtained as the result of full trajectory calculations [83].

At UT Austin, a purpose-build DSMC code has been developed to simulate astrophysical phenomena, such as the rarefied atmosphere of Jupiter's volcanic moon Io [84, 85]. However, the Austin group also has worked on applications directly relevant to Earth atmospheric entry [86, 87, 88].

Another influential group in the development of the DSMC method itself, and in its application to high-speed compressible flows is the one of the late Ivanov at the Institute of Theoretical and Applied Mathematics (ITAM) in Novosibirsk, Russia. Although Ivanov's early work was not well-known in the west, he made important contributions to developing the theoretical background for the DSMC method [89]. A review article [90] summarizes many of the groups developments in the field up to the end of the 1990's. For simulating large-scale aerothermodynamic

problems, they developed the SMILE DSMC code [91]. This software package has been used to study many practical problems, such as the aerodynamics of the Mir space station during its demise [92]. The state of the art in physico-chemical models at the time were integrated into the SMILE code [93, 94]. A long-time user of SMILE in the United States is the group of Levin at Penn State and later UIUC. Among other topics, this group is working on the integration into DSMC of state-specific models for vibrational relaxation and molecular dissociation of nitrogen [95, 96]. Since the “Russian school” developed the DSMC method on a somewhat different basis than Bird in the west, the resulting particle selection algorithms exhibit some differences. In [97], Bird’s no time counter (NTC) and Ivanov’s majorant collision frequency (MCF) schemes were compared for the first time within the same code.

In Asia, the development of DSMC was initially concentrated in Japan. In the early 1970’s Koura was one of the earliest adopters of the method [98]. Simultaneously, Nanbu developed his own version of the DSMC method from a strong mathematical viewpoint, closely adhering to the Boltzmann equation [99]. Throughout the 1990’s, Koura’s group was very active in the development of DSMC. He proposed the still widely-used variable soft sphere (VSS) model [100, 101], which allowed more accurate modeling of diffusion in gas mixtures. Koura also was one of the early proponents of using classical trajectory calculations (CTC), replacing the random sampling of post-collision states. This was useful in the case of diatomic molecules, which possess internal degrees of freedom in addition to the translational ones [102, 103]. His work inspired Schwartzentruber to continue developing the combined DSMC-CTC approach (see above). In China, inspired by the work of Hassan, Hash and Koura, Fan proposed the Generalized Soft-Sphere (GSS) model [104]. This model combined the attractive-repulsive behavior of the GHS model with the anisotropic scattering of the VSS model. It was later modified by Kim [105] to better reproduce the high-temperature behavior predicted by high-fidelity collision integrals.

In Europe, several groups have been active in the development of DSMC for aerospace applications. While working at DLR, Bergemann, together with Bird proposed a new discretized version of the Larsen-Borgnakke model for the vibrational mode of diatomic molecules [106]. This marked a shift away from the until-then common practice of assuming continuously distributed energies for the vibrational mode and was adopted by many other researchers. Also during the 1990’s, at the University of Stuttgart, Laux and Fasoulas developed a DSMC code (Las Vegas) with aerospace applications in mind [107, 108]. The code was optimized for parallel execution on unstructured grids [109] with the help of local time-stepping [110]. Its successor is called Pi-CLas [111], and includes the added capability of the Particle-in-Cell method for charged species in ionized flows. Meanwhile, at the University of Strathclyde, the group of Scanlon is developing DSMCfoam, based on the popular OpenFoam CFD package [112].

## 2.3. State-to-state models for internal energy excitation and molecular dissociation in nitrogen

Several groups have worked on introducing state-to-state models into gas-kinetic simulations methods such as DSMC. An early implementation of a state-to-state model in DSMC was proposed by Anderson et al. [113]. They considered a model gas with only a few internal states defined at arbitrary energy levels. The cross sections in their model were computed explicitly from expressions, which were designed such that detailed balance would be satisfied. If, however these cross sections are applied to the internal levels of a real gas, the transition rates will generally not match those known from experiment, and therefore they are not suited to real-life applications, such as atmospheric entry flows. Bruno et al. [114] implemented a vibrationally-specific model for nitrogen. In their work 66 distinct vibrational levels for the nitrogen molecule. For diatom-atom collisions, i.e.  $N_2(v) + N$ , they used cross-section data based on quasi-classical trajectory (QCT) calculations performed by the group at the University of Bari. Data were available for both excitation/deexcitation [115] and dissociation [4]. This was one of the earliest instances where QCT databases were used successfully within DSMC. More recently, Li and Levin [95] have combined cross sections based on the forced harmonic oscillator (FHO) model for vibrational-translational (VT) transitions and on QCT for dissociation reactions in state-to-state simulations of shock waves in nitrogen.

In the state-specific approach each molecule's internal state, defined by its internal quantum numbers, must be tracked during the simulation. Two particles of a given chemical species (i.e.  $N_2$  in its ground electronic state) with identical vibrational and rotational quantum numbers ( $v, J$ ) are both considered to belong to the same separate "pseudo-species" (e.g.  $N_2(v, J)$ ), which is distinct from all other rovibrational energy levels of  $N_2$ . For molecular nitrogen the total number of coupled rovibrational levels in the ground electronic state alone is on the order of 10000. Therefore, the number of separate species to be considered in a state-specific description is orders of magnitude larger than in the traditional approach, even if only a pure gas is considered. Since each quantum state of a molecule is treated as a separate species, transitions between states become equivalent to chemical reactions. This includes transitions of a molecule between different pre- and post-collision quantum numbers (i.e. excitation/deexcitation), but also the state-specific chemical reactions such as dissociation/recombination and exchange reactions. Since dissociation can occur with a given probability from any initial quantum state, the number of separate dissociation reactions for a single molecule increases with the total number of internal levels considered. One immediate consequence of such a detailed description is that a full set of state-specific cross sections is required to determine the outcome of each collision. These cross-section data must typically be obtained by computational quantum chemistry calculations. However, even nowadays this remains a formidable task, and for many mixtures of interest (i.e. Earth, Mars at-

mosphere), full sets of cross-section data are not yet available. Quantum chemical data have been limited mostly to two-component systems, such as  $N_2 + N$ , where often only collisions of a molecule with an atom are taken into account. One of the most detailed sources of cross-section data available is based on the *ab initio* quasi-classical trajectory calculations (QCT) of Jaffe et al. [5] for the  $N_2 + N$ -system. This database has already been used by Kim and Boyd [116] within the framework of DSMC simulations.

While state-to-state models based on quantum-chemical databases incorporate very accurate cross section data derived from first principles, they come at the added cost of introducing a large number of species and reactions into the computational model. This makes using the full  $N_2 + N$  database prohibitively expensive for full-scale engineering simulations. As a remedy, so-called “coarse-grain” models have been proposed. One such model is the uniform rovibrational (URVC) bin model of Magin et al. [117], which had been developed for continuum Computational Fluid Dynamics (CFD) applications, but whose extension to gas-kinetic simulation techniques is currently underway. A major goal of the present work is to provide a methodology to generate reaction cross-section data for the URVC model based on the database developed at NASA Ames Research Center.

This remainder of this chapter is structured as follows: In Sec. 2.4 a high-fidelity model for molecular nitrogen is introduced. It forms the basis for obtaining the rovibrational energy levels in the ground electronic state of  $N_2$ , which are used throughout this work. The quantum-chemical database developed at NASA Ames is briefly introduced in Sec. 2.5. Next, in Sec. 2.6 the uniform rovibrational (URVC) bin model for internal energy exchange is reviewed, and in Sec. 2.7 the Arrhenius-fitted forms of the state-specific rate coefficients are discussed.

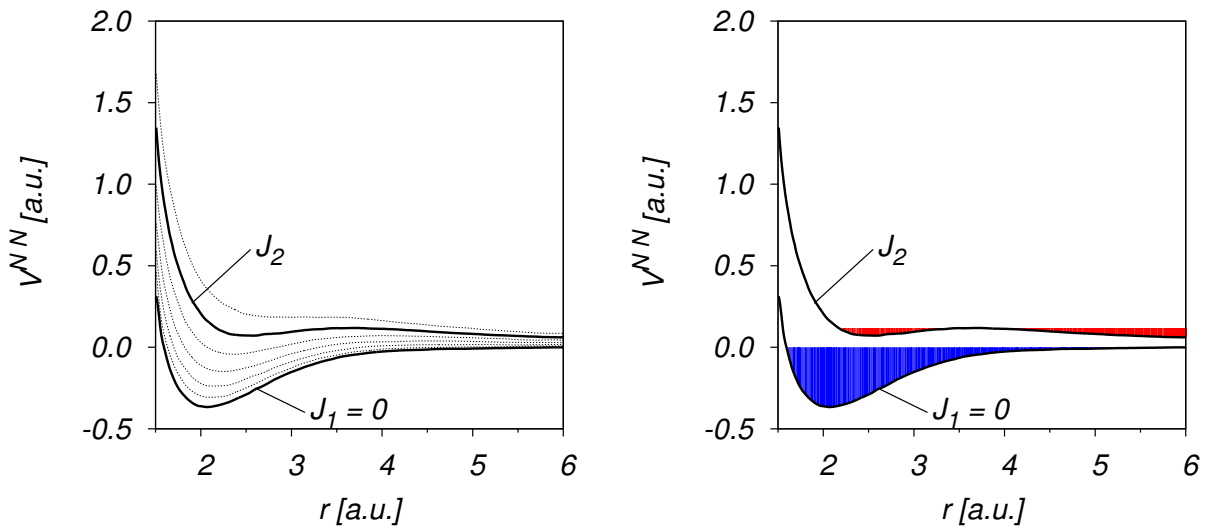
### **2.4. High-fidelity model for $N_2$ : Rovibrational levels derived from the modified Le Roy potential**

The rigid rotor and harmonic oscillator represent the simplest models to approximate the behavior of diatomic molecules. They are accurate enough to determine the thermodynamic properties of gases at moderate temperatures and still find widespread use in numerical modeling of hypersonic flows. However, they are less suited in the context of high-temperature chemically reacting flows, where predicting correct rates of internal energy transfer and dissociation depends on an accurate representation of the intermolecular potential. This has been recognized in the aerospace community for a long time, but only since fairly recently are accurate data based on *ab initio* quantum chemistry calculations being incorporated into CFD and other numerical simulation methods. One such effort was undertaken by the quantum chemistry group at NASA Ames research center [5]. They began by computing the 9390 rovibrational levels in the ground electronic state of  $N_2$

based on a modified version of the high-fidelity Le Roy potential [118]. Several instances of this fitted potential are plotted in Fig. 2.3, which has been adapted from [119]. Fig. 2.3(a) shows the potential energy as a function of the inter-atomic distance, both expressed in terms of Hartree atomic units, for several rotational quantum numbers, starting from the lowest at  $J = 0$ . The precise energies for a molecule with a given combination of vibrational and rotational quantum numbers would be indicated by straight horizontal lines bounded by these potential energy curves. Individual lines are not shown, as they are closely clustered together, making it difficult to distinguish them. One can see that for all  $J$  the potential energy rises steeply as  $r \rightarrow 0$ , implying that both N-atoms strongly repel each other the shorter the internuclear distance. Although not clearly visible in Fig. 2.3(a), at very large inter-atomic distances, the potential energy for all curves will tend towards zero. This represents the condition when the  $N_2$ -molecule is fully dissociated, and the two atoms no longer exert any force on one another. In between these two extremes, all but the highest-energy curve exhibit visible local potential energy minima in the vicinity of  $r \approx 2.1 \dots 2.5$  atomic units. When the pair of N-atoms finds itself in this region, they are said to be trapped in the “potential well”, and remain together as a molecule. Two distinct variations of this condition are shown in Fig. 2.3(b) for the cases with  $J_1 = 0$  and a second curve at a much larger rotational number, labeled  $J_2$ . For  $J_1 = 0$ , the local minimum is also the global minimum, and the blue shaded region covers all values where  $V^{NN} < 0$ . The minimum value of this curve lies 0.358 Hartree energy units below zero, which corresponds to 9.75 eV. This is exactly the amount of energy needed to dissociate the molecule when it is located in its rovibrational ground state, i.e. ( $v = 0, J = 0$ ). In order to lift a molecule out of the potential well, external energy, e.g. in the form of relative translational energy during a collision with a third particle, must always be added to the system. Therefore, these are stable molecule configurations and the rovibrational states below  $V^{NN} = 0$  are called *truly bound*. A different situation is encountered for the second curve at a much higher rotational number. Although a potential well exists here as well, allowing for a bound N-N pair in states ( $v, J_2$ ), it is much shallower than in the previous case. The energy difference between the bottom of the well and the neighboring local maximum of the so-called centrifugal barrier is now much smaller. This means that significantly less energy has to be added to the system in order to lift it above the centrifugal barrier and separate the two atoms. Furthermore, since  $V^{NN} > 0$ , any molecule located in the potential well in principle already possesses enough energy to dissociate on its own. The permissible states of such a molecule are indicated by the two regions shaded in red, to the left- and right of the centrifugal barrier. Due to quantum tunneling effects, such molecules can transition spontaneously from inside the potential well to the outside region to the right. Therefore, these configurations are unstable in the long term, and such rovibrational states are called *quasi-bound*, or *pre-dissociated*. Many of the potential energy curves for rotational quantum numbers between  $J_1 = 0$  and  $J_2$  allow for a combination of both truly bound and quasi-bound levels. This is the case where the bottom of the potential well lies below  $V^{NN} = 0$ , but where the centrifugal barrier exists and is located above zero. The distribution of all permitted combinations of rotational and vibrational numbers is sketched in Fig. 2.4(a),

## 2. Theoretical Background

and one can see that for all rotational quantum numbers below  $J = 214$ , a fraction of the levels is truly bound and the other is pre-dissociated. Finally, the highest-energy curve in Fig. 2.3(a) shows the expected trend with ever-increasing  $J$ . The potential well disappears above  $J = 279$ , which means that the intermolecular force will act to repel the two atoms at any internuclear distance, and thus no bound states of any kind are allowed to exist beyond this point. This limit is seen in the top left corner of Fig. 2.4(a), where the last filled dot is located at  $(v = 0, J = 279)$ . Focusing now on the nomenclature used, each level is identified by a unique pair of vibrational



(a) Potential energy curves for selected rotational quantum numbers  $J$

(b) Blue shaded area: Possible energies for truly bound levels at  $J_1 = 0$ , Red shaded area: Possible energies for quasi-bound levels at  $J_2 > 0$

Figure 2.3.: Modified Le Roy potential for describing interaction between two atoms composing a nitrogen molecule

and rotational quantum numbers  $(v, J)$ . These are distributed among 61 vibrational levels, each one comprising a distinct number of rotational levels, as shown in Fig. 2.4(a). The degeneracy associated with each level is a function of the rotational quantum number  $J$ :

$$a_{v,J} = \begin{cases} 6 \cdot (2J + 1) & \text{for } J \text{ even,} \\ 3 \cdot (2J + 1) & \text{for } J \text{ odd.} \end{cases} \quad (2.2)$$

Here, the species sub-script has been dropped for convenience, i.e.  $a_{v,J} = a_{N_2(v,J)}$ . The multiplying factors of 6 and 3, distinguishing even and odd rotational quantum numbers, are a product of taking into account the nuclear spin degeneracy. After choosing a suitable ordering scheme for the individual rovibrational levels, it is possible to map their quantum number pairs  $(v, J)$  to a

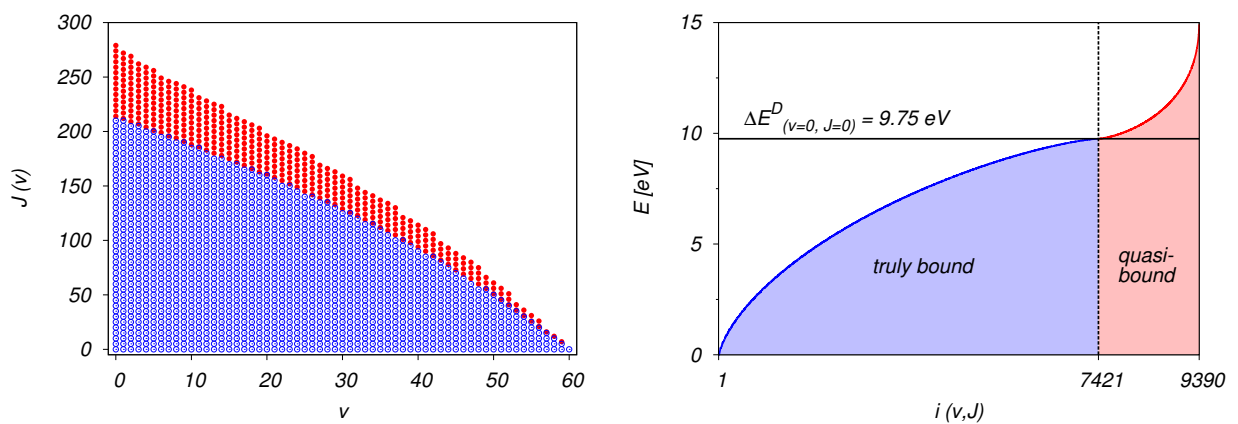
global index  $i$ . The two notations are related by:

$$\begin{aligned} i = i(v, J), \quad \text{with } v = 0, \dots, v_{\max} \\ \text{and } J = 0, \dots, J_{\max}(v), \end{aligned} \quad (2.3)$$

with an inverse relation existing as well:

$$v = v(i), \quad J = J(i), \quad i \in \mathcal{I}_{\text{N}_2}. \quad (2.4)$$

In Eq. (2.4) the set of rovibrational levels of  $\text{N}_2$ , which contains all level indices  $\mathcal{I}_{\text{N}_2} = \{1,$



(a) Distribution of rovibrational levels of  $\text{N}_2$  sorted by vibrational and rotational quantum numbers: every fifth rotational level is plotted. Open circles designate truly bound, filled circles represent quasi-bound or pre-dissociated. Levels with energy lower than 9.75 eV ( $v, J$ ) are truly bound. Those with higher energies are quasi-bound levels.

Figure 2.4.: Rovibrational energy levels in the electronic ground state of  $\text{N}_2$

$\dots, 9390\}$ , has been introduced. The precise ordering of the levels is arbitrary, but a convenient choice is to sort them in ascending order according to their energy. This particular choice will be especially advantageous for the rovibrational bin model introduced in Sec. 2.6. If the levels are arranged by increasing energy, as shown in Fig. 2.4(b), contiguous levels will have non-sequential  $(v, J)$  quantum numbers. However, this representation makes it easier to distinguish so-called truly bound from quasi-bound, or pre-dissociated levels. Truly bound levels are those whose energy lies below  $\Delta E_{(v=0, J=0)}^D = 9.75$  eV, which is the exact amount of energy required to dissociate a nitrogen molecule in the lowest rovibrational level. The fact that  $\Delta E_{(v=0, J=0)}^D > 0$  means that the dissociation reaction is endothermic (for truly bound levels only), i.e. it requires external energy to proceed. By convention, the energy of formation of the molecule in its ground state is assumed to be exactly zero, i.e.  $E_{\text{N}_2(v=0, J=0)} = 0^1$ . The dissociation energy mentioned above is in fact the difference between the formation energies of the two newly created nitrogen

atoms with respect to that of the original molecule:

$$\Delta E_{(v=0,J=0)}^D = 2 E_N - E_{N_2(v=0,J=0)}. \quad (2.5)$$

Any nitrogen molecule populating a truly bound level will have an amount of internal energy, which lies in the range  $0 < E_{(v,J)} < \Delta E_{(v=0,J=0)}^D$ . These levels are shown in Fig. 2.4(b), left of the vertical dividing line. Such molecules will require additional external energy, e.g. from collisions with other particles, in order to dissociate. By contrast, molecules which populate quasi-bound levels have internal energies lying above  $\Delta E_{(v=0,J=0)}^D$ . This makes it possible for them to dissociate spontaneously without the need of external energy, hence their alternative name: pre-dissociated. Quasi-bound levels are located to the right of the dividing line in Fig. 2.4(b). Based on this sub-division, one may define the set of truly bound levels  $\mathcal{I}_B = \{1, \dots, 7421\}$ , as well as the set of all pre-dissociated levels  $\mathcal{I}_P = \{7422, \dots, 9390\}$ . Of course, one has that  $\mathcal{I}_{N_2} = \mathcal{I}_B \cup \mathcal{I}_P$ . In addition to this,  $\mathcal{I}_B \cap \mathcal{I}_P = \emptyset$ , which means that the sets of truly bound- and pre-dissociated level indices do not overlap. Fig. 2.4 makes it clear that the great majority of rovibrational levels of  $N_2$  are truly bound. Although not explicitly mentioned before, it should be noted that in this model the rotational and vibrational modes are coupled, in contrast to the conventional approach of using a combination of the harmonic oscillator and rigid rotor models. The NASA Ames database for detailed chemistry of the  $N_2 - N$  system discussed in Sec. 2.5 uses precisely the set of levels discussed in this section. Furthermore, the coarse-grained models discussed in Sec. 2.6 are also linked to it.

## 2.5. NASA Ames N3 *ab initio* database

The NASA Ames N3 database contains a detailed listing of reaction cross sections for collisions of molecular nitrogen with atomic nitrogen, i.e.:  $N_2(v, J) + N$ . It was compiled at NASA Ames Research Center by the quantum chemistry group of Jaffe et al [5]. The cross sections were obtained as statistical averages over a large number of quasi-classical trajectory (QCT) calculations involving three separate nitrogen nuclei, hence the name N3. Recall that the set of rovibrational energy levels for the nitrogen molecule, previously discussed in Sec. 2.4, was obtained using the semi-empirical Leroy potential. However, the pre-requisite to performing the QCT calculations is an intermolecular potential energy surface (PES) involving three separate nitrogen nuclei. This PES allows to determine the forces exerted on the three separate nitrogen nuclei as they interact with one another. Determination of this PES is based on *ab initio* quantum-mechanical calculations, and a comprehensive description of the methodology is given by Jaffe and co-workers in

---

<sup>1</sup>Notice that this convention differs from the one adopted in Fig. 2.3. There, the molecule in the rovibrational ground state had an energy of  $-9.75$  eV, corresponding to the bottom of the potential well for  $v = 0, J = 0$ . By shifting all curves in Fig. 2.3 upwards by  $9.75$  eV, they become consistent with the present convention.

[120]. Fig. 2.5 shows the shape of the potential energy surface corresponding to a particular geometric arrangement of the three nuclei. During the course of a trajectory calculation, the shape of this surface changes along with the instantaneous relative positions of the three nuclei, affecting the resulting intermolecular forces. The three nuclei have been labeled  $N_a$ ,  $N_b$  and  $N_c$  in order to distinguish them. The relative location of the nuclei is described using so-called Jacobi coordinates. This set of coordinates consists of two inter-nuclear distances, e.g. linking  $N_a - N_b$  and  $N_a - N_c$ , plus the angle  $\theta$  (mentioned in Fig. 2.5) in the plane spanned by these two lines, with  $N_a$  at the vertex. This is all the information needed to specify the potential energy. The “height” of the surface shown in Fig. 2.5 corresponds to the magnitude of the potential energy. This is reinforced by the coloring of the surface, with the lowest-energy regions colored in blue and the higher-energy regions transitioning towards red. Four points have been given labels, denoting specific configurations of the three-nuclei system: First, the two lowest-energy states in the bottom part of the PES are labeled  $N_a + N_b N_c$  and  $N_a N_b + N_c$  respectively. These correspond to the potential energy of the system when two of the three nuclei (either  $N_b$  and  $N_c$ , or  $N_a$  and  $N_b$ ) form a bond strong enough to coexist as a molecule, with the third nucleus as a separate nitrogen atom. On the “top” of the energy surface, the point labeled  $N_a + N_b + N_c$  in the region colored in red, represents the configuration of a fully dissociated molecule. Here, all three nuclei are essentially independent from one another, existing as separate atoms. Finally, there is a fourth point found at intermediate energies, labeled  $N_a N_a N_a$ . This point lies in a small local minimum of the potential energy surface and represents a configuration where all three nitrogen nuclei are bonded together in a meta-stable type of “ $N_3$ -molecule”. This state, although theoretically possible, does not last for very long in nature and can be neglected in the following discussion. Although not immediately apparent from the image, the PES is symmetric along the plane cutting vertically through these last two points. This has to be the case, since from the full quantum-mechanical point of view the three nuclei are indistinguishable from one another. Thus, the two stable configurations involving a molecule-and-atom pair discussed before, must have the same potential energy associated to them. The labeling used here is necessary for the trajectory calculations, which rely on classical mechanics. In this approximate treatment of the collision process, one must be able to distinguish the three interacting particles. With the PES available as a function of the Jacobi coordinates, trajectory calculations involving three nitrogen nuclei are performed with a multitude of initial conditions. These conditions are selected such that a wide range of relative collision energies and impact parameters is covered. The collective results of these trajectory calculations are then evaluated statistically to determine the cross sections for the different types of detailed chemistry reactions.

The main part of the N3 database consists of the reaction cross sections and rate coefficients for collisional processes between nitrogen molecules and atoms (see Tab. 2.3).

1. Excitation/deexcitation:  $N_2(v, J) + N \rightleftharpoons N_2(v', J') + N$ . During an excitation reaction, part of the translational energy of the colliding particles is converted into rovibrational

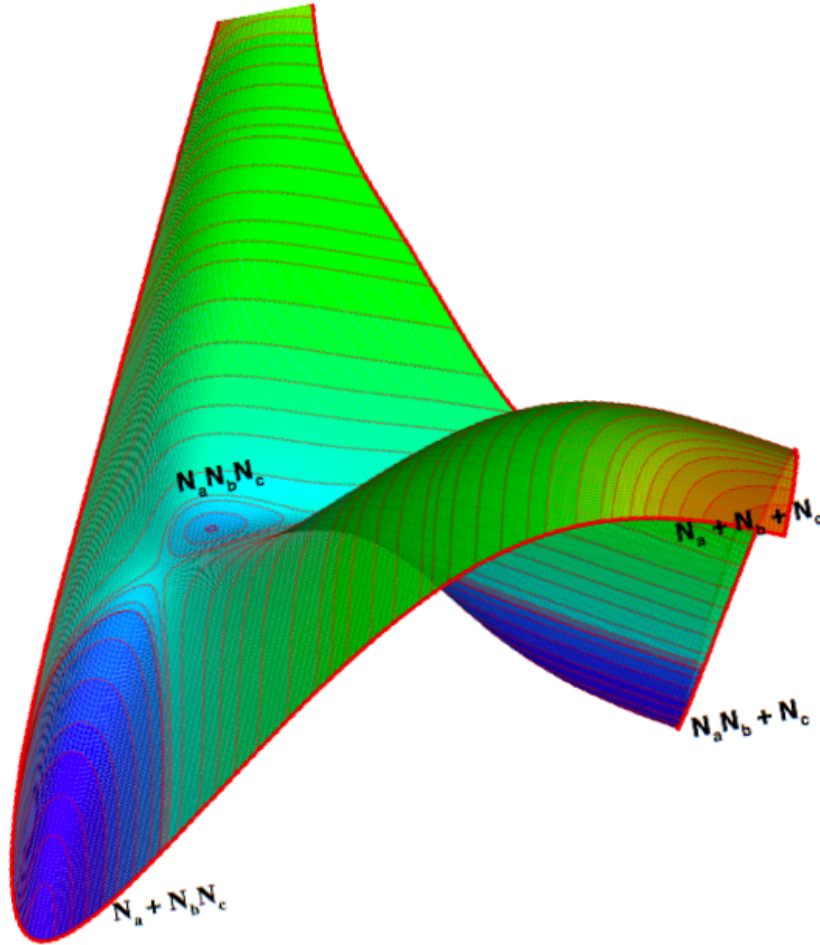


Figure 2.5.: Potential energy surface for N3-system for the particular angle  $\theta = 105^\circ$

energy of the  $N_2$  molecule (thus  $E(v', J') > E(v, J)$ ). Conversely, during a deexcitation reaction, internal energy is released by the molecule and the relative translational energy of the collision pair increases. In the special case of elastic collisions,  $(v, J) = (v', J')$ , the internal energy of the molecule remains unchanged. A distinction is made within the database between:

- a) Purely scattering (inelastic or elastic) collisions, where the nitrogen molecule remains intact during the collision, i.e.:  $N_a N_b(v, J) + N_c \rightleftharpoons N_a N_b(v', J') + N_c$ .
- b) So-called “exchange” collisions, where one of the nitrogen atoms is exchanged between the two collision partners, i.e.:  $N_a N_b(v, J) + N_c \rightleftharpoons N_a + N_b N_c(v', J')$

This distinction is only noticeable at the microscopic level, where the trajectory of each nitrogen nucleus can be tracked, but is not meaningful at the macroscopic scale. Therefore, both types of collisions involving the same pre- and post-collision quantum numbers count towards the relevant excitation/deexcitation cross section to be used in DSMC and CFD calculations.

2. Dissociation/recombination:  $\text{N}_2(v, J) + \text{N} \rightleftharpoons 3\text{N}$ . During a dissociation reaction the nitrogen molecule splits into two atoms, absorbing part of the initial collision energy. For example, breaking up the chemical bond in an  $\text{N}_2$  molecule in the rovibrational ground state requires  $\Delta E_{(v=0, J=0)}^D = 2 E_N - 0 = 9.75 \text{ eV}$ , where  $E_N$  is the energy of formation of a single nitrogen atom in its electronic ground state. Depending on the initial relative translational energy of the collision pair, dissociation is possible for molecules from both truly bound and quasi-bound levels. Recombination is the reverse elementary process.

The quantum numbers  $(v, J)$  mentioned in Tab. 2.3 point to the rovibrational levels of the  $\text{N}_2$  molecule in its electronic ground state. The precise energy of each level was determined based on the Le Roy potential, previously discussed in Sec. 2.4. Recall also the single-index notation:  $i = i(v, J)$ , introduced to identify a particular rovibrational level. Analogously, the post-collision level can be designated as  $i' = i(v', J')$ . This notation will sometimes be used in the following discussion, whenever it helps to make the mathematical expressions less cumbersome. Considering all possible combinations of pre- and post-collision states for the 9390 levels of  $\text{N}_2$ , the total number of distinct excitation/deexcitation and dissociation reactions could be more than  $88 \times 10^6$ . In practice however, many of these processes have negligibly small probabilities of occurrence and can be neglected. In addition, there exist a large number of so-called forbidden transitions whose reaction cross sections are zero due to quantum-mechanical selection rules. Therefore, the overall number of processes for which rate data is available, reduces to approximately  $23 \times 10^6$ . The N3 database provides the state-specific cross sections  $\sigma_R(E)$  as already-integrated values over the full range of post-collision scattering angles. Therefore, they are only a function of the pre-collision relative translational energy  $E = \frac{\mu_{\text{N}_2-\text{N}}}{2} g^2$ , where  $\mu_{\text{N}_2-\text{N}}$  is the collision pair's reduced mass and  $g$  is the magnitude of the pair's pre-collision relative velocity. The index  $R$  in Tab. 2.3 stands for the given reaction type, with  $\Delta E_R$  being the energy difference between products and reactants. Furthermore,  $E_{a,R}$  is the activation energy associated to every specific reaction sub-type. This threshold corresponds to the minimum amount of pre-collision translational energy, which is required in addition to the molecule's internal energy, to form the reaction products. Below this threshold the cross section (and the associated probability of reaction) must be zero. Consequently, the activation energy is set to zero for all collision types, where the reactants' internal energy is greater than, or equal to that of the products. Several example cross sections extracted from the database are plotted in Fig. 2.6. Fig. 2.6(a) shows the elastic cross section for level  $(v = 12, J = 8)$ . For a given pre-collision level, the elastic cross section is typically several times greater than the inelastic ones. This is due to the fact that most elastic collisions, especially at larger impact parameters, are so-called grazing collisions, i.e. collisions causing only small trajectory changes of the colliding particles. In this case, the interaction between the two collision partners is often not strong enough to disturb the internal structure of the nitrogen molecule. Returning to Fig. 2.6(a), the elastic cross section is non-zero starting almost immediately above  $E = 0$  and remains relatively constant around  $30 \text{ \AA}^2$  until approximately  $E = 10 \text{ eV}$ . At higher

Table 2.3.: Heats of reaction  $\Delta E_R$  and activation energies  $E_{a,R}$  for  $N_2 + N$  collision processes considered in the Ames N3 database

**Internal energy exchange:  $N_2(v, J) + N \rightarrow N_2(v', J') + N$**

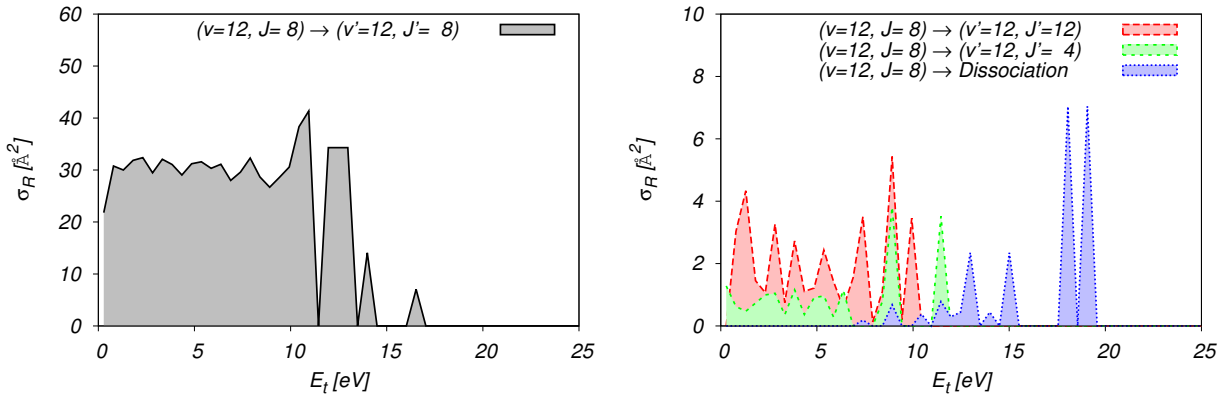
$$\Delta E_{(v,J) \rightarrow (v',J')}^E = E(v', J') - E(v, J)$$

	$E_{a,R}$
1) Excitation: $E(v, J) < E(v', J')$	$\Delta E_{(v,J) \rightarrow (v',J')}^E$
2) Deexcitation: $E(v, J) > E(v', J')$	0
3) Elastic collision: $E(v, J) = E(v', J')$	0

**Dissociation:  $N_2(v, J) + N \rightarrow N + N + N$**

$$\Delta E_{(v,J)}^D = 2E_N - E(v, J)$$

	$E_{a,R}$
1) from truly bound state	$\Delta E_{(v,J)}^D$
2) from quasi-bound state	0



(a) Integrated elastic cross section for rovibrational level ( $v = 12, J = 8$ ).

(b) Selected integrated inelastic cross sections for rovibrational level ( $v = 12, J = 8$ ). Shaded in red: excitation to level ( $v' = 12, J' = 12$ ); shaded in green: deexcitation to level ( $v' = 12, J' = 4$ ); shaded in blue: dissociation.

Figure 2.6.: Cross sections extracted from the N3 database. The cross sections have been integrated over the full post-collision solid angle.

energies the value begins to decrease and beyond 15 eV the elastic cross section is practically zero. Several inelastic cross sections for the same pre-collision level are shown in Fig. 2.6(b). The excitation and deexcitation cross sections to levels ( $v' = 12, J' = 12$ ) and ( $v' = 12, J' = 4$ ), respectively, have non-zero values up to around 10-12 eV but drop off quickly at higher collision energies. Compared to the elastic cross section, they exhibit much stronger oscillations in

magnitude. These oscillations may be a physical feature of this type of interaction, where transitions are much more probable at specific intervals of  $E$ , but may also be due in part to statistic noise introduced by the limited number of trajectories available to compute the cross section. In terms of energy difference, the pre- and post-collision levels chosen here lie fairly close to one another. It is assumed that such transitions are much more likely than those involving larger energy jumps and that they contribute to most of the internal energy exchanged in the gas. The third cross section shown in Fig. 2.6(b) is for dissociation from level ( $v = 12, J = 8$ ). The internal energy of this level lies approximately 3.25 eV above the rovibrational ground state. Therefore, the minimum energy required for dissociation is  $\Delta E_{(v=12, J=8)}^D = 2 E_N - 3.25 \text{ eV} = 6.5 \text{ eV}$ , and below this threshold the dissociation cross-section is zero. Beyond this value, the dissociation cross section increases and oscillates slightly in the range of 1 to  $2 \text{ \AA}^2$  up to around  $E = 15 \text{ eV}$ . Finally, it exhibits two large peaks at energies around 17 and 19 eV, before it then drops down to zero at higher energies. Due to the large number of transitions in the database, not all cross sections could be thoroughly examined, but it is assumed that their behavior will be very similar to that exhibited by the samples in Fig. 2.6.

Temperature-dependent rate coefficients  $k_R(T)$  for every reaction are obtained by thermally averaging the corresponding cross sections, as given by Eq. (2.6). Although theoretically the integration limits range from zero to infinity, most of the cross sections are non-zero only within a certain energy range. The lower integration limit is given by either 0 or  $\Delta E_R > 0$  (see Tab. 2.3), while practically all cross sections considered in the database are zero at energies above 30 eV. Thus, when numerically computing the rate coefficients, it is enough to perform the integration in Eq. (2.6) up to this limit.

$$k_R(T) = \frac{1}{\sqrt{\pi} \mu_{N_2-N}} \left( \frac{2}{k_B T} \right)^{3/2} \int_{E_{a,R}}^{\infty} \sigma_R(E) \exp\left(-\frac{E}{k_B T}\right) E dE \quad (2.6)$$

For the cross sections of Fig. 2.6 the corresponding rate coefficients are plotted in Fig. 2.7. Just like the cross sections they are derived from, these rate coefficients span a wide range of values. The largest one is again the elastic rate coefficient (solid line), while in this example both the excitation and deexcitation (both dashed lines) rate coefficients are roughly one order of magnitude smaller. The rate coefficients tend to increase with temperature. This is especially true for the dissociation rate coefficient (dotted line), which increases 4 —5 orders of magnitude between 7500 and 50000 K. This behavior is a consequence of the relatively large energy threshold for dissociation. At temperatures below 10000 K approximately, the fraction of collisions in the gas with enough relative translational energy to surpass the dissociation barrier ( $\Delta E_{(v=12, J=8)}^D = 6.5 \text{ eV}$ ) is very small and the dissociation rate remains negligible. As the temperature increases, the maximum of the velocity distribution function shifts to higher energies and with it the fraction of collisions possessing enough energy to dissociate increases as well. This in turn causes the

dissociation rate coefficient to increase significantly at higher temperatures. One important fact is that, unlike the cross sections they are derived from, the rate coefficients exhibit a much smoother behavior over the temperature range considered. This is because the integration in Eq. (2.6) effectively causes some of the oscillations in the cross sections to be “filtered out.” Consequently, it becomes much easier to fit the rate coefficients to a simple analytical form, such as the well-known Arrhenius-type expressions. Before introducing the coarse-grain model used for reduction of the

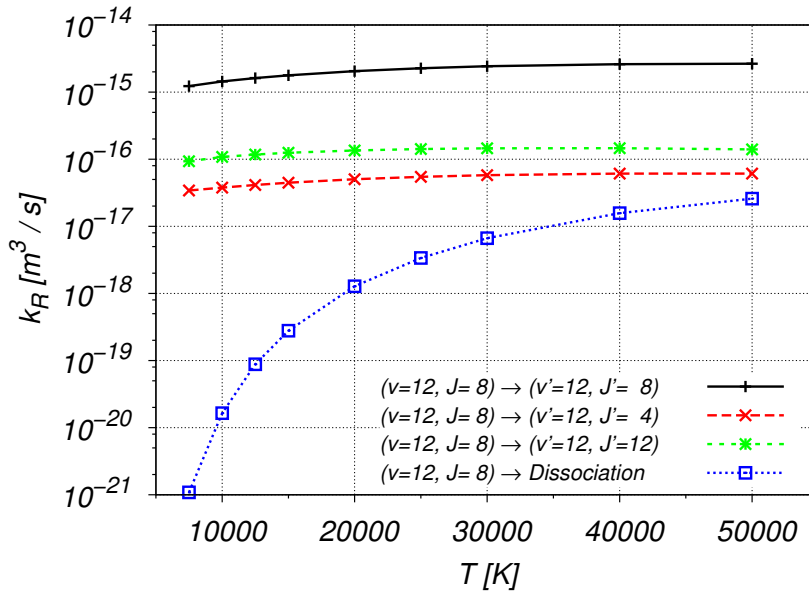


Figure 2.7.: Selected rate coefficients for level  $(v = 12, J = 8)$ . Solid curves: elastic rate; short dashed line: deexcitation to level  $(v' = 12, J' = 4)$ ; long dashed line: excitation to level  $(v' = 12, J' = 12)$ ; dotted line: dissociation.

full database, it is of interest to examine the dissociation rate coefficients more closely. For this purpose, Fig. 2.8 shows a comparison between several equilibrium dissociation rate coefficients for the reaction  $\text{N}_2 + \text{N} \rightarrow 3\text{N}$ . Data from three different sources are plotted: the open circles represent the rate coefficients determined from the NASA Ames database. These values have been computed assuming a Boltzmann distribution of the rovibrational levels at the equilibrium temperature  $T$ , according to the expression:

$$k_{\text{eq}}^D(T) = \frac{1}{Z_{\text{N}_2}^{\text{int}}(T)} \sum_{i \in \mathcal{I}_{\text{N}_2}} a_i k_i^D(T) \exp\left(-\frac{E_i}{k_B T}\right) \quad (2.7)$$

where  $a_i$  and  $k_i^D$  are, respectively, the degeneracy and the dissociation rate coefficient for rovibrational level  $i$   $(v, J)$ . In the denominator,  $Z_{\text{N}_2}^{\text{int}}$  represents the internal partition function over all rovibrational levels of  $\text{N}_2$ :

$$Z_{\text{N}_2}^{\text{int}}(T) = \sum_{i \in \mathcal{I}_{\text{N}_2}} a_i \exp\left(-\frac{E_i}{k_B T}\right) \quad (2.8)$$

The solid line in Fig. 2.8 represents the Arrhenius curve fit for these rate coefficients. For com-

parison, the dashed line shows the equilibrium rate coefficient given by Park [121]. This rate is obtained by setting  $T = T_v$  in Park's two-temperature model. The third dissociation rate, plotted as a dotted curve, is taken from the data of Moss et al. [122] and can be traced back to a report by Bortner from the 1960's. It is included here, because it is the standard dissociation rate provided in the RGDAS DSMC code, which is further discussed in Ch. 5. However, for the reference simulations with RGDAS, discussed in Sec. 5.2 and Sec. 5.3, the thermal rate coefficient based on the NASA N3 fit was used. The Arrhenius form for the fitted rate coefficients of Fig. 2.8 is given

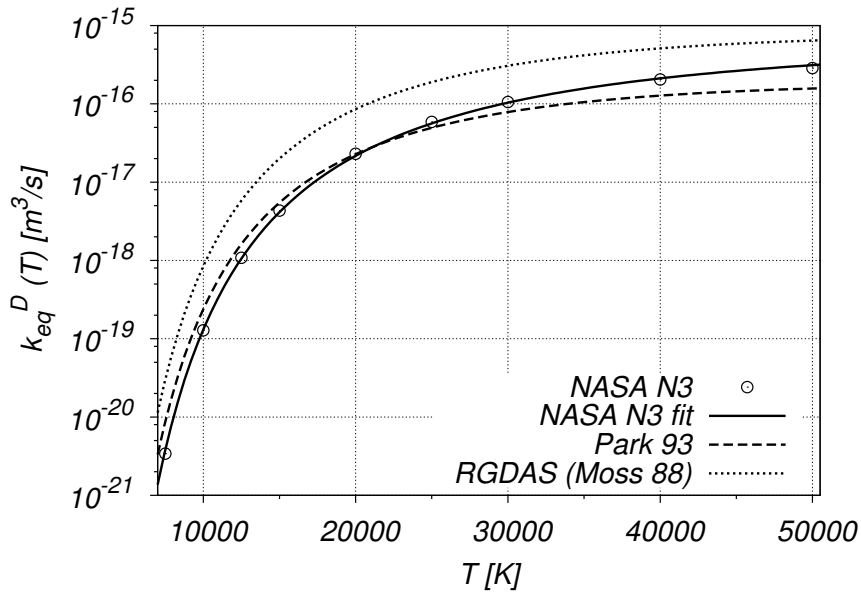


Figure 2.8.: Comparison of rate coefficients for the dissociation reaction:  $N_2 + N \rightarrow 3N$  at equilibrium

by:

$$k_{\text{eq}}^D(T) = A_{\text{eq}}^D \cdot T^{b_{\text{eq}}^D} \exp\left(-\frac{E_a^D}{k_B T}\right), \quad (2.9)$$

where the necessary numerical parameters are listed in Tab. 2.4. In all three cases, the activation energy in the exponential term of Eq. (2.9) has been set equal to  $\Delta E_{(v=0, J=0)}^D = 2 E_N = 9.75$  eV. Fairly close agreement between the dissociation rate coefficient extracted from the Ames database with Park's data is observed over the whole temperature range. Surprisingly, the data used by Moss et al. consistently predicts a dissociation rate, which is at least an order of magnitude greater than the other two. The NASA Ames database has recently been extended to include

Table 2.4.: Arrhenius fit parameters for equilibrium dissociation rate coefficient

	$A_{\text{eq}}^D$ [ $\text{m}^3 \cdot \text{s}^{-1}$ ]	$b_{\text{eq}}^D$	$E_a^D$ [J]
NASA Ames N3	$1.59 \times 10^{-11}$	-0.79	$1.561 \times 10^{-18}$
Park 93	$4.98 \times 10^{-8}$	-1.6	$1.561 \times 10^{-18}$
Moss 88	$6.90 \times 10^{-8}$	-1.5	$1.561 \times 10^{-18}$

the “N4”-processes, i.e. inelastic collisions between two nitrogen molecules. However, at the

moment of writing this thesis, these rate data were not available to us. Furthermore, it should be noted that the Ames database is not the only set of QCT-based cross sections for nitrogen currently available. Already in the late 1990's the group of Capitelli in Bari published results on vibrational-specific excitation and dissociation rates for the N<sub>3</sub>-system [4, 115]. More recently, the Truhlar group at the University of Minnesota has published results on a potential energy surface for the N<sub>4</sub>-system [123, 124]. This PES was later used to perform trajectory calculations, in order to determine dissociation rates for the reactions.  $N_2 + N_2 \rightarrow N_2 + 2 N$  and  $N_2 + N_2 \rightarrow 4 N$  [6]. It is likely that this PES will be used in the future to obtain internal energy exchange rates for the N<sub>2</sub>+N<sub>2</sub>-pair, but may also be adapted to yield the corresponding rates for the N<sub>2</sub>+N pair.

### 2.6. Uniform rovibrational collisional (URVC) energy bin model

The full NASA Ames N<sub>3</sub> database has been successfully used in CFD studies of the dynamics of internal energy excitation and dissociation in nitrogen mixtures [125, 7], while Kim and Boyd [116] have integrated it into a DSMC solver. Both hydrodynamic and kinetic simulations using the full set of levels are extremely computationally expensive, due to the large number of internal energy states and processes involved. Thus, they have mostly been limited to master equation studies involving space-homogeneous heat baths and one-dimensional inviscid flows, such as flow across idealized normal shocks. To remedy this situation several types of coarse-grain models have been proposed over the years. The details of the reduction vary for each flavor of model, but the basic concept is always to approximate the behavior of the full set of levels with a much smaller number of suitably defined internal energy "bins", whose properties are averages over the constituting levels. This lumping-together of internal energy states automatically leads to a significant reduction in the number of associated state-to-state reaction rates and greatly reduces the cost of simulations. Here we enumerate some of the binning strategies that have been proposed in recent years, with particular emphasis on those used with the NASA Ames N<sub>3</sub> database:

1. A vibrational-specific collisional (VC) model was originally used by Bruno and co-workers [114] to simulate thermochemical nonequilibrium in shock waves using DSMC. In their implementation the roughly 60 vibrational levels of the N<sub>2</sub>-molecule were treated using a state-to-state approach, while the rotational energy exchange was handled using the conventional Larsen-Borgnakke model [36]. More recently, within the context of classical CFD, Munafò et al. [126] used a vibrational-collisional model to study the chemical nonequilibrium and chemically frozen flow in nozzle expansions. In this work, the independently obtained QCT databases of NASA Ames [5] and of the Bari group [4, 115] were compared. Since the VC model maintains the classic paradigm of keeping vibrational and rotational levels separate, in the hydrodynamic description it is assumed that the rotational levels always follow a

Boltzmann distribution at the common rotational-translational temperature  $T = T_{\text{rot}}$ . This equilibrium assumption was found in later work [127] to be the cause for overestimation of the dissociation rates within shock waves. Any coarse-grain model, which overcomes this deficiency must therefore be formulated without this assumption.

2. One attempt at formulating such a model is the Uniform Rovibrational collisional (URVC) bin model, which will be discussed more in detail in this section, and which forms the basis for all the simulations of this thesis. It was previously studied by Magin et al. [117] in the context of classical CFD applications. In this model, all the 9390 rovibrational levels are lumped together into a small number of bins (See the remainder of this section). Unlike in the VC model, the levels assigned to each bin are not grouped together according to their vibrational quantum numbers, but rather according to their energy.
3. Beyond the URVC model, the Boltzmann Rovibrational collisional (BRVC) bin model has been particularly successful in reproducing the thermodynamic properties and chemical-kinetic behavior of the full set of levels [128]. This model and its later evolution, called Hybrid bin vibrational collisional (HyBVC) [129] allow to reduce the number of bins to numbers significantly less than 10. However, in both cases it requires the use of suitable temperatures to determine the individual level populations within a bin. Although this poses no problems when using a hydrodynamic description, the use of macroscopic parameters, such as temperature, to determine the internal states of individual DSMC particles is in conflict with the kinetic description and should in principle be avoided. This fact became evident to the author after a failed attempt at implementing the BRVC model within the VKI DSMC code [130], where it was impossible to attain the correct excitation/deexcitation rates necessary to maintain equilibrium bin populations within an adiabatic reservoir. Therefore, these models were not pursued in the subsequent DSMC implementation.
4. The group of Levin [96, 131] have proposed an alternative so-called two-dimensional binning strategy. Unlike the URVC model discussed in this section, in their approach they attempt to maintain the distinction between rotation and vibration by only allowing levels within a certain range of rotational and vibrational quantum numbers to be lumped together in a given bin. This approach may have potential advantages when the precise populations of rotational and vibrational levels need to be reconstructed from a bin-based solution (e.g. for determining radiative properties of the gas within the flow field).

In order to make the notation in the remainder of this section less cumbersome, simplified indices will be introduced for designating the internal energy levels, etc. As was already mentioned in Sec. 2.4, the pair of quantum numbers designating a particular rovibrational level point to a single index:  $N_2(v, J) \Rightarrow N_2(i)$ , where for convenience, all levels have been ordered with ascending energy. Furthermore, the short-hand notation  $N_2(i) = i$  will be used to simplify the sub-indices relating to properties of individual levels of  $N_2$ . For example, the energy of a given level will be

designated as  $E_i$ , instead of  $E_{N_2(i)}$ . This simplification will not cause ambiguity in the expressions presented in this text, since the only mixture components considered here are  $N_2$  and  $N$ . Since it is also assumed that atomic nitrogen only exists in its electronic ground state, it requires no separate indices to label its internal energy levels. Post-collision rovibrational level indices will be primed, i.e.  $i'$ . The rovibrational bins will be labeled correspondingly with indices  $k$  and  $k'$ , and the set of all bins belonging to molecular nitrogen will be labeled  $\mathcal{K}_{N_2}$ . Analogously to the convention introduced in Sec. 2.4, this set is sub-divided into the set of bins containing only truly bound levels  $\mathcal{K}_B$  and a second set of bins exclusively composed of pre-dissociated levels:  $\mathcal{K}_P$ . Thus,  $\mathcal{K}_{N_2} = \mathcal{K}_B \cup \mathcal{K}_P$ , with  $\mathcal{K}_B \cap \mathcal{K}_P = \emptyset$ . Quantities which refer to averages over a bin are designated with an over-bar, e.g. the average energy of bin  $k$  is  $\bar{E}_k$ . The binning procedure for the URVC model is explained at length by Magin et al [117] and here only the most important aspects will be discussed.

Having sorted the rovibrational levels in ascending order according to their energy, as shown in Fig. 2.4(b), a set of arbitrarily sized energy intervals is defined. In the original approach followed by Magin and co-workers, the chosen number and width of energy intervals was free, except for the fact that truly bound and quasi-bound levels are not mixed in the same bin. Fig. 3.7 shows this schematically for a 10-bin system. Here, the height of the “boxes” corresponds to the weighted average energy  $\bar{E}_k$  of all levels within the given bin. The lower seven bins are composed only of truly bound levels, while the upper three bins are composed only of quasi-bound levels, possessing energies above  $E_{\text{diss}} = \Delta E_{(v=0, J=0)}^D$ . Another, alternative choice of 10 bins can be seen in Fig. 3.9, with all the pre-dissociated levels contained in the last bin. Notice that in both examples the bin indices  $k$  are also automatically sorted in ascending order, according to their average energy  $\bar{E}_k$ . In what follows, we now define the bin-specific quantities: The number density of molecules belonging to bin  $k$  is determined by summing over all levels involved:

$$\bar{n}_k = \sum_{i \in \mathcal{I}_k} n_i, \quad k \in \mathcal{K}_{N_2}, \quad (2.10)$$

where  $n_i$  is the number density of level  $i$ , and  $\mathcal{I}_k$  is the set of indices pointing to all rovibrational levels  $i$  contained within bin  $k$ . The degeneracy of bin  $k$ , i.e.  $\bar{a}_k$ , is given as the sum over all level degeneracies  $a_i$  contained within the bin:

$$\bar{a}_k = \sum_{i \in \mathcal{I}_k} a_i, \quad k \in \mathcal{K}_{N_2}. \quad (2.11)$$

The central assumption of the URVC bin model is that the individual level populations within each bin are fixed by the ratio of the level-to-bin degeneracies:

$$\frac{n_i}{\bar{n}_k} = \frac{a_i}{\bar{a}_k}, \quad i \in \mathcal{I}_k, \quad k \in \mathcal{K}_{N_2}. \quad (2.12)$$

The bin average energy  $\bar{E}_k$  is defined as the weighted average over the level energies within the bin:

$$\bar{E}_k = \frac{1}{\bar{a}_k} \sum_{i \in \mathcal{I}_k} a_i E_i, \quad k \in \mathcal{K}_{N_2}. \quad (2.13)$$

The same weighted averaging is applied to the rate coefficients for the reactions listed in Tab. 2.3. In particular, for the internal energy exchange processes between rovibrational levels,  $N_2(i) + N \rightarrow N_2(i') + N$ , the level-specific rate coefficients  $k_{N_2(i), N \rightarrow N_2(i'), N}^E$  are lumped together to yield the terms  $\bar{k}_{N_2(k), N \rightarrow N_2(k'), N}^E$ , i.e. the bin-averaged excitation rate coefficient for the process  $N_2(k) + N \rightarrow N_2(k') + N$ . The indices  $k$  and  $k'$  respectively represent the pre-collision and post-collision bins occupied by the  $N_2$ -molecule, while the second species index emphasizes that the rate coefficients discussed here are specific to collision with an N-atom. In order to make the following notation less cumbersome, we again reduce  $N_2(k) \Rightarrow k$  and omit this second species index, as it is implied that all reactions discussed in what follows always involve N as collision partner.

Depending on the energies of the pre- and post-collision bins involved, three possibilities exist:

1.  $\bar{E}_{k'} > \bar{E}_k$ : Excitation from bin  $k$  to the higher-energy bin  $k'$ . In this case, any pre-collision rovibrational levels  $i \in \mathcal{I}_k$  will have energies lower than those of the post-collision levels  $i' \in \mathcal{I}_{k'}$ . For excitation reactions, the rate coefficients are computed according to:

$$\bar{k}_{k \rightarrow k'}^E(T) = \frac{1}{\bar{a}_k} \sum_{i \in \mathcal{I}_k} a_i \sum_{i' \in \mathcal{I}_{k'}} k_{i \rightarrow i'}^E(T), \quad k < k'. \quad (2.14)$$

2.  $\bar{E}_{k'} < \bar{E}_k$ : Deexcitation from bin  $k$  to the lower-energy bin  $k'$ . In analogy to case 1, any pre-collision rovibrational levels  $i \in \mathcal{I}_k$  will have energies higher than those of the post-collision levels  $i' \in \mathcal{I}_{k'}$ . For deexcitation reactions the rate coefficients are computed in a manner which is automatically consistent with detailed balance for the bin populations:

$$\bar{k}_{k \rightarrow k'}^E(T) = \frac{\bar{k}_{k' \rightarrow k}^E(T)}{\bar{K}_{k' \rightleftharpoons k}^{\text{eq}}(T)}, \quad k > k'. \quad (2.15)$$

Here, the coefficient  $\bar{k}_{k' \rightarrow k}^E$  on the right-hand-side is the corresponding excitation rate coefficient for the transition  $k' \rightarrow k$  and the constant relating the number densities of bins  $k$  and  $k'$  at equilibrium is given by:

$$\bar{K}_{k' \rightleftharpoons k}^{\text{eq}}(T) = \left[ \frac{n_k}{\bar{n}_{k'}} \right]^{\text{eq}} = \frac{\bar{a}_k}{\bar{a}_{k'}} \exp\left(-\frac{\bar{E}_k - \bar{E}_{k'}}{k_B T}\right). \quad (2.16)$$

As was just mentioned, using this approach ensures that all deexcitation rate coefficients automatically verify detailed balance at the bin level, and effectively only the excitation rate coefficients have to be extracted from the N3 database. However, it also implies that all of

the deexcitation rate coefficients directly coming from the database are ignored. This was a conscious decision, because due to the remaining stochastic noise in the QCT-derived cross sections (e.g. recall Fig. 2.6) it is not automatically ensured that they will always be compatible with the detailed balance requirement. Since the ability of the model to maintain the correct compositions at equilibrium was a desirable feature, it was preferred to ignore part of the database. A slightly different approach was taken by Munafò in his work [132]. In order to retain more of the original information, he used the excitation rate coefficients for whichever transitions were found in the N3 database. In addition to this, he complemented the mechanism by applying detailed balance to deexcitation rates for those processes, whose corresponding excitation rate coefficients were missing.

3.  $\bar{E}_{k'} = \bar{E}_k$ : Pre- and post-collision bins are the same. In this case some of the inelastic processes between different rovibrational levels, which happen to be lumped into the same bin (i.e. those where  $i \neq i'$ , but with  $i$  and  $i'$  both belonging to  $\mathcal{I}_k$ ), will be mixed together with the truly elastic collisions, i.e. those where  $i = i'$ . When added together, all these processes will count towards the “elastic” collision rate coefficient for bin  $k$ , which we will call  $\bar{k}_k^{\text{el}}$ :

$$\bar{k}_k^{\text{el}}(T) = \frac{1}{\bar{a}_k} \sum_{i \in \mathcal{I}_k} a_i \sum_{i' \in \mathcal{I}_k} k_{i \rightarrow i'}^E(T). \quad (2.17)$$

This type of process is a special case, because elastic collisions by definition do not influence the inelastic, or chemical source terms given by Eq. (A.28), Eq. (A.29) and Eq. (A.30) in the macroscopic balance equations. Elastic collisions are nevertheless mentioned here, because this process is important for the DSMC implementation later on. It must be mentioned that the quality of the original elastic integrated cross sections for each rovibrational level recorded in the database, i.e. the  $\sigma_{i \rightarrow i}^I$ , was called into question by the NASA chemists themselves. Since their original aim when generating the database was primarily to determine the state-specific excitation- and dissociation rate coefficients for use in CFD applications, they selected initial parameters in their trajectory calculations which would preferentially cause these types of collisions. As a result, no particular care was taken in ensuring the accuracy of the elastic cross sections, and the ones that were recorded regardless should be considered as sort of a by-product of the QCT-process. These problems notwithstanding, the  $\sigma_{i \rightarrow i}^I$  from the database are still used in determining the “elastic” rate coefficients for their corresponding bins. There the uncertainty of these data is offset by lumping them together with the additional inelastic cross sections, which also count towards the overall elastic rate coefficient of the bin.

Obtaining the the bin-averaged dissociation rate coefficients is done analogously, by grouping together all rate coefficients for the level-specific dissociation reactions  $\text{N}_2(i) + \text{N} \rightarrow 3\text{N}$ . They

are given by:

$$\bar{k}_k^D(T) = \frac{1}{\bar{a}_k} \sum_{i \in \mathcal{I}_k} a_i k_i^D(T) \quad k \in \mathcal{K}_{N_2}, \quad (2.18)$$

where  $\bar{k}_k^D$  becomes the bin-averaged dissociation rate coefficient for the process  $N_2(k) + N \rightarrow 3N$ . The corresponding bin-averaged recombination rate coefficient is determined with the help of detailed balance and is given by:

$$\bar{k}_k^R(T) = \frac{\bar{k}_k^D(T)}{\bar{K}_{k \rightleftharpoons 2N}^{\text{eq}}(T)} \quad k \in \mathcal{K}_{N_2}, \quad (2.19)$$

where now the constant relating the equilibrium number density of bin  $k$  with that of atomic nitrogen is given by:

$$\bar{K}_{k \rightleftharpoons 2N}^{\text{eq}}(T) = \left[ \frac{n_N^2}{\bar{n}_k} \right]^{\text{eq}} = \frac{[Z_N^{\text{tra},*}(T) a_N]^2}{Z_{N_2}^{\text{tra},*}(T) \bar{a}_k} \exp\left(-\frac{2E_N - \bar{E}_k}{k_B T}\right), \quad k \in \mathcal{K}_{N_2} \quad (2.20)$$

with the following expressions for the translational partition functions of molecular and atomic nitrogen:

$$Z_{N_2}^{\text{tra},*} = \frac{Z_{N_2}^{\text{tra}}}{V} = \left( \frac{2\pi m_{N_2} k_B T}{h_P^2} \right)^{\frac{3}{2}} \quad \text{and} \quad Z_N^{\text{tra},*} = \frac{Z_N^{\text{tra}}}{V} = \left( \frac{2\pi m_N k_B T}{h_P^2} \right)^{\frac{3}{2}} \quad (2.21)$$

Once the rate coefficient data provided in the N3 database have been reduced by applying the formulas just presented, they could in principle be used for master equation studies, or other CFD applications. One could, for example, generate a database of numerical values with all the bin-specific rate coefficients tabulated at specific temperatures. In conjunction with suitable interpolation schemes, this would be sufficient to calculate the required rate coefficients at any temperature within the range of interest. In fact, the bin-specific rate coefficients were originally tabulated at nine distinct temperatures between 7500 and 50000 K. However, a more compact, and computationally more efficient alternative is to fit these tabulated rate coefficients to analytical expressions of a simple form. In Sec. 2.7 a simple Arrhenius-type form is used for the forward rate coefficients, while the corresponding backward rate coefficients are again determined by applying detailed balance.

As an example, Fig. 2.9 shows the bin-averaged rate coefficients for pre-collision bin  $k = 5$  out of a 10-bin system. For better visibility, the deexcitation and elastic rate coefficients are plotted together in Fig. 2.9(a), while the endothermic rate coefficients are shown in Fig. 2.9(b). By far the largest rate coefficient over the whole temperature range is the elastic one:  $\bar{k}_{5 \rightarrow 5}$ . It is almost two orders of magnitude bigger than the transition rates to the nearest-lying bins  $\bar{k}_{5 \rightarrow 4}$  and  $\bar{k}_{5 \rightarrow 6}$ . For transitions with larger jumps, the rates are even smaller. This behavior is typical for the whole N3 database, where processes with closely lying pre- and post-collision states are much more likely to occur than those where the two states are spaced far apart. Due to the activation energy

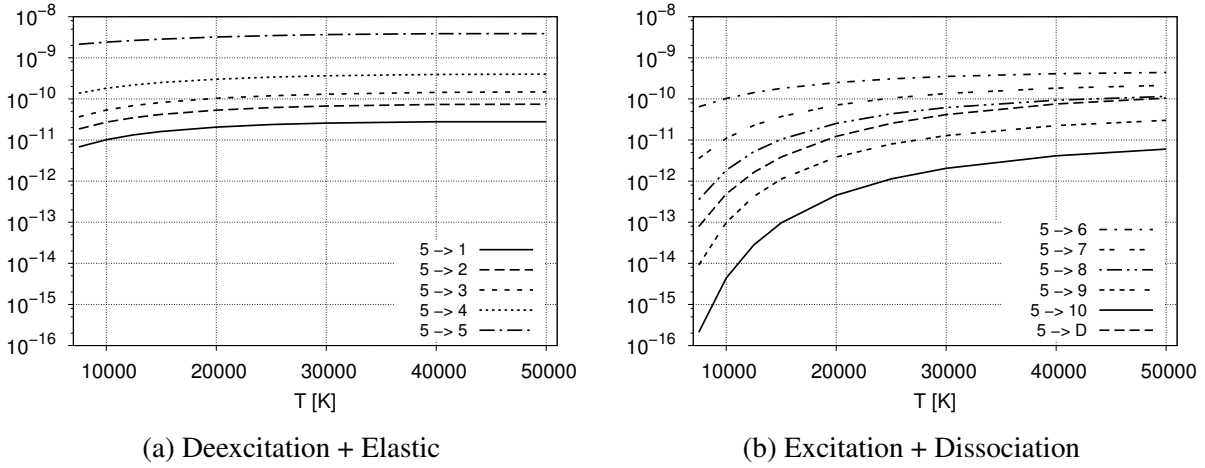


Figure 2.9.: Binned rate coefficients [ $\text{cm}^3/\text{s}$ ] for pre-collision bin 5 out of 10.

required, the rates of endothermic processes drop significantly at lower temperatures. This drop is accounted for by the exponential term in the Arrhenius-type rate coefficients. The temperature range given in this plot, i.e. 7500 – 50000 K, corresponds to the one used for the Arrhenius fits.

## 2.7. Arrhenius fitting of binned rate coefficients

The following Arrhenius-form for the bin-to-bin excitation rate coefficients is used:

$$\bar{k}_{k \rightarrow k'}^E(T) = A_{k \rightarrow k'}^E T^{b_{k \rightarrow k'}^E} \exp\left(-\frac{\Delta E_{k \rightarrow k'}^E}{k_B T}\right), \quad \bar{E}_k < \bar{E}_{k'} \quad (2.22)$$

Each fitted rate coefficient results in a pair of bin-specific Arrhenius parameters:  $A_{k \rightarrow k'}^E$  and  $b_{k \rightarrow k'}^E$ . Furthermore, Eq. (2.22) includes an exponential term with an activation energy specific to the given reaction. This threshold has been chosen as the minimum amount of energy required for the particular transition to proceed. In the case of excitation from bin  $k$  to another bin  $k'$  with higher energy, it corresponds to  $\Delta E_{k \rightarrow k'}^E = \bar{E}_{k'} - \bar{E}_k$ . When fitting the forward *excitation* rate coefficients of Eq. (2.22), the data are directly extracted from the tabulated rate coefficients derived from the N3 database. The corresponding *deexcitation* rate coefficients however, are computed by invoking detailed balance, as per Eq. (2.15) and Eq. (2.16). With the particular choice for the energy threshold just introduced the resulting analytical expression for the deexcitation rate coefficients then simplify to:

$$\bar{k}_{k' \rightarrow k}^E(T) = \frac{\bar{a}_k}{\bar{a}_{k'}} A_{k \rightarrow k'}^E T^{b_{k \rightarrow k'}^E}, \quad \bar{E}_k < \bar{E}_{k'} \quad (2.23)$$

Effectively, this means that they can be re-written as:

$$\bar{k}_{k' \rightarrow k}^E(T) = A_{k' \rightarrow k}^E T^{b_{k' \rightarrow k}^E}, \quad \text{where} \quad A_{k' \rightarrow k}^E = \frac{\bar{a}_k}{\bar{a}_{k'}} A_{k \rightarrow k'}^E \quad \text{and} \quad b_{k' \rightarrow k}^E = b_{k \rightarrow k'}^E \quad (2.24)$$

This fact becomes useful in Sec. 3.3, where the integration of the bin model into an external DSMC code is discussed. Although using Eq. (2.23) to compute the deexcitation rates implies that a sizable fraction of the data in the original N3 database is ignored (namely all the deexcitation cross sections), it ensures that the rates for corresponding forward and backward processes will be consistent with one another and that the correct bin populations are maintained when the gas is in thermal equilibrium. Analogous to the excitation rates, the coefficients for the dissociation reaction can be fitted to an Arrhenius form:

$$\bar{k}_k^D(T) = A_k^D T^{b_k^D} \exp\left(-\frac{\Delta E_k^D}{k_B T}\right), \quad (2.25)$$

For dissociation from bins composed of truly bound levels the imposed energy threshold is the difference between the formation energy of the pair of nitrogen atoms and that of the pre-collision bin of the molecule:

$$\Delta E_k^D = 2 E_N - \bar{E}_k, \quad k \in \mathcal{K}_B. \quad (2.26)$$

For dissociation from bins containing only quasi-bound levels, the condition  $\bar{E}_k > 2 E_N$  always holds. Notice that this implies that dissociation from a quasi-bound level is actually an exothermic reaction, opposite to what is the case for truly bound levels. Therefore the corresponding energy threshold is:

$$\Delta E_k^D = 0, \quad k \in \mathcal{K}_P. \quad (2.27)$$

The rate coefficient for recombination into bin  $k$  is also obtained from detailed balance by substituting Eq. (2.25) and Eq. (2.20) into Eq. (2.19), resulting in:

$$\bar{k}_k^R = A_k^D T^{b_k^D} \frac{Z_{N_2}^{\text{tra},*} \bar{a}_k}{[Z_N^{\text{tra},*} a_N]^2}, \quad k \in \mathcal{K}_B \quad (2.28)$$

for recombination into bins containing truly bound levels and:

$$\bar{k}_k^R = A_k^D T^{b_k^D} \frac{Z_{N_2}^{\text{tra},*} \bar{a}_k}{[Z_N^{\text{tra},*} a_N]^2} \exp\left(\frac{2E_N - \bar{E}_k}{k_B T}\right), \quad k \in \mathcal{K}_P \quad (2.29)$$

for recombination into bins containing pre-dissociated levels. Since in this case  $2E_N < \bar{E}_k$ , this is an endothermic reaction.

Recombination reactions are essential to maintaining chemical equilibrium in the  $N_2, N$ -mixture. The effect of neglecting them is discussed briefly in Sec. 4.1, where our DSMC implementation of the URVC bin model is verified with the help of master equation simulations. While their inclusion as part of the reaction mechanism in classical CFD codes is trivial, recombination reactions pose some challenges for a DSMC algorithm. This is because they involve three-body collisions, which are usually neglected in classical kinetic theory. Although several researchers have included recombination reactions as part of their DSMC chemistry modeling [1, 60], the

details of their algorithms are not clearly explained, and seem to be more of an ad-hoc addition to the original algorithms, rather than a fully consistent treatment of the kinetic processes involved. At the moment it is therefore not clear how to properly implement these types of reactions in our state-to-state DSMC model, and they have been neglected in this work. Fortunately this does not cause major problems, since for the flow conditions in normal shock wave problem discussed in Sec. 4.2, and the atmospheric entry-type flows of Ch. 5, recombination reactions are known to not play a major role.

Finally, the “elastic” rate coefficient can be fitted to an Arrhenius-type form as well:

$$\bar{k}_k^{\text{el}}(T) = A_k^{\text{el}} T^{b_k^{\text{el}}}, \quad (2.30)$$

which applies to all collisions where pre- and post-collision bin are the same. These collisions are called elastic in the context of the bin model, although they include many inelastic transitions between rovibrational levels belonging to the same bin. Their energy threshold is automatically zero, and thus no exponential term appears in Eq. (2.30). Within the framework of continuum CFD the elastic rate coefficients are only required for the calculation of transport properties, because only excitation/deexcitation and dissociation/recombination processes contribute to the chemical source terms in the governing equations (refer to Eq. (A.28) and Eq. (A.29)). By contrast, in a gas-kinetic description this is not the case. In Sec. 3.2 it will be shown that elastic collisions contribute significantly to the overall collision rate and can therefore not be neglected in the DSMC method.

## 3. Implementation of URVC bin model in VKI DSMC code

After having introduced the NASA Ames database and the uniform rovibrational bin model in Sec. 2.3, the present chapter will discuss the manner in which the information from the database can best be integrated into a DSMC algorithm. In Sec. 3.1 two alternative methods (analytical inversion vs. direct binning) of obtaining bin-specific collision cross sections from the full database are outlined, and results of the two approaches are subsequently compared in Sec. 3.2. Additions/modifications to the collision algorithm necessary to implement the state-to-state bin model into a DSMC code are discussed in Sec. 3.3. Finally, in Sec. 3.4 the effect of the uniform bin approximation on the thermodynamic properties of the  $N_2$ , N-mixture is discussed.

### 3.1. Analytical inversion of URVC rate coefficients

In order to use the URVC bin model within the framework of a DSMC algorithm, the bin-specific reaction cross sections must be available. The naive method for obtaining them would be to apply the binning formulas discussed in Sec. 2.6 for the rate coefficients, i.e. Eq. (2.14), Eq. (2.17) and Eq. (2.18) directly to the original cross sections. For the excitation reactions this means:

$$\bar{\sigma}_{k \rightarrow k'}^E(E) = \frac{1}{\bar{a}_k} \sum_{i \in \mathcal{I}_k} a_i \sum_{i' \in \mathcal{I}_{k'}} \sigma_{i \rightarrow i'}^E(E) \quad k < k' \in \mathcal{K}_{N_2}, \quad (3.1)$$

for the elastic cross sections:

$$\bar{\sigma}_k^{\text{el}}(E) = \frac{1}{\bar{a}_k} \sum_{i \in \mathcal{I}_k} a_i \sigma_i^{\text{el}}(E) \quad k \in \mathcal{K}_{N_2} \quad (3.2)$$

and for dissociation:

$$\bar{\sigma}_k^D(E) = \frac{1}{\bar{a}_k} \sum_{i \in \mathcal{I}_k} a_i \sigma_i^D(E) \quad k \in \mathcal{K}_{N_2} \quad (3.3)$$

Although in principle this approach requires no additional manipulation of the original cross sections, it also introduces a new problem. The bin-average cross sections of Eq. (3.1), Eq. (3.2)

and Eq. (3.3) effectively lump together cross sections for processes spanning many different pre- and post-collision rovibrational levels. Since each of these level-specific cross sections has its own distinct activation energy, the resulting bin-average cross section will begin to be non-zero at energies below the bin's own activation energy, effectively causing the bin-specific activation threshold to be "smeared out" over a range of collision energies. As a consequence, these directly binned cross sections will predict non-zero reaction probability, even though the collision energy available may not be high enough for the post-collision species to be formed. An additional inconvenience is that the directly binned cross sections are only available in tabulated form at distinct values of the collision energy  $E$  (recall Fig. 2.6). During the course of a DSMC simulation the outcomes of many millions of individual collisions need to be determined, and the relative translational energy of each collision pair is a random value. Therefore, for most of the collisions it would be necessary to interpolate between tabulated values. These additional operations would add significantly to the overall running time of the simulation. Furthermore, the memory requirements for storing a large number of tabulated cross sections make this approach impractical for large-scale simulations. To alleviate these problems, an alternative method of obtaining the binned cross sections was investigated. It was proposed to extract analytical expressions for the cross sections from the binned rate coefficients by inverting Eq. (2.6). This approach may seem somewhat counter-intuitive, but is actually very similar to what has been common practice in conventional DSMC chemistry models so far (e.g. TCE method [24], [1]). In this approach, the first assumption is that all rate coefficients can be approximated by Arrhenius-type expressions, as discussed previously in Sec. 2.7:

$$k_R(T) = A_R T^{b_R} \exp\left(-\frac{E_{a,R}}{k_B T}\right), \quad (3.4)$$

where the Arrhenius parameters  $A_R$  and  $b_R$ , as well as the energy threshold  $E_{a,R}$  are particular to the specific process in question. Next, an analytical expression with two adjustable parameters for the cross section is proposed:

$$\sigma_R(E) = \begin{cases} \frac{C_R (E - E_{a,R})^{\eta_R}}{E} & \text{if } E > E_{a,R}, \\ 0 & \text{otherwise.} \end{cases} \quad (3.5)$$

Substituting both Eq. (3.5) into the general expression of Eq. (2.6) turns out to exactly yield the functional dependence on temperature as the rate coefficient given by Eq. (3.4). By comparing

terms on both sides of the equation, this automatically determines the two parameters:

$$C_R = \frac{A_R}{2 \cdot \Gamma(3/2 + b_R)} \sqrt{\frac{\pi \mu_{N_2, N}}{2}} k_B^{-b_R}, \quad (3.6)$$

$$\eta_R = b_R + 1/2.$$

Thus, all cross sections obtained in this manner effectively share the same functional form, and are only distinguished by the Arrhenius parameters  $A_R$ ,  $b_R$  and the reaction-specific activation energy  $E_{a,R}$ .

The resulting set of cross sections need to verify the micro-reversibility relations already mentioned in Sec. 2.6. This is expressed by Eq. (3.7) for the specific case of excitation/deexcitation cross sections (see, [133]). According to this principle the integrated cross section for deexcitation from bin  $k$  to a lower-energy bin  $k'$  must be related to the corresponding excitation cross-section in the opposite sense via the relationship:

$$\bar{\sigma}_{k \rightarrow k'}^E(E) = \frac{\bar{a}_{k'} E'}{\bar{a}_k E} \cdot \bar{\sigma}_{k' \rightarrow k}^E(E'), \quad k > k' \in \mathcal{K}_{N_2}, \quad (3.7)$$

where the translational energy after deexcitation  $E'$  is equal to:

$$E' = E + \overbrace{(\bar{E}_k - \bar{E}_{k'})}^{E_{a,k' \rightarrow k}^E}. \quad (3.8)$$

Notice that the difference  $\bar{E}_k - \bar{E}_{k'}$  in Eq. (3.8) is equal to the energy threshold imposed by the excitation  $k' \rightarrow k$ . This is illustrated in Fig. 3.1, where the cross section pair for transitions between bins 5 and 6 out of a 10-bin system is shown. The cross section for excitation  $\bar{\sigma}_{5 \rightarrow 6}^E$  remains zero until the energy threshold  $E_{a,R} = \bar{E}_6 - \bar{E}_5$  has been reached. By contrast, the corresponding deexcitation cross-section  $\bar{\sigma}_{6 \rightarrow 5}^E$  has no such threshold and is greater than zero over the whole energy range.

Recall from the discussion in Sec. 2.6 that the principle of detailed balance has its equivalent form at the macroscopic scale. There it was expressed as the requirement that the backward (i.e. deexcitation) reaction rate coefficients must be equal to the ratio of the forward rate coefficient with the equilibrium constant. By plugging Eq. (3.7) into Eq. (2.6) and evaluating the integral, one can show that Eq. (2.15) is indeed verified. The added value of Eq. (3.7) is that it is valid at the level of the cross sections, and thus needs to be respected when generating the cross sections.

Before examining the results of the analytical inversion and comparing them to directly binned cross sections in the following section, it should be briefly mentioned that alternative methods for obtaining cross sections based on rate coefficients exist. A short summary of methods found in

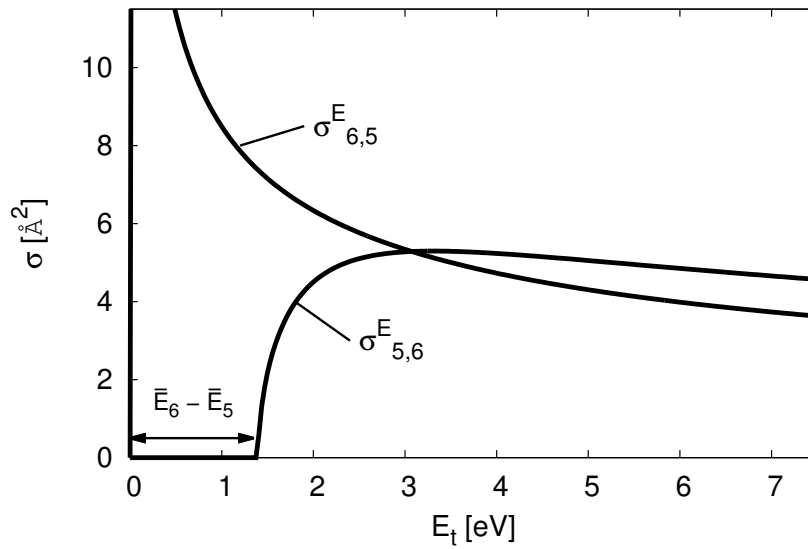


Figure 3.1.: Excitation/deexcitation cross sections between bins 5 and 6 from a 10-bin system.

literature follows:

- The inverse Laplace transform used by the group of Kustova [134] is another method for obtaining the cross sections in analytical form. It is based on the realization that the expression for the rate coefficient in Eq. (2.6), can be interpreted as a Laplace transform of the corresponding cross section. It is quite similar to the inversion method presented in this section, and can be viewed as a generalization of our approach. However, it too requires one to propose functional forms for the cross sections, which are compatible with physical constraints. If this is not the case, the cross sections obtained by inverse Laplace transform may become negative .
- Tikhonov regularization [135] (also known as the Phillips–Twomey method) is a numerical technique for the regularization of ill-posed problems, such as the one of extracting unknown cross sections from known rate coefficients. It was used by Bondar and Ivanov [136] to determine the reaction probabilities for DSMC, which would match the behavior of a two-temperature dissociation rate coefficient. This approach, although more flexible than the inverse Laplace transform method just mentioned, relies on a numerical approach wherein a possible shape for the cross section is found iteratively. Since the problem is ill-posed, there is no prior guarantee that the obtained cross sections will be “well-behaved” and considerable user input is necessary in each individual case. Since the detailed-chemistry mechanisms considered in the present work involve hundreds, or even thousands of individual cross sections, this approach was deemed impractical.
- Minelli et al. [137] used the non-linear constrained optimization method of Nelder and Mead [138], aka. downhill-simplex method, for finding dissociation cross sections, which

would best satisfy the relationship of Eq. (2.6). As a numerical technique, this approach shares many advantages and drawbacks with Tikhonov regularization. Similarly, finding each individual cross section requires a lot of user surveillance and is therefore not well-suited to the present case.

## 3.2. Comparison of directly binned and analytically inverted cross sections

As before, a 10-bin system has been chosen to visualize some of the cross sections that can be extracted from the full N3 database by the methods described in Sec. 3.1. For this purpose, the results of the two alternative approaches, i.e. analytically inverting the binned rate coefficients vs. direct binning of the original cross sections, are now compared.

Although a 10-bin system is much smaller than the original database, it still contains too many processes to thoroughly examine every single cross section. This is because for every pre-collision bin  $k = 1 \dots 10$ , there exist 10 possible post-collision bins  $k' = 1 \dots 10$ , plus one dissociation reaction. Therefore only a small sample of the whole set of cross sections is shown here. A comparison is made for all transitions from pre-collision bin  $k = 5$  in Figures Fig. 3.2 and Fig. 3.3. In the figures, the solid lines represent the directly binned cross sections, the dashed lines the analytically inverted ones. Several aspects are noteworthy. First, the directly binned cross sections exhibit noticeable statistical noise, as was already noted in Sec. 2.6. By contrast, the cross sections obtained via the analytical inversion procedure show a much smoother behavior. The second difference is that the directly binned cross sections show a marked decrease starting roughly at energies between 15 and 20 eV. This fact was mentioned in Sec. 2.5 while discussing cross sections involving individual level-to-level transitions. The gradual decrease in the cross sections means that at high enough collision energies, the QCT method predicts that the given processes become unlikely. By contrast, the analytical cross sections for the same transition decrease much more slowly (e.g. Fig. 3.2(d)), or in some cases keep increasing with energy (e.g. Fig. 3.3(e)). This seems to be due to the constraints (or lack thereof) imposed on the functional form of the analytical cross-sections. Recalling Eq. (3.5) and Eq. (3.6), there exist only two adjustable parameters ( $C_R$  and  $\eta_R$ ), which in turn depend on the Arrhenius fit parameters  $A_R$  and  $b_R$ . These parameters influence the curvature and the maximum of the cross section, but the asymptotic behavior at high energies is not explicitly defined by Eq. (3.5). A related phenomenon is visible for deexcitation (e.g. Fig. 3.2(d)) and elastic processes (e.g. Fig. 3.2(e)) at very low relative energies. For these types of processes, the cross sections obtained from direct binning all tend towards zero as  $E \rightarrow 0$ , while the analytical cross sections tend towards infinity at small collision energies. This is due to the hyperbolic term involving  $E$  included in Eq. (3.5). The third difference between the analytical and direct cross-sections was already mentioned in Sec. 2.6 and

### 3. Implementation of URVC bin model in VKI DSMC code

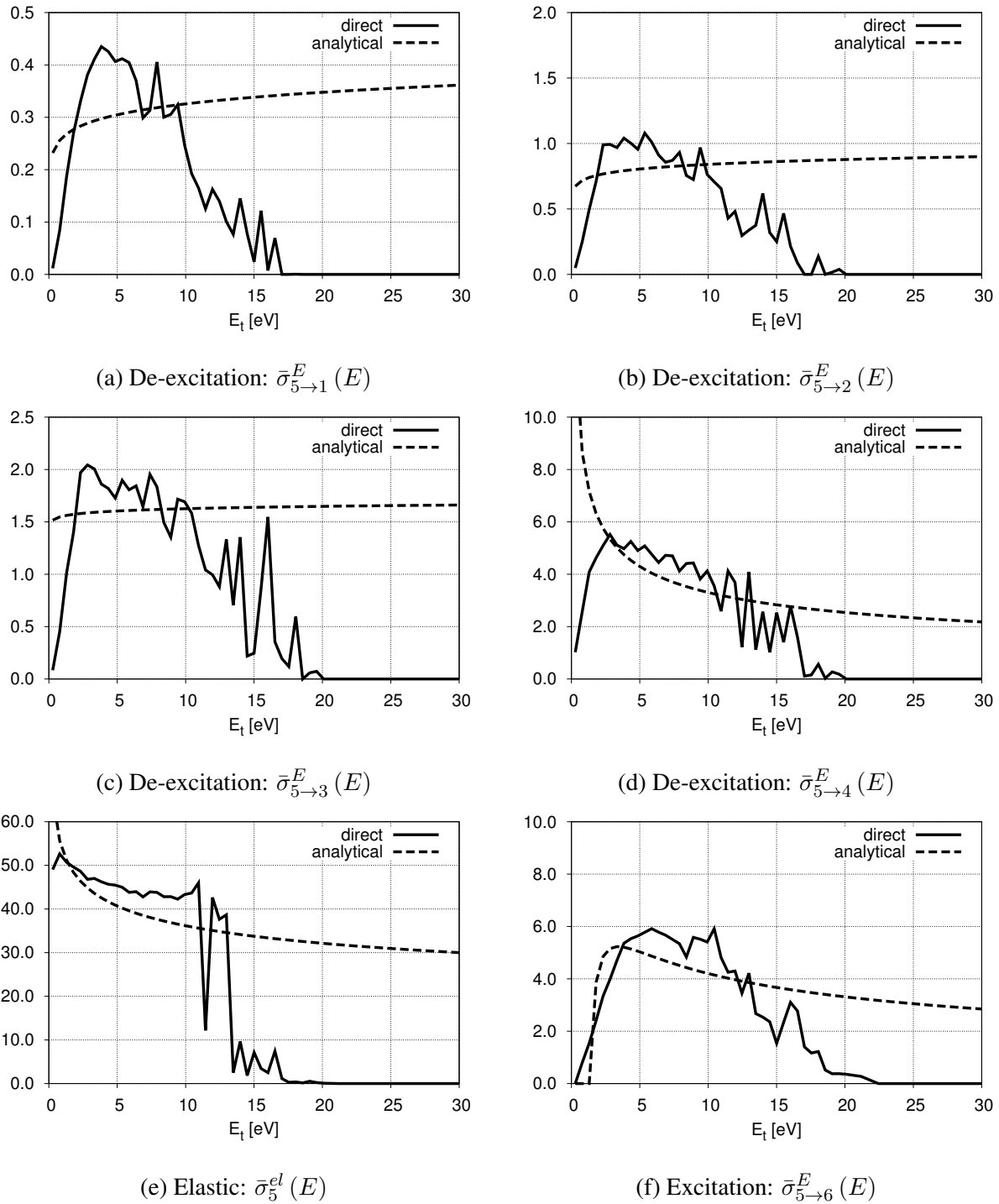


Figure 3.2.: Comparison of integrated cross sections measured in  $\text{\AA}^2$  for pre-collision bin 5 out of 10. Solid lines: direct binning; dashed lines: analytically inverted.

is noticeable only for the endothermic processes, i.e. those with a defined energy threshold  $E_{a,R}$ . This threshold is captured well in the analytical curves (e.g. Fig. 3.2(f), because it is explicitly built into the functional form of Eq. (3.5)).

The exact shapes may differ, but both sets of cross sections show roughly similar behavior in the collision energy range  $0 < E < 15 - 20$  eV. This is a fortunate fact, because it means that both

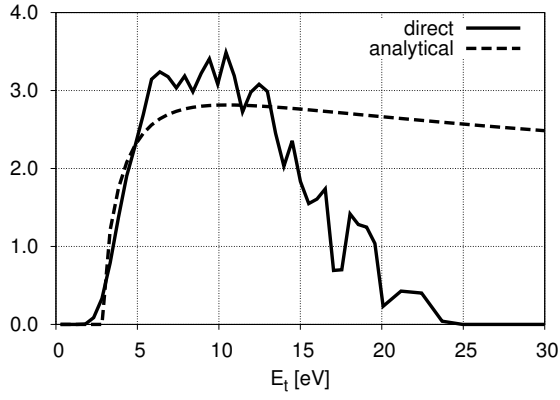
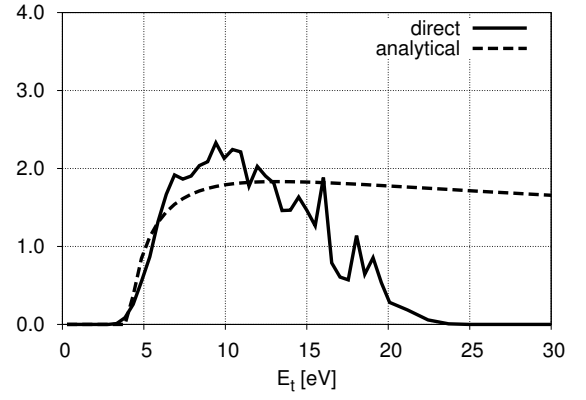
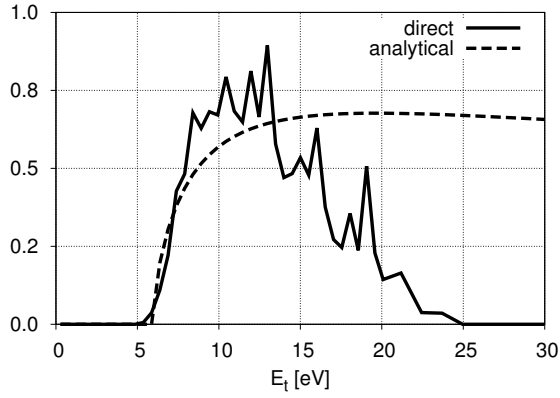
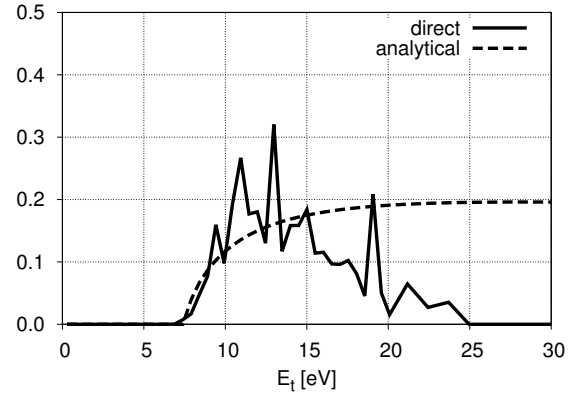
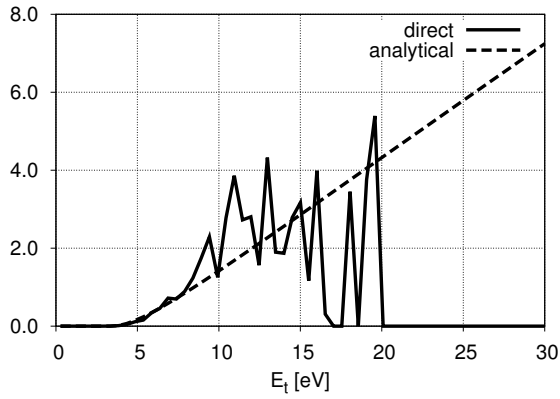

 (a) Excitation:  $\bar{\sigma}_{5 \rightarrow 7}^E(E)$ 

 (b) Excitation:  $\bar{\sigma}_{5 \rightarrow 8}^E(E)$ 

 (c) Excitation:  $\bar{\sigma}_{5 \rightarrow 9}^E(E)$ 

 (d) Excitation:  $\bar{\sigma}_{5 \rightarrow 10}^E(E)$ 

 (e) Dissociation:  $\bar{\sigma}_5^D(E)$ 

Figure 3.3.: Comparison of integrated cross sections measured in  $\text{\AA}^2$  for pre-collision bin 5 out of 10 (continued). Solid lines: direct binning; dashed lines: analytically inverted.

sets of cross sections will predict similar reaction rates, at least for this lower range of collision energies. The discrepancies at  $E > 20$  eV are less of a problem, if one considers that such high-energy collisions have fairly low probabilities of occurrence at temperatures below 60000 K.

The somewhat convoluted procedure of first computing rate coefficients based on the full N3 system, subsequently reducing the mechanism by applying the URVC binning rules and finally analytically inverting these coefficients back to obtain analytical expressions for the cross sections, has the effect of “smoothing-out” some of the noise contained in the original cross-sections. The individual “shape” of each particular cross section is controlled by the two Arrhenius-fit parameters obtained from the corresponding rate coefficient. Coupled with the fact that no interpolation is necessary to evaluate the cross section at any given  $E$ , this makes the analytical expressions better suited to use within a DSMC code.

### 3.3. Integration of state-specific cross sections into DSMC collision algorithm

Several modifications have to be made to a DSMC code in order to integrate the detailed chemistry model described so far. However, the most important additions to the algorithm concern the collision routines and only the particular modifications necessary to integrate the URVC bin model for N3 are mentioned here. For simplicity this discussion will assume that Bird’s No Time Counter (NTC) scheme as discussed in [1] is being used. The explanation given here also reflects the manner in which the model was implemented in the VKI DSMC code. Before outlining the collision algorithm itself, two relevant points will be discussed. The first one concerns the determination of the state-specific total cross section in Sec. 3.3.1. The second point is related and concerns the determination of the state-specific reaction probabilities, which are introduced in Sec. 3.3.2.

#### 3.3.1. State-specific total cross section for $N_2(k) + N$ -pair

The total integrated collision cross section  $\bar{\sigma}_k^T$  of the species pair  $N_2(k) + N$  is calculated as the sum over all inelastic, elastic and reactive cross sections for this particular pseudo-species pairing:

$$\bar{\sigma}_k^T(E) = \sum_{k' \in \mathcal{I}_k} \bar{\sigma}_{k \rightarrow k'}^E(E) + \bar{\sigma}_k^D(E), \quad k \in \mathcal{K}_{N_2} \quad (3.9)$$

Here,  $\bar{\sigma}_{k \rightarrow k'}^E$  represents the full set of excitation, elastic (i.e.  $\bar{\sigma}_k^{\text{el}} = \bar{\sigma}_{k \rightarrow k}^E$ ) and deexcitation cross sections from pre-collision bin  $k$  to all other post-collision bins  $k'$ . Recall from the discussion in Sec. 2.6 that so far the notation of the species indices had been simplified. Thus,  $\bar{\sigma}_k^T$  is actu-

ally equivalent to  $\bar{\sigma}_{N_2(k),N}^T$ , while  $\bar{\sigma}_{k \rightarrow k'}^E$  corresponds to  $\bar{\sigma}_{N_2(k),N \rightarrow N_2(k'),N}^E$  and  $\bar{\sigma}_k^D$  is equivalent to  $\bar{\sigma}_{N_2(k),N \rightarrow 3N}^D$ .

The sum expressed in Eq. (3.9) is represented graphically in Fig. 3.4(a). Each possible outcome of the collision has its own integrated cross section, which is represented by one of the shaded areas. For example, the deexcitation reaction to the adjacent lower bin, i.e.  $N_2(k) + N \rightarrow N_2(k-1) + N$  is labeled as  $k \rightarrow k-1$  and is shaded in blue. At a given relative translational energy  $E$ , the cross section for this process is then given by the “height” of the corresponding shaded area (indicated by the double-headed arrows). As can be inferred from Fig. 3.4(a), the individual cross sections for all possible outcomes have been “stacked on top of each other” in sequence of the post-collision bin  $l$ . Thus, immediately above  $k \rightarrow k-1$  follows the special case where the post-collision bin remains unchanged, i.e.  $k \rightarrow k$ , which has been labeled as “elastic” and is shaded in green. Further cycling through all possible post-collision outcomes, the following cross sections all represent excitation processes to higher-energy bins  $k' > k$  and are again shaded in blue. The final cross section is that of dissociation, i.e.  $N_2(k) + N \rightarrow 3N$ , which is shaded in red. The overall sum of all these contributions yields the total collision cross section for the pair  $N_2(k) + N$ , which is represented in Fig. 3.4(a) by the thick red line.

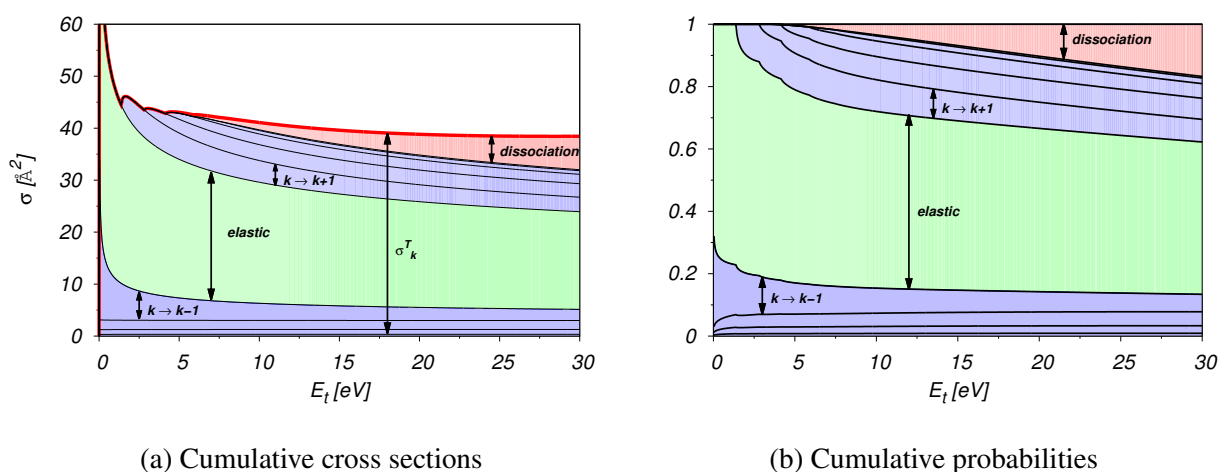


Figure 3.4.: Schematic of cumulative state-specific cross sections and probabilities for collision pair  $N_2(k) + N$  as a function of relative translational energy  $E = \frac{1}{2} \mu_{N_2,N} g^2$

Notice in the definition of Eq. (3.9) the dependence on parameter  $k$ , which implies the fact that a different total cross section exists for each pre-collision pseudo-species pairing  $N_2(k) + N$ . This is in contrast with most conventional DSMC implementations, where it is usually assumed that the total cross section for a given species pair is independent of the internal energy states of the colliding particles (e.g. when using the VHS/VSS models). The dependence of the total cross section on the pre-collision internal energy states was also recognized in previous state-to-state DSMC implementations of the NASA N3 database [77].

The total cross section is needed to determine the acceptance probability of a given collision pair

in Bird's NTC scheme (see Sec. 3.3.3), but is also necessary for determination of the state-specific reaction probabilities discussed in the following section.

### 3.3.2. State-specific reaction probabilities for $N_2(k)+N$ -pair

The relative frequencies (or probabilities) of the collision yielding a given post-collision state are given by the ratio of each individual cross section to the pair's total cross section:

$$P_{k \rightarrow k'}^E(E) = \frac{\bar{\sigma}_{k \rightarrow k'}^E(E)}{\bar{\sigma}_k^T(E)} \quad k, k' \in \mathcal{K}_{N_2} \quad \text{and} \quad P_k^D(E) = \frac{\bar{\sigma}_k^D(E)}{\bar{\sigma}_k^T(E)} \quad k \in \mathcal{K}_{N_2}. \quad (3.10)$$

Adding up the individual terms for all post-collision outcomes represented by Eq. (3.10) one-by-one in the same sequence as the cross sections in Eq. (3.9) yields the corresponding cumulative probabilities. They can be represented in an array  $P_k^{\text{Sum}}$ , which is constructed in the following manner:

$$P_k^{\text{Sum}} = \begin{pmatrix} P_{k \rightarrow 1}^E \\ P_{k \rightarrow 1}^E + P_{k \rightarrow 2}^E \\ \vdots \\ P_{k \rightarrow 1}^E + P_{k \rightarrow 2}^E + \cdots + P_{k \rightarrow n_{\text{bins}}}^E \\ P_{k \rightarrow 1}^E + P_{k \rightarrow 2}^E + \cdots + P_{k \rightarrow n_{\text{bins}}}^E + P_k^D \end{pmatrix} \quad (3.11)$$

This array has length  $n = n_{\text{bins}} + 1$ , each row corresponding to one of the possible outcomes available to the collision pair  $N_2(k) + N$ . Notice that for the last element  $P_k^{\text{Sum}} \stackrel{!}{=} 1$ , since it is calculated as the sum over all individual probabilities. As an example Fig. 3.4(b) shows the cumulative probabilities corresponding to the state-specific cross sections of Fig. 3.4(a). Again, the individual probabilities of all transitions are stacked on top of each other, with the "height" of each shaded strip representing the probability of that particular outcome. The cumulative probabilities of Eq. (3.11) are represented by the solid dividing lines between the shaded areas. Although not strictly necessary, the definition given by Eq. (3.11) is introduced here, because as will be seen in Sec. 3.3.4, it is a convenient device for determining the post-collision outcome in the DSMC routines.

### 3.3.3. Collision acceptance probability of $N_2(k)+N$ -pair

Recall that according to the NTC method, in a particular collision cell with a total number of particles  $N_P$ , a particle weighting factor  $W_P$ , a time step size  $\Delta t$  and cell volume  $V_{\text{cell}}$ , the number of pairs to be *tested* for collision is given by:

$$N_{\text{pairs}} = \frac{N_P(N_P - 1)}{2} [\sigma^T(g) \cdot g]_{\text{max}} \frac{W_P \Delta t}{V_{\text{cell}}}, \quad (3.12)$$

where  $[\sigma^T(g) \cdot g]_{\max}$  is the cell-specific maximum of  $[\sigma^T(g) \cdot g]_{\text{pair}}$  recorded over all previously tested collision pairs, regardless of the species of the particular collision partners. For all pairs which are composed of one  $\text{N}_2(k)$ -molecule and one N-atom at the particular relative translational energy  $E_{\text{pair}} = \frac{1}{2} \mu_{\text{N}_2, \text{N}} g_{\text{pair}}^2$ , the *probability of acceptance* is given by the ratio:

$$P_{\text{pair}} = \frac{[\sigma_k^T(g) \cdot g]_{\text{pair}}}{[\sigma^T(g) \cdot g]_{\max}} \quad (3.13)$$

For every such random pair the total cross section must then be evaluated according to Eq. (3.9) at the pair's specific relative energy  $E_{\text{pair}}$ . As usual in the NTC method, the pair is accepted for collision only if  $P_{\text{pair}} > R_f$ , where  $R_f$  is a random real number in the interval  $[0, 1]$ .

During the remainder of the pair acceptance/rejection phase this process has to be repeated independently for every other random pair, which happens to involve  $\text{N}_2(k)$  and N as collision partners. By affecting the acceptance probabilities of individual pairs, the total cross section of Eq. (3.9) directly influences the collision rate between pseudo-species  $\text{N}_2(k)$  and N.

### 3.3.4. Determination of post-collision state of $\text{N}_2(k)$ +N-pair

Once all  $N_{\text{pairs}}$  potential collision pairs have been flagged either for acceptance or rejection, a second loop is performed over the accepted pairs. If a given  $\text{N}_2(k)$ +N-pair has been accepted for collision, the following task is to randomly select its post-collision outcome in accordance with its state-specific reaction probabilities given by Eq. (3.10). This is where the set of cumulative probabilities as defined in Eq. (3.11) becomes useful, since selecting the post-collision outcome is straightforward by generating a random fraction  $R_f$  in the interval  $[0, 1]$  and comparing it in sequence to each element in vector  $P_k^{\text{Sum}}$ . The collision outcome whose cumulative probability is closest to, but still greater than  $R_f$  will be chosen. This algorithm can be represented by the flow chart shown in Fig. 3.5. Notice that if the random number turns out to be greater than all but the last element of  $P_k^{\text{Sum}}$ , the dissociation reaction is chosen by default, since the last cumulative probability in the array is equal to one by design. Alternatively, a graphical interpretation of the procedure is to plot the point  $(E_{\text{pair}}, R_f)$  on the graph of Fig. 3.4(b) and to select the post-collision outcome according to the particular interval in which the point lies.

Once a given collision outcome has been selected, the remainder of the procedure depends on whether the  $\text{N}_2$ -molecule remains intact, or whether dissociation occurs. These two different paths, designated in Fig. 3.5 as “binary collision routines” and “dissociation routines” will now be explained.

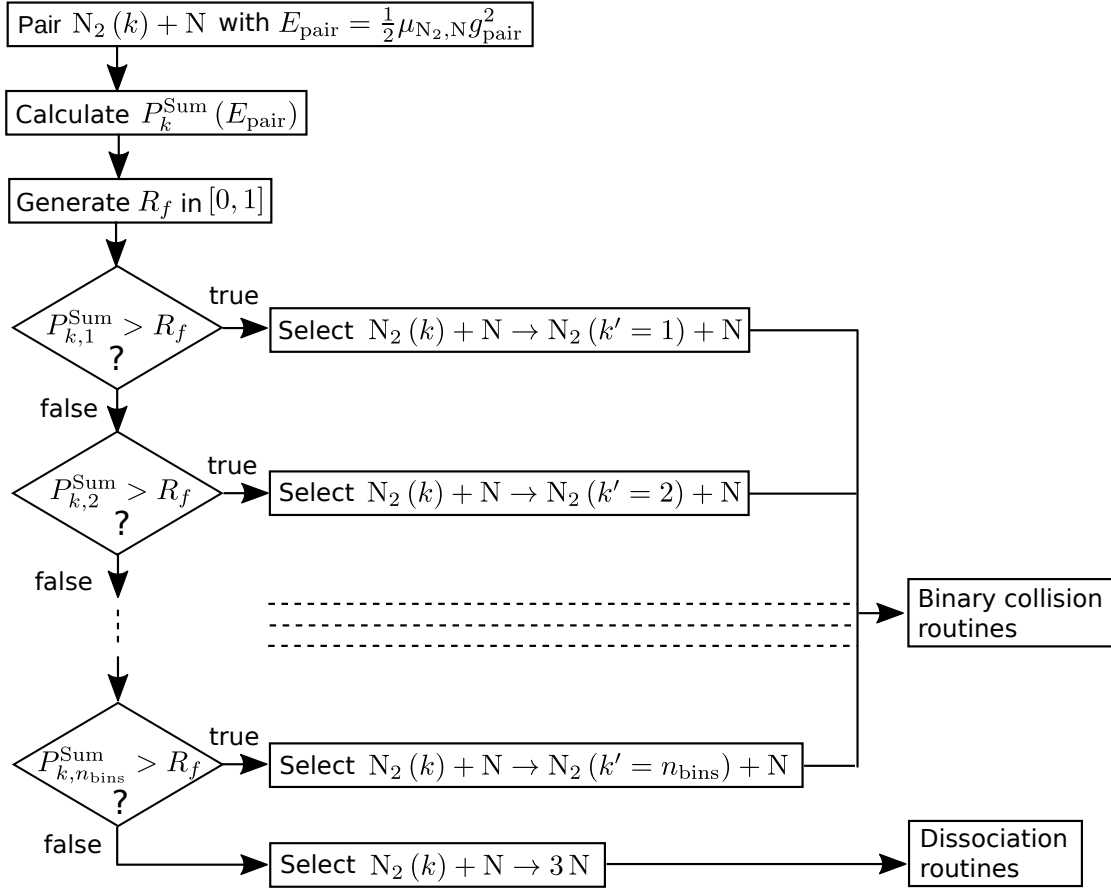


Figure 3.5.: Schematic of post-collision state selection algorithm for  $N_2(k)+N$ -pair

### Binary collision routines

If the  $N_2(k)+N$ -pair merely transitions to a new post-collision bin, it is only necessary to update its internal pseudo-species label, reflecting the fact that it has transitioned to state  $k'$ , as well as to determine the post-collision relative velocity of the pair (for the labeling, refer to Fig. 3.6(a)):

$$g'_{12} = g_{12} + \sqrt{2(\bar{E}_k - \bar{E}_{k'}) / \mu_{N_2,N}}. \quad (3.14)$$

Once this value is known, the post-collision velocities of the  $N_2(k')+N$ -pair are determined assuming isotropic scattering at  $g'_{12}$ , exactly as would be the case for an elastic hard-sphere collision.

The main reason for assuming isotropic scattering lies in the fact that the NASA N3 database contains only cross section data integrated over all deflection angles. This means that all of the information on the possible anisotropy of the binary collisions has been lost. This is again a consequence of these data having been compiled with CFD applications in mind, rather than for DSMC.

## Dissociation routines

In case dissociation is selected, the remaining procedure is slightly more involved. In order to better visualize the sequence of events and the labeling of each particle, refer to Fig. 3.6(b). Due to the internal workings of the VKI DSMC code the procedure is split into two parts. In the first phase the  $N_2$ -particle, which will later split up into two N-atoms, is labeled as an “activated complex”,  $N_2^*$ , and a regular binary collision between this intermediate particle and the original nitrogen atom is performed. Then, after all collision pairs have been processed, a loop over those particles in the cell which had previously been labeled as activated complexes is performed in order to split them into atoms. The whole procedure is performed in such a manner as to conserve momentum and overall energy in each collision.

The first phase proceeds as follows:

1. Sample the post-collision relative translational energy of the  $N_2^*+N$ -pair from a uniform distribution in the interval  $[0, E_{\max}]$ , i.e.  $E'_{1(23)} = E_{\max} \cdot R_f$ , where again  $R_f$  is a random number sampled from  $[0, 1]$ . The upper limit  $E_{\max}$  constitutes the maximum available energy to be distributed among the collision products after the dissociation energy  $2E_N$  has been deducted:

$$E_{\max} = \frac{\mu_{N_2,N}}{2} g_{12}^2 - (2E_N - \bar{E}_k). \quad (3.15)$$

The remaining collision energy, which is associated to the activated complex, is calculated as  $E^* = E_{\max} - E'_{1(23)}$  and is kept in memory for use in the second phase.

2. Based on  $g'_{1(23)} = \sqrt{2 E'_{1(23)} / \mu_{N_2,N}}$ , determine velocity  $\mathbf{c}'_1$  of the original nitrogen atom and  $\mathbf{c}'_{23}$  of the activated complex, assuming isotropic scattering.

The second phase involves only the activated complex-particles:

1. For each given  $N_2^*$ , re-assign its velocity  $\mathbf{c}'_{23}$  to be the center-of-mass velocity of the two new N-atoms.
2. Retrieve  $E^*$  from memory and calculate  $g'_{23} = \sqrt{2E^* / \mu_{N,N}}$ , which will become the post-collision relative speed between the two atoms.
3. Re-label the activated complex particle as an N-atom and generate an additional particle to be the third N-atom.
4. Based on  $g'_{23}$  determine the velocities  $\mathbf{c}'_2$  and  $\mathbf{c}'_3$  of both N-atoms assuming isotropic scattering.

It should be noted that, although this procedure conserves momentum and energy in each collision, the post-collision velocities  $\mathbf{c}'_1$ ,  $\mathbf{c}'_2$  and  $\mathbf{c}'_3$  determined via this algorithm are somewhat arbitrary. They come about as a direct result of the assumed uniform distribution of the post-collision

energy  $E_{\max}$  between the between the three particles and by assuming isotropic scattering in each case. Again, this is a choice which had to be made due to the lack of more precise information on the deflection angles in the original N3 database. This concludes the details on the DSMC

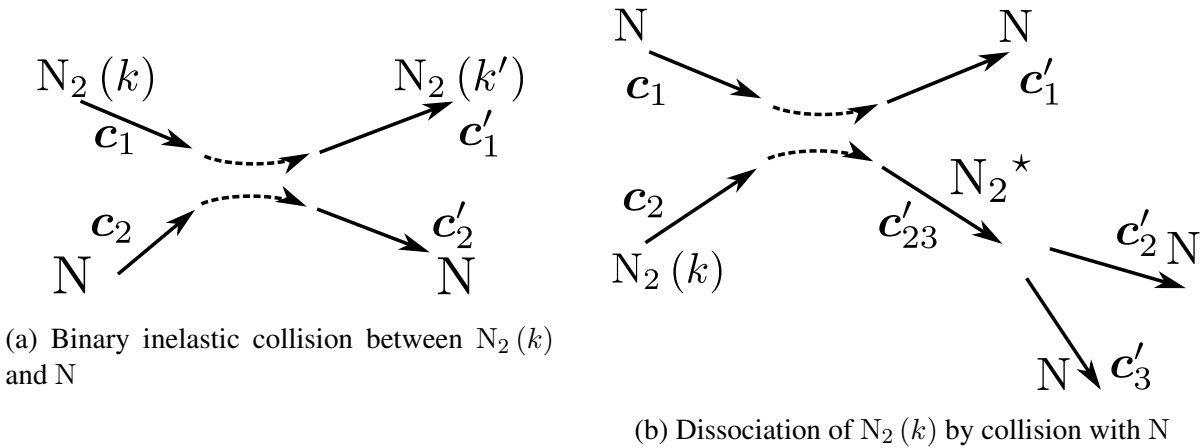


Figure 3.6.: Schematic of collision processes and definition of pre- and post-collision velocities

implementation of the N3 bin model in the VKI DSMC code. It was first tested on the reservoir case discussed in Sec. 4.1 and subsequently used to simulate internal energy excitation and dissociation across a normal shock wave in Sec. 4.2. Subsequently, the URVC bin model was applied to the two additional test cases in Ch. 5. There, an external DSMC code was used, which required several modifications to the algorithm explained in this section. These issues are discussed in Sec. 5.1.

Before moving on to the next section, it should be mentioned that recombination reactions of the type  $N + N + N \rightarrow N_2(k) + N$  were not implemented in the current state-to-state chemistry algorithm. Although it may seem trivial to “invert” the arrows in Fig. 3.6(b), so as to reverse the sense of the reaction, devising the correct DSMC algorithm for this process is not straightforward. The first problem is the one of determining the correct three-particle collision rate, based on the particles in a given DSMC cell. Since practically all of the kinetic theory developed in the past has been limited to binary collisions, no rigorous approach for this problem seems to have been proposed so far. The second difficulty lies in the lack of knowledge of the state-specific recombination cross sections, which must be consistent with the corresponding dissociation cross sections to ensure detailed balance. In fact, at the moment it is not clear if an unambiguous definition of such cross sections is even possible, since the number of degrees of freedom of the three-particle system is greater than that of the resulting particle pair after recombination. Therefore, the choice of parameters by means of which one defines a particular collision does not seem to be unique [133] and a consistent recombination algorithm can not be presented at the moment.

## 3.4. Effect of URVC binning on thermodynamic properties of N<sub>2</sub>

So far the discussion of the URVC bin model has centered around the methods by which the bin-averaged rate coefficients and cross sections are obtained, and around how this model can be integrated into a DSMC code. The shapes of the cross sections obtained by means of the two alternative approaches, i.e. analytical inversion vs. direct binning, were compared and analyzed in more detail in Sec. 3.2. For this comparison, an example system comprised of 10 bins was used. However, during the whole discussion the question of the optimum number of bins and their particular sizes has not been addressed. Although the most important expressions defining the bin-average quantities, such as rate coefficients and bin-average energies were introduced in Sec. 2.6, no specific mention was made of the actual sub-division of the rovibrational levels into bins. It is the goal of this section to provide additional information on the selection of the overall bin number and their individual sizes, as well as to show how the particular choice of bins in the URVC model directly affects the thermodynamic properties of the gas mixture.

It should be noted that the early stages of the work in this section were conducted together with Bariselli as part of his research master project at VKI [139]. He initially proposed the 9:1 ratio for bins containing truly bound vs. pre-dissociated levels and the transformation of the bin energy intervals represented by Eq. (3.16) and Fig. 3.8.

In order to better explain the precise sub-division of the rovibrational levels into bins, the same 10-bin example system from previous sections will be used here. Such a system is convenient, as it is detailed enough to be used in actual simulations (as will be seen in Ch. 4 and Ch. 5), while simultaneously being compact enough to discuss all of the relevant details of the procedure without being overwhelmed by the size of the system. To begin, recall from the discussion in Sec. 2.4 that the full set of levels can be broadly sub-divided into truly bound and quasi-bound levels. Truly bound levels are those whose energy lies below  $\Delta E_{v=0, J=0}^D = 9.75$  eV, i.e. the threshold required for spontaneous dissociation, while pre-dissociated levels possess energies above this characteristic value. This separation was indicated in Fig. 2.4(b) by drawing the region of truly bound levels in blue and that of the quasi-bound levels in red. As can be seen from this plot, about 3/4 of all levels are truly bound and only 1/4 are quasi-bound levels. Based on this ratio the initial choice was to assign 7 bins to the truly bound levels and 3 bins to the pre-dissociated ones. In this, and all cases thereafter, care was taken not to mix truly bound and pre-dissociated levels within the same bin. The initial choice was to use bins of equal size, defined as equal fractions of the given energy range. Thus, for the truly bound levels the size of each bin was given by  $\Delta E^B = (9.75 \text{ eV} - 0 \text{ eV}) / 7 = 1.39 \text{ eV}$ . For the pre-dissociated levels the size of each bin was given by  $\Delta E^P = (14.92 \text{ eV} - 9.75 \text{ eV}) / 3 = 1.72 \text{ eV}$ , where the upper limit corresponds to the energy of the highest-lying level, i.e.  $E_{9390} = 14.92 \text{ eV}$ . With these equally-sized intervals

the sets of indices for the levels belonging to each bin, i.e. the  $\mathcal{I}_k$ 's, are automatically determined. The whole set of data is collected in Tab. 3.1. Apart from indicating the level indices belonging to each bin in the second column, the third column lists the bins degeneracy, as defined by Eq. (2.11). Meanwhile, the limits of the energy range of each bin are listed in column four, and the fifth column shows the weighted average energy of each bin, as defined by Eq. (2.13).

Table 3.1.: Average properties of the full set of levels lumped into 10 bins. The 7 lower bins are composed exclusively of truly bound levels, the upper 3 bins of quasi-bound levels

$k$	$i \in \mathcal{I}_k$	$\bar{a}_k$	$E_i$ [eV]	$\bar{E}_k$ [eV]
1	1 ... 282	76596	0.00 ... 1.39	0.89
2	283 ... 793	218817	1.39 ... 2.79	2.17
3	794 ... 1476	380712	2.79 ... 4.18	3.54
4	1477 ... 2380	585147	4.18 ... 5.57	4.92
5	2381 ... 3508	827016	5.57 ... 6.97	6.31
6	3509 ... 4960	1172946	6.97 ... 8.36	7.71
7	4961 ... 7421	1831185	8.36 ... 9.75	9.13
8	7422 ... 8854	1975419	9.75 ... 11.48	10.48
9	8855 ... 9277	869799	11.48 ... 13.20	12.21
10	9278 ... 9390	263841	13.20 ... 14.92	13.79

Superimposing these bins onto the levels of Fig. 2.4(b), one obtains the image shown in Fig. 3.7. Here the reduced system of 7+3 bins from Tab. 3.1 has been drawn on top of the original curve representing the 9390 rovibrational levels, with each rectangle representing one bin. The width of each bin represents the range of levels shown in the second column of Tab. 3.1, while the height is given by the value in the last column.

Although the energy intervals for each bin have been kept constant here, it is clear from the width of the bins that the number of individual levels in each bin varies considerably. With 2461 levels, bin number 7 contains the most, while with only 113, bin number 10 contains the fewest levels. As will be shown in the comparison later in this section and the verification test cases discussed in Ch. 4, there are however good reasons to use a non-uniform spacing for the energy intervals. Without going into too much detail at this point, a major reason for using energy intervals of variable size is to improve the accuracy of the bin model at the low temperatures, i.e.  $T_\infty \leq 300$  K, prevailing in the free stream gas in atmospheric entry flows. At such low temperatures only the lowest-lying energy levels are populated to a significant degree, and any slight change in the distribution of  $N_2$ -molecules among these levels implies a large jump in the gas temperature. Since 283 of the lowest-lying levels are lumped together into the first bin, the choice of bins of Tab. 3.1 is not able to accurately resolve the internal energy distribution in the low temperature range.

A straightforward remedy would be to increase the overall number of bins until the differences with respect to the full set of levels become negligible. In this way, fewer levels would be lumped

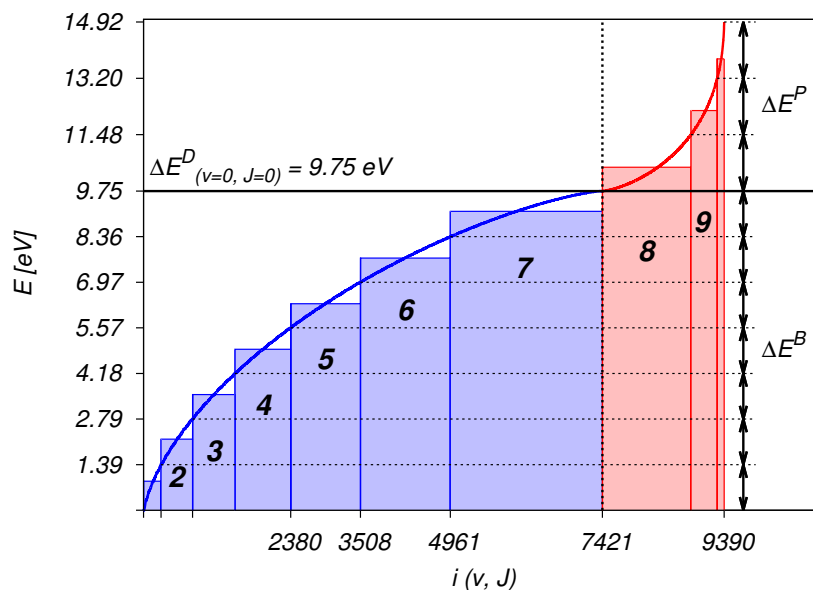


Figure 3.7.: All 9390 rovibrational levels lumped into 10 energy bins. The first seven bins below the dissociation energy (blue boxes) are composed of truly bound levels. The upper three (red boxes) contain only quasi-bound ones. Equal-size energy intervals of width  $\Delta E^B$  are used for all truly bound, and of width  $\Delta E^P$  for the quasi-bound bins, respectively

together into a single bin, and the low-temperature resolution of the model would automatically improve. This approach is considered in the comparison later in this section and in the test cases of Ch. 4, demonstrating that the equally-spaced bins can indeed deliver accurate results. However, as will be seen in these comparisons, using equally-spaced energy intervals requires about 100 bins or more to reach a satisfactory level of accuracy at low temperatures. Since the original justification to introducing a coarse-grain model was to reduce the size of the detailed chemistry mechanism as much as possible, increasing the number of bins to such large numbers is counterproductive. Instead, the goal should be to re-arrange the existing number of bins in such a manner as to better resolve the low-energy behavior of the whole set of levels. Therefore, an alternative approach is proposed here. First, re-distribute the existing 10 bins such that the first nine of them lie below the dissociation limit  $\Delta E_{v=0, J=0}^D$ . This results in an equal energy spacing of  $(9.75 \text{ eV} - 0 \text{ eV}) / 9 = 1.08 \text{ eV}$  for the 9 bins below the dissociation threshold. The pre-dissociated levels are all lumped together into a single bin in the energy interval  $(14.92 \text{ eV} - 9.75 \text{ eV}) / 1 = 5.17 \text{ eV}$ . Second, re-define the energy limits between the first nine bins, such that their size grows with the power  $n$ :

$$E_{k, \text{lim}}^V = (E_{k, \text{lim}}^E)^n \quad k \in \mathcal{K}_B \quad (3.16)$$

Here, the upper indices “E” and “V” stand for “equally-spaced” and “variably-spaced” energy intervals. The sub-index “lim” refers to the energy limits of the particular bin  $k$ , and the set  $\mathcal{K}_B$  includes all bins containing truly bound levels. The transformation from equally-spaced to

the stretched bin boundaries is shown in Fig. 3.8, where an exponent  $n = 2$  has been used. It becomes immediately clear that the width of the first few bins is much smaller than that in the original, equally-spaced approach.

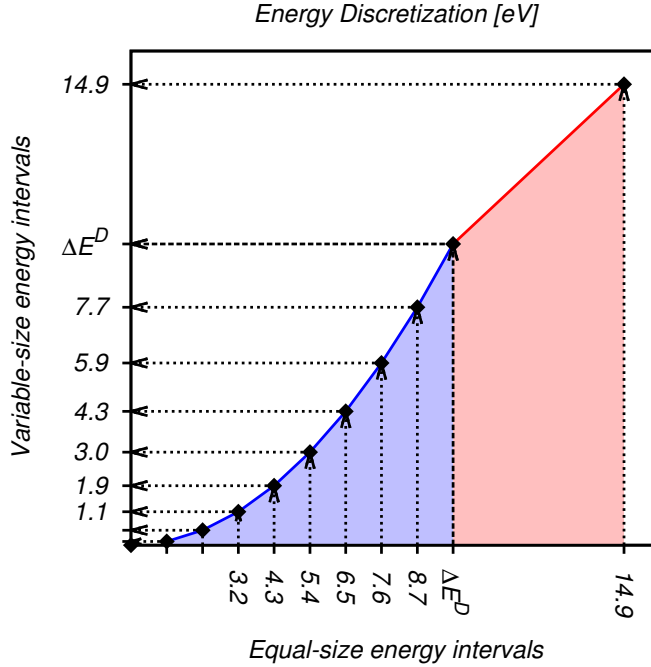


Figure 3.8.: Transformation of original equally-sized energy intervals  $\Delta E_k^E$  (abscissa) to variable-sized energy intervals  $\Delta E_k^V$  (ordinate).

After re-defining the bin boundaries in this manner, the updated bin-average quantities have been listed in Tab. 3.2. Notice that the first bin now only contains 22 rovibrational levels. In fact, with this new approach the first three bins together contain fewer levels than the first bin in the original scheme of Tab. 3.1.

Table 3.2.: Average properties of the full set of levels lumped into 10 bins. The 9 lower bins are composed exclusively of truly bound levels, the tenth bin of all the quasi-bound levels

$k$	$i \in \mathcal{I}_k$	$\bar{a}_k$	$E_i$ [eV]	$\bar{E}_k$ [eV]
1	1 ... 22	2145	0.00 ... 0.12	0.06
2	23 ... 72	9987	0.12 ... 0.48	0.33
3	73 ... 201	36699	0.48 ... 1.08	0.82
4	202 ... 452	93810	1.08 ... 1.93	1.54
5	453 ... 889	201444	1.93 ... 3.01	2.51
6	890 ... 1574	388311	3.01 ... 4.34	3.72
7	1575 ... 2615	697080	4.34 ... 5.90	5.17
8	2616 ... 4227	1228542	5.90 ... 7.71	6.87
9	4228 ... 7421	2434401	7.71 ... 9.75	8.86
10	7422 ... 9390	3109059	9.75 ... 14.92	11.25

The graphical representation of this transformation can be seen in Fig. 3.9, with the upper image in Fig. 3.9(a) showing the full range of rovibrational levels, along with the new variably-sized

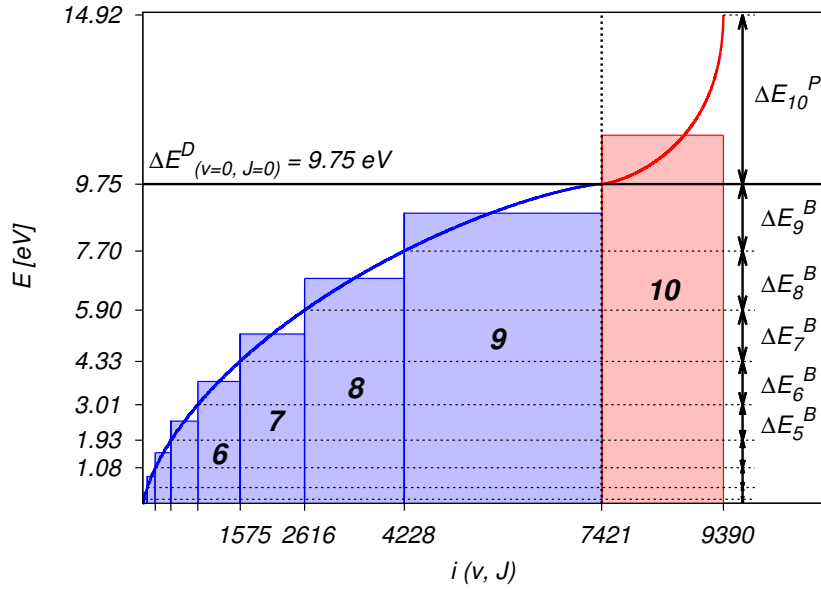
bins. As can be seen, the first 4-5 bins are now too small to be clearly distinguished in the full view. Therefore, Fig. 3.9(b) shows a close-up of the lowest-energy levels and the first 4 bins. Along with the newly defined “heights” of each bin, their “width” also grows with increasing energy, due to there being an increasing number of levels lumped together as the bin number increases. The two examples shown here were used as templates for all of the bin combinations tested in the following parametric study. While the study was conducted also using overall bin numbers much greater than 10, the goal was to arrive at a bin distribution, which would yield results equivalent to the full set of levels with essentially the smallest number of bins possible.

This parametric study was conducted in order to assess the effect of varying the relative sizes of the bins, their distribution among truly bound and pre-dissociated levels, as well as their overall number on the thermodynamic properties of N<sub>2</sub>. The goal was to find a “binning strategy”, which would yield a good enough agreement between the thermodynamic properties of N<sub>2</sub> as predicted by the bin model and those predicted by the full set of rovibrational levels, while simultaneously keeping the overall number of bins as low as possible. For this comparison the overall number of bins was varied between 4 and 500. The ratio of bins containing only truly-bound levels to those containing only quasi-bound levels was kept at 7:3 and 9:1, i.e. the same ratios as before. The full set of tested combinations is tabulated in Tab. 3.3. In order to vary the relative spacing of the truly bound bins, four different choices of the exponent, i.e.  $n = 1, 1.5, 2$  and  $3$  were examined.

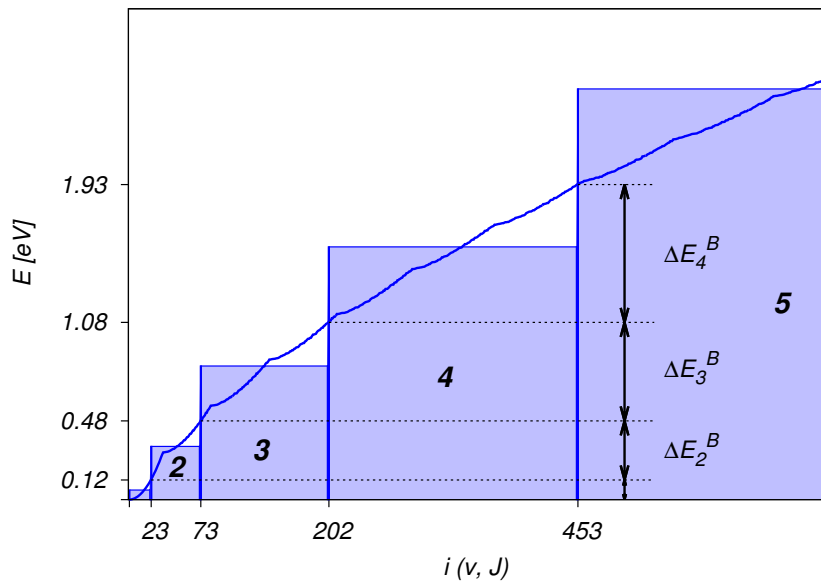
Table 3.3.: Thermodynamic properties of URVC bin model: Tested combinations of truly-bound to quasi-bound bins

total bins	n = 1	n = 1.5	n = 2	n = 3
4	3:1	3:1	3:1	3:1
6	5:1	5:1	5:1	5:1
10	7:3	7:3	7:3	7:3
	9:1	9:1	9:1	9:1
20	14:6	14:6	14:6	14:6
	18:2	18:2	18:2	18:2
100	70:30	70:30	70:30	69:30
	90:10	90:10	90:10	87:10
200	140:60	140:60	140:60	130:60
	180:20	180:20	180:20	159:20
500	350:150	347:150	323:150	275:150
	450:50	438:50	404:50	338:50

Notice that for some of the combinations listed in Tab. 3.3, the sum of truly bound and pre-dissociated bins does not add up to the overall number listed in the first column. This was the case when, due to the particular variable sized-spacing of the truly bound bins, some of them turned out to contain no rovibrational levels at all, and were thus being ignored in the overall count.



(a) Variable-sized energy bins: The lower 9 bins only contain truly bound levels, the last bin contains all the pre-dissociated levels above lying above  $\Delta E_{(v=0, J=0)}^D$ .



(b) Close-up of the lowest-lying energy bins

Figure 3.9.: Altered 10 bin system with variable-size energy intervals  $\Delta E_k$  for the truly bound levels. The lowest bins contain fewer levels and have much smaller average energies  $\bar{E}_k$ .

The first thermodynamic property to be examined is the specific thermal energy of  $N_2$ . It is defined in the present case as:

$$e_{N_2}(T) = \frac{3}{2} \frac{k_B T}{m_{N_2}} + e_{N_2}^{\text{int}}(T) \quad (3.17)$$

where the contribution of the internal energy modes is contained in the second term, given by Eq. (A.34).

The comparison of  $e_{N_2}$  is shown in Fig. 3.10 and Fig. 3.11. Each row shows the results for a particular choice of the exponent  $n$ , ranging from  $n = 1$  to 3. In each row the figure on the left shows the curves of  $e_{N_2}$  over the entire temperature range between 200 and 50000 K. The corresponding figure on the right shows a close-up of the same curves in the low-temperature limit, below 5000 K. Each set of bins is identified by a particular line color and pattern, which is carried over all of the plots in this section. Additionally, in each plot a solid black curve represents the energy obtained with the full set of rovibrational levels. For reference a dashed black line representing the quantity  $\frac{5}{2}R_{N_2}T$  is also included in each plot. This would correspond to the specific thermal energy of  $N_2$ , if only the rotational mode were fully excited, i.e. if the specific heat ratio were  $\gamma = 1.4$ .

Going through all the variations shown in Fig. 3.10 and Fig. 3.11, one can make several general observations. First, as would be expected, the greater the overall number of bins used, the better agreement with the behavior of the full set of levels. In fact, for all of the curves using 100 bins or more, practically no deviation from the full system can be observed over the whole temperature range. By contrast, it seems that for the cases where fewer than 10 total bins were used, the behavior of the thermal energy deviates so strongly from the reference values that the uniform bin approximation becomes unusable in practice. The most noticeable evidence of this is in the behavior of the “3+1”-curve in Fig. 3.10(a) to Fig. 3.11(a), where it consistently over-predicts the value of the energy at all temperatures, and exhibits strong oscillations for  $n = 3$ , as shown in Fig. 3.11(b). For the remaining sets of curves with 10, or 20 bins, the biggest deviations from the reference values occur at the lower end of the temperature scale. These deviations are the greatest for  $n = 1$ , i.e. with equally-sized bins, and become less noticeable at the higher values of  $n$ . As was mentioned before, obtaining a good estimate of the thermal energy at low temperatures is of interest when simulating atmospheric entry flows, since the incoming free stream is usually relatively cold. The sensitivity of the whole flow to this parameter can be observed in the test cases of Ch. 4, especially in Sec. 4.2, where the post-shock conditions are strongly affected by the thermodynamic properties of the gas.

Comparing the behavior of the 10-bin and 20-bin curves in the low-temperature range, one may observe that when a 9:1 ratio of truly bound- to pre-dissociated bins is used, the agreement with the full set of levels tends to be better than when the 7:3 ratio is applied. Thus, it seems that increasing the “resolution” of the bins in the energy range of the truly bound levels has the greatest impact to improving the accuracy of the uniform bins as a whole. The second thermodynamic property to be examined is the specific constant-volume heat capacity of pure  $N_2$ . It is, of course, directly related to the thermal energy of Eq. (3.17), because it represents its partial derivative with respect to temperature at constant specific volume. It appears in the “frozen” part of the

### 3. Implementation of URVC bin model in VKI DSMC code

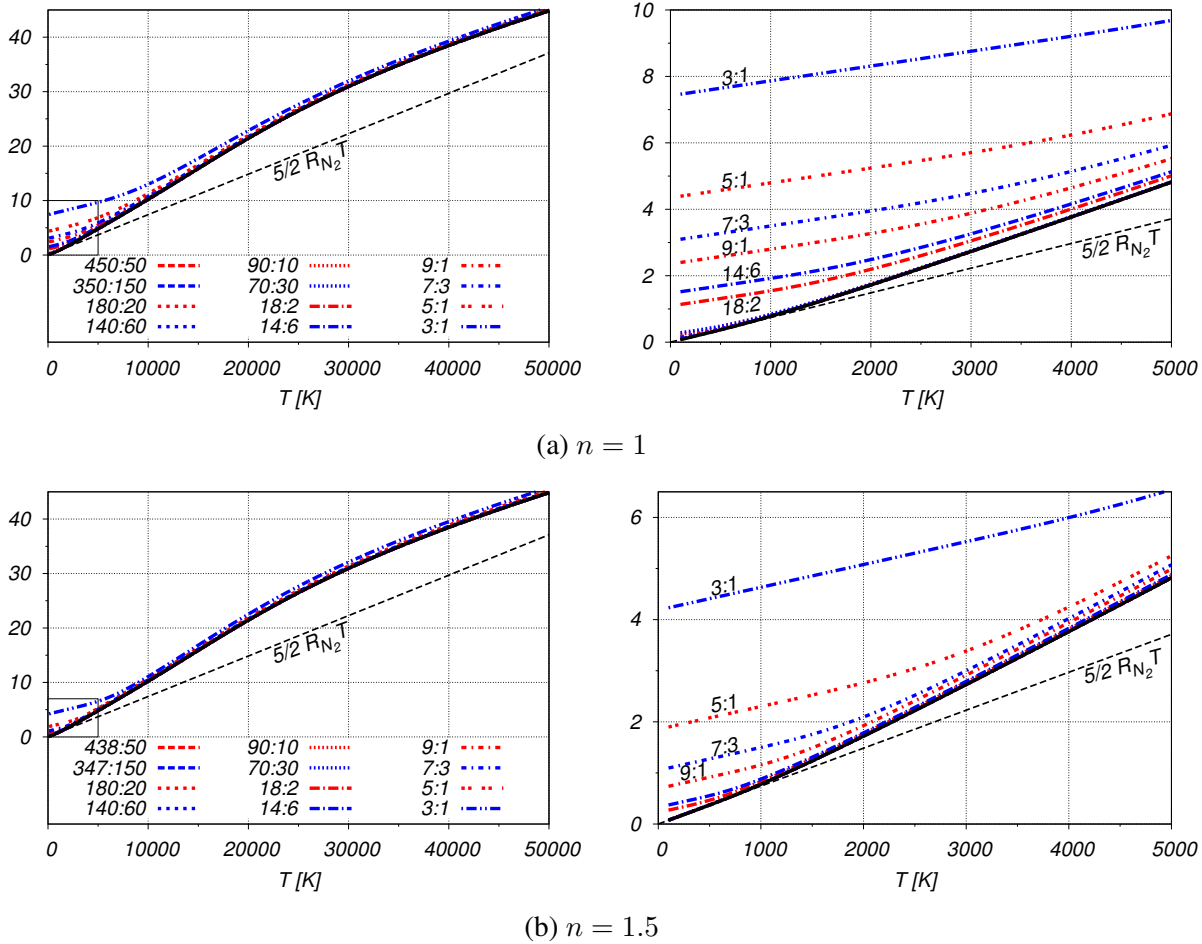


Figure 3.10.: Specific thermal energy of pure  $N_2$  in MJ/kg as a function of temperature

mixture- $c_v$  and is defined as:

$$c_{v,N_2}(T) = \frac{\partial e_{N_2}}{\partial T} = \frac{3}{2} \frac{k_B}{m_{N_2}} + \frac{1}{m_{N_2} k_B T^2} \left[ \frac{\bar{B}_{N_2}^{\text{int}}(T)}{\bar{Z}_{N_2}^{\text{int}}(T)} - \left( \frac{\bar{A}_{N_2}^{\text{int}}(T)}{\bar{Z}_{N_2}^{\text{int}}(T)} \right)^2 \right], \quad (3.18)$$

where the function  $\bar{A}_{N_2}^{\text{int}}(T)$  is given by:

$$\bar{A}_{N_2}^{\text{int}}(T) = \sum_{k \in \mathcal{K}_{N_2}} \bar{a}_k \bar{E}_k \exp\left(-\frac{\bar{E}_k}{k_B T}\right), \quad (3.19)$$

$\bar{B}_{N_2}^{\text{int}}(T)$  by:

$$\bar{B}_{N_2}^{\text{int}}(T) = \sum_{k \in \mathcal{K}_{N_2}} \bar{a}_k \bar{E}_k^2 \exp\left(-\frac{\bar{E}_k}{k_B T}\right), \quad (3.20)$$

and  $\bar{Z}_{N_2}^{\text{int}}$  is the partition function of the internal energy mode, as given by Eq. (A.33). The comparison of  $c_{v,N_2}$  for all combinations of parameters is shown in Fig. 3.12. The line patterns and colors are carried over from Fig. 3.10 and Fig. 3.11. Again, the solid black line represents the reference value of the heat capacity obtained with the full set of levels. There are two additional

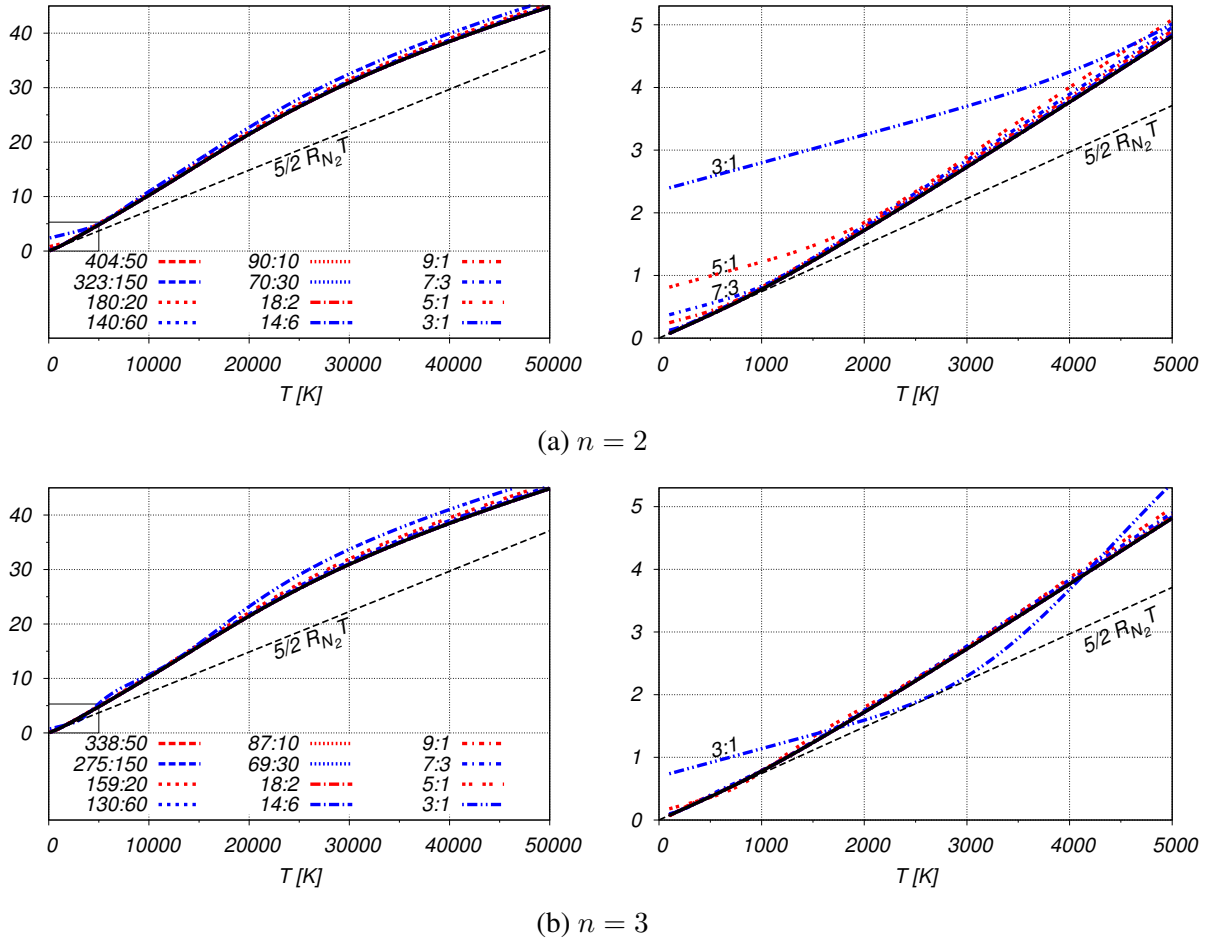


Figure 3.11.: Specific thermal energy of pure  $N_2$  in MJ/kg as a function of temperature (continued)

horizontal dashed lines, drawn for reference. The first one, at  $\frac{3}{2}R_{N_2}$  represents the contribution to the  $c_v$  of the translational mode alone. The second line, at  $\frac{5}{2}R_{N_2}$  represents the  $c_v$  one would obtain, if one included only the contribution of the fully excited rotational mode. Thus, it represents the slope of the dashed lines from the plots in Fig. 3.10 and Fig. 3.11. As was the case for the thermal energy, the heat capacity is plotted in the images on the left over temperatures ranging from 200 to 50000 K, while the images on the right hand side show a close-up of the low-temperature behavior below 5000 K. Notice from the behavior of the solid black lines that the  $c_v$  predicted by the full set of levels tends towards its limiting value of  $\frac{5}{2}R_{N_2}$  at temperatures below  $\approx 400$  K. Thus, it correctly predicts that at these low temperatures the vibrational mode is practically not excited.

Concerning the behavior of the different binned  $c_v$ -curves, it is clear that they show much greater variation than for the thermal energy. Focusing first on the bins using uniform spacing, shown in Fig. 3.12(a), one can see that there are significant deviations from the full model for all binned systems. This can be clearly seen in the close-up image on the right. The deviations are especially severe for the systems with 20 bins, or less. Below temperatures of 1000 K, these curves

completely miss the excitation of the internal modes, and significantly under-predict the value of the  $c_v$  for temperatures up to 20000 K. Using 100 bins or more, the low-temperature behavior improves somewhat, but even for the largest systems using 500 bins the low-temperature limiting value of  $\frac{5}{2}R_{N_2}$  is never fully reached.

Moving on to the variably-sized bins obtained with  $n = 1.5$ , in Fig. 3.12(b), one can observe a significant improvement in the low-temperature behavior of all binned systems. While not yet perfect, with 100 bins and more close agreement with the full system is recovered for temperatures as low as  $\approx 300$  K. While significant deviations are still evident for those systems with 20 bins or less, all of the curves have moved closer to the reference values. While using variably-sized bins with  $n = 1.5$  generally helps improve the low-temperature accuracy of the binned systems, undesirable oscillations start to appear in the “3+1”-curve when the full temperature range is considered. An overshoot of this curve is especially noticeable in the range between 10000 and  $\approx 20000$  K. Moving on to the curves with  $n = 2$ , shown in Fig. 3.13(a), one can see that this phenomenon starts to affect the larger systems with 10, or 20 bins as well, while the oscillations for the smallest systems become more severe. Thus, using the variably-spaced bins does not always represent an improvement over the original uniformly-spaced approach. Judging from the strong oscillations affecting the  $c_v$ -curves at Fig. 3.13(b), one may conclude that the variable bin spacing with  $n = 3$  is unsuitable for all of the variants using 10 bins, or less.

The plots in Fig. 3.14 show the effect of the different choices of bins on the predicted equilibrium number density ratios of atomic- to molecular nitrogen as a function of temperature. This ratio is affected by the binning strategy due to a shift in the constant for the chemical equilibrium  $N_2 \rightleftharpoons 2N$ . If number densities are used to represent the species concentrations, the equilibrium constant for the present comparison becomes:

$$\left[ \frac{n_N^2}{n_{N_2}} \right]^{\text{eq}} = K_{N_2 \rightleftharpoons 2N}^{\text{eq},n} = \frac{[Z_N^{\text{tra},*}(T) a_N]^2}{Z_{N_2}^{\text{tra},*}(T) \bar{Z}_{N_2}^{\text{int}}(T)}. \quad (3.21)$$

where  $a_N = 12$ , the translational parts of the partition functions of N and  $N_2$  are evaluated according to Eq. (2.21), and the internal partition function of molecular nitrogen is evaluated in each case using the particular choice of bins according to Eq. (A.33).

The figures in Fig. 3.14 showing the comparisons of the equilibrium constant (in units of  $\text{m}^{-3}$ ), are organized in a similar manner as for the previous two quantities. Each row shows the results for a particular choice of the exponent  $n$  and covers the same selection of bins as before. Two plots are shown for each  $n$ : The one on the left covers the high-temperature range between 10000 and 50000 K, while the figure on the right gives a close-up of the lower temperatures between 200 and 10000 K. Notice that the sense of the temperature scale on the abscissa has been inverted and is non-linear. In addition to this, a logarithmic scale for the equilibrium constant has been used on the ordinate. Due to the particular functional form of the equilibrium constant, this arrangement

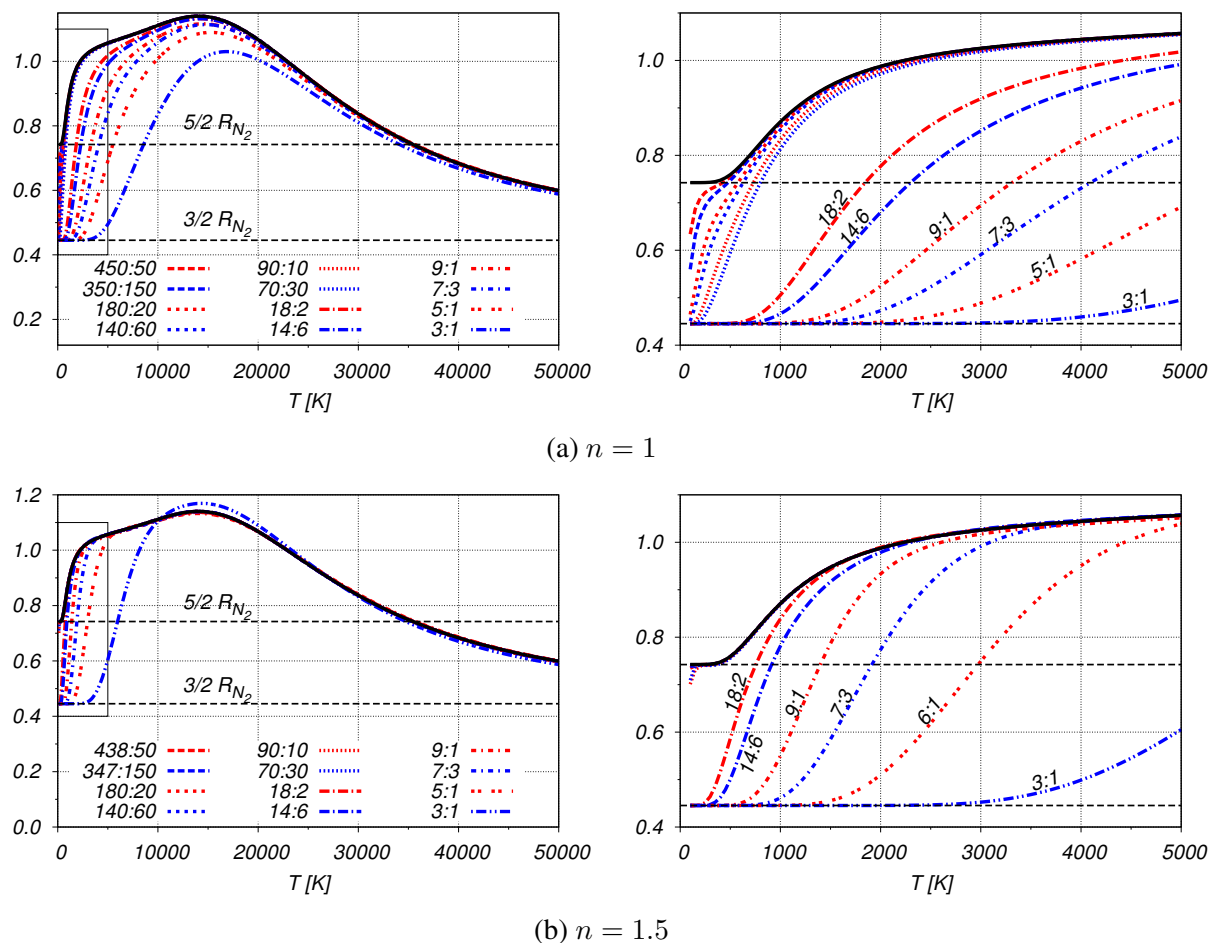


Figure 3.12.: Specific constant-volume heat capacity of pure  $N_2$  in  $\text{kJ/kg K}$  as a function of temperature

was thought to make it easier to compare the individual curves.

The same exact line patterns as before have been used in each plot to identify a particular combination of truly bound to pre-dissociated bins. For the equilibrium constant, the different curves are fairly close to one another over most of the temperature range, regardless of the particular choice of  $n$ . The greatest discrepancies can be observed in Fig. 3.14(a) at the lower temperature limit. Not all curves have been labeled in this plot (top right), but the ones that deviate noticeably from the behavior of the full set of levels range between 4 and 20 bins. With  $n = 2$ , all curves move closer to the reference values. This is especially noticeable at the lower temperature limit shown in the plot on the right. Now only the curves between 4 and 10 bins can be distinguished from the reference.

The potential size reduction of the chemical mechanism achieved as a consequence of careful adjustment of the bin model parameters is remarkable. Being able to reduce the number of internal states of  $N_2$  from 9390 rovibrational levels to only about 10 bins, without severely degrading the quality of the model, implies significant savings in computational expense. Considering only

### 3. Implementation of URVC bin model in VKI DSMC code

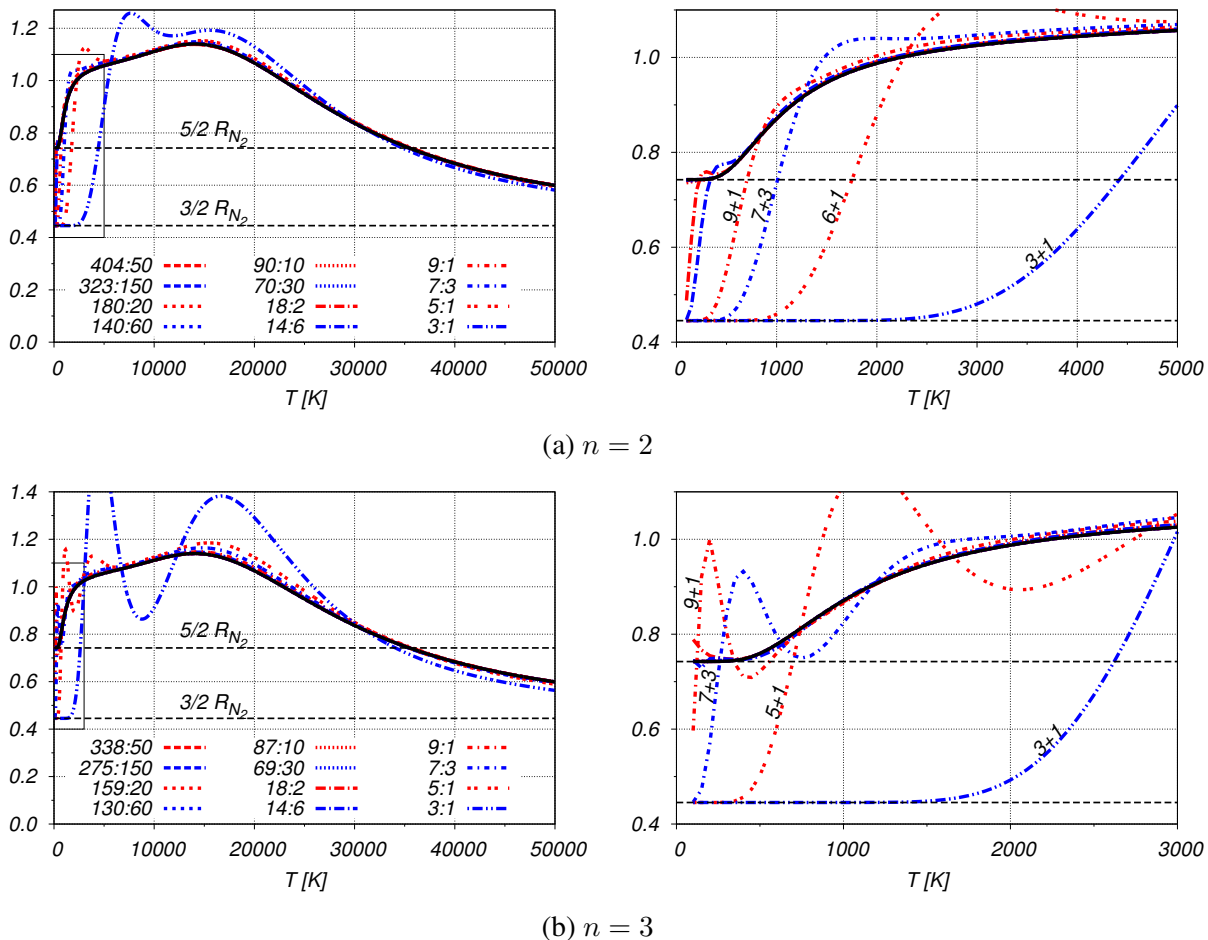


Figure 3.13.: Specific constant-volume heat capacity of pure  $N_2$  in  $\text{kJ/kg K}$  as a function of temperature (continued)

the set of reactions comprised in Tab. 2.3, the potential number of unique forward reaction cross sections decreases from roughly  $44.1 \times 10^6$  with the full set of levels to only 65 when using 10 bins. Of course, these numbers exclude the reverse reactions, which are computed through detailed balance relations. The size reduction is even more dramatic, if one considers for a moment all possible reaction paths involving  $N_2(k) + N_2(l) \rightleftharpoons N_2(k') + N_2(l')$ -collisions. When transitions from all possible pre-collision states  $k, l$  to all possible post-collision states  $k', l'$ , plus the two possible dissociation reaction types  $N_2(k) + N_2(l) \rightleftharpoons N_2(k') + 2N$  and  $N_2(k) + N_2(l) \rightleftharpoons 4N$  are considered, the number of cross sections for the full set of levels is estimated at a staggering  $9.72 \times 10^{14}$ . After the reduction to 10 bins, this number decreases to “only” 2145. While still very large, it is still conceivable to run academic test cases with the bin model, whereas the mechanism involving the full set of levels would be completely out of the question.

After the comparison presented in this section, what remains to do is to narrow down the preferred binning strategy to be applied in the test cases studied in Ch. 4 and Ch. 5. First, since it was found that in many situations using fewer than 10 bins resulted in significant errors in the thermodynamic properties, these systems will no longer be considered. At the other end of the

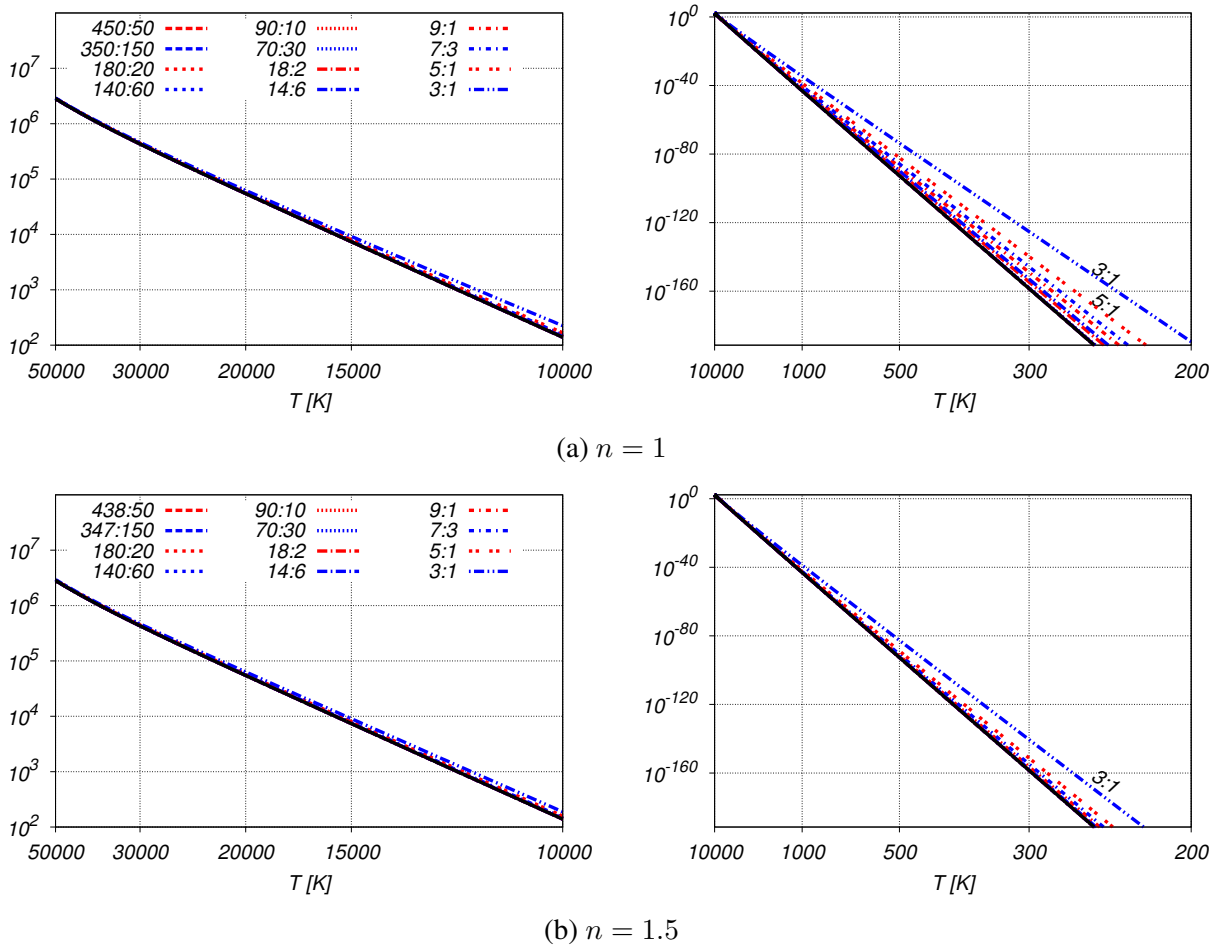
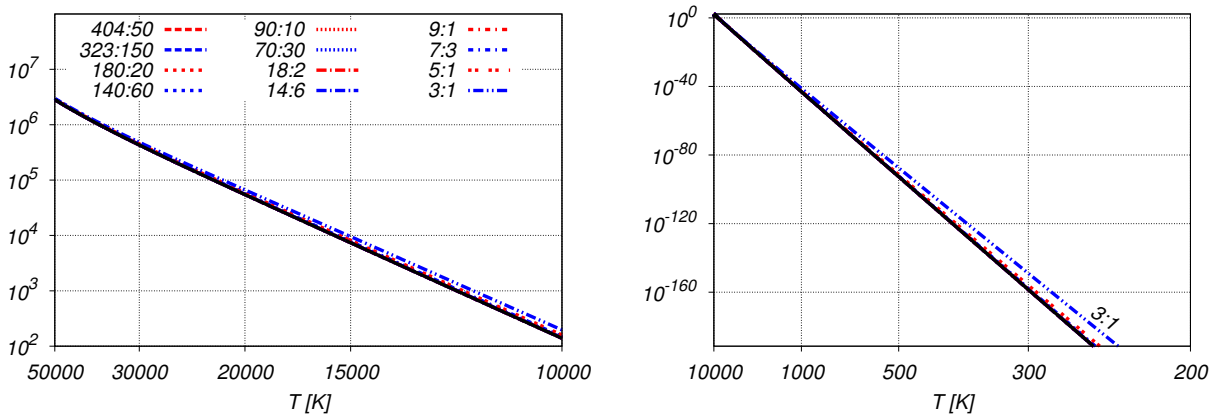


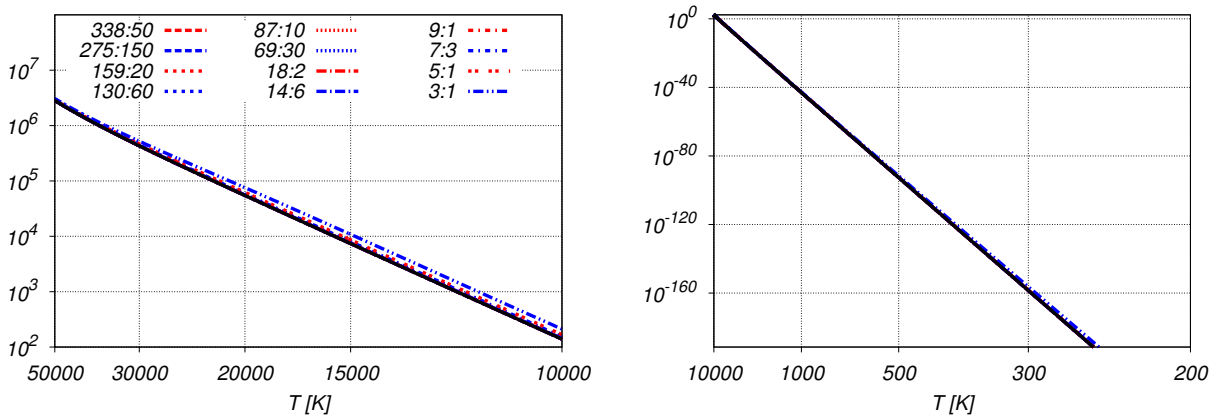
Figure 3.14.: Equilibrium number density ratio for  $N_2 \rightleftharpoons 2N$  in  $m^{-3}$  as a function of temperature

spectrum one may conclude that no more than 100 or 200 bins will ever be needed to approximate the behavior of the full set of levels. Also, significant improvements over the baseline strategy of using equally-sized bins can be achieved for even a moderate number of bins, if the individual bin sizes are varied in a convenient manner. Thus, in what follows the variably-sized bins with a ratio of 9:1 of truly bound- to predissociated bins will be used, along with the stretching exponent of  $n = 1.5$  or  $n = 2$ . It should be noted that in the present comparison only the thermodynamic properties were involved. However, in order to observe the effect that the different binning choices have on the detailed chemical kinetics of the  $N_3$  system, one would have to compare the individual rate coefficients as well. Due to the large number of coefficients involved it is preferable to study this behavior as part of an actual test case. The test case discussed in Sec. 4.1 has the dual function of studying the effect of different binning strategies on the kinetics of the system, as well as verifying the DSMC implementation of the state-to-state model.

### 3. Implementation of URVC bin model in VKI DSMC code



(a)  $n = 2$



(b)  $n = 3$

Figure 3.15.: Equilibrium number density ratio for  $N_2 \rightleftharpoons 2N$  in  $m^{-3}$  as a function of temperature (continued)

## 4. Verification of URVC bin model in VKI DSMC code

This section presents two test cases, which demonstrate the integration of the state-to-state URVC bin model with the VKI DSMC code. The basic algorithms in this code are based on the standard routines of Bird [1], and it is capable of handling simple 0D and 1D flows. It is therefore especially suited for the reservoir- and normal shock test case discussed in this chapter. The DSMC implementation of the state-to-state algorithm for internal energy exchange was partially verified in [140] against results originally obtained by Anderson [113]. Furthermore, it has been used in several test cases to verify equivalent results obtained by a deterministic Boltzmann solver [141].

The first test case, discussed in Sec. 4.1, consists of a simple space-homogeneous adiabatic reactor, which is used to study the unsteady internal energy exchange and dissociation processes occurring in a mixture of molecular and atomic nitrogen. In order to verify the implementation of the bin model, the DSMC results are compared with equivalent master equation results. The same test case is re-run for a selection of the different binning parameters discussed in Sec. 3.4. This helps to demonstrate the sensitivity of the system to the precise choice of the bin size and number. Reinforcing the results already obtained by studying the thermodynamic properties of the bin model in Sec. 3.4, it is found that 100 bins are practically enough to reproduce the behavior of the full system of 9390 rovibrational levels. Furthermore, the advantage of defining variable-sized energy intervals, as compared to equally-sized ones, is demonstrated for the cases when the number of bins is kept at 10. A preliminary version of this study was previously presented in [142].

The second test case, where the URVC bin model is also used in conjunction with the VKI DSMC code, is discussed in Sec. 4.2. It involves the compression of a mixture of molecular and atomic nitrogen across a normal shock wave. After the verification case of Sec. 4.1, the normal shock is the natural next step and aims to demonstrate the behavior of the bin model in a slightly more realistic configuration. Of particular interest in this case is the structure of the shock front, the length of the relaxation region and the distance behind the initial compression, after which full dissociation of molecular nitrogen occurs. In this case, the simulation using 100 equally-sized bins serves as the reference calculation. Both other simulations use only 10 bins, and compare the equally-sized bins listed in Tab. 3.1 to the variable-sized ones of Tab. 3.2. The

better representation of the thermodynamic properties at low temperatures of the latter binning choice is clearly demonstrated with this test case.

Based on the findings of these two test cases, a 10-bin system with variable-sized energy intervals is then used in the simulations discussed in Ch. 5, where the URVC bin model is used in conjunction with an external 2D/3D DSMC solver.

## 4.1. Internal energy excitation and dissociation in adiabatic reactor

As the first verification test case for the URVC bin model, adiabatic relaxation towards equilibrium in a reservoir of constant volume was studied. It should be noted that the test case discussed in this section was simulated with the 0-D version of the VKI DSMC code, developed by the author. The master equation results used for comparison were generated by a separate code written by Munafò as part of his dissertation work [132] at VKI. The flow configuration used is radically simplified by assuming that the gas is spatially homogeneous and does not interact with external boundaries. Therefore, the problem can be confined to a single cell and all portions of the DSMC algorithm concerned with particle motion are inactive. In the equivalent fluid-dynamic description, this situation is governed by a system of master equations describing the evolution of the populations of all bins of  $N_2$ , plus one for the concentration of atomic nitrogen:

$$\frac{d\bar{\rho}_k}{dt} = \bar{\omega}_k^{\text{in}} + \bar{\omega}_k^{\text{re}} \quad k \in \mathcal{K}_{N_2} \quad (4.1)$$

$$\frac{d\rho_N}{dt} = \omega_N. \quad (4.2)$$

The source terms on the right-hand-side of Eq. (4.1) are given by Eq. (A.28) and Eq. (A.29) of Sec. A.2, while the source term for Eq. (4.2) is given by Eq. (A.30). Since the system is isolated from the surroundings, both its overall mass, momentum and energy remain constant. The hydrodynamic velocity of the gas can be arbitrarily set to zero, and remains constant over time. In this case the energy equation can be manipulated to yield the instantaneous translational temperature of the mixture directly from the populations:

$$T_t = \frac{\rho e_0 - \left[ \sum_{k \in \mathcal{K}_{N_2}} \bar{n}_k \bar{E}_k + n_N E_N \right]}{\frac{3}{2} k_B \left[ \sum_{k \in \mathcal{K}_{N_2}} \bar{n}_k + n_N \right]} \quad (4.3)$$

where the density  $\rho$  remains constant and the initial energy of the system is imposed as:

$$e_0 = \left( \frac{1 - y_N^0}{m_{N_2}} + \frac{y_N^0}{m_N} \right) \frac{3}{2} k_B T_t^0 + \frac{(1 - y_N^0)}{m_{N_2}} \sum_{k \in \mathcal{K}_{N_2}} \frac{\bar{a}_k \bar{E}_k}{\bar{Z}_{N_2}^{\text{int}}(T_{\text{int}}^0)} \exp\left(-\frac{\bar{E}_k}{k_B T_{\text{int}}^0}\right) + \frac{y_N^0}{m_N} E_N, \quad (4.4)$$

with  $T_t^0$  and  $y_N^0$  being the initial translational temperature and atomic nitrogen mass fraction respectively. The macroscopic initial conditions chosen are summarized in Tab. 4.1(a), and are intended to approximate the flow immediately behind a strong shock wave. Initially, the gas is in a state of thermal and chemical non-equilibrium, with all particle velocities following a Maxwellian distribution at  $T_t^0 = 62546$  K and a static pressure of 3164 Pa, while the initial bin populations of  $N_2$  follow a Boltzmann distribution at  $T_{\text{int}}^0 = 300$  K. A small quantity of atomic nitrogen (mass fraction:  $y_N^0 = 0.014$ ) is also added to the initial mixture. The atomic nitrogen is necessary to initiate the processes of internal energy exchange and dissociation, since the present reaction mechanism only includes rate data for  $N_2(k) + N$ -collisions. If the reservoir contained only  $N_2$  molecules, no reactions could occur and no change in the bin concentrations could be observed.

In each of the cases studied, the gas mixture is initially represented by approximately  $8 \times 10^4$  DSMC simulator particles. As the simulation progresses, this number gradually increases to about  $1.3 \times 10^5$ , due to the dissociation of  $N_2$ . A constant time step  $\Delta t = 10^{-8}$  s was chosen, which is well below the mean collision time. All simulations were run on the same quad-core workstation and the instantaneous macroscopic samples are ensemble-averages over four independent simulations. Thus, the macroscopic samples are based on a total of  $3.2 \times 10^5 - 5.2 \times 10^5$  particles. Tab. 4.1 summarizes both the initial and final states of the reservoir. The same test case was repeated for  $n_{\text{bins}} = 10, 20, 100$  and 200. As discussed in Sec. 3.4, increasing the overall number of bins effectively improves the ‘‘resolution’’ of the bin model and brings its thermodynamic properties closer to those of the full set of rovibrational levels. The first series of simulations were performed using the original model, i.e. with equally-sized bins (where  $n = 1$  according to the definitions of Sec. 3.4). The final equilibrium conditions for these simulations are listed Tab. 4.1(b). Notice that, due to the variation in thermodynamic properties, both the final equilibrium temperature, as well as the equilibrium mass fraction of the mixture are affected by the number of bins used. For comparison, the equilibrium conditions for the full model with its 9390 levels, are listed in the last row.

In Fig. 4.1(a) profiles of translational and internal temperature are shown, while the corresponding mass fraction profiles are given in Fig. 4.1(b). The lines correspond to the DSMC simulations, while the symbols represent the equivalent master equation results. Note that while the master equation solutions are given for simulation times up to 10 seconds, proceeding until reaching full chemical and thermal equilibrium in the reservoir, the DSMC results (lines) are only shown up to  $t = 0.01$  seconds. There are two reasons for this: first, using the above-mentioned constant

$\Delta t = 10^{-8}$  s for the DSMC simulations would require a total of  $10^9$  time steps. With the present code, such a simulation would require several weeks to be completed. Since the goal of this test case was to verify the correct implementation of the bin model and its ability to reproduce the master equation results for the early stages of the relaxation process, it was enough to run the DSMC simulations until reaching  $t = 0.01$  seconds. By comparison, the implicit time integration scheme used in the master equation solver is able to adapt the computational time step, and is capable of providing the full solution in less than a second of real time. The second reason for stopping the DSMC runs at  $t = 0.01$  seconds is that in the current DSMC implementation recombination reactions, i.e.  $3N \rightarrow N_2(k) + N$ , have been neglected. This makes it impossible for the DSMC results to match the final equilibrium concentrations of N and  $N_2$ , as predicted by the master equations. Neglecting recombination reactions is not a problem for the early stages of the process, when the temperature in the reservoir is high, and the dissociation of molecular nitrogen is the dominant reaction. However, once the gas has cooled off to somewhere below 8000 K, the recombination rate would gradually increase to balance out the declining dissociation rate, finally reaching dynamic equilibrium between the two processes. Since recombination has been neglected in the DSMC model, it is incapable of attaining this equilibrium regime.

For illustration purposes the difference in behavior is demonstrated in Fig. 4.3(a) and Fig. 4.3(b), where master equation results for the 100-bin case are shown with and without recombination enabled. In this situation, with recombination reactions not being taken into account, the remaining  $N_2$  will eventually dissociate completely, and the final state of the system diverges from the correct equilibrium state. Returning to the early stages of the process, Fig. 4.1 shows that for

Table 4.1.: Internal energy excitation and dissociation in adiabatic reactor: reservoir conditions at  $t = 0$  and at final equilibrium state ( $t \rightarrow \infty$ ).

(a) Initial nonequilibrium state

	$T_t^0$ [K]	$T_{int}^0$ [K]	$p_0$ [Pa]	$y_N^0$
Initial	62546	300	3164.0	0.014

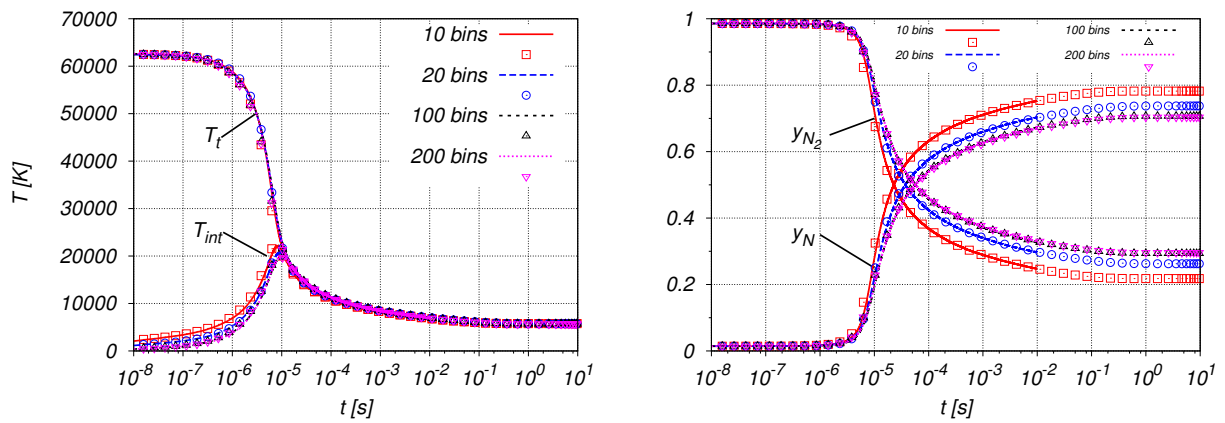
(b) Final equilibrium state, (Equally-sized energy bins with  $n = 1$ )

	B:P	$T_{eq}$ [K]	p [Pa]	$y_N$
10 bins	7:3	5763	512.3	0.782
20 bins	14:6	5737	497.2	0.737
100 bins	70:30	5699	485.2	0.707
200 bins	140:60	5695	484.0	0.704
full system		5693	483.4	0.702

(c) Final equilibrium state, (Variable-sized energy bins with  $n = 2$ )

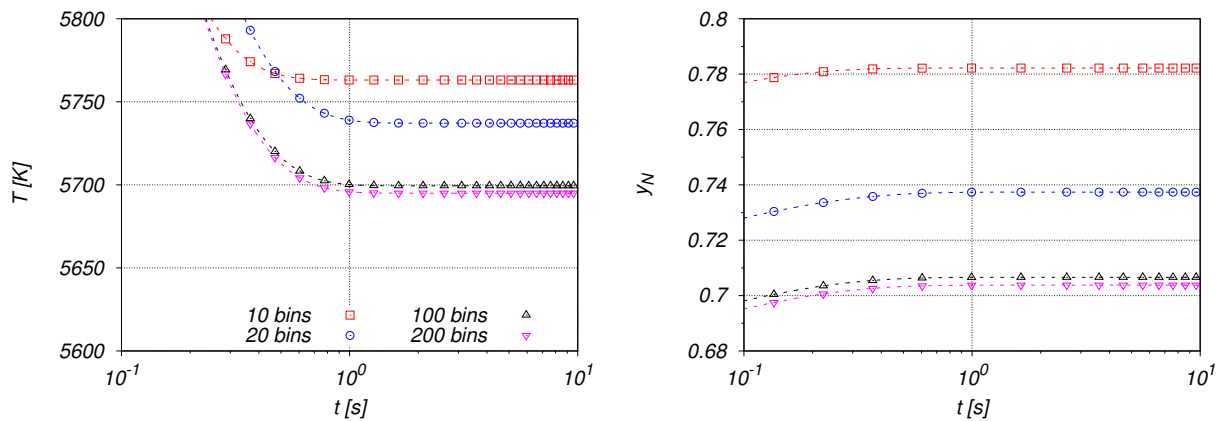
	B:P	$T_{eq}$ [K]	p [Pa]	$y_N$
10 bins	9:1	5699	488.6	0.719
20 bins	18:2	5693	484.5	0.706
100 bins	90:10	5693	483.4	0.702
200 bins	180:20	5693	483.4	0.702
full system		5693	483.4	0.702

the smaller values of  $n_{\text{bins}}$ , internal energy exchange and dissociation proceed slightly faster. Regardless of the number of bins chosen, it can be seen that about  $10^{-5}$  seconds are required for the translational and internal modes to relax to a single temperature, slightly above 20000 K. At the beginning internal energy exchange reactions seem to play the dominant role, while the mass fractions of N and  $N_2$  in Fig. 4.1(b) remain essentially constant up to about  $2.0 \times 10^{-6}$  seconds. Only after this “incubation period” do the dissociation reactions really become significant. The final equilibrium composition in the reservoir is strongly affected by the choice of the number of bins, as can be seen in Tab. 4.1. For 10 bins the final mass fraction of N is about 0.782, while for 200 bins it approaches 0.704. The late stages of the evolution towards equilibrium are shown in Fig. 4.1(c) for the temperatures and in Fig. 4.1(d) for the mass fractions of atomic nitrogen. In both graphs only master equation results, represented by symbols joined by dotted lines, are shown. The same test case was re-run using the variable-sized bins discussed in Sec. 3.4, i.e. those



(a) Mixture translational temperature and internal temperature of  $N_2$

(b) Mass fraction profiles of  $N_2$  and N



(c) Close-up of mixture translational temperature and internal temperature of  $N_2$  as  $t \rightarrow \infty$  (Only master equation results)

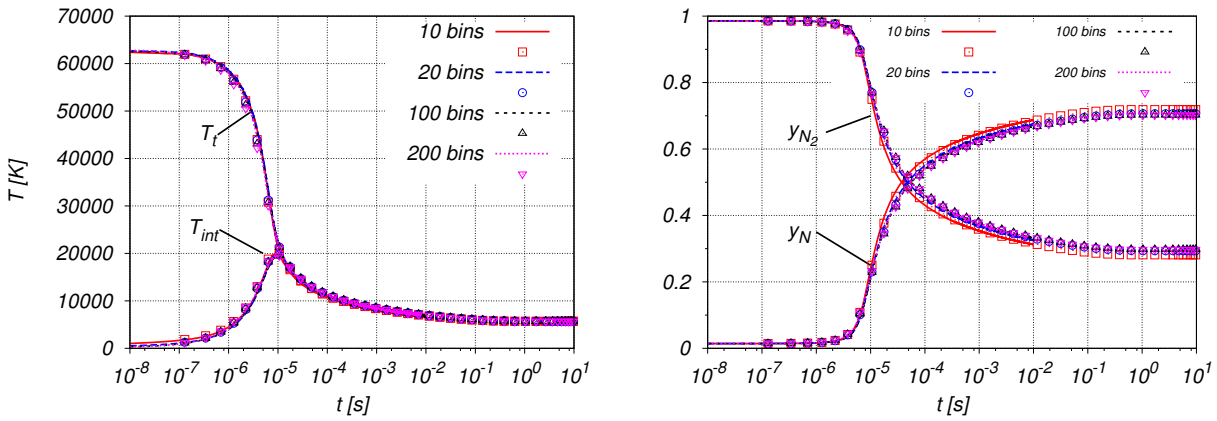
(d) Close-up of mass fraction profiles of N as  $t \rightarrow \infty$  (Only master equation results)

Figure 4.1.: Comparison of DSMC calculations (lines) with master equation results (symbols) using equally-sized bins

with a ratio of 9 truly bound- to 1 pre-dissociated bin, and an exponent of  $n = 2$ . This means

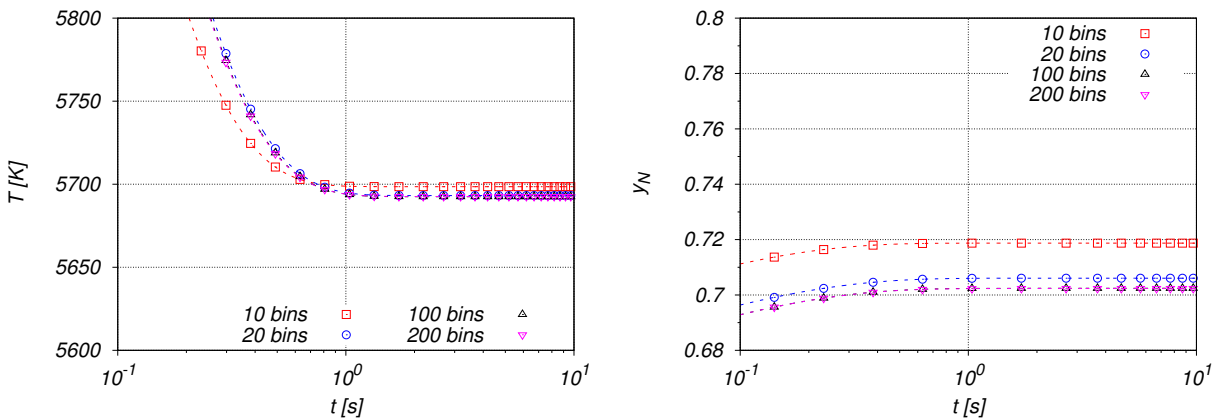
#### 4. Verification of URVC bin model in VKI DSMC code

that now the 10-bin system corresponds to 9:1, the 20-bin system to 18:2, the 100-bin system to 90:10 and the 200-bin system to 180:20. The final equilibrium conditions for these simulations are listed in Tab. 4.1(c). Focusing on the mass fractions of atomic nitrogen, the largest deviation from the full model occurs for the 10-bin case, with less than 3% of relative error. The final equilibrium temperature is also predicted to within less than 1% error using only 10 bins. This is a remarkable improvement over the original equally-sized bins. The last two cases, where 100 and 200 bins were considered, are practically indistinguishable from one another. This suggests that they behave almost exactly as the full system with its 9390 levels would. The improved behavior of the variable-size bins is confirmed when the time evolution of temperatures and species mass fractions is analyzed. These profiles are plotted in Fig. 4.2(a) and Fig. 4.2(b). Compared to the previous simulations of Fig. 4.1, which used equally sized bins, one can notice that the profiles for all four cases are now much closer to one another over the whole length of the process. Again, Fig. 4.2(c) and Fig. 4.2(d) provide a close-up of the late stages of the simulation.



(a) Mixture translational temperature and internal temperature of  $N_2$

(b) Mass fraction profiles of  $N_2$  and  $N$



(c) Close-up of mixture translational temperature and internal temperature of  $N_2$  as  $t \rightarrow \infty$  (Only master equation results)  
 (d) Close-up of mass fraction profiles of  $N_2$  as  $t \rightarrow \infty$  (Only master equation results)

Figure 4.2.: Comparison of DSMC calculations (lines) with master equation results (symbols) using variable-sized bins

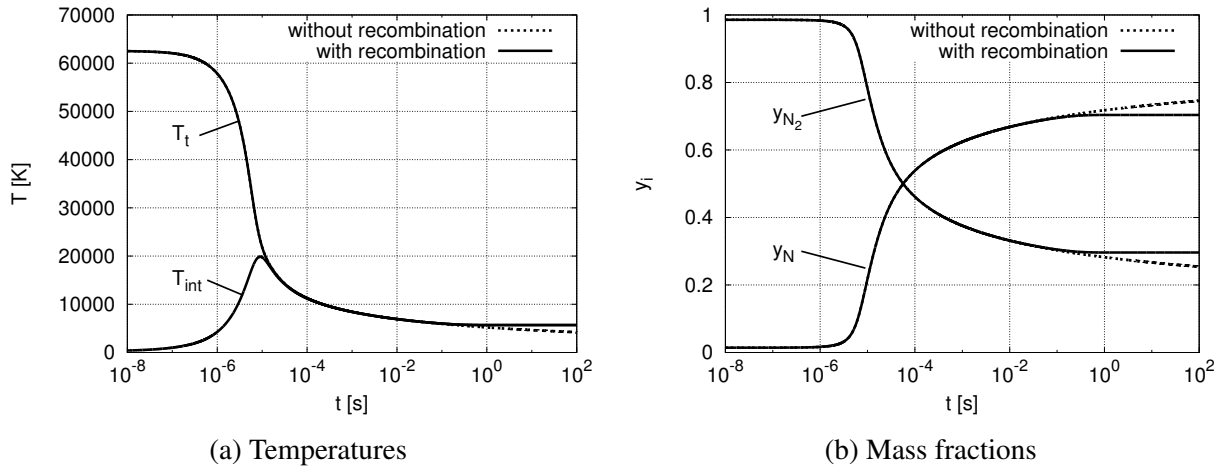


Figure 4.3.: Master equation calculations for the 100 bin system, with (solid lines) and without recombination (dotted lines)

Before concluding this section, it is worth discussing the computational cost associated with the use of the bins. The comparison presented here is not rigorous in an absolute sense, since the run-time depends on the precise settings used in the test case, the type of CPU used and on the manner in which the algorithm itself is implemented. However, comparing the relative run-times listed in Tab. 4.2 can give an indication of the cost as a function of the number of bins. Since in the present test case particle motion is inactive within the DSMC code, practically all the effort is spent on computing the collisions. There are thus two main parts of the algorithm, which are responsible for the run-time: the computation of the total cross section and the determination of the collision outcome. Both these parts require a loop over all bins, which makes the computational effort directly dependent on the overall number of bins. The values listed in Tab. 4.2 suggest that the computational time spent in the collision routines is roughly proportional to the number of bins used. From the results of this section several conclusions can be drawn. First, the collision

Table 4.2.: Run times for DSMC code ( $10^6$  time steps) using an Intel(R) Xeon(R) X5650 CPU at 2.67GHz with variable-sized bins

	CPU time [h]
10 bins	16.4
20 bins	24.5
100 bins	93.1
200 bins	200

routines related to the bin model were successfully implemented in the VKI-DSMC code and verified against the existing master equation results. The second conclusion is that the variable-sized bins offer much better accuracy in terms of reproducing the thermodynamic properties of the full system, even with as few as 10 bins. Since the computational cost of the bin model increases significantly with the number of bins, it is desirable to keep this number as low as possible, especially once the URVC model is used with 2D or 3D applications. This point applies

to DSMC, but also to continuum CFD implementations, where each additional bin requires an additional mass balance equation to be solved. Based on the comparisons made in this section, it is reasonable to assume that 10 variable-sized bins provide enough accuracy for the test case to follow, as well as the ones treated in Sec. 5.2 and Sec. 5.3.

## 4.2. Internal energy excitation and dissociation across normal shock wave

After verifying the DSMC implementation of the URVC bin model in the adiabatic reactor discussed in Sec. 4.1, the current test case consists of a steady, one-dimensional flow across a normal shock. Here, a relatively cold stream of molecular nitrogen is compressed through a strong shock wave, causing excitation of the internal energy modes and eventually, complete dissociation of all  $N_2$ -molecules. The flow is set up according to the diagram shown in Fig. 4.4: Both extremes of the domain are treated as open stream boundaries. The high-speed flow enters from the left, and after traversing the standing shock wave, leaves the domain towards the right. The boundary conditions, expressed in terms of the equilibrium macroscopic flow parameters, are listed in Tab. 4.3. The velocity distributions of the particles injected into the domain at both boundaries conform to Maxwellians with the respective average velocities and equilibrium temperatures. The particles representing molecular nitrogen, which are injected at the left boundary, populate the rovibrational bins according to a Boltzmann distribution at the undisturbed pre-shock equilibrium temperature. As was the case in Sec. 4.1, a small amount of atomic nitrogen has been added to the incoming free stream, in order to trigger the inelastic collision processes, since neither internal energy exchange, nor dissociation by  $N_2$ - $N_2$  collisions are included in the present model. The

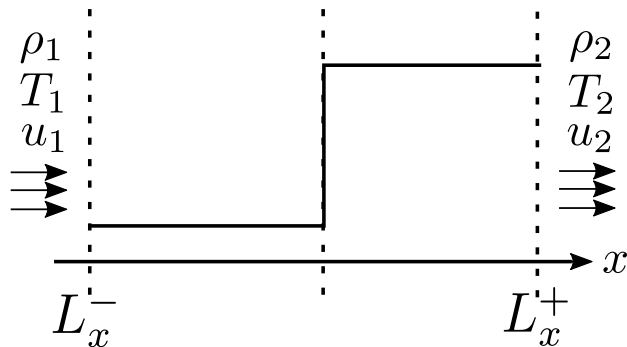


Figure 4.4.: Standing normal shock wave: Problem set up

post-shock equilibrium state imposed at the boundary to the right was determined by applying the Rankine-Hugoniot jump conditions. However, in the present case the gas is not chemically inert. Due to the strong temperature increase, its chemical composition changes across the shock. This fact, together with the need to take into account the partially excited rovibrational energy

mode of  $N_2$ , means that the ratio of specific heat capacities, i.e.  $\gamma = c_p/c_v$ , is not constant across the shock. This, in turn prevents the use of the well-known analytical normal shock relations derived for inert gases, and an iterative numerical procedure, outlined by Anderson [2], is used instead. Three different post-shock equilibrium states are listed in Tab. 4.3, because the test case was repeated with three different choices of rovibrational bins. The first one, which is labeled “10 bins (E)”, uses the set of 10 equally-sized rovibrational bins (7:3 ratio), which were also part of the verification in Sec. 4.1. The second entry, labeled “100 bins (E)”, uses 100 equally-sized bins (70:30 ratio). As was confirmed by the results of Sec. 4.1, 100 bins were found to be enough to approximate the full 9390 rovibrational levels of  $N_2$ . Therefore, this data set will be used as the reference case in the present study. Finally, the third entry, which is labeled “10 bins (V)” uses 10 variable-sized bins (9:1 ratio). When comparing the post-shock conditions listed in Tab. 4.3, it becomes clear that the thermodynamic properties of the bin model have a noticeable effect on the predicted final equilibrium state. The simulation parameters are listed in Tab. 4.4. Given the

Table 4.3.: Normal shock wave using bin model: Macroscopic boundary conditions

	$\rho$ [ $\text{kg} \cdot \text{m}^{-3}$ ]	$T$ [K]	$u$ [ $\text{m} \cdot \text{s}^{-1}$ ]	$y_N$
pre-shock: 1	$1.110 \times 10^{-7}$	300.0	10000.0	0.014
post-shock: 2				
100 bins (E)	$1.508 \times 10^{-6}$	11494.5	736.1	1.000
10 bins (E)	$1.286 \times 10^{-6}$	13290.0	863.0	1.000
10 bins (V)	$1.512 \times 10^{-6}$	11468.3	734.3	1.000

low densities in this test case, a cell size of 0.01 m was found to be sufficiently small to resolve the mean free path everywhere in the domain. For the chosen domain size, this results in a total of 25000 cells. The ratio of real to simulated particles was set so as to maintain a minimum of 20 particles per cell in the pre-shock region. Triggering the initial formation of the shock front was achieved as follows: At  $t = 0$ , the domain was filled with particles at the pre-shock and post-shock Maxwell-Boltzmann distributions, generated respectively to the left and right of a discontinuity 40 m away from the left boundary. Following this, all three simulations were run for a total of 70000 time steps, to allow the shock front to be fully established. After the initial transient had died out, macroscopic samples were taken every 10 time steps and time-averaged for an overall interval of 40000 steps. In order to further reduce the statistical noise, these macroscopic samples were also ensemble-averaged over 64 independent simulations running simultaneously.

Table 4.4.: Normal shock wave using URVC bin model: DSMC Simulation parameters

Cell size	[m]	0.01
Time step	[s]	$5 \times 10^{-6}$
Overall domain size	[m]	250
Simulator particles		$\approx 1.1 \times 10^7$
Transient steps		70000
Sampling steps		40000/10

The cross section data used in this test case are the same as in Sec. 4.1. For all  $N_2(k)+N$ -collisions, the total cross section is determined by the procedure discussed in Sec. 3.3, and the same is true for the selection of the post-collision outcomes. Isotropic scattering is assumed when determining the post-collision velocities of the departing particles. Collisions between two nitrogen molecules, i.e.  $N_2(k)+N_2(l)$  are assumed to be elastic. This is done out of necessity, since the Ames database provides no detailed chemistry information for these processes. Similarly, N+N-encounters are also treated as elastic collisions. For lack of availability of better data, the total cross sections in both of these cases are determined using the VHS model. The relevant parameters have been taken from Stephani et al.[87], and are listed in Tab. 4.5.

Table 4.5.: VHS parameters used in elastic collisions

	$d_{\text{ref}}$ [Å]	$\omega$ [-]	$T_{\text{ref}}$ [K]
$N_2-N_2$	3.20	0.680	2880
N-N	2.60	0.700	2880

The run times for the DSMC simulations in this section are listed in Tab. 4.6. The overall times are sub-divided into the initial transient phase, during which the shock structure is established, and the subsequent time required to obtain the steady-state flow macroparameters. Each of the three cases was run on the VKI cluster, performing a total of 64 independent simulations in parallel, which were used for ensemble-averaging of the macroscopic samples.

Table 4.6.: Normal shock wave using bin model: DSMC simulation run times

	transient [h] (70000 steps)	sampling [h] (40000 steps)
100 bins (E)	204.2	159.1
10 bins (E)	114.1	82.6
10 bins (V)	135.4	99.4

Using the 100(E)-simulation for reference, one can see that reducing the number of bins by a factor of ten decreases the run-times by about 45 % for the 10(E)-case and by about 35 % for the 10(V)-case. Thus, in the present situation, the simulation run-times are not directly proportional to the total number of bins. This is in contrast to the behavior observed for the 0D-reactor in Sec. 4.1. This difference can be explained by the fact that for the present simulations, particle motion across the domain must be taken into account. Unlike the collision routines, which took up most of the run-times in Sec. 4.1, particle motion and indexing routines are insensitive to the number of bins, but make up a significant fraction of the overall run time.

Several macroscopic flow quantities for the three different simulations are now compared. Fig. 4.5 shows the mass density profiles across the whole domain, while Fig. 4.8(a) zooms in on the shock front region. All profiles have been normalized with the pre-shock equilibrium value  $\rho_1$  listed in Tab. 4.3. The three different curves are color-coded in the same way as the entries in that

table: black for the 100-bin case with equally-spaced energy intervals, red for the 10-bin case, also with equally-spaced energy intervals, and blue for the 10-bin case with variable-size energy intervals. For convenience, these will be referred to as 100(E), 10(E) and 10(V) respectively. All profiles have been displaced along the  $x$ -axis, so as to have a common origin at the location where the density is equal to  $\rho_0 = \frac{1}{2}(\rho_1 + \rho_2)$ . This measure becomes necessary, because the precise position of the shock inside the domain is never exactly the same in every simulation. Furthermore, due to random walk in the net number of particles, the shock front may begin to move across the domain over the course of many time steps. This means that averaging of instantaneous samples to obtain steady-state flow macroparameters can not be performed for an arbitrarily long time interval.

Returning to Fig. 4.5, a clear difference is noticeable between the 10(E)-case and the other two simulations. Although the distance needed to reach the post-shock equilibrium density is similar in all three cases, the 10(E)-profile approaches the much lower post-shock density predicted in Tab. 4.3. This is clearly a consequence of the very different thermodynamic properties exhibited by the equally-spaced bins used in the 10(E)-case. Notice also the distance measured along the  $x$ -axis. All plots show the evolution of the shock profiles towards equilibrium for approximately 200 meters. However, even this distance is not enough to fully reach the predicted equilibrium state. This is not immediately evident by observing the density profiles, but becomes clear by examining the  $N_2$ -temperature profiles in Fig. 4.7, which show that the translational and internal modes are not yet equilibrated at the domain boundary to the right. The reason for the large post-shock relaxation lengths predicted in all three test cases lies in the extremely low densities involved. The pre-shock conditions given in Tab. 4.3 correspond to a pressure of only 0.01 Pa. At such pressures the collision rate in the gas is low, and the corresponding characteristic times for internal energy relaxation and chemistry are large. If the simulations were repeated at a higher pressure, the shock front would be compressed into a much narrower region, with all the processes exhibited in the present case occurring across a much shorter distance.

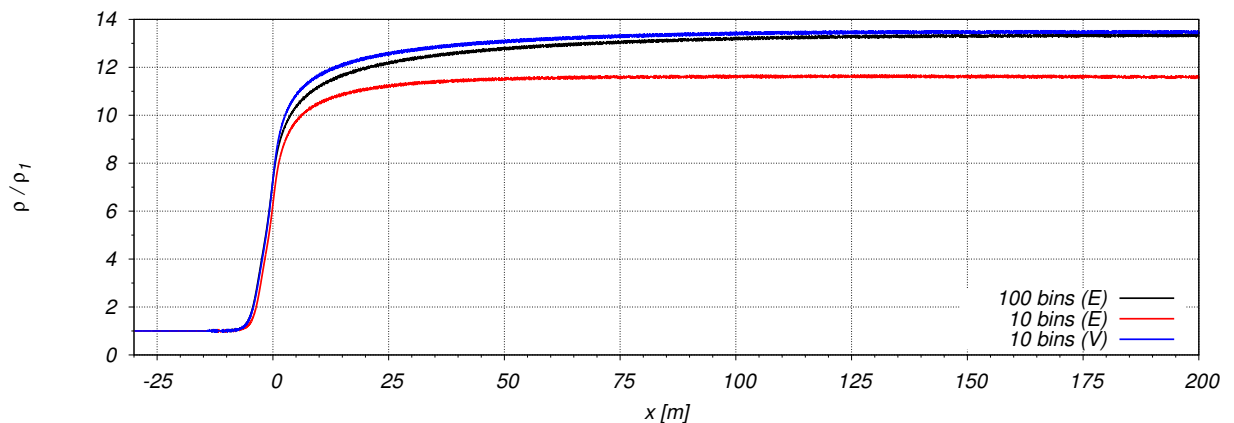


Figure 4.5.: Normal shock wave using bin model, density ratio:  $\rho/\rho_1$

The mass fraction profiles for molecular and atomic nitrogen are shown in Fig. 4.6. The initial

stages of dissociation, seen more clearly in Fig. 4.8(b), are very similar for all three cases. The generation of atomic nitrogen begins slightly after the initial density rise, at  $x \approx -4$  m. The 50% mass fraction mark is reached in all three cases at almost the same location at  $x \approx 1$  m. After this point, the differences become more apparent. The fastest dissociation is predicted by the 10(E)-case, where the mass fraction of molecular nitrogen drops below 1% about 43 meters behind the origin. The 10(V)-profiles follow it closely, up until  $x \approx 3$  m, after which dissociation proceeds more slowly than for the 10(E)-case. It takes until  $x \approx 97$  m for  $y_{N_2}$  to fall below 1%. Finally, dissociation in the 100(E) case is the slowest of all three. The mass fraction profiles for this case diverge from the other two immediately behind the 50% mark and trail behind the other two for the remainder of the flow downstream. With 100 bins the threshold for  $y_{N_2} = 0.01$  is reached at  $x \approx 134$  m, i.e. far later than for the other two cases.

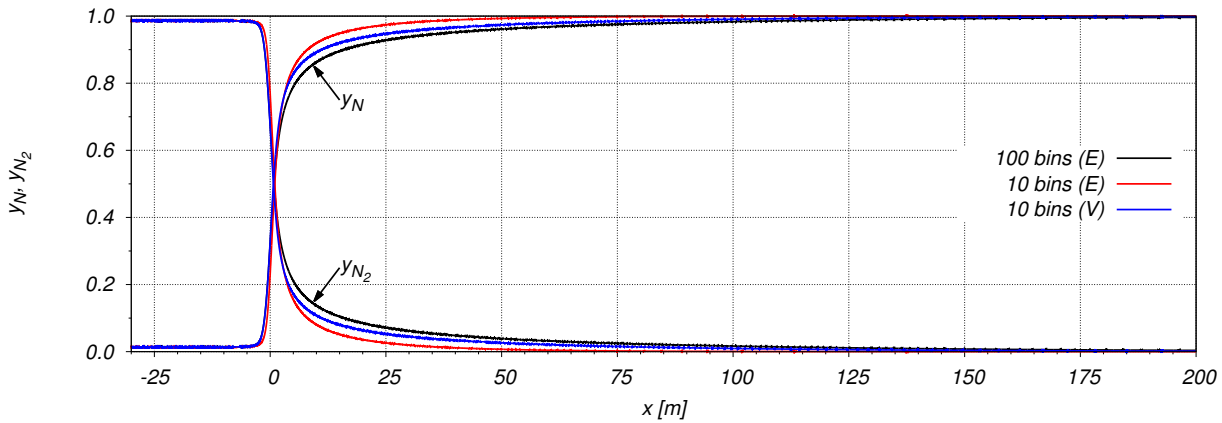


Figure 4.6.: Normal shock wave using bin model, species mass fractions

Temperature profiles for  $N_2$  are compared in Fig. 4.7, and a close-up of the shock front is shown in Fig. 4.8(c). Two separate curves are plotted for each case, with the higher value being the translational temperature of  $N_2$  and the lower value the internal temperature. All three cases exhibit a severe overshoot of the translational temperature, with maximum values of nearly 60000 K reached around the same location. For the 100(E)- and 10(V)- cases  $T_{t,max}$  is reached at  $x \approx -4$  m, while for the 10(E)-case it lies closer to  $x \approx -3$  m. Comparing with Fig. 4.8(a), this roughly corresponds to 2 m behind the location where the density first begins to deviate from its free-stream equilibrium value. After reaching its maximum, the translational temperature quickly drops below 15000 K, and then slowly approaches the post-shock equilibrium values predicted in Tab. 4.3 towards the right domain boundary.

Meanwhile, the internal temperature profiles show very different behavior, depending on which one of the three cases is considered. For the 10(V)- and 100(E)-cases, the internal temperatures lag behind their respective translational temperatures by about 5 – 6 m, and then reach their maximum values around 20000 K at  $x \approx 0.5$  m. After this point the internal temperatures decrease in both cases, with the temperature decrease in the 100(E)-case being slightly slower. By contrast, the internal temperature rise of the 10(E)-case seems to begin immediately on the left inflow

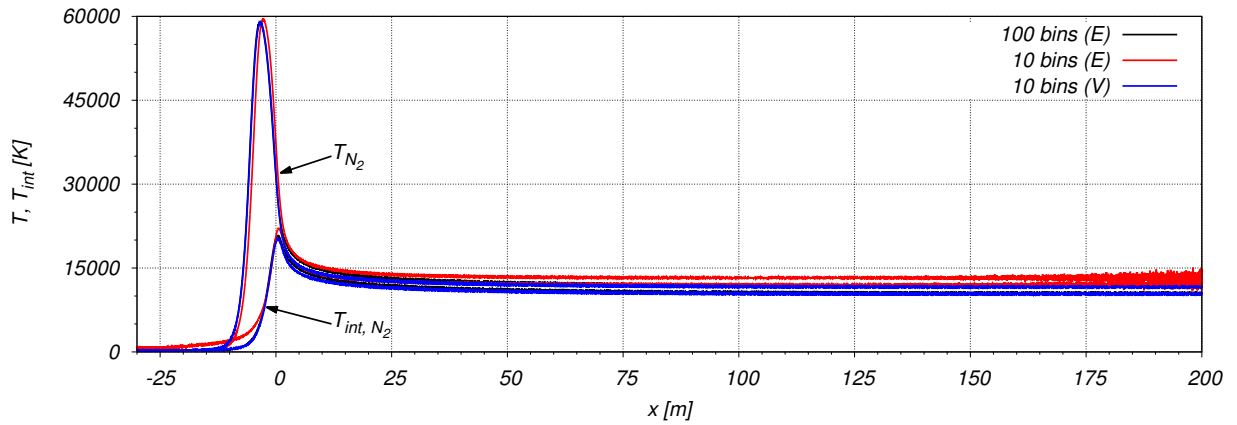
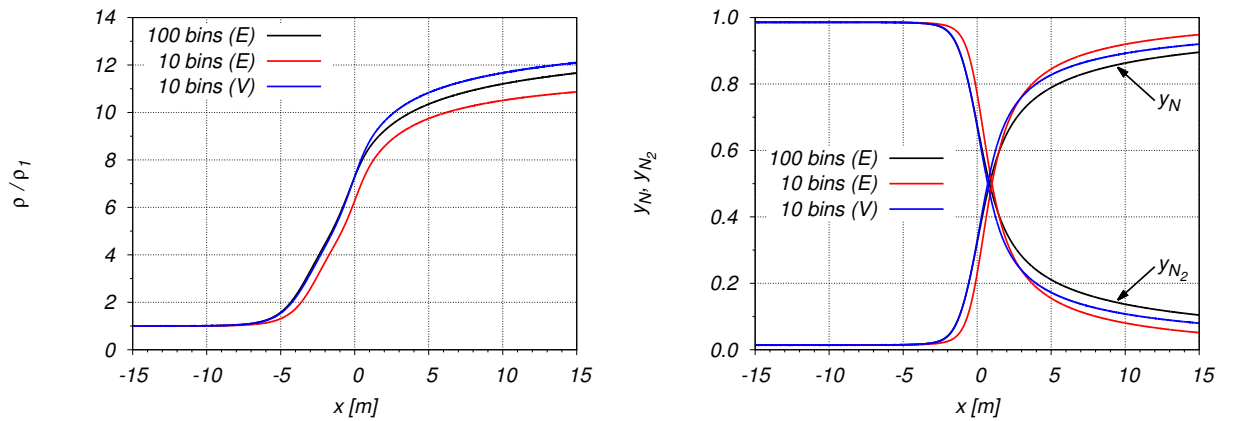
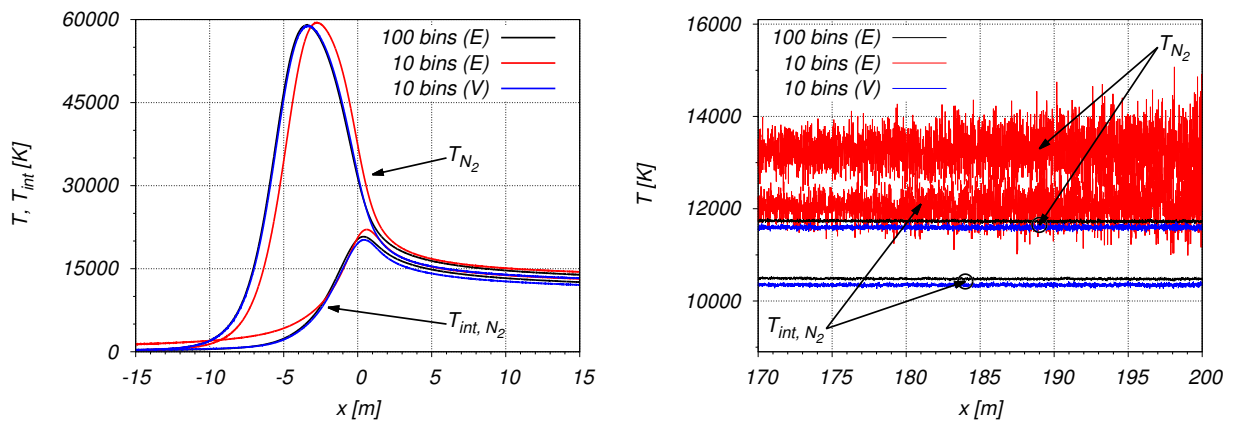


Figure 4.7.: Normal shock wave using bin model: Translational and internal temperatures of  $N_2$



(a) Close-up of density ratios  $\rho/\rho_1$  across shock front (b) Close-up of mass fractions  $y_{N_2}, y_N$  across shock front



(c) Close-up of temperature profiles of  $N_2$  across shock front (d) Close-up of temperature profiles of  $N_2$  far behind shock front

Figure 4.8.: Normal shock wave using bin model: Close-ups of macroparameters across shock front and in post-shock region

boundary, far ahead even of the corresponding translational temperature rise. At  $x \approx -15$  m, where the translational temperature has risen to 335 K, the internal temperature is already found to be four times higher. This can be observed more clearly in the close-up of the early stages of compression, shown in Fig. 4.8(c). This behavior is unexpected, because it seems to suggest that the internal energy modes of  $N_2$  are excited long before the translational mode. This contradicts the known physical fact that relaxation of translational energy by collisional processes must always be faster, or at least as fast as internal energy relaxation. The unusual behavior of the internal temperature relative to the other two cases can be explained by examining the particular choice of rovibrational bins used. For the 10(E)-case, the bin energies are plotted in Fig. 3.7, and the corresponding numerical values are listed in Tab. 3.1. As can be seen, the lowest-lying bin already contains over 280 rovibrational levels and has an average energy of 0.89 eV. The second bin contains even more than 500 levels and has an average energy of 2.17 eV. This means that with the 10(E)-bins it becomes especially difficult to accurately resolve the internal energy content of the flow at low temperatures. Recall from the discussion of Sec. 3.4 that the thermodynamic properties of the  $N_2$ -mixture are strongly dependent on the choice of bins. A wide range of binning choices were examined in that section, and the thermodynamic properties predicted for all variants were plotted in Fig. 3.10 to Fig. 3.14. Note that the labeling convention of the different binning choices in those figures is different from the one used in this test case. The corresponding cases relevant for this discussion are listed in Tab. 4.7.

Table 4.7.: Normal shock wave using bin model: Correspondence between labeling scheme of Fig. 3.10 to Fig. 3.14 and the current test cases

	bound bins	quasi-bound bins	equivalent to
100(E)	70	30	70 + 30, ( $n = 1$ )
10(E)	7	3	7 + 3, ( $n = 1$ )
10(V)	9	1	9 + 1, ( $n = 2$ )

Focusing on the internal energy of  $N_2$ , cases 100(E) and 10(E) are both plotted in Fig. 3.10(a), whereas case 10(V) is plotted in Fig. 3.11(a). In those figures, the plots on the right-hand-side are close-ups covering the lower temperature range between 200 and 5000 K. Recall that in all those images the reference properties, as predicted with the full set of rovibrational levels, are given by the solid black line. One can clearly see that with the 10(E)-bins the internal energy at 300 K is over-predicted by a significant amount (line labeled “7+3” in Fig. 3.10(a)). The deviation with respect to the full set of 9390 levels is about 1300 %. By contrast, for the 100(E)-case (labeled “70+30”) the deviation, while still substantial, is only 69 %. The approximation to the full model is even slightly better with the 10(V)-bins (labeled “9+1” in Fig. 3.11(a)). Here, the deviation of the internal energy is only 51 % at 300 K. To understand the dramatically improved low-temperature behavior of the 10(V)-case with respect to the 10(E)-case, it is necessary to examine its bin energies plotted in Fig. 3.9, or the corresponding numerical values listed in Tab. 3.2, and

compare them to the 10(E)-case. For the DSMC simulation of the 10(E)-case, the large size of the lowest-energy bins means that the overwhelming fraction of  $N_2$ -molecules fed into the domain at the upstream boundary will be assigned to the first bin. Meanwhile, the probability of generating particles populating any higher-lying bins is vanishingly small. Recall also that the internal temperature is determined as an implicit solution to Eq. (A.35). Finding the solution to this equation becomes difficult if all  $N_2$ -molecules tend to populate only a single bin. In fact, the obtained internal temperature can become physically meaningless at this limit. An additional comment concerns the depletion of the  $N_2$ -molecules due to progressive dissociation towards the outflow boundary at  $x = 200$  m. The small number of remaining molecules makes determination of both the translational and internal temperatures of  $N_2$  more difficult in this region, as can be seen in Fig. 4.8(d). Especially in the 10(E)-case, where dissociation is the fastest, by the time the flow reaches the outlet, the number of remaining  $N_2$ -molecules is so small, that significant statistical noise is introduced in the temperature signals. By contrast, Fig. 4.6 shows that the 10(V)- and 100(E)-cases predict much slower dissociation, such that many more nitrogen molecules reach the boundary to the right. This explains the lower noise levels for the translational and internal temperatures of  $N_2$  near the outlet boundary for both these cases.

The large discrepancy between the internal temperature profiles for the three cases considered here can be better explained by analyzing the Boltzmann plots in Fig. 4.9. These plots show for all three cases the bin number densities  $\bar{n}_k$  at several locations across the shock, normalized by their respective bin degeneracies  $\bar{a}_k$  and the number density of  $N_2$  as a function of the average internal energy of each bin,  $\bar{E}_k$ . Recall that when plotting these quantities on a logarithmic scale, the populations corresponding to a Boltzmann distribution fall along a straight line, with its negative slope inversely proportional to the corresponding equilibrium temperature. Such lines are drawn in all three sub-figures indicating the pre- and post-shock Boltzmann distributions at the respective pre- and post-shock equilibrium temperatures given in Tab. 4.3.

Focusing now on the 10(E)-case shown in Fig. 4.9(b), a comparison of the populations at the  $x = -10$  m mark (given by the green x's) with the line representing the Boltzmann distribution at 300 K, reveals significant discrepancies in the populations. While the lowest-energy bin population lies approximately on the 300 K-line, the higher-lying bins seem to be significantly overpopulated. This raises the actual internal temperature obtained via Eq. (A.35) to  $T_{\text{int}} \approx 1380$  K, a significant amount above the upstream equilibrium value. The cause of this overpopulation is not entirely clear. It might be due to too many  $N_2$ -particles being excited into higher-energy bins inside the shock and then diffusing towards the upstream equilibrium region. In any case, the vast range of orders of magnitude over which the bin populations vary highlights a problem encountered when extracting them from DSMC simulations. At low temperatures this task is complicated by the fact that the bin number densities are determined based on the average number of particles in each cell. If, as is the case in this situation, only a trace amount of particles is found in any of the higher-lying bins, the associated statistical errors can surpass the actual

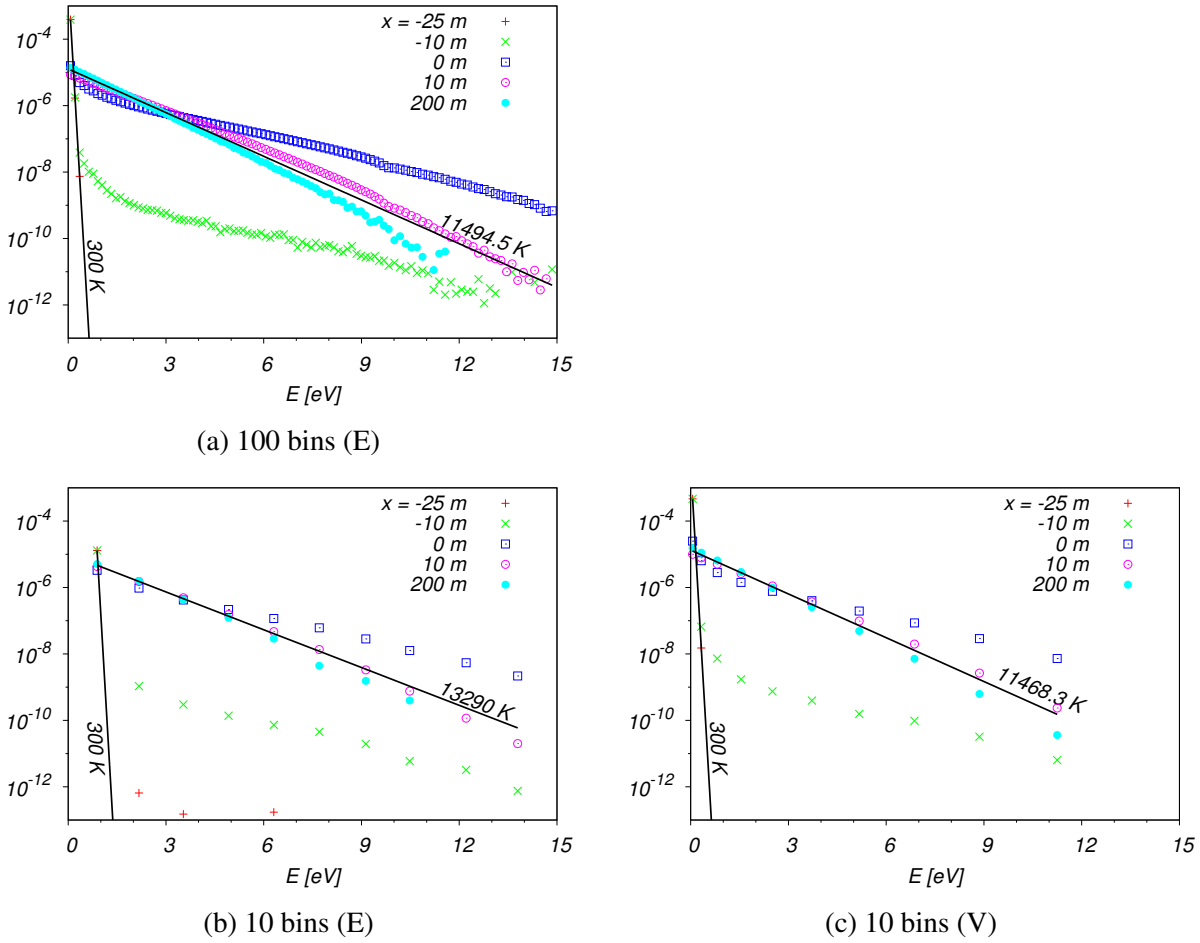


Figure 4.9.: Normalized bin populations,  $n_k / (n_{N_2} \cdot a_k)$ , for selected locations along shock front. The black lines indicate pre-and post-shock equilibrium Boltzmann distributions

values by many orders of magnitude, and strongly affect the obtained internal temperature. In the 10(V)-case, the lowest-energy bins are much smaller, and at least the first and second bin are populated to a significant degree at the pre-shock conditions. This can be seen in Fig. 4.9(c). As a consequence, the internal temperature can be determined more accurately for this case. Observe also Fig. 4.9(a), which shows the bin populations for the 100(E)-case used as the reference. Even with ten times as many bins to resolve the whole energy range, only the lowest two or three bins are actually populated at 300 K (red crosses).

Moving downstream to  $x = 0$  m, the bin populations in Fig. 4.9 are given by the blue squares. For all three cases this is the location where the highest internal temperatures were extracted. One can observe an overpopulation of the higher-energy bins with respect to what would be given by a straight-line Boltzmann distribution. Focusing on Fig. 4.9(a), a small but noticeable kink in the distribution can be observed around the 10 eV-mark. Recall from the discussion in Sec. 2.4 that 9.75 eV is the energy, which divides the truly bound levels from the higher-energy quasi-bound ones. Thus, in the present case, there seems to be somewhat different dynamic behavior for the two classes of bins. Obviously, such fine details cannot be captured in the 10-bin cases, because

there only 3, or even just a single bin are used to collect all the pre-dissociated levels.

After passing the maximum values around 20000 K near  $x \approx 1$  m, the internal temperature decreases in all three cases and slowly tends to approach the corresponding translational temperature. This relaxation process however, is so slow that in all three cases  $T_{\text{int},\text{N}_2}$  remains several hundred kelvin below  $T_{\text{N}_2}$  for the remainder of the domain. This can be observed in a close-up of the outflow region near the boundary to the right, shown in Fig. 4.8(d), and is also confirmed by the populations extracted at  $x = 200$  m (light-blue filled circles in Fig. 4.9), which deviate in all three cases from the respective post-shock Boltzmann distributions.

Notice that at  $x = 200$  m, bins 9 and 10 in the 10(E)-case are missing from the Boltzmann plot (see filled light blue circles in Fig. 4.9(b)). Somewhat similar behavior is observed in Fig. 4.9(a), where bins at energies above 11 eV seem to be severely under-populated, and do not even appear within the range of the plot. The lack of  $\text{N}_2$ -molecules in such high-lying internal energy states may be due to a combination of two factors. First, since these bins contain only quasi-bound levels,  $\text{N}_2$ -molecules populating them possess enough energy to dissociate in any collision, regardless of the relative translational energy of the collision pair. Thus, as they travel along the domain from left to right, they are much more likely to have dissociated before reaching the outlet than  $\text{N}_2$ -molecules populating lower-energy bins composed of truly bound states. Second, recall that for the 10(E)- and 100(E)-cases all pre-dissociated levels are distributed across the 3, or 30 highest-lying bins respectively, as opposed to the 10(V)-case where all pre-dissociated levels are all lumped together into a single bin. Therefore, in the equally-spaced bin cases, the already small number of  $\text{N}_2$ -particles responsible for generating the bin population “signal” becomes more easily “diluted” among this larger range of possible bins than in the variably-spaced bin case.

The gap between the translational and internal temperatures, which persists for the whole flow downstream of the shock front, suggests that the chosen domain is not nearly long enough to capture the internal energy relaxation process in its entirety. Reaching this point would require a domain size many times greater than the one used in the present simulations, which in turn would increase the necessary number of cells downstream of the shock by a significant amount. Performing such a simulation using the DSMC method alone would be extremely costly, because of the requirement of resolving the local mean free path everywhere in the domain. In the present simulations, by the time the gas has reached the outflow boundary around  $x = 200$  m, the translational modes of  $\text{N}_2$  and  $\text{N}$  have practically thermalized at the post-shock equilibrium temperature. This means that the underlying velocity distributions are nearly Maxwellian, and the main advantage of the DSMC method (that of resolving non-Maxwellian distributions) is no longer crucial to the accuracy of the simulation. Under these conditions, the remainder of the relaxation processes downstream of the shock could be simulated much more efficiently using classical CFD methods based on a hydrodynamic description of the flow.

In order to obtain an estimate of the full relaxation length, simulations using a 1D inviscid relax-

ation flow solver was performed by Munafò. This code solves a system of equations similar to the one used in Sec. 4.1, but augmented by a global momentum- and energy equation for inviscid flow. Such a system now describes the steady-state evolution in one dimension of the species populations behind an infinitely thin normal shock. Thus, instead of marching in time, the solution is advanced along the  $x$ -direction, which represents the location behind the shock concentrated at  $x = 0$ . The same free-stream conditions as in Tab. 4.3 were used to compute the initial conditions for the inviscid flow solver. In the present approach the shock is not captured. Instead, it is assumed that only the translational mode is initially affected by compression across the shock. Therefore, the classical Rankine-Hugoniot jump relations [2] with  $\gamma = 5/3$  are used, while internal energy excitation and chemistry remain frozen. This results in an initial kinetic temperature of  $T = 62540$  K, a density of  $\rho = 4.42 \times 10^{-7}$  kg/m<sup>3</sup> and a velocity of  $u = 2511.3$  m/s. The initial bin populations are again computed according to a Boltzmann distribution at  $T_{\text{int}} = 300$  K and the initial mass fraction of atomic nitrogen is  $y_{\text{N}} = 0.014$ . The simulations were performed for the same three sets of bins already used in the DSMC cases.

The results of these calculations are shown in Fig. 4.10. In the top left corner, Fig. 4.10(a) shows the density ratios  $\rho/\rho_1$  behind the shock front for all three cases. Notice that the initial behavior of the density profiles is very different from the DSMC results of Fig. 4.8(a). Since the shock is not “captured” as-such, but artificially assumed to be concentrated at  $x = 0$ , the early density profiles differ considerably from the DSMC results<sup>1</sup>. This is made obvious by the dotted horizontal line, which represents the free-stream density. Notice, however that the final downstream equilibrium densities exactly correspond to the values seen in the DSMC simulations. This is confirmed by the close-up images in Fig. 4.10(b), where the post-shock density ratios, as predicted in Tab. 4.3 are represented by the dashed horizontal lines.

The temperature profiles in Fig. 4.10(c) show a similar behavior to that obtained with the 0D-adiabatic reactor discussed in Sec. 4.1. As was the case in that situation, the best way to represent the whole length of the relaxation process, while simultaneously being able to resolve its initial stages, is to use a logarithmic scale along the abscissa. Notice, however that the final post-shock equilibrium temperatures are much higher than the ones observed in the 0D reactor. This is due to the additional flow kinetic energy, initially contained in the free stream, being mostly dissipated into thermal energy behind the shock. A close-up of the temperature profiles during the later stages of the relaxation process is shown in Fig. 4.10(d). Here, one can see clear differences in the relaxation lengths that the three sets of bins predict. The fastest relaxation towards a common temperature is predicted by the 10 equally-spaced bins at around  $x \approx 200$  m, while the 10 variably-spaced bins require a distance of roughly 300 meters. At  $x \approx 500$  m, the longest relaxation length is predicted by the 100 equally-spaced bins. This information was not easily discernible in the DSMC profiles of Fig. 4.7 and Fig. 4.8(c), due to the considerable statistical noise in the temperature signals. The present results also confirm that the domain length for the

---

<sup>1</sup>In addition to the fact that a logarithmic scale has been used on the  $x$ -axis

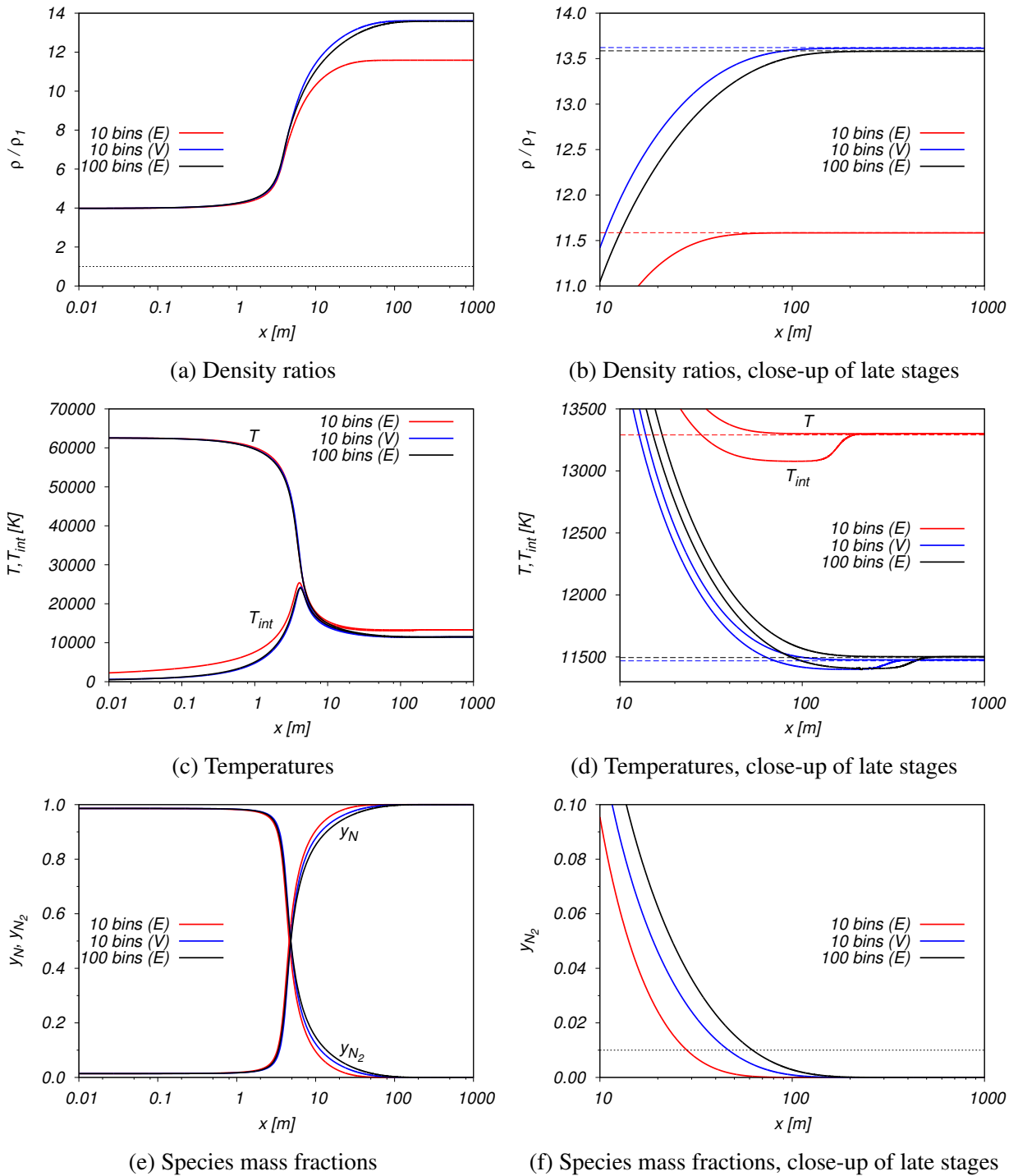


Figure 4.10.: Normal shock wave using bin model: comparison calculations using 1D-inviscid relaxation flow solver

DSMC calculations was not large enough to fully capture the entire process.

Finally, the mass fraction profiles of molecular- and atomic nitrogen are plotted in Fig. 4.10(e). Consistent with the behavior in the 0D-reactor, one can observe that dissociation of  $N_2$  is preceded by initial excitation of the internal energy modes. On the right, Fig. 4.10(f) focuses on the later stages of dissociation, in order to compare the location where  $y_N$  drops below 1 %. Roughly speaking, this occurs at 38 m for the 10(E)-case, at 46 m for the 10(V)-case and at 62 m for the 100(E)-case.

Although the order in which the three sets of bins reach this value is the same as in the DSMC simulations, the exact  $x$ -values differ considerably from those predicted by this inviscid solution (recall the discussion of Fig. 4.6, where the corresponding distances found from the DSMC profiles were 43, 97, and 134 meters respectively). This can in part be attributed to the fact that the origin of the  $x$ -axis in both simulations has been selected arbitrarily, and does not correspond to the exact same physical conditions. In addition to this, the fact that DSMC takes into account mass diffusion, as well as other viscous effects, while the 1D-inviscid relaxation code does not, may explain the significantly longer distances observed in the DSMC profiles. This tentative explanation should thus be verified by re-running these test cases with the shock-capturing 1D Navier-Stokes solver, also developed by Munafò as part of his his thesis [132].

To summarize this section, in the present test case the URVC bin model was applied to the simulation of nitrogen flow across a normal shock wave. Two different choices of rovibrational bins were compared (equally-sized vs. variably-sized), and it was found that variably-sized energy bins noticeably improve the accuracy of the bin model, especially at lower temperatures. With 10 bins, they exhibit a behavior comparable to that of the reference simulations, which used 100 bins. The conclusion of this test case is that 10 variable-sized bins should be sufficiently accurate, and simultaneously inexpensive enough to be used in the more demanding 2D and 3D test cases discussed in Ch. 5.

## 5. Application of URVC bin model to atmospheric entry flows

In this section, the behavior of the URVC bin model is investigated in a 2D- and a 3D flow configuration. While the test cases presented here are intended to more closely represent entry of a space vehicle into Earth's atmosphere, they share the limitation that only a pure nitrogen atmosphere is considered. Due to the limitations of the VKI DSMC code used to test the bin model in Ch. 4, such as lack of 2D/3D capability and limited parallel performance due to lack of domain decomposition, an external DSMC code had to be used. Thus, an additional challenge in the present work was to adapt the state-to-state cross section data previously extracted from the NASA Ames N3 database to the conventions followed by established DSMC codes. Such codes usually rely on a combination of the variable hard sphere (VHS) model of Bird [25] for computing the total collision cross section, on the classical model for internal energy exchange by Borgnakke and Larsen [36] (LB) and on the total collision energy (TCE) method of Bird [24] to model chemical reactions. The DSMC code used to simulate the test cases in the present chapter incorporates all of these conventions. It is called RGDAS and differs from the VKI code in a number of ways: RGDAS stands for Rarefied Gas Dynamics Analysis System and was developed by the group of Ivanov at the Institute for Theoretical and Applied Mechanics (ITAM) for use by the European Space Agency (ESA). It shares many features with the well-known SMILE code developed by the same group [91]. Through ongoing collaborations with ESA this software had previously been used at the von Karman Institute for Fluid Dynamics to study the aerodynamics of reentry vehicles, such as the Intermediate eXperimental Vehicle (IXV) [143].

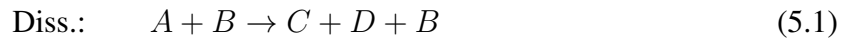
Before discussing the two test cases in Sec. 5.2 and Sec. 5.3, some of the adaptations necessary to integrate the URVC bin model into the framework of RGDAS will be explained in Sec. 5.1. It should be noted that a preliminary version of the material covered in that section and Sec. 5.2 has been presented in [144].

## 5.1. Integration of state-to-state bin model into RGDAS

In order to better understand how the bin model was integrated into RGDAS, it is necessary to review the relevant details of how the existing conventional algorithms for chemistry (based on the TCE method) and internal energy exchange (based on the Larsen-Borgnakke method) are implemented in this code. These routines will be partially re-used to set up the detailed chemistry mechanism of the bin model, as will be explained in Sec. 5.1.2.

### 5.1.1. Conventional framework for chemistry and internal energy exchange in RGDAS

The conventional TCE algorithm in RGDAS distinguishes between two main “types” of reactions to guide its internal chemistry routines. For a collision between two particles of species  $A$  and  $B$  respectively, they can be written in the general forms:



Eq. (5.1) is a dissociation reaction, where a particle of species  $A$  is split due to collision with a particle of species  $B$ , producing two particles of species  $C$  and  $D$  in the process, while the particle of species  $B$  remains intact. Focusing exclusively on the nitrogen mixture relevant in this thesis, when a conventional description is used (as opposed to the state-to-state description discussed in Sec. 5.1.2),  $A$  would only refer to  $\text{N}_2$ , while  $B$  could be either  $\text{N}$ , or  $\text{N}_2$  depending on the random pairing. Eq. (5.2) on the other hand, represents an exchange reaction, where species  $A$  exchanges (usually) an atom with species  $B$ , producing the new species  $C$  and  $D$  in the process. In the  $\text{N}_2$ ,  $\text{N}$ -mixture (in the conventional description), the only “reaction” which follows this template would be  $\text{N}_2 + \text{N} \rightarrow \text{N} + \text{N}_2$ . Since such a reaction would not modify the macroscopic state of the mixture, it is not included as part of the conventional reaction mechanism.

Assuming for a moment that during a given time step, in a given collision cell, particle selection routines have determined that a specific particle pair of species  $A + B$ , should collide, the first task of RGDAS’s chemistry routine would then be to calculate their overall reaction probability:

$$P_{A+B}^{\text{React}}(E_c) = \sum_{i \in \mathcal{I}_{A+B}^{\text{React}}} P_{i,A+B}^{\text{TCE}}(E_c), \quad (5.3)$$

where the set of  $\mathcal{I}_{A+B}^{\text{React}} = \mathcal{I}_{A+B}^{\text{Diss}} \cup \mathcal{I}_{A+B}^{\text{Exch}} = \{1, \dots, i, \dots, n_{\text{React}}\}$  over which the sum is taken, contains indices pointing to all possible dissociation and exchange reactions available to the pair  $A + B$ , and  $P_{i,A+B}^{\text{TCE}}$  is the TCE reaction probability for the “ $i$ -th” reaction from this set, evalu-

ated as per Eq. (6.10) in Bird [1]. Recall that by definition this probability is equal to the ratio  $\sigma_{i,A+B}^{\text{TCE}}/\sigma_{A+B}^T$ , where  $\sigma_{A+B}^T = \sigma_{A+B}^{\text{VHS}}$  in Bird's TCE method. All probabilities are evaluated at the total pre-collision energy  $E_c = \frac{1}{2}\mu_{AB}g^2 + \bar{\zeta}$ , where  $\bar{\zeta} = \frac{1}{2}(\zeta_A^{\text{rot}} + \zeta_A^{\text{vib}} + \zeta_B^{\text{rot}} + \zeta_B^{\text{vib}})$  represents the average contribution of the rotational and vibrational degrees of freedom of both particles.

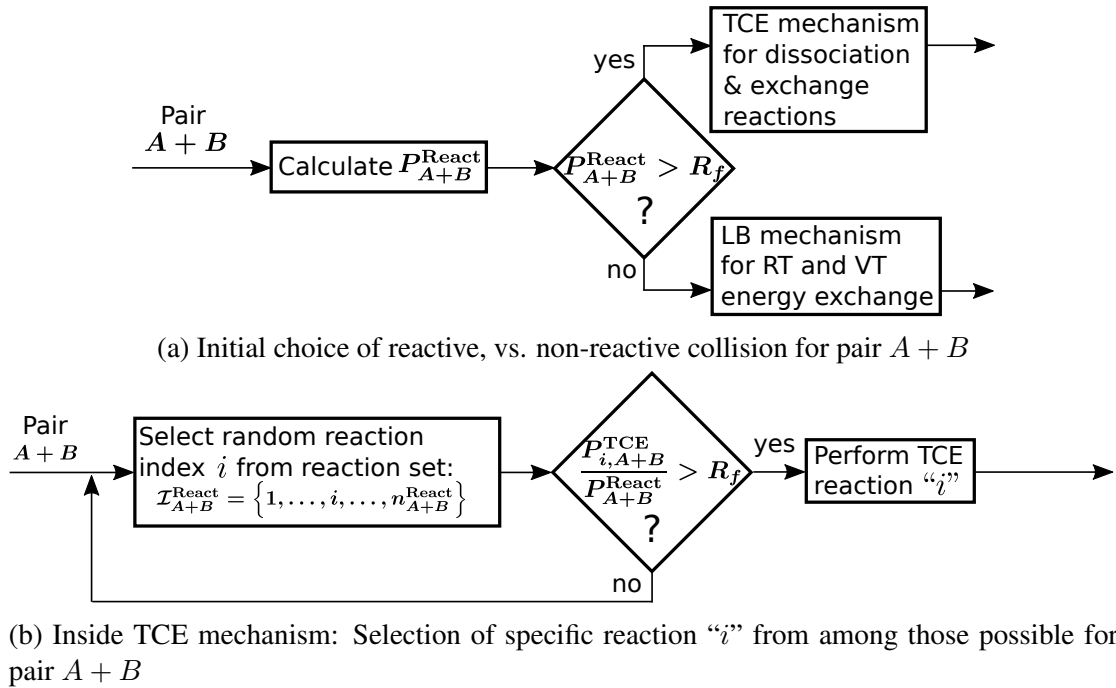


Figure 5.1.: Conventional chemistry routines in RGDAS

Once  $P_{A+B}^{\text{React}}$  has been determined, RGDAS checks it against a random fraction  $R_f$  in the interval  $[0, 1]$  to decide whether to proceed with the TCE chemistry routines, or alternatively perform a non-reactive collision. This is represented by the flow chart in Fig. 5.1(a). Depending on the given species pairs, the non-reactive branch includes the possibility of R-T, or V-T energy exchange for either  $A$ , or  $B$  via the Larsen-Borgnakke method [36]. The applicable flow chart for the LB routines is of secondary importance here, and details are available elsewhere [93]. Suffice it to say that if no internal energy exchange takes place, an elastic collision must occur. At the very end of the non-reactive path, the two particles scatter according to either VHS, or VSS logic. By contrast, if the reactive path is chosen, the next step is to determine the specific reaction to occur between  $A$  and  $B$ . As shown schematically in Fig. 5.1(b), the index “ $i$ ” chosen from among the set  $\mathcal{I}_{A+B}^{\text{React}}$  via the acceptance-rejection scheme, then points to a particular reaction, which the pair  $A + B$  will undergo. Depending on the specific case, now either the dissociation, or exchange routines are called to continue with the remainder of the algorithm. The post-reaction total collision energy  $E'_c = E_c - \Delta E_i^{\text{React}}$  is determined by taking into account the heat of reaction for reaction “ $i$ ”. Here,  $\Delta E_i^{\text{React}} > 0$  represent endothermic reactions, while  $\Delta E_i^{\text{React}} < 0$  implies chemical energy release during the reaction. Recall from the discussion in Sec. 2.5 that for the dissociation  $\text{N}_2 + \text{N} \rightarrow 3\text{N}$  the heat of reaction  $\Delta E_i^{\text{React}} = 2 E_N = 9.75 \text{ eV}$  (assuming that  $\text{N}_2$  lies in its ground rovibrational state). Before the end of the reactive branch, all particles are

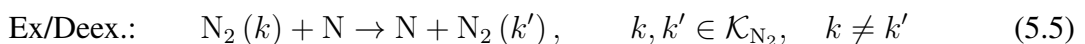
re-labeled with their new species indices, and new internal energies for all remaining molecular species are sampled using standard LB routines. Similar to the non-reactive branch, at the very end the post-reaction particles scatter according to VHS routines.

Outlining these conventional routines is necessary here, because in the following section this information will be used to explain the adaptations introduced due to the bin model.

### 5.1.2. Adaptation of URVC bin model to RGDAS chemistry framework

Since the desire is to use RGDAS without modifications to its source code, the idea is now to “co-opt” the conventional TCE chemistry routines already in place for their use with the bin model. The task is essentially to re-format the data file, which RGDAS parses to set up its TCE chemical mechanism, filling it with the bin-specific reaction rate data instead. In order to allow RGDAS to interpret these data correctly, a gas mixture with a total of  $n_s = n_{\text{bins}} + 1$  chemical species is defined. Each bin  $N_2(k)$  will thus be represented by an individual chemical species within the RGDAS framework, while N is the only other chemical component in the mixture.

The bin-specific rate data are supplied in the classical Arrhenius-type format, as was discussed in Sec. 2.7. This implies that for every reaction “ $R$ ” four separate parameters are needed: 1) The Arrhenius temperature coefficient  $A_R$ , 2) the temperature exponent  $b_R$ , 3) the reaction’s particular activation energy  $E_{a,R}$  and 4) the heat of reaction  $\Delta E_R^{\text{React}}$ . In order for RGDAS to properly interpret the individual reaction types, one must now cast every one of the bin-specific reactions in terms of the template recognized by the code’s TCE routines. For example, adapting the generic form of Eq. (5.1) to the bin-specific dissociation reactions, one now sets  $A = N_2(k)$ ,  $B = N$  for the reactants and  $C = D = B = N$  for the products. The resulting set of dissociation reactions are then of the form of Eq. (5.4), and a total of  $n_{\text{bins}}$  of these reactions have to be specified, one for each  $k$ .



For excitation/deexcitation processes, which in the state-to-state description now become proper chemical reactions, the template of Eq. (5.2) for TCE exchange reactions is adapted accordingly, with  $A = N_2(k)$ ,  $B = N$  for the reactants and  $C = N$  and  $D = N_2(k')$  for the products. Note that while the resulting form of Eq. (5.2) makes it appear as though an atom is always exchanged

between the two initial particles, this is not necessarily the case <sup>1</sup>. The reason for writing the chemical equation in this way is only to comply with RGDAS’s expectations.

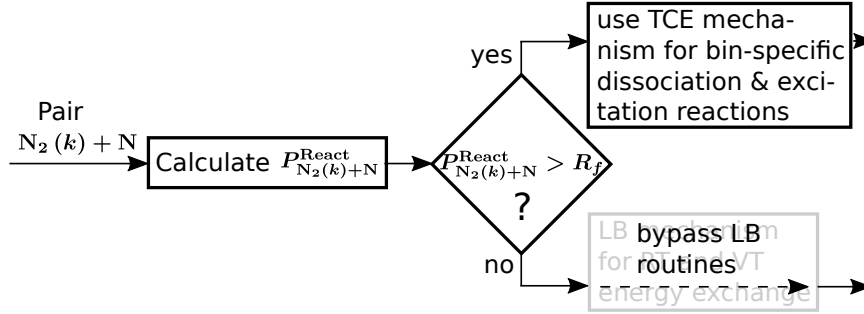
Since the TCE mechanism does not automatically “know” about the detailed balance relations linking the rate for  $\text{N}_2(k) + \text{N} \rightarrow \text{N}_2(k') + \text{N}$  with the reverse reaction rate, it is up to the user to supply the corresponding excitation and deexcitation rate data in such a way as to fulfill this requirement. Recall from the beginning of Sec. 2.7 that this can be accomplished by computing the Arrhenius parameters  $A_{k' \rightarrow k}^E$  and  $b_{k' \rightarrow k}^E$  for the deexcitation reaction according to Eq. (2.24), and recognizing that the activation energy is  $E_{a,k' \rightarrow k}^E = 0$  in these cases. The set of indices in Eq. (5.5) implies that now for each bin  $\text{N}_2(k)$ , a total of  $n_{\text{bins}} - 1$  deexcitation/excitation reactions have to be specified, linking it to all post-collision bins  $\text{N}_2(k')$ , for which  $k' \neq k$ . Therefore, a total of  $n_{\text{bins}} \times (n_{\text{bins}} - 1)$  distinct sets of Arrhenius parameters have to be entered into the RGDAS chemistry data file, each one corresponding to a specific transition  $k \rightarrow k'$ . However, note that the “elastic” cases  $k = k'$  have been excluded here. The reason for this becomes clearer, once one re-considers RGDAS’s chemistry routines in the context of the bin model. Adapting the chart of Fig. 5.1(a) for  $A = \text{N}_2(k)$  and  $B = \text{N}$ , one arrives at Fig. 5.2(a). Notice here that in the non-reactive branch all routines related to the Larsen-Borgnakke scheme are being bypassed. Thus, all RGDAS-internal variables related to the Larsen-Borgnakke model are set to zero, or otherwise de-activated. This means that,  $\bar{\zeta} = 0$  and  $E_c = \frac{1}{2}\mu_{\text{N}_2,\text{N}}g^2$  in all  $\text{N}_2(k) + \text{N}$ -collisions. Essentially, RGDAS “thinks” that it is dealing with a mixture of  $n_{\text{bins}} + 1$  different monoatomic species, which may undergo certain TCE-type chemical reactions, but none of which possess rotational, nor vibrational degrees of freedom. Of course, the internal energy content of  $\text{N}_2$  is implicitly given by the collective concentrations of all bins  $\text{N}_2(k)$  in the mixture. When the non-reactive branch in Fig. 5.2(a) is now chosen, it can only result in “elastic” collisions, i.e. those where  $k = k'$ . Although this implies that the “elastic” rate data is not specified as part of the TCE mechanism, this information will become relevant in another manner, which is discussed in Sec. 5.1.3.

Considering now the overall reaction probability  $P_{\text{N}_2(k)+\text{N}}^{\text{React}}$  in Fig. 5.2(a), it is computed as the sum over all individual reaction probabilities relevant for the pair  $\text{N}_2(k) + \text{N}$ . The set of reaction indices  $\mathcal{I}_{\text{N}_2(k)+\text{N}}^{\text{React}}$  in Fig. 5.2(b) thus now comprises all  $n_{\text{bins}} - 1$  transitions to other post-collision bins, plus the single dissociation reaction from bin  $k$ . After one particular reaction “ $i$ ” out of this set has been chosen by the acceptance-rejection scheme, the TCE chemistry routines update the particles’ species labels accordingly and determine the post-collision total energy. The heat of reaction to be deducted now depends on the specific pre- and post-collision bins of the particles

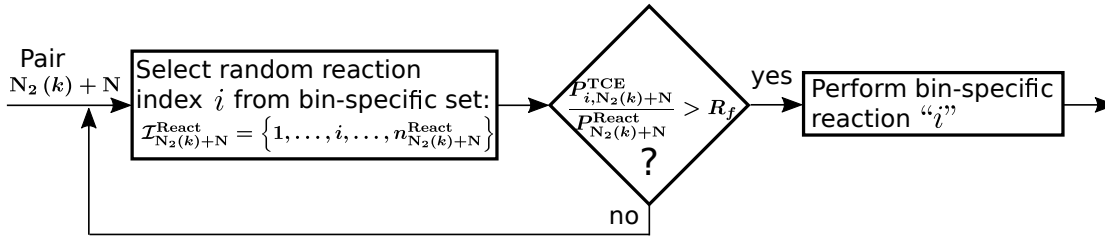
<sup>1</sup>Although such “exchange” reactions are observed in the original QCT-calculations, and significantly contribute to the overall transition rates, the reactions here are only specified in this particular form to satisfy RGDAS’s internal exchange reaction template and handle the chemistry appropriately. From the macroscopic point of view, there would be no difference if the order of the product species in Eq. (5.5) were inverted.

## 5. Application of URVC bin model to atmospheric entry flows

involved, i.e. for excitation/deexcitation  $\Delta E_i^{\text{React}} = \bar{E}_{k'} - \bar{E}_k$ <sup>2</sup> and for dissociation from bin  $k$ ,  $\Delta E_i^{\text{React}} = 2\bar{E}_k - \bar{E}_k$ . Recall that, since the data relevant to the Larsen-Borgnakke model have been de-activated, the corresponding routines are being by-passed in this step as well.



(a) Initial choice of reactive, vs. non-reactive (i.e. elastic) collision for pair  $N_2(k) + N$



(b) Inside TCE mechanism: Selection of bin-specific reaction “ $i$ ” from among those possible for species pair  $N_2(k) + N$

Figure 5.2.: Conventional chemistry routines in RGDAS

### 5.1.3. Shortcomings of the current RGDAS integration

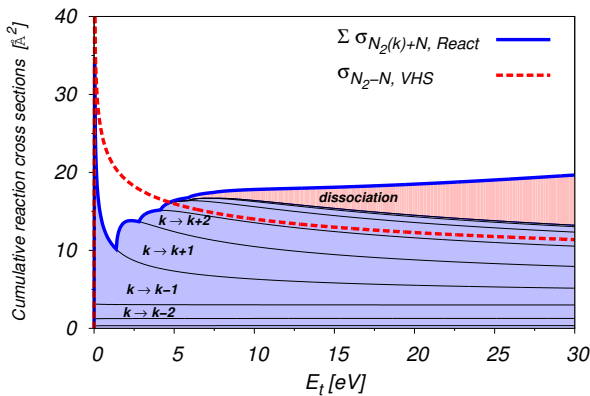
In the previous section some of the necessary adaptations for integrating the detailed chemistry mechanism into RGDAS were discussed. As was seen, the most important of these changes can be performed by simply modifying the chemistry input file and re-using the existing routines supplied by RGDAS’ framework. However, it must be mentioned that this approach also brings several difficulties along with it. In order to illustrate these shortcomings, recall first the 10-bin system used as an example in Sec. 3.2 and Sec. 3.3. For this system a set of Arrhenius parameters for a total of 10 bin-specific dissociation reactions, plus 90 excitation/deexcitation reactions (9 possible inelastic transitions for each of the 10 possible pre-collision bins, excluding elastic collisions) would have to be specified<sup>3</sup>. Recall also Fig. 3.4(a), which showed the cumulative cross sections for the particular collision pairing  $N_2(k=5)+N$ . While in the algorithm implemented in

<sup>2</sup>In Sec. 2.7 it was implied that for all endothermic reactions the heat of reaction  $\Delta E_R^{\text{React}}$  and the activation energy  $E_{a,R}$  are the same. However, for exothermic reactions this is not the case. For those types of reactions,  $E_{a,R} = 0$ , while  $\Delta E_R^{\text{React}} < 0$ . This is why both quantities have to be supplied separately to the RGDAS chemistry data file.

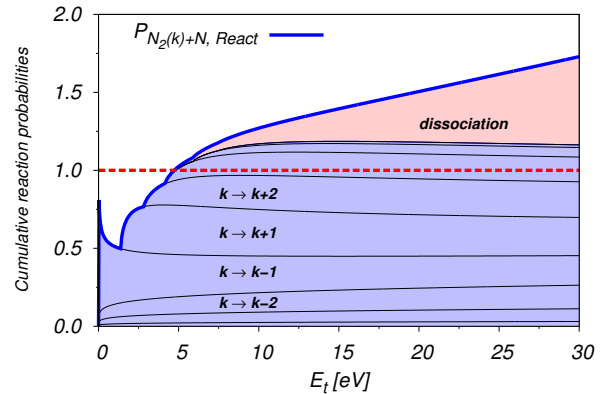
<sup>3</sup>Since RGDAS’s chemistry routines are not automatically “aware” of the detailed balance relations linking excitation/deexcitation reactions between bins  $k$  and  $k'$ , the complete consistent set of Arrhenius parameters, as described in Sec. 2.7, has to be supplied by the user.

the VKI DSMC code these cross section are used as-is, the exact same cannot be done in RGDAS. The reason lies in the particular branching-out into reactive and non-reactive paths (as indicated in Fig. 5.2(a)) initially performed by RGDAS. Here, all reactions resulting in transitions to post-collision bins  $k' \neq k$ , or dissociation are handled by the “reactive” branch of the algorithm, while those collisions which result in no change to the internal state of  $N_2$  follow the non-reactive path by default.

Re-plotting Fig. 3.4(a), but leaving out the “elastic” cross section leads to the picture in Fig. 5.3(a). Here, the sum of all inelastic and reactive cross sections is indicated by the blue line, which has been labeled as  $\sum \sigma_{N_2(k)+N}^{\text{React}}$ . In addition to this, the red dashed line represents the VHS cross section for  $N_2 + N$ , which RGDAS would normally use in conjunction with the conventional models to determine the collision frequency of this particular species pairing, regardless of the specific bin  $k$ . As can be clearly seen, this cross section is noticeably smaller than the cumulative reactive cross sections at all collision energies above  $E_t \approx 4 \text{ eV}$ . Since the reaction probabilities for all processes are computed internally as the ratio  $\sigma_{i,N_2(k)+N}^{\text{TCE}} / \sigma_{N_2+N}^{\text{VHS}}$  (recall Eq. (6.10) of Bird [1]), the resulting overall reaction probabilities become significantly greater than 1 above this collision energy. This can be seen in Fig. 5.3(b), where the blue line now represents the overall reaction probability  $P_{N_2(k)+N}^{\text{React}}$  used in selecting either the reactive, or non-reactive branches in Fig. 5.2(a). Obviously, if this probability is greater than one for most collision energies, the algorithm will always select the reactive branch, and no “elastic” collisions are ever performed for energies above  $E_t \approx 4 \text{ eV}$ .



(a) Original cumulative cross sections for inelastic+reactive processes for  $N_2 (k = 5)+N$

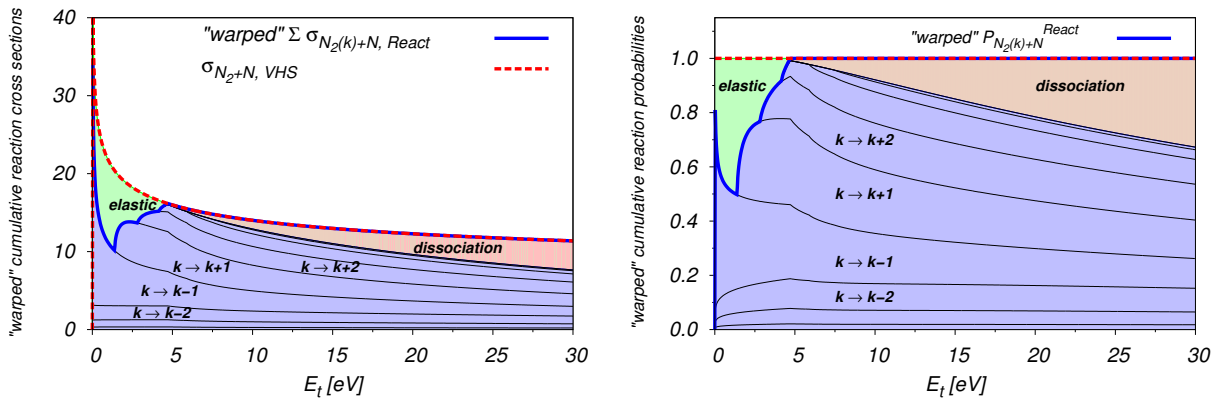


(b) Original cumulative TCE probabilities, i.e.  $\sigma_{i,N_2(5)+N}^{\text{TCE}} / \sigma_{N_2+N}^{\text{VHS}}$  for inelastic+reactive processes computed internally by RGDAS

Figure 5.3.: “Overflow” of bin-specific inelastic and reactive cross sections/probabilities with conventional VHS cross section for  $N_2+N$

Recall from Fig. 5.2(b) now that in the subsequent step, RGDAS normalizes all individual reaction probabilities with  $P_{N_2(k)+N}^{\text{React}}$ . Although this normalization “fixes” the problem of having the cumulative reaction probabilities becoming greater than one, it also distorts the relative sizes of

the individual probabilities above  $E_t \approx 4$  eV. This “warping” can be observed in Fig. 5.4(b). Notice the kink in the individual black curves occurring at  $E_t \approx 4$  eV. Multiplying each one of these cumulative probabilities by the VHS cross section for the  $N_2+N$ -pair now reveals the effective cumulative cross sections actually “seen” by the collision pair. The resulting shapes are shown in Fig. 5.4(a). Compare this to Fig. 5.5(a), which is essentially the same as Fig. 5.3(a), but with the original “elastic” cross section added back on top. It is noticeable how most the elastic cross section has simply been truncated by adhering to the much smaller VHS cross section for  $N_2 + N$ . As a consequence, if one were to use these “warped” cross sections in an actual simulation, the rates of internal energy exchange and dissociation occurring in the gas would be over-represented with respect to the elastic ones, which in turn would lead to significantly higher relaxation and dissociation rates than those predicted had the original cross sections of Fig. 3.4(a) been used. Incidentally, ignoring such a significant number of elastic collisions would also under-estimate the thermalization (i.e. approach to the local Maxwellian VDF) rates inside each bin.



(a) “warped” cumulative cross sections for all pro-  
cesses due to normalization in RGDAS

(b) “warped” cumulative probabilities for all pro-  
cesses due to normalization in RGDAS

Figure 5.4.: “Warping” of cross section due to RGDAS algorithm for collision pairing  $N_2 (k = 5)+N$  out of 10-bin system

The question of how best to remedy this problem now arises. If one wants to reproduce -at least in an approximate manner- the full elastic collision rate predicted by the bin model, one should increase the total cross section used by RGDAS to approximately follow the thick black curve shown on top of all the cumulative cross sections in Fig. 5.5(a). This would increase the overall acceptance rate of individual  $N_2 (k)+N$ -collisions, and a greater number of such collisions would be selected to follow the non-reactive branch (recall Fig. 5.2(a)). However, one must remember that RGDAS, and in fact most established DSMC codes, automatically expect the total cross section to be computed in terms of the VHS functional form:

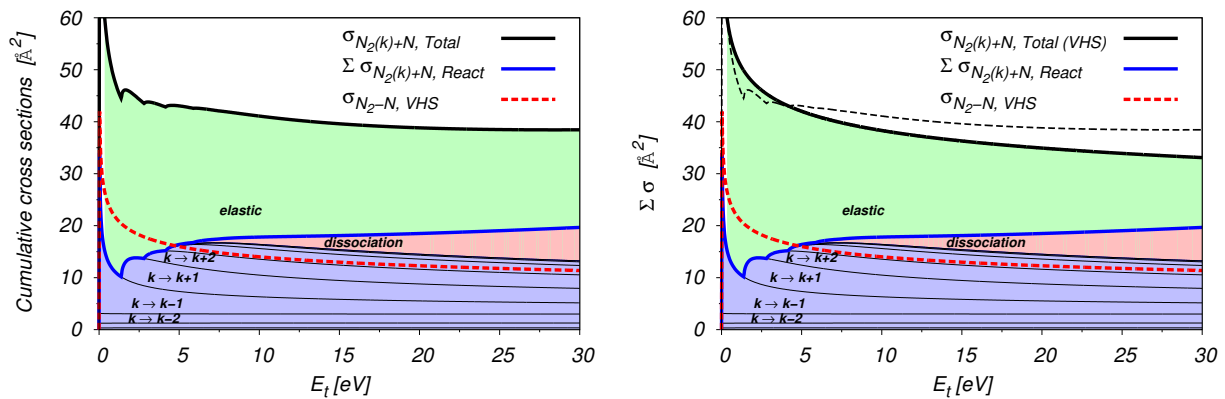
$$\sigma_{AB}^{\text{VHS}} = \frac{\pi d_{\text{ref},AB}^2}{\Gamma(5/2 - \omega_{AB})} \left( \frac{k_B T_{\text{ref}}}{E} \right)^{\omega_{AB} - 1/2} \quad (5.6)$$

With this constraint in mind, the proposed “fix” is now to re-fit the total cross sections for all  $N_2(k)+N$ -pairings and re-express in terms of a collection of  $n_{\text{bins}}$  distinct VHS parameters. More concretely, this means determining the VHS parameters  $d_{\text{ref},AB}$ , and  $\omega_{AB}$  for each of the combinations  $A = N_2(k)$  and  $B = N$ .

In order to find these values, the proposed method is very similar to the manner in which the bin-specific Arrhenius parameters were first determined in Sec. 2.7 and subsequently used to generate the cross sections in analytical form, as was described in Sec. 3.1. In the first step, one thermally averages the total cross sections for each bin by means of Eq. (2.6), ending up with temperature-dependent functions of the type:

$$\langle \sigma_{N_2(k)-N}^T \cdot g \rangle (T) = \frac{1}{\sqrt{\pi} \mu_{N_2-N}} \left( \frac{2}{k_B T} \right)^{3/2} \int_0^{\infty} \sigma_{N_2(k)-N}^T \exp\left(-\frac{E}{k_B T}\right) E dE \quad (5.7)$$

As was done for the rate coefficients in the original Ames database, the integration over the relative translational energy  $E_t$  in Eq. (5.7) is performed numerically at selected equilibrium temperatures  $T$ , within a range of interest (in this case between 500 and 50000 kelvin). At the end, the tabulated temperature-dependent values of  $\langle \sigma_{N_2(k)-N}^T \cdot g \rangle (T)$  are fitted to the VHS functional form of Eq. (5.6) to produce a set of values for  $d_{\text{ref},N_2(k)+N}$ , and  $\omega_{N_2(k)+N}$ . These bin-specific VHS parameters can then be supplied to RGDAS as part of its chemistry data file. Returning to the case of bin  $k = 5$ , used as an example here, the resulting total cross section conforming to the VHS model is shown in Fig. 5.5(b).



(a) Original cumulative and total cross sections for bin  $N_2(k = 5) + N$  (b) Total cross section for bin  $N_2(k = 5) + N$  fitted to VHS shape

Figure 5.5.: Original and VHS-adjusted total cross section for bin  $N_2(k = 5) + N$

Notice the new solid black line, labeled as  $\sigma_{N_2(k)+N}^{\text{Total,(VHS)}}$ . It follows the shape dictated by Eq. (5.6) when the specific VHS reference quantities for the pairing  $N_2(k = 5)+N$  are used. In addition to this, the original total cross section has been repeated as the black dashed line for comparison. As can be seen, although the agreement is not perfect, the VHS-fitted curve does a decent job of

following the original curve. Most important though, it remains well above the solid blue curve, which represents the contribution of the inelastic and reactive processes to the total cross section. Thus, with  $\sigma_{N_2(k)+N}^{\text{Total,VHS}}$  now being used, the problem of obtaining reaction probabilities greater than one disappears (at least in the collision energy range of interest).

Notice furthermore in Fig. 5.5(b) that the bin-specific total cross section is about 2-3 times greater than the typical VHS cross section for  $N_2+N$ -collisions, which has again been represented by the red dashed line. Similar behavior was found for all other bins in this data-set. Although such large discrepancies might seem suspicious at first, they are consistent with data reported by Kim and Boyd [77], who also studied the Ames N3 database for use with DSMC. The main difference between their approach and the one presented in this thesis is that they performed no reduction of the detailed chemistry mechanism, and thus their state-specific total cross sections are dependent on the pre-collision rovibrational level of the colliding nitrogen molecule.

The increased size of these bin-specific total cross sections will have a noticeable effect on the behavior of the  $N_2,N$ -mixture as a whole. Recall that RGDAS uses the Majorant collision frequency scheme [145] to determine the collision rate within each DSMC cell. Although this scheme differs somewhat from Bird's NTC method, the number of collisions for the species combination  $A + B$  to be processed each time step is determined in an analogous manner. Essentially this number is proportional to  $[\sigma_{A+B}^T \cdot g]_{\text{max}}$ , a quantity which is recorded and updated during a simulation within each DSMC cell. Therefore, the relatively large total cross sections for the  $N_2(k)+N$ -pairs will cause their collision rate to be significantly greater than had the original  $N_2+N$  VHS cross section been used. In addition to this, increasing the total cross sections, and with them the reference diameters  $d_{\text{ref},N_2(k)+N}$ , has a knock-on effect on the reference diameters used to compute  $N_2(k)+N_2(k)$  cross sections, since within the RGDAS framework both are connected via the expression:

$$d_{\text{ref},N_2(k)+N} = \frac{d_{\text{ref},N_2(k)+N(k)} + d_{\text{ref},N+N}}{2}, \quad k \in \mathcal{K}_{N_2}. \quad (5.8)$$

If  $d_{\text{ref},N+N}$  is kept constant, Eq. (5.8) implies that  $d_{\text{ref},N_2(k)+N_2(k)}$ , and with it the  $N_2(k)+N_2(k)$ -collision rate must also increase accordingly. Even though no detailed chemistry data is currently available for these  $N_2(k)+N_2(k)$ -collisions, and by default they are treated chemically inert in the current model, their larger total cross sections will significantly raise the elastic collision rate within the gas. With all things equal, this change will cause the gas to behave more "continuum-like" than with the previous, much smaller VHS cross sections.

## 5.2. 2D case: Cylinder of infinite length in hypersonic cross flow

The first test case to be simulated with RGDAS is a high-speed flow of nitrogen impinging on a cylinder of infinite length perpendicular to its central axis. This geometry was chosen for its relative simplicity, while still being representative of the blunt-body shapes typical of space craft entering Earth's atmosphere. Since the flow field is periodic along the direction parallel to the cylinder's axis, this idealized case can be simulated more efficiently using the 2D-version of RGDAS. The set up for this problem is sketched in Fig. 5.6.

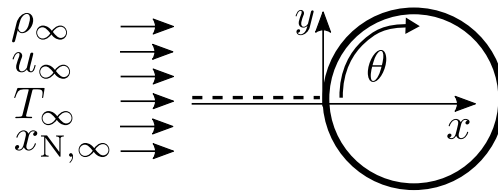


Figure 5.6.: Cylinder in hypersonic cross flow: Set up

The cross section of the cylinder is represented by the circle, where the undisturbed free stream entering from the left is oriented parallel to the  $x$ -axis. The central point of this circle is located at the coordinates  $x = 0.1524 \text{ m}$ ,  $y = 0.0 \text{ m}$ . Given the cylinder's position, the flow field will be symmetric on both sides of the  $x$ -axis, and the stagnation point stream line is indicated with a dashed line. Considering the cylinder's diameter of  $D = 0.3048 \text{ m}$ , the forward stagnation point will be located precisely at  $x = 0 \text{ m}$ ,  $y = 0 \text{ m}$ . The inflow conditions used in the simulations are listed in Tab. 5.1(a). Two conditions, which differ only in the imposed free stream density, were examined. The global Knudsen numbers used to refer to these two distinct conditions were computed based on the approximate mean free path of the free stream and the cylinder diameter as the characteristic length scale.

Additional simulation parameters are listed in Tab. 5.1(b), where the four columns represent four separate simulations. The first two involve the state-to-state bin model, with a total of 10 bins (9 bound:1 pre-dissociated) used. These two simulations differ only by the amount of atomic nitrogen (1% vs. 5%) artificially added to the free stream. Recall that this small amount of N is necessary to trigger possible inelastic collision processes in the gas, since the bin model at present only contains inelastic cross sections for  $\text{N}_2\text{-N}$  collisions. The fact that only the dissociation reaction  $\text{N}_2(k) + \text{N} \rightarrow 3\text{N}$  is modeled, is emphasized by the label **N3**. The two different free stream concentrations were used to assess the sensitivity of the flow to this arbitrary amount of atomic nitrogen. Furthermore, in order to compare the bin model to the conventional state-of-the-art in DSMC, two reference calculations (the two rightmost columns in Tab. 5.1(b)) were performed using the discrete Larsen-Borgnakke [36, 38, 106] model for internal energy exchange and the TCE model [24] for dissociation of molecular nitrogen. These two simulations differ

Table 5.1.: Cylinder in hypersonic cross flow: Free stream conditions and wall boundary conditions

(a) Free stream conditions					
$\text{Kn}_D$		$\approx 0.04$	$\approx 0.004$		
$V_\infty$	[km · s <sup>-1</sup> ]	10	10		
$T_\infty$	[K]	200	200		
$\rho_\infty$	[kg · m <sup>-3</sup> ]	$5.6 \times 10^{-6}$	$5.6 \times 10^{-5}$		

(b) Additional boundary conditions					
		10 bins		LB + TCE	
		N3, 1%	N3, 5%	N3, 1%	full
$x_{N,\infty}$		0.01	0.05	0.01	0
$x_{N_2(1),\infty}$		0.99	0.95	-	-
$T_{rot,\infty}$	[K]	-	-	200	200
$T_{vib,\infty}$	[K]	-	-	200	200
$\alpha_{\text{int}}$		0	0	-	-
$\alpha_{\text{rot}}$		-	-	1	1
$\alpha_{\text{vib}}$		-	-	1	1
$T_{\text{wall}}$	[K]	1000	1000	1000	1000

among each other in the fact that the first one only takes into account the dissociation reaction  $\text{N}_2 + \text{N} \rightarrow 3\text{N}$  to be consistent with the limitations of the bin model. This is indicated by the label **N3** of the third column from the left. In the second simulation with the conventional model, labeled as **full**, the dissociation reaction  $\text{N}_2 + \text{N}_2 \rightarrow 2\text{N} + \text{N}_2$  is enabled as well, and no atomic nitrogen has to be added to the free stream.

For the bin model simulations, some of the VHS parameters had to be extracted from fits of the bin-specific total cross sections according to the procedure discussed in Sec. 5.1.3. Since in RGDAS's framework all VHS reference diameters have to be specified for each mixture component, in the present case a total of 11 such values have to be provided. They are listed in the first column of Tab. 5.2(a). Based on these values the actual reference diameter for any arbitrary particle pair then corresponds to the arithmetic mean of the two participating species. The VHS temperature exponents (i.e. the  $\omega$ -values) on the other hand, have to be supplied separately for each species pairing, resulting in the values listed in the rightmost column of Tab. 5.2(a). Notice that specific values are given for each  $\text{N}_2(k)+\text{N}$ -pairing, since these could be extracted from the aforementioned fits of the bin-specific total cross sections to the VHS shape. For  $\text{N}_2(k)+\text{N}_2(l)$ -collisions on the other hand no such specific data was available, and the same  $\omega$ -value as in the conventional models was used for all such pairings. Recall also that all such collisions are modeled as purely elastic, given the lack of detailed chemistry data for the N4-system. A common reference temperature of  $T_{\text{ref}} = 2880$  K was used with all species combinations.

For the conventional model simulations the VHS parameters listed in Tab. 5.2(b) were used.

Again, the reference diameters are given separately for each species component, with the collision pair's reference diameter computed as the arithmetic mean of the two colliding species, and again the same reference temperature of  $T_{\text{ref}} = 2880$  K was used with all species. For the conventional models the Arrhenius parameters to compute the rate coefficients for dissociation of nitrogen are listed in Tab. 5.2(c). They were taken from two different sources. The parameters for the  $\text{N}_2 + \text{N}$ -dissociation rate were determined by fitting the NASA N3 thermal dissociation rate coefficient to an Arrhenius form (recall the first row in Tab. 2.4), while the parameters for  $\text{N}_2 + \text{N}_2$ -dissociation were taken from Park's data [121]. Concerning internal energy exchange, RGDAS uses temperature-dependent rates of thermal relaxation. The characteristic number of rotation-translation (RT) energy exchange,  $Z_{\text{RT}}$  is computed according to Parker's [146] model, with the constants  $Z_{\text{r},\infty} = 18.1$  and  $T^* = 91.5$  K for nitrogen. The rotational energy is discretized in a manner similar to the rigid rotor (RR) approximation used in [58], with a characteristic temperature of rotation of  $\theta_R = 2.88$  K for nitrogen. However, the distorting effect of vibration on the rotational energy levels is included via an additional weighting factor:

$$E_J = k_B \theta_R J(J+1) \left( 1 - 4\eta_R \left( \frac{\theta_R}{\theta_V} \right)^2 J(J+1) \right) \quad (5.9)$$

where  $\eta_R = 1$  has been set used. For vibration-translation (VT) energy exchange, Millikan and White's [147] correlations, in addition to Park's high-temperature correction [148] are used to determine  $Z_{\text{VT}}$ . The vibrational energy is discretized according to the anharmonic (AHO) oscillator approximation, with a characteristic temperature of vibration of  $\theta_V = 3371$  K and an anharmonicity parameter of  $\eta_V = 0.82$  for nitrogen.

At a temperature of 200 K the free stream is relatively cold. At such low temperatures only the lowest-lying rovibrational levels of  $\text{N}_2$  are populated to any significant degree. Therefore, in the 10-bin system, all the incoming molecular nitrogen molecules occupy the first bin. In the conventional models, the rotational and vibrational levels of entering nitrogen molecules are populated according to Boltzmann distributions at  $T_{\text{rot}} = 200$  K and  $T_{\text{vib}} = 200$  K respectively. In the simulations where the bin model is used, the internal modes are not accommodated to the wall temperature, i.e.  $\alpha_{\text{int}} = 0$ . This is the case, because RGDAS never modifies the species labels of molecules (which are used here to identify the bin they belong to) when they are reflected from the body's surface. In continuum CFD, the closest equivalent treatment would be to impose an isothermal boundary condition for the temperature using  $T = T_w$ , while imposing zero normal gradients for the bin number density profiles at the surface. This essentially "freezes" the bin populations near the surface, regardless of the wall temperature. By contrast, in the conventional model, both translational and internal (i.e. rotational and vibrational) energy are fully accommodated at the wall, which is indicated by  $\alpha_{\text{rot}} = 1$  and  $\alpha_{\text{vib}} = 1$ . This would correspond to a fully isothermal wall in the hydrodynamic description. These differences in the imposed boundary conditions will become an issue later in this section, when the surface heat transfer rates are

Table 5.2.: VHS and Arrhenius parameters used in RGDAS simulations

(a) VHS parameters used with bin model in RGDAS

species	$d_{\text{ref}}$ [Å]	pair	$\omega$ [-]
N <sub>2</sub> (1)	6.27	N <sub>2</sub> (1) + N	0.558
N <sub>2</sub> (2)	6.54	N <sub>2</sub> (2) + N	0.584
N <sub>2</sub> (3)	6.71	N <sub>2</sub> (3) + N	0.597
N <sub>2</sub> (4)	6.86	N <sub>2</sub> (4) + N	0.606
N <sub>2</sub> (5)	7.02	N <sub>2</sub> (5) + N	0.618
N <sub>2</sub> (6)	7.15	N <sub>2</sub> (6) + N	0.623
N <sub>2</sub> (7)	7.24	N <sub>2</sub> (7) + N	0.623
N <sub>2</sub> (8)	7.48	N <sub>2</sub> (8) + N	0.637
N <sub>2</sub> (9)	7.97	N <sub>2</sub> (9) + N	0.668
N <sub>2</sub> (10)	12.1	N <sub>2</sub> (10) + N	0.939
N	3.20	N + N	0.700
		N <sub>2</sub> ( $k$ ) + N <sub>2</sub> ( $l$ )	0.680

(b) VHS parameters used in conventional (LB+TCE) cases

species	$d_{\text{ref}}$ [Å]	pair	$\omega$ [-]
N <sub>2</sub>	3.20	N <sub>2</sub> -N <sub>2</sub>	0.680
N	2.60	N-N	0.700
		N <sub>2</sub> -N	0.690

(c) Arrhenius parameters for nitrogen TCE dissociation rates used in conventional (LB+TCE) cases

	$A$ [m <sup>3</sup> · s <sup>-1</sup> ]	$b$ [-]	$E_a$ [J]
N <sub>2</sub> -N	$1.587 \times 10^{-11}$	-0.793	$1.561 \times 10^{-18}$
N <sub>2</sub> -N <sub>2</sub>	$1.162 \times 10^{-8}$	-1.6	$1.561 \times 10^{-18}$

discussed more in detail. Before moving on, it should be noted that catalytic recombination on the body's surface was not taken into account in any of the cases considered here, whether with the bin model nor with the conventional ones.

The computational parameters for all sets of simulations are summarized in Tab. 5.3. The simulations for the higher Knudsen number were performed on a quad-core desktop machine, whereas the lower Knudsen number required the use of 64 processors on the cluster available at the von Karman Institute. While the individual simulation times varied from case to case, they took approximately 3 - 4 days for the higher Knudsen number and 10 - 11 days for the lower Knudsen number, transient and sampling steps included. Especially at  $Kn_D = 0.004$ , the run times of the simulations using the bin model were noticeably longer than those using the conventional models. This can be attributed to the fact that the state-to-state algorithm has to cycle through 10 potential chemical reactions every time a collision pair N<sub>2</sub>+N is chosen. By contrast, in the conventional routines, only Larsen-Borgnakke internal energy exchange, or a single dissociation reaction has to be evaluated. As can be seen from the domain boundaries indicated in Tab. 5.3, in order to

reduce the computational expense, only the upper half of the flow field was simulated, and a symmetry boundary condition was imposed along the axis where  $y = 0$ . The background cells mentioned in Tab. 5.3 were sized in a way so as to resolve the mean free path in the free stream inflow. In regions with large density increases, such as in the vicinity of the forward stagnation point, RGDAS used a cell refinement algorithm to reduce the collision cell size based on the local number of particles. In the present simulations, the algorithm was set to keep the number of particles at approximately 10 per collision cell. The requirement of resolving the mean free path in each collision cell was verified during post-processing of the flow macroparameters.

Table 5.3.: Cylinder in hypersonic cross flow: Computational parameters

$\text{Kn}_D$		0.04	0.004
Time step size	[s]	$1 \times 10^{-6}$	$1 \times 10^{-7}$
Transient steps		10000	250000
Sampling steps		400000	200000
Domain size	[m]	$-0.5 \leq x \leq 1.5$	$-0.2 \leq x \leq 0.8$
	[m]	$0 \leq y \leq 0.65$	$0.0 \leq y \leq 0.35$
Background cells		$800 \times 260$	$4000 \times 1400$
Simulator particles		$2.3 \times 10^6$	$83 \times 10^6$
Processors		4	64

In what follows, a comparison of the flow fields obtained with both models is shown. In order to save space, this comparison for the moment is limited to the cases **10 bins, N3 1%** and **LB+TCE, N3 1%**, neglecting the two other sets of simulations listed in Tab. 5.1(b). However, these missing simulations will become relevant when the stagnation line profiles and surface parameters are discussed later in this section.

Plots of the local density fields, normalized with the respective free stream density, are shown in Fig. 5.7(a) for the higher Knudsen number, and in Fig. 5.7(b), for the lower Knudsen number. Both plots are sub-divided into two separate halves cut off at the symmetry line along the  $x$ -axis. The results for the bin model with a molar fraction of 1% atomic nitrogen in the free stream are shown on the upper half, and the equivalent results using the conventional (Larsen-Borgnakke + TCE) models are shown on the lower half of the graph. For easier comparison the same color scheme and contour levels have been used in all plots. The contour lines labeled “1.01” correspond to a density ratio of  $\rho/\rho_\infty = 1.01$ , intended to better pin-point the initial rise in density above the free stream value. As would be expected, the results at the higher Knudsen number show shock stand-off distances much larger (approximately 2 – 2.5 times greater) than at the lower Knudsen number (pay attention to the change in scale between Fig. 5.7(a) and Fig. 5.7(b)). This is true both for the bin model and the conventional model results. The results at  $\text{Kn}_D = 0.04$  also show a much more diffuse shock structure. These differences can be visualized more easily by focusing on the density profiles on the forward stagnation stream line. They are compared separately in Fig. 5.12(a) and Fig. 5.12(c).

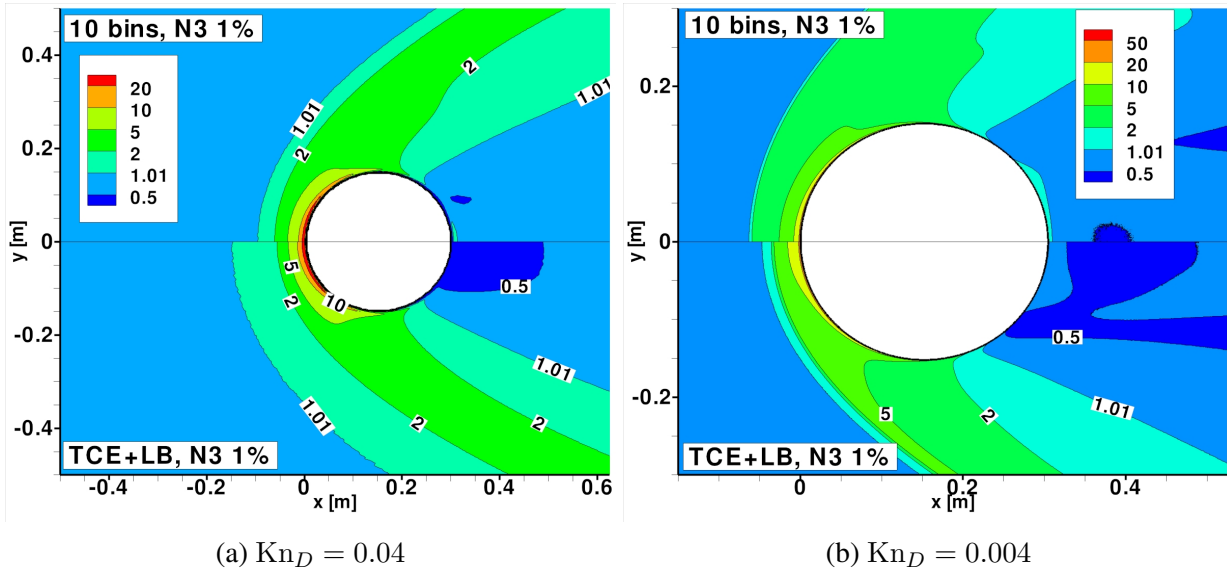


Figure 5.7.: Cylinder in hypersonic cross flow: Density ratios  $\rho/\rho_\infty$ , comparison between bin model (upper half) and conventional models (lower half)

The translational temperature fields are shown in Fig. 5.8. The same sub-division as in the density plots of Fig. 5.7 is kept here, with the bin model results shown on the upper half and the conventional model results shown on the lower half. In all cases the translational temperature rise across the bow shock precedes the one of the density by a small, but noticeable margin. The most obvious difference between the bin model and the conventional model results is the magnitude of the temperature levels observed throughout the flow field. Especially in the bow shock region, and near the forward stagnation point, the bin model predicts much higher translational temperatures. Focusing first on the higher Knudsen number, Fig. 5.8(a) reveals maximum temperatures above 50000 K with the bin model, compared to 20000 K with the conventional models. Closer to the surface, these temperatures drop below 5000 K in both models. Similar behavior is observed in Fig. 5.8(b) for the lower Knudsen number. Again, the maximum translational temperatures in a fairly large region behind the shock surpass 50000 K in the bin model, while the conventional results predict a much more localized temperature spike. The gradients of translational temperature along the forward stagnation streamline are much steeper at this lower Knudsen number, a fact that can be better observed on the stagnation stream line by comparing the profiles shown in Fig. 5.13. At the lower Knudsen number, the wake region immediately behind the cylinder is much colder, reaching values below 5000 K with the bin model and 2000 K with the conventional models, before heating up again farther behind.

Plots showing the rovibrational temperature extracted from the bin populations of  $N_2$ , called  $T_{int}$ , vs. the rotational temperature based on the rigid rotor levels in the conventional models, are shown in Fig. 5.9. A direct comparison between the two models using these different temperatures is difficult, as they represent different fractions of the overall internal energy of  $N_2$ . With the bin model, levels belonging to a range of rotational and vibrational quantum numbers are lumped

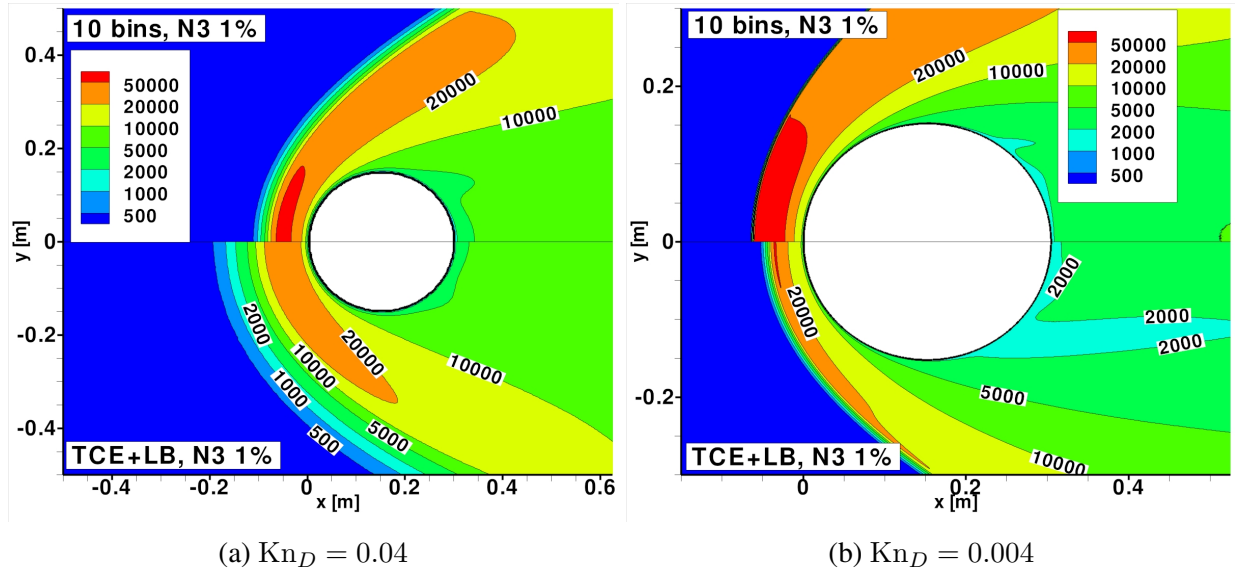


Figure 5.8.: Cylinder in hypersonic cross flow: Translational temperature  $T$  [K], comparison between bin model (upper half) and conventional models (lower half)

together in the same bin, whereas in the conventional model, rotational and vibrational modes are considered to be separate and independent of one another. Therefore, a full comparison must also include the vibrational temperatures from the conventional models. These are shown in the lower half of the plots in Fig. 5.10.

Focusing first on the results for the higher free-stream Knudsen number, shown in Fig. 5.9(a), it is clear that the internal and translational modes are severely out of equilibrium. This is especially true with the bin model. Whereas the translational temperatures shown in Fig. 5.8(a) reach values above 50000 K in the bow shock, the internal temperatures for the same case barely surpass 20000 K before reaching the surface of the cylinder. With the conventional models the predicted rotational temperatures are actually of the same order of magnitude as for the internal temperature of the bin model, reaching values above 10000 K in the bow shock and near the outer parts of the wake. However, the region in which this rotational temperature increase takes place is slightly wider for the conventional model results. The profiles shown in the lower half of Fig. 5.10(a) reveal a lower degree of vibrational excitation for the conventional models, with the vibrational temperature reaching values above 10000 K only in a small region in the bow shock immediately ahead of the cylinder. This is consistent with the much shorter characteristic times predicted for R-T relaxation [146], when compared to those of V-T relaxation processes [147, 148].

At the lower Knudsen number, the situation is somewhat different. Comparing the internal and translational temperatures for the bin model, shown in the upper halves of Fig. 5.9(b) and Fig. 5.8(b) respectively, the most noticeable differences exist in the bow shock region (see also 5.13). While the maximum translational temperature lies above 50000 K inside a considerable region behind the shock, the internal temperature reaches 20000 K only in a narrow region ahead of the body. In the immediate vicinity of the cylinder and wake, the agreement between the

translational and internal temperature contours is much closer. This suggests that, although there exists significant thermal nonequilibrium in the bow shock, the higher collision rate drives the two modes to equilibrate faster in the region above and behind the cylinder. For the conventional models, the rotational temperature profiles shown in the lower part of Fig. 5.9(b) show closer agreement with the translational temperatures in the lower half of Fig. 5.8(b). This is especially true for the profiles in the vicinity of the body and the wake region. Except for the region in the bow shock, where  $T > 20000$  K, the rotational and translational temperatures in the conventional model results closely match one another. This suggests that both modes are nearly equilibrated throughout most of the flow field. By contrast, the vibrational temperatures shown in Fig. 5.10(b) show a different behavior.

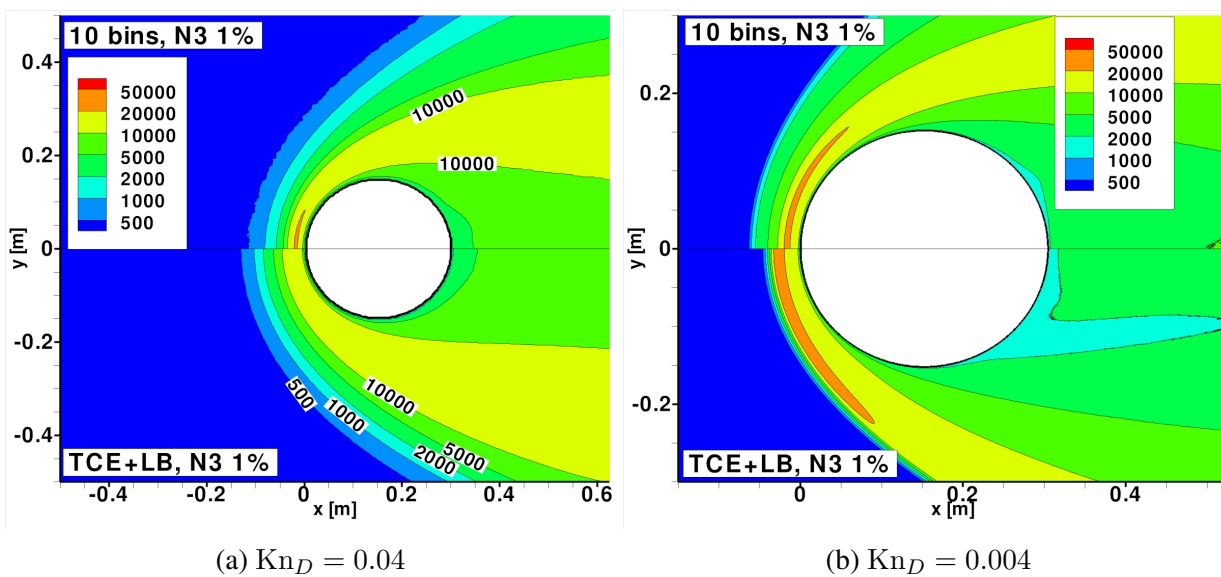


Figure 5.9.: Cylinder in hypersonic cross flow: Comparison between  $T_{int}$  [K] in bin model (upper half) and  $T_{rot}$  [K] in conventional models (lower half)

Plots of the molar fraction of atomic nitrogen are shown in Fig. 5.11 for both free-stream Knudsen numbers considered. Both plots are sub-divided in the same manner as with the previous macroparameters in order to directly compare the bin model to the conventional ones. The results for the higher Knudsen number are shown on the left, in Fig. 5.11(a).

The large discrepancy of the bin model with respect to the conventional ones is immediately noticeable. Whereas the conventional model predicts fairly strong and continuous dissociation behind the shock, reaching  $x_N > 0.5$  around the surface of the body, dissociation with the bin model seems to be delayed behind the bow shock. The most likely explanation for this big difference is that the state-to-state model tends to predict a longer “incubation distance” for the onset of dissociation compared to conventional TCE chemistry model, which does not include vibrational favoring. Similar conclusions have previously been obtained with hydrodynamic codes [117, 7] while studying the dissociation and excitation of  $N_2$  past a shock wave with equivalent state-to-state models and comparing to the conventional Park multi-temperature model. At relatively high

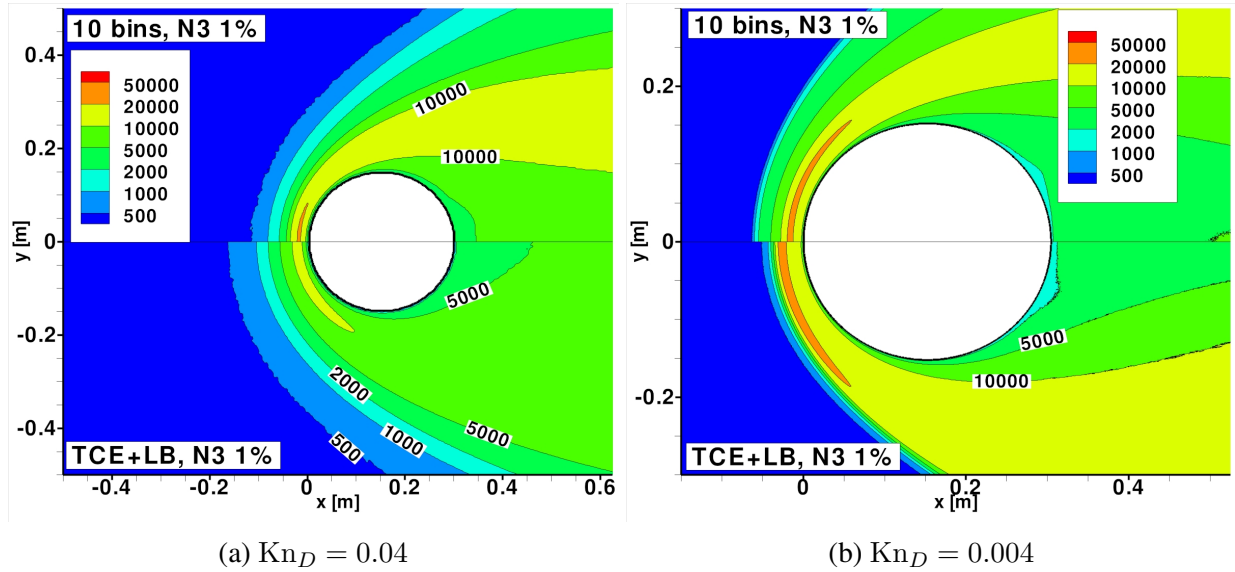


Figure 5.10.: Cylinder in hypersonic cross flow: Comparison between  $T_{int}$  [K] in bin model (upper half) and  $T_{vib}$  [K] in conventional models (lower half)

free-stream Knudsen numbers, such as the ones considered here, the collision rate is low enough for this incubation distance to be of the same order of magnitude as the characteristic length scale of the flow. The highest concentrations of atomic nitrogen, at around 60 % are predicted by both models model in the wake region immediately behind the body. This effect is likely to be caused by diffusion of N into these slightly colder regions of the flow field.

The results for the lower Knudsen number are shown on the right, in Fig. 5.11(b). In this case the difference between the two models, although still clearly noticeable, is less severe. While the conventional model predicts values of  $x_N$  greater than 0.9 in the vicinity of the body's surface, the bin model predicts maximum values slightly above  $x_N = 0.8$ . From the contours one can also infer that the conventional model predicts a quicker rise in the concentration of atomic nitrogen along the stagnation stream line with respect to the bin model.

The structure of the bow shock region can be more easily studied by focusing on the stagnation stream line ahead of the body. This line coincides with the  $x$ -axis, as is indicated in Fig. 5.6. The two plots in the left column of Fig. 5.12 show the overall mass densities along the stagnation stream line for  $Kn_D = 0.04$  and  $Kn_D = 0.004$  respectively, while the two figures in the column to the right show the corresponding mole fraction profiles of atomic nitrogen. In addition to the two baseline cases with 1% atomic nitrogen in the free stream compared above, now the two additional cases listed in Tab. 5.1, i.e. the bin model with 5% N in the free stream and the full LB+TCE model, are shown as well. In each plot the four lines are color-coded to more easily separate the different results and the labeling of the curves corresponds to the headings used in Tab. 5.1(b). Focus first on the density profiles for the higher free-stream Knudsen number in Fig. 5.12(a). For all four cases, one observes the very diffuse shock structure characteristic of transitional flows. In fact, it is not really possible to clearly separate the density rise across the

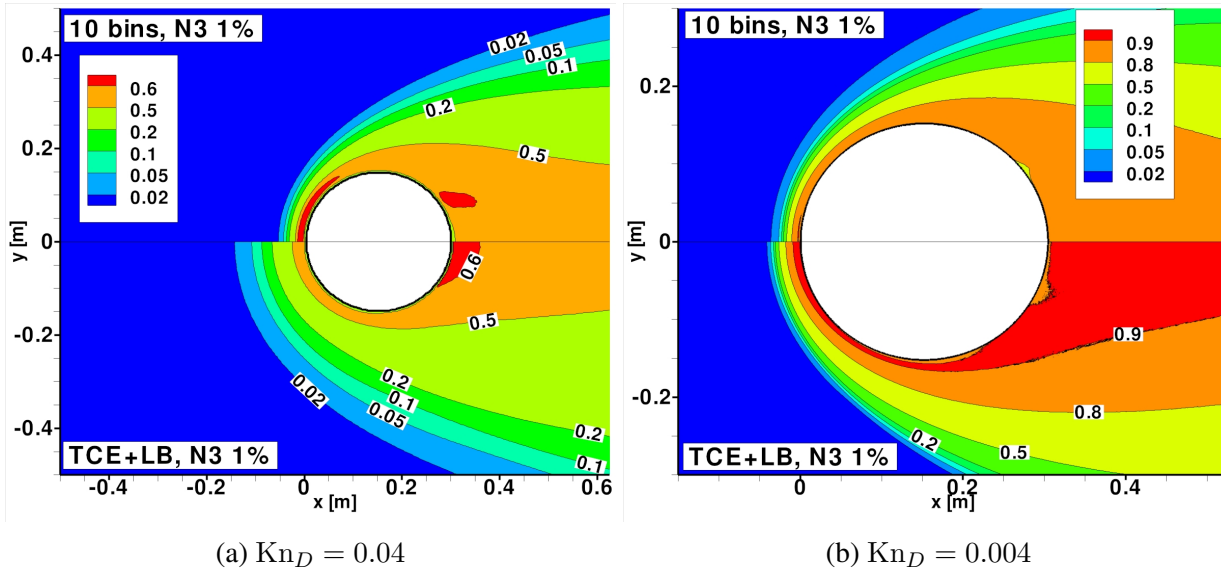


Figure 5.11.: Cylinder in hypersonic cross flow: Molar fraction of atomic nitrogen, comparison between bin model (upper half) and conventional models (lower half)

bow shock from the subsequent compression near the stagnation point. However, one can observe some differences between the simulations run with the bin model and those using the conventional models. Whereas the bin model profiles exhibit a steeper initial rise in the density, the two simulations performed with the conventional model predict a more-or-less continuous increase in the density as one approaches the stagnation point at  $x = 0$ . The corresponding mole fraction of atomic nitrogen along the stagnation stream line is plotted in Fig. 5.12(b). As can be seen, the N-concentration in all four simulations rises above 50% ahead of the stagnation point. However, the initial location along the x-axis where dissociation starts to be noticeable differs significantly between the bin- and the conventional model cases. Whereas dissociation with the conventional models begins even ahead of the initial density rise, at  $x \approx -0.12$  m, with the bin model this location is shifted much closer to the stagnation point itself, i.e. to  $x \approx -0.05$  m. When comparing all four profiles, one can observe a certain trend: the most vigorous dissociation is predicted by the conventional models with both  $N_2+N_2$ - and  $N_2+N$ -dissociation reactions enabled. It is followed by the same conventional model, but with only  $N_2+N$ -dissociation. Both bin model simulations seem to behave in a similar manner, with all of the chemical activity concentrated in the region immediately adjacent to the body. Their two concentration profiles seem identical, with the only real difference being the additional atomic nitrogen present in the flow in the 5%-case. All four simulations predict a slight decrease of the atomic nitrogen concentration immediately in front of the stagnation point. Since recombination reactions are not modeled in any of the simulations discussed here, this is most likely an effect caused by diffusion of the heavier molecular nitrogen towards the cold wall.

In order to better understand this behavior, it is necessary to take into account the temperature profiles along the stagnation stream line. For  $Kn_D = 0.04$  these profiles are plotted in two fig-

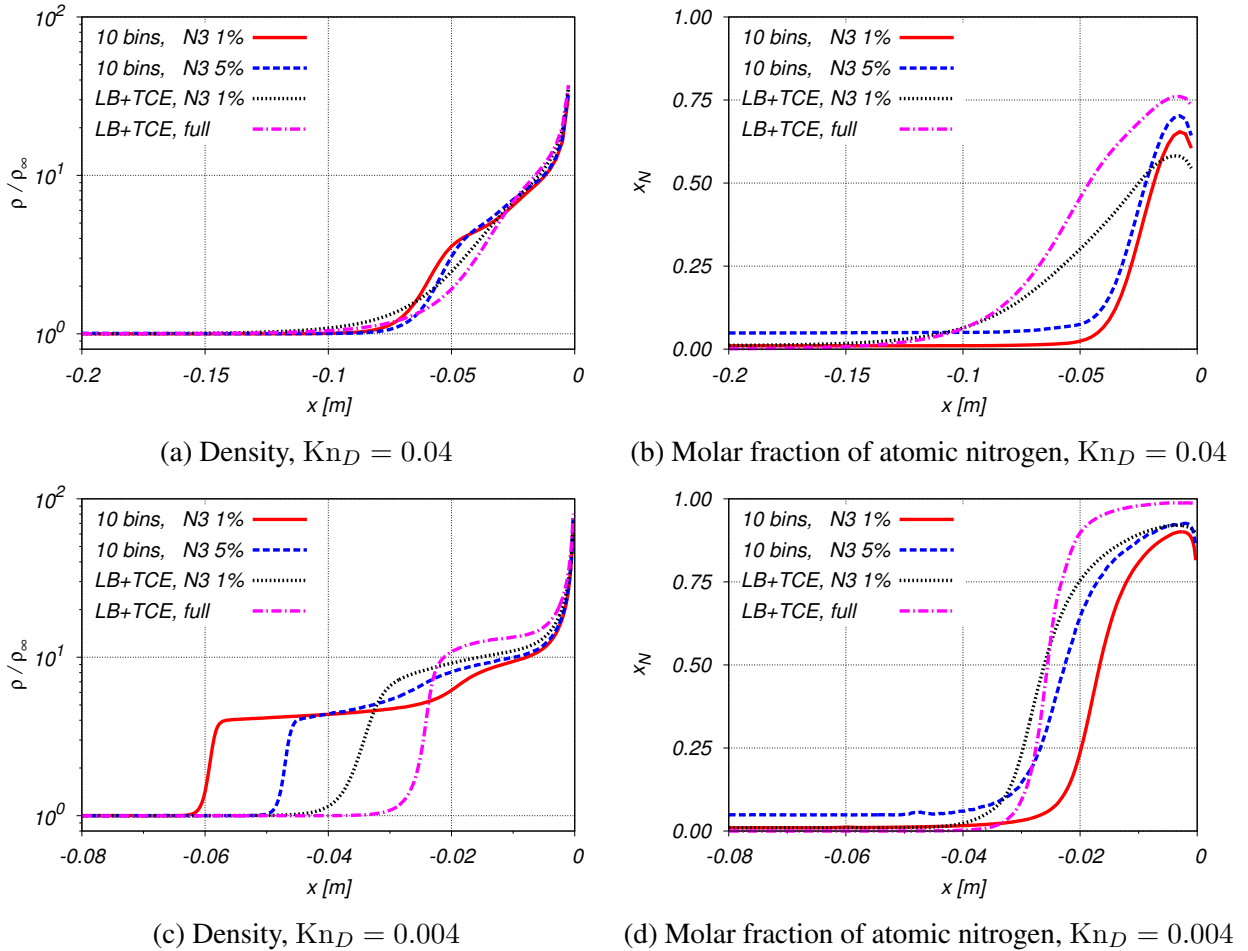


Figure 5.12.: Cylinder in hypersonic cross flow: Comparison of densities (left) and mole fractions of atomic nitrogen (right) along stagnation stream line

ures in the top row of Fig. 5.13. For better visibility, the two bin model simulations are shown separately in Fig. 5.13(a), while the two simulations with the conventional models are shown in Fig. 5.13(b). In the bin model plots, profiles for the translational and the internal mode temperatures are shown, whereas for the conventional model translational, rotational and vibrational temperatures are plotted. Two major differences between the two types of models can be observed. First, the initial rise of the translational temperature is much more pronounced with the bin model. For both variants shown in Fig. 5.13(a), it begins fairly abruptly at  $x \approx -0.1$  m and reaches its maximum value at around  $x = -0.05$  m. By contrast, the translational temperature rise in the conventional model simulations is much more gradual and spread out over a greater distance. Incidentally, in all four simulations the maximum values of translational temperature are recorded at approximately the same location. The second major difference between the bin and conventional models is the maximum temperatures reached in both cases. Whereas the conventional models predict peak translational temperatures of 35000-45000 kelvin, the maximum values with the bin model lie above 60000 K. Thus, with the bin model a much greater amount of flow kinetic energy is initially absorbed by the translational mode, before the rovibrational

modes slowly become excited and finally dissociation is triggered. This delay in internal energy excitation can be observed in Fig. 5.13(a), where  $T_{\text{int}}$  initially lags behind  $T$  by a considerable distance. It only begins to rise noticeably at around  $x = -0.05$  m and reaches maximum values slightly above 20000 K, just before equalizing with the translational temperature. By contrast, in the conventional model simulations, the dissociation reactions (see 5.12(b)) seem to take place at more-or-less the same rate as the translational temperature increase and without any delay. The much lower peak temperatures seen in Fig. 5.13(b), can be attributed to a greater fraction of the flow kinetic energy being directly absorbed by the endothermic dissociation reactions.

For the lower free-stream Knudsen number, i.e. at  $\text{Kn}_D = 0.004$ , the density profiles on the stagnation stream line are plotted in Fig. 5.12(c), with the same line formatting and color scheme as before. The ten-fold rise in free-stream density has the effect of bringing the flow much closer to the continuum regime, i.e. the density profiles now exhibit much sharper jumps across the bow shock than those in Fig. 5.12(a). The bow shock is now positioned somewhat closer to the cylinder's surface, and one can clearly distinguish the locations at which the initial density increase occurs. Unlike at the higher Knudsen number, the shock stand-off location for each one of the four simulations is predicted at clearly different locations. With a distance of about 0.06 m from the stagnation point, it is greatest for the bin model with 1% atomic nitrogen in the free stream and smallest for the conventional model with both dissociation reactions enabled, at approximately 0.03 m. The corresponding profiles of atomic nitrogen mole fraction are shown in Fig. 5.12(d). Unlike with the results for  $\text{Kn}_D = 0.04$ , the distinction between the bin- and conventional model profiles no longer seems as clear-cut. Although the degree of dissociation predicted with the conventional models is still greater than that obtained with the bin model (nearly 100 % when both dissociation reactions are enabled vs.  $\approx 85$  % with the bin model), this process now is triggered at comparable distances from the body in all four cases. However, this does not mean that the rovibrational favoring, which resulted in the delayed dissociation predicted by the bin model is no longer present. In order to realize this, the temperature profiles along the stagnation stream line again prove useful. They are plotted in Fig. 5.13(c) for the two bin model simulations and in Fig. 5.13(d) for the conventional model simulations. Notice now that the quite different shock-standoff distances suggested by the density profiles of Fig. 5.12(c) are mirrored by these temperatures. For the bin model with 1 % atomic nitrogen in the free stream, the steep rise in density at  $x \approx -0.06$  m is preceded slightly by an equally steep rise in translational temperature. Next, the bin model case with 5 % N in the free stream predicts the initial rise in  $T$  at  $x \approx -0.05$  m, closely matched by its corresponding density profile. As for the two simulations with the conventional model, their temperature profiles are also displaced along the  $x$ -axis consistent with the behavior of the density. Compared to the bin model cases, the conventional models predict a more gradual increase in the translational temperature and comparatively fast excitation of the rotational and vibrational energy modes. Simultaneously, dissociation of  $\text{N}_2$  seems to be triggered by the conventional models as soon as the translational temperature rises across the

shock. By contrast, the translational temperature in the bin model rises much farther away from the stagnation point and to much higher values than with the conventional models. The most extreme example of this is, of course, the case with  $x_{N,\infty} = 0.01$ , where  $T$  first rises to nearly 65000 K at  $x \approx -0.06$  m and then only very gradually decreases over the next 3.5-4 centimeters. It is only at  $x \approx -0.03$  m that dissociation is slowly commencing in this case, preceded by a gradual excitation of the internal energy modes. To a lesser extent, similar behavior can be observed with the bin model, but with  $x_{N,\infty} = 0.05$ . Here, a translational temperature plateau is no longer visible, and the rovibrational energy modes become excited at a faster rate (due to there being a greater fraction of  $N_2(k)+N$ -collisions happening in the gas), but the dissociation is still triggered at a distance roughly 3 cm behind the bow shock front.

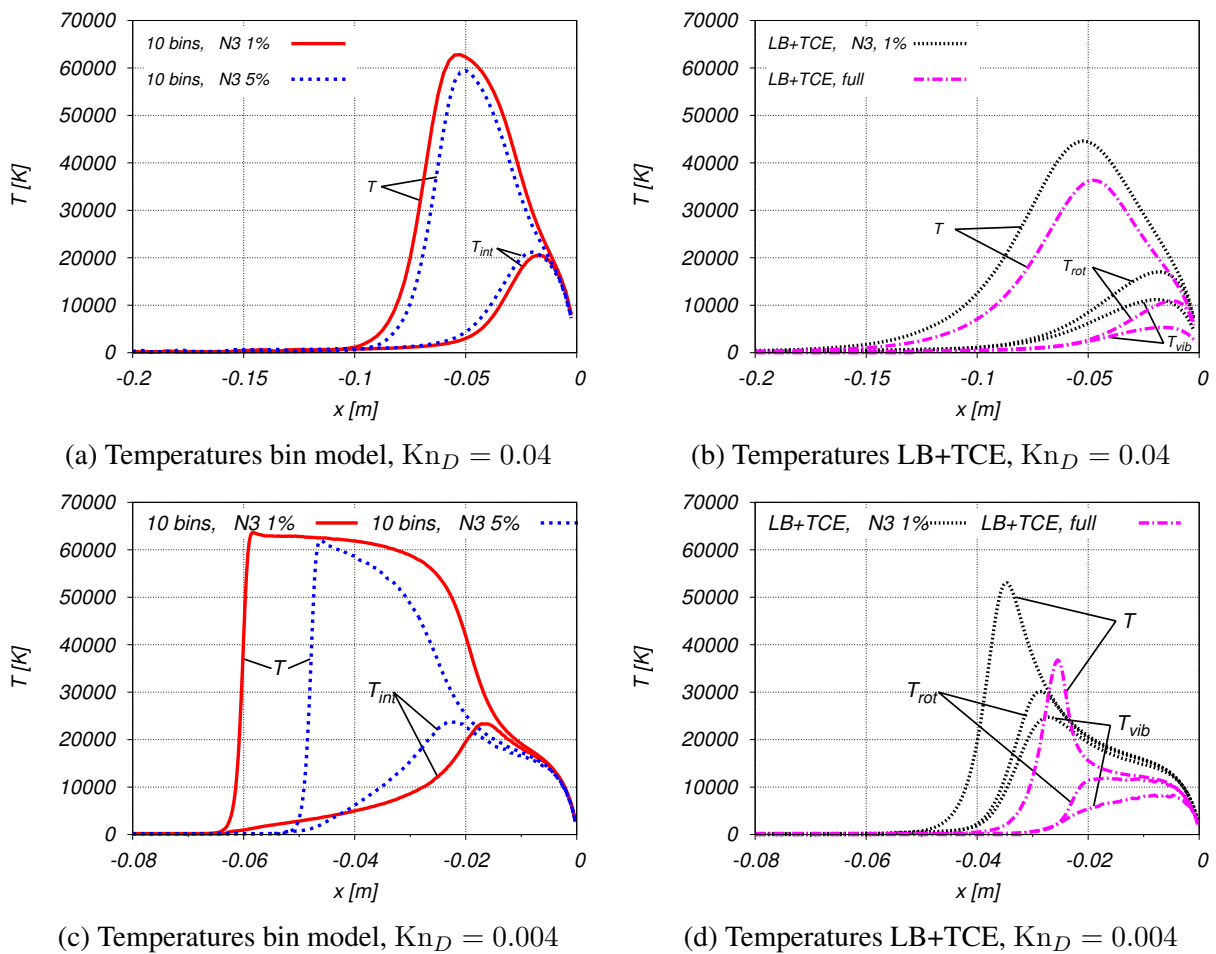


Figure 5.13.: Cylinder in hypersonic cross flow: Comparison of translational and internal mode temperatures for bin model (left) and conventional models (right) along stagnation stream line

The significant differences in chemical activity observed along the stagnation stream line between the bin- and conventional models justify closer examination. For this purpose it is useful to separately plot the contributions of the individual species' energy modes along the stagnation stream line. These quantities are shown in Fig. 5.14. For simplicity, and as was done with the flow field contour plots, only the two sets of simulations in columns 1 and 3 of Tab. 5.1(b) are

compared here. Every one of the four plots in Fig. 5.14 uses the same line pattern and coloring scheme. The black solid line represents  $h_0$ , i.e. the total specific enthalpy of the flow, whereas the black dash-dotted line shows the specific kinetic energy of the bulk flow. The remaining lines are colored and represent the individual contributions of both mixture components to the overall thermal energy with respect to the overall mixture mass. The solid red line shows the translational thermal energy of N, while the green line shows the corresponding value for N<sub>2</sub>. The blue line represents the contribution of the internal (rotational and vibrational) energy levels of N<sub>2</sub> to the thermal energy. In the bin model this quantity is computed based on the bin populations, while in the conventional model the rotational and vibrational energies are determined based on the rotational and vibrational level populations before being added together. Finally, the magenta line stands for the contribution due to the formation energy of atomic nitrogen. Recall that following the conventions established previously, the formation energy of molecular nitrogen in its ground rovibrational state is always exactly zero and is therefore not included.

Focusing first on the plots in the upper row, where the results for  $K_{nD} = 0.04$  are compared, Fig. 5.14(a) shows the profiles for the bin model, while Fig. 5.14(b) shows the equivalent results for the conventional models. In both images, one can see how the flow kinetic energy gradually decreases across the rather diffuse compression region, while simultaneously the translational thermal energy of N<sub>2</sub> rises. Consistent with the delayed dissociation of nitrogen observed previously (red solid line line in Fig. 5.12(b)), the contribution of N to the translational energy is practically zero in the bin model case until about  $x \approx -0.05$  m. By contrast, as could be seen for the conventional model (black dotted line in Fig. 5.12(b)) a quite significant amount atomic nitrogen is produced all along the region between  $x \approx -0.15$  m and the stagnation point. As a consequence, a fairly substantial increase in the translational thermal energy of N can be observed in Fig. 5.14(b). In both the bin- and conventional models some degree of rovibrational energy excitation of N<sub>2</sub>, represented by the solid blue line, can be observed. However, it seems to be fairly weak, especially for the conventional model case. Apparently, at  $K_{nD} = 0.04$  the internal energy relaxation rates are too low for the internal mode to achieve equilibrium with the translational modes before reaching the wall and a large fraction of the flow kinetic energy is directly absorbed by the dissociation reactions. Finally, the contribution due to the formation energy of atomic nitrogen is quite substantial in both the bin model and conventional case, especially near the stagnation point. In fact, at the stagnation point, it constitutes the greatest single contribution to the total enthalpy  $h_0$ .

A similar comparison can be made for the stagnation line profiles at  $K_{nD} = 0.004$ . The bin model results are shown in Fig. 5.14(c) and the corresponding results for the conventional models in Fig. 5.14(d). As was observed during the discussion of Fig. 5.13, the gradients in the flow macroparameters along the stagnation line at these conditions are much steeper than at  $K_{nD} = 0.04$  and the shock position is much more clearly defined. In addition to this the shock stand-off distance is now significantly smaller. In the bin model, one can observe the steep rise of

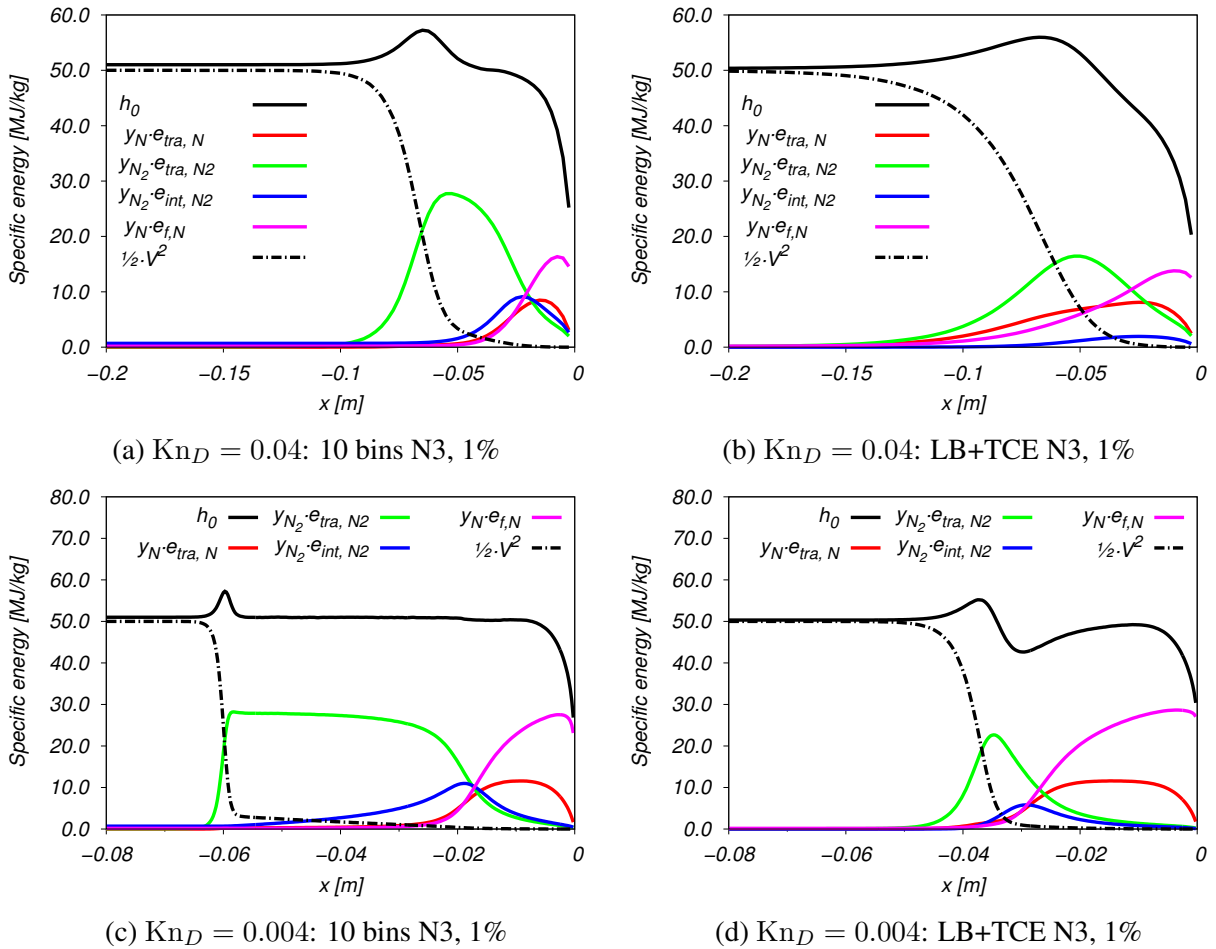


Figure 5.14.: Cylinder in hypersonic cross flow: Contributions to specific energy along stagnation stream line. Comparison between bin model (left column) and TCE+LB model exclusively with dissociation by atomic nitrogen impact and  $x_{N,\infty} = 0.01$  (right column)

the translational energy of  $N_2$ , which coincides with the initial drop in the flow kinetic energy. After this rise, the translational energy of  $N_2$  remains fairly high and only gradually decreases while the internal modes of  $N_2$  slowly become excited. It is only at  $x \approx -0.025$  m that the translational energy of atomic nitrogen starts to become significant. Of course, this coincides with the onset of dissociation and the increased production of atomic nitrogen (recall the solid red line in Fig. 5.12(d)). Beyond this location, while approaching the stagnation point, most of the energy in the flow is absorbed by the translational mode of N and bound in the formation energy of atomic nitrogen. By contrast, the conventional models predict a somewhat different behavior. Unlike in the bin model there is no significant delay in the onset of dissociation, as atomic nitrogen is produced almost as soon as the flow kinetic energy is released across the shock. The rapid dissociation absorbs the majority of this energy, as can be seen by the magenta curve in Fig. 5.14(d). This means that the translational and internal modes of  $N_2$  never manage to become excited to the same degree as in the bin model. Correspondingly, the peak translational temperatures along the stagnation stream line predicted by the conventional models are much

lower than the equivalent bin model values (recall the red solid vs. the dotted black curve in Fig. 5.13(c) and Fig. 5.13(d)). Notice that in all four cases shown in Fig. 5.14 the total enthalpy  $h_0$  first slightly increases as the free stream encounters the shock front and then begins to decrease the more the flow approaches the wall. These changes in  $h_0$  are caused by dissipative effects, specifically heat transfer and viscous stresses within the gas. By contrast, gas phase chemistry and internal energy mode excitation do not affect the total enthalpy.

Before moving on to examining the pressure, shear stress and heat flux distributions recorded on the cylinder's surface, it is worthwhile to quickly comment on the degree of rarefaction in the flows studied here. Judging by the global Knudsen numbers used to identify the two distinct sets of free stream conditions, i.e.  $Kn_D = 0.04$  and  $Kn_D = 0.004$ , one might assume that the flow conditions are very close to the continuum regime. This is especially true for the latter Knudsen number. However, when examining the macroscopic profiles in Fig. 5.12 and Fig. 5.13 one cannot but notice the diffuse features in the shock profiles and the significant degree of translational and internal energy nonequilibrium along the stagnation stream line. Thus, the conditions on the stagnation stream line, and indeed in much of the flow field surrounding the cylinder, do not lie fully in the continuum regime in either case. This apparent inconsistency can be attributed to the fact that the two Knudsen numbers are based on global reference quantities, which do not necessarily reflect the precise conditions at every point in the flow field. Recall that in both cases the mean free path at the free stream conditions  $\lambda_\infty$  is used, along with the cylinder's diameter  $D$  as reference length. Although using these quantities is convenient, since they are easily determined even before the simulations are performed, they are misleading. This realization is not new and the issue has been raised previously by others, such as Boyd et al [149], who investigated the problem of continuum breakdown precisely for the type of hypersonic reentry flows considered here. They determined that a reliable estimate of the degree of rarefaction in the flow field is possible using local gradient-based Knudsen numbers. In this approach, a local mean free path at every point in the flow field is determined a posteriori from the simulation results, along with a local reference length. This reference length is based on local gradients of macroscopic flow parameters, such as the density:

$$Kn_{GLL,\rho} = \lambda \frac{\nabla \rho}{\rho} \quad (5.10)$$

In their paper Boyd and co-workers determined that the density-gradient-based local Knudsen number reliably predicts continuum breakdown for values  $Kn_{GLL,\rho} > 0.05$ . Thus, one should re-examine the current stagnation line profiles using this criterion. Plotting the local Knudsen number, as defined in Eq. (5.10), along the stagnation stream line for the cases just discussed results in the images of Fig. 5.15. The image on the left shows  $Kn_{GLL,\rho}$  for both the bin model and the conventional models at the lower free stream density, while the image on the right shows the equivalent results for the higher free stream density. One can see that in both cases the local Knudsen number in the free stream is orders of magnitude lower than in the regions where

the compression takes place. The noise in the signal can be attributed to small fluctuations in the density, which are magnified when the density gradients are computed numerically. In all cases the peak in  $\text{Kn}_{GLL,\rho}$  roughly coincides with the steep increases of density and the accompanying translational temperature rises across the shock. Although the  $\text{Kn}_{GLL,\rho}$  then decrease again, in all cases they remain significantly above the free stream values. At the conditions of Fig. 5.15(a), the conventional models actually predict higher local Knudsen numbers, reaching maximum values of  $\text{Kn}_{GLL,\rho} \approx 0.7 - 0.8$ . These values then decrease as one approaches the stagnation point, but remain slightly above the continuum breakdown criterion of  $\text{Kn}_{GLL,\rho} = 0.05$ . By contrast, the local Knudsen numbers observed for the bin model cases only reach peak values of  $\text{Kn}_{GLL,\rho} \approx 0.2 - 0.3$ , and subsequently decrease to nearly 0.05 near the stagnation point. This behavior can be explained by the larger total cross sections used with the bin model (compare the reference diameters in Tab. 5.2(a) to those in Tab. 5.2(b)), which affect the local mean free path. At the higher-density conditions of Fig. 5.15(b), the local Knudsen numbers still reach peak values between approximately 0.3 and 0.7 depending on the particular case. However, for most of the distance along the stagnation stream line, the curves for all four cases considered remain well below Boyd's cutoff value of 0.05. Thus, apart from the shock fronts themselves, most of the flow at these higher-density conditions can be considered close to the continuum regime.

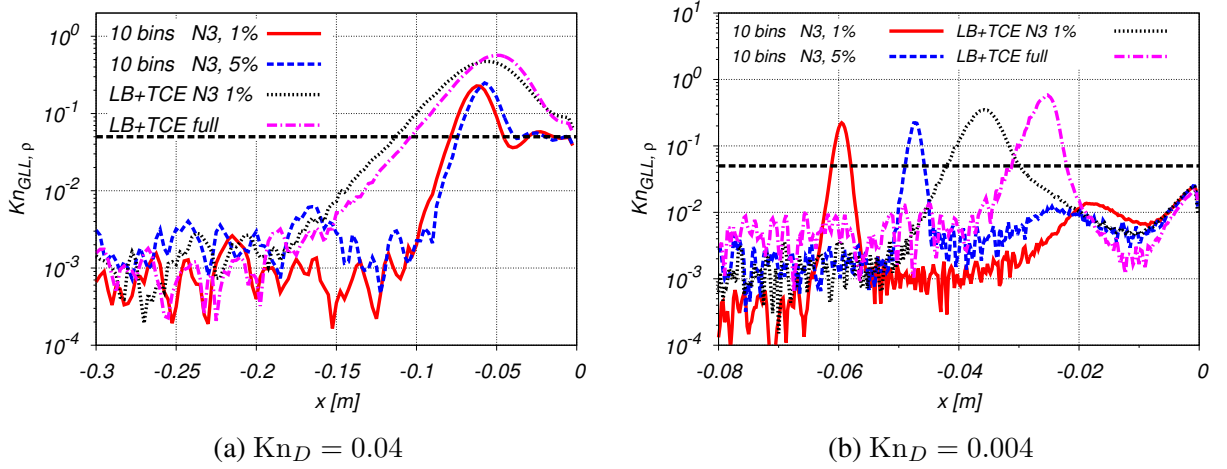


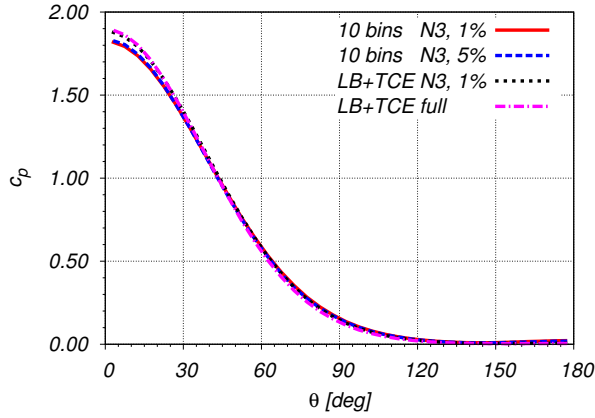
Figure 5.15.: Cylinder in hypersonic cross flow: Density-gradient-based local Knudsen numbers along stagnation stream line. Comparison between bin model with 1 % (red solid lines) and 5 % (blue dashed lines) of free-stream atomic nitrogen and TCE+LB model exclusively with dissociation by atomic nitrogen impact and  $x_{N,\infty} = 0.01$  (black dotted lines) and full LB+TCE model (purple dash-dotted lines)

The distributions of surface pressure, wall shear stress and wall heat flux are plotted in Fig. 5.16. They are reported as coefficients normalized using the free stream flow parameters:

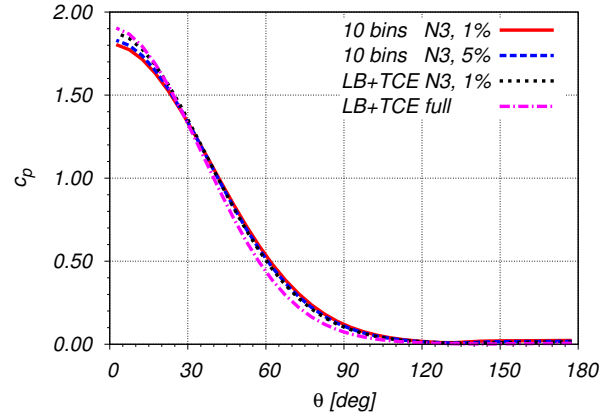
$$c_p = \frac{p - p_\infty}{\frac{1}{2}\rho_\infty V_\infty^2}, \quad c_f = \frac{\tau_w}{\frac{1}{2}\rho_\infty V_\infty^2}, \quad \text{and} \quad c_h = \frac{q_w}{\frac{1}{2}\rho_\infty V_\infty^3}. \quad (5.11)$$

Only the distributions on the upper half of the cylinder's circumference are shown, with the angle  $\theta$  measured clockwise starting at the forward stagnation point, as was indicated in Fig. 5.6. A total of 36 panels was used to represent the half-cylinder's surface, meaning that each data point represents an average over a 5 degree arc. Fig. 5.6 is sub-divided into two columns, with the plots on the left showing the surface distributions for  $\text{Kn}_D = 0.04$ , while the plots on the right are for  $\text{Kn}_D = 0.004$ . Beginning with the higher Knudsen number, the pressure coefficient plotted in Fig. 5.16(a) shows no strong sensitivity to the chemistry model used, as expected. The maximum value near the forward stagnation point is slightly lower for the bin model cases, at around  $c_p \approx 1.84$ , while the simulations with the conventional model predict a value closer to  $c_p \approx 1.9$ . Subsequently, as one moves along the circumference towards the rear of the half-cylinder, the pressure decreases faster in the conventional model than in the bin model. The skin friction coefficient, plotted in Fig. 5.16(c), is more sensitive to the model used, as expected. Here, the bin model curves predict maximum values of  $c_f \approx 0.11 - 0.115$  at an angle of approximately 40 degrees, while the maxima for the conventional model,  $c_f \approx 0.16 - 0.17$  are noticeably larger. The most noticeable difference between the two models is in the curves for the heat transfer coefficient, plotted in Fig. 5.16(e). Here, both bin model simulations give very similar results to one another, but they differ widely from the profiles predicted by the conventional models. The highest heat transfer rates are predicted by the conventional model with 1% of atomic nitrogen in the free stream, followed by the conventional model with both dissociation reactions enabled. Both bin model simulations predict noticeably smaller heat transfer rates. Focusing on the forward stagnation point, the conventional model with 1% atomic nitrogen predicts the highest normalized heat flux, with  $c_h \approx 0.23$ , while the same conventional model, but with both dissociation reactions enabled, predicts  $c_h \approx 0.185$ . Both bin model cases show very similar stagnation point values of  $c_h \approx 0.135$ . These differences are remarkable, and possible causes will be discussed later.

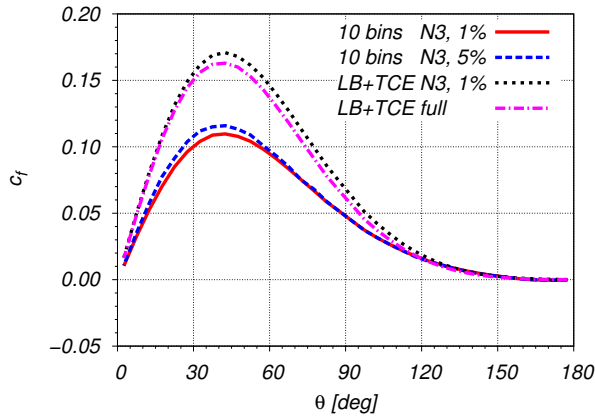
The surface distributions for  $\text{Kn}_D = 0.004$  are shown in the right column of Fig. 5.16. Again, all curves use the color-scheme of the previous figures and the values shown have been normalized according to the definitions of Eq. (5.11). The pressure coefficients are plotted in Fig. 5.16(b). The general shape of the profiles is similar to those at  $\text{Kn}_D = 0.04$ , although the pressure seems to be shifted slightly to the front part of the cylinder. Apart from this, the difference between the two Knudsen numbers seem to be negligible. The skin friction coefficients for  $\text{Kn}_D = 0.004$  are plotted in Fig. 5.16(d). Compared to the equivalent data for  $\text{Kn}_D = 0.04$ , the maxima in  $c_f$  are now just about 1/4-1/3 of the respective values shown in Fig. 5.16(c). This is an indication of the ten-fold increase in the global Reynolds number,  $\text{Re}_D = \rho_\infty V_\infty D / \eta_\infty$ , which is proportional to the free stream density, and the corresponding rise in importance of the inertial forces with respect to friction forces. The location of the maxima in  $c_f$  again occur at angles of approximately 40-45 degrees. An interesting phenomenon can be observed towards the rear of the cylinder, at angles greater than about 140 degrees. There, the skin friction coefficients for the bin model



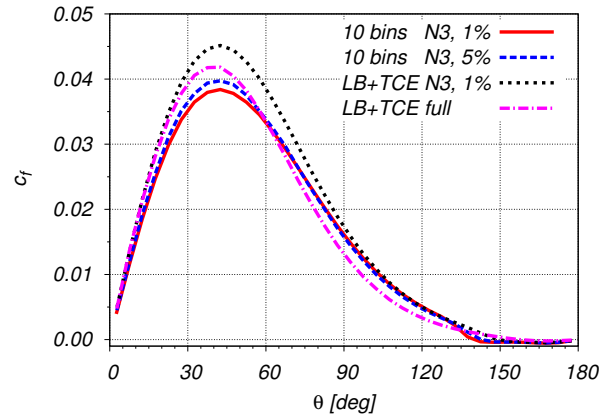
(a) Surface pressure coefficient,  $Kn_D = 0.04$



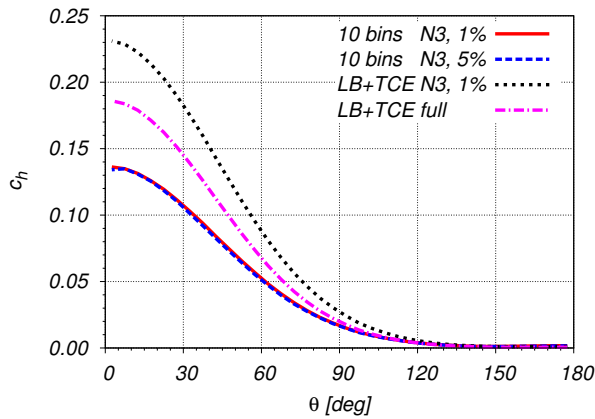
(b) Surface pressure coefficient,  $Kn_D = 0.004$



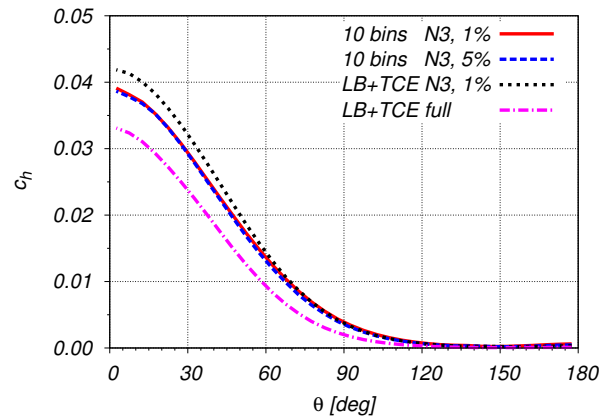
(c) Skin friction coefficient,  $Kn_D = 0.04$



(d) Skin friction coefficient,  $Kn_D = 0.004$



(e) Heat transfer coefficient,  $Kn_D = 0.04$



(f) Heat transfer coefficient,  $Kn_D = 0.004$

Figure 5.16.: Cylinder in hypersonic cross flow,  $Kn_D = 0.04$ : Comparison of normalized surface distributions along upper half of cylinder circumference

simulations become negative, indicating an inversion in the direction of the wall shear stress. Closer examination of the stream lines in the flow field, plotted along with the velocity magnitude in Fig. 5.17(b), reveals a recirculation bubble in the wake region. The separation point is located precisely at the zero-crossing of the skin friction coefficient curve in Fig. 5.16(d). Such a recirculation bubble is also observed in the wake when the conventional models are used, although it is somewhat smaller than in the bin model case. Returning to Fig. 5.16(d), compared to the higher free-stream Knudsen number case, now the maximum  $c_f$  values predicted by all simulations lie much closer to one another. Although the conventional models still predict slightly higher maxima for  $c_f$ , these values now lie only about 10-20 % above the bin model results.

Finally, the heat transfer coefficients for  $\text{Kn}_D = 0.004$  are plotted in Fig. 5.16(f). While the differences between the four cases considered are not as pronounced as for the higher free-stream Knudsen number, they are still noticeable especially near the forward stagnation point. Both simulations with the bin model predict practically the same heat flux profiles, with  $c_h \approx 0.038$  near the forward stagnation point. By contrast, the conventional model with only  $\text{N}_2+\text{N}$ -dissociation predicts a slightly higher heat flux with a stagnation point value of  $c_h \approx 0.042$ . The conventional model with both dissociation reactions enabled predicts a much lower heat flux with a stagnation point value of approximately  $c_h \approx 0.032$ . The reason for this significantly lower heat flux is most likely the almost complete degree of dissociation predicted for this case (recall the  $x_N$ -profiles in Fig. 5.12(d)) as opposed to the other three cases. The larger amounts of energy absorbed by the endothermic reactions then prevent the flow from heating the wall to the same degree as in the conventional model case when only  $\text{N}_2+\text{N}$ -dissociation is taken into account. The differences with respect to the bin model simulations are likely due to the differing boundary conditions used. This point will be addressed later in this section. Although barely noticeable in Fig. 5.16(f), the recirculation zone in the wake of the cylinder has the effect of promoting heat transfer to the surface at the rear stagnation point, slightly increasing  $c_h$  in this region. This effect was not observed in the  $c_h$ -curves at the higher Knudsen number, shown in Fig. 5.16(e), and this is consistent with the lack of a recirculation bubble in the cylinder wake of Fig. 5.17(a).

Integrated values of the surface distributions are listed in Tab. 5.4. The drag force (per unit length) is defined as the component of the force acting on the body, which is aligned with the free stream velocity vector. In the current test case this value is calculated as the  $x$ -component of the sum of pressure- and friction forces over the 36 panels representing the upper half-cylinder's surface. This value is then doubled to account for the symmetric lower half of the cylinder, which was not simulated. As can be seen from Tab. 5.4(a),  $F_D$  only weakly depends on the chemistry model used. Comparing the four different cases at  $\text{Kn}_D = 0.04$ , observed deviations between the most extreme values are of approximately 6 %, and at  $\text{Kn}_D = 0.004$  these deviations are on the order of 3 %. Moving to a comparison between the two Knudsen numbers, one can see that increasing the free stream density ten-fold, roughly increases the drag force by a factor of 9. This less-than-proportional increase can be explained by the slight reduction in the skin friction coefficient

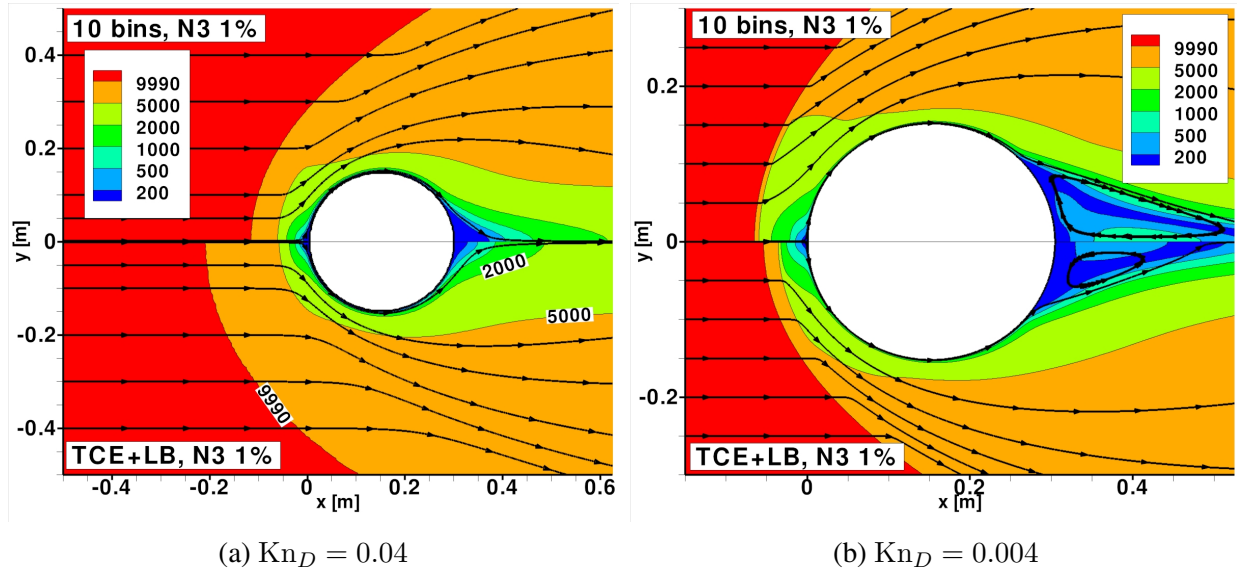


Figure 5.17.: Cylinder in hypersonic cross flow: Comparison between bin model (upper half) and conventional models (lower half) of velocity magnitude  $[\text{m} \cdot \text{s}^{-1}]$  and stream lines

observed when moving from  $\text{Kn}_D = 0.04$ , shown in Fig. 5.16(c) to  $\text{Kn}_D = 0.004$ , shown in Fig. 5.16(d), while the pressure coefficient remains basically unaffected during this change in Knudsen number; (compare Fig. 5.16(a) to Fig. 5.16(b)). The drag, which results as the integrated action of pressure and shear stresses on the surface, therefore is not exactly ten times larger for the lower Knudsen number case. It is noticeable that the predicted drag values in all four simulations are very close to one another. Based on the integrated surface quantities, one can conclude that the chemistry model is of secondary importance for the aerodynamic forces. This is due to the fact that these forces are the result of momentum transfer between the impinging particles and the surface. Therefore, the surface properties embodied by the scattering law, i.e. fully diffuse vs. specular, will be much more influential on this parameter than the precise chemical composition of the flow field. This weak sensitivity of aerodynamic forces to the chemistry model is well-known and is thus not surprising. By contrast, the energy transfer rates towards the wall are more noticeably affected by the particular chemical behavior of the gas-phase.

The heating rate per unit length over the cylinder's whole circumference is given in Tab. 5.4(b). This quantity has been calculated by integrating the wall heat flux distributions over the 36 panels constituting the upper half of the cylinder and doubling the given value. Here a clear trend can be observed when comparing the different simulations. At  $\text{Kn}_D = 0.04$  the highest heating rate is observed when using the bin model with 1 % N in the free stream. This value drops by approximately 2 % with the same model, but with  $x_{\text{N},\infty} = 0.05$ . The conventional models predict slightly higher heating rates. Again, comparing to the bin model with  $x_{\text{N},\infty} = 0.01$ , the equivalent simulation with conventional models shows a significant increase of approximately 68 % in the heating rate, and with a deviation of +32 % an noticeably higher heating rate is also predicted with the conventional model when  $\text{N}_2\text{-N}_2$  dissociation is taken into account. While there definitely is a

Table 5.4.: Cylinder in hypersonic cross flow: Integrated surface parameters

(a) Drag force per unit length  $F_D$  [ $\text{N} \cdot \text{m}^{-1}$ ]

	10 bins		LB+TCE	
$\text{Kn}_D$	<b>N3, 1%</b>	<b>N3, 5%</b>	<b>N3, 1%</b>	<b>full</b>
0.04	114	114	121	120
0.004	1050	1060	1080	1060

(b) Heating rate per unit length  $\dot{Q}$  [ $\text{kW} \cdot \text{m}^{-1}$ ]

	10 bins		LB+TCE	
$\text{Kn}_D$	<b>N3, 1%</b>	<b>N3, 5%</b>	<b>N3, 1%</b>	<b>full</b>
0.04	112	110	188	148
<i>tra</i>	112	110	155	135
<i>int</i>	0	0	33.0	13.0
0.004	302	296	323	232
<i>tra</i>	302	296	306	231
<i>int</i>	0	0	17.0	1.0

(c) Stagnation point heat flux  $q_w$  ( $\theta = 0$ ) [ $\text{kW} \cdot \text{m}^{-2}$ ]

	10 bins		LB+TCE	
$\text{Kn}_D$	<b>N3, 1%</b>	<b>N3, 5%</b>	<b>N3, 1%</b>	<b>full</b>
0.04	381	381	649	536
<i>tra</i>	381	381	535	474
<i>int</i>	0	0	114	62.0
0.004	1090	1080	1260	942
<i>tra</i>	1090	1080	1110	920
<i>int</i>	0	0	150	22.0

trend towards a lower heat transfer rate with increasing degree of dissociation in the gas phase, this is not the only cause for the observed differences in heating rate between the bin- and conventional models. As will be further discussed later in this section, one major cause is likely to be the different internal energy accommodation coefficients being used with the bin model- as opposed to the conventional model simulations. This can be inferred from the heat transfer rates subdivided according to the contributions of translational and internal (i.e. rotational and vibrational) modes. These values are listed in Tab. 5.4(b) in the second- and third rows for each of the two free-stream conditions. As can be seen, for the two bin model simulations listed in the first two columns the contribution of the internal energy modes is exactly zero, consistent with the internal energy accommodation coefficient listed in Tab. 5.1(b). By contrast, the two simulations with the conventional model show that a small fraction of the overall heat transferred to the surface, i.e. 17 % or 9 % respectively, are contributions due to the full accommodation of the internal energy modes. The behavior observed for the higher-density simulations at  $\text{Kn}_D = 0.004$  is slightly more complex. Although the stagnation-point degree of dissociation for the two bin model simulations and the conventional model with 1 % free-stream atomic nitrogen are essentially the same (see the

profiles in Fig. 5.12(d)), the heat transfer rate with the conventional model is about 7 % greater than with the bin model. As can be seen from the sub-division, this difference is caused by the contribution of the internal energy modes. It is thus again a consequence of the differences in the boundary conditions applied in the bin model- as opposed to the conventional model simulations. Finally, in the fourth column the heating rate for the conventional model with both dissociation reactions is listed. Since in this case the flow reaching the surface of the cylinder is practically composed of pure atomic nitrogen, the contribution of the internal energy modes becomes almost negligible. This case also exhibits the overall lowest heating rate, because it has the greatest amount of energy absorbed by dissociation of  $N_2$  when compared to the other cases. In addition to this, one may compare the sets of results for the two distinct free-stream Knudsen numbers in Tab. 5.4(b) to one another. This reveals that increasing the free stream density by a factor of ten only seems to raise the overall surface heating rate by a factor 1.6-2.7. This trend is observed for all four simulations. An explanation for this less-than-proportional increase could be that the increased dissociation rates in the flows at  $Kn_D = 0.004$  are responsible for a smaller fraction of the overall free-stream energy to reach the body's surface. In other words, a larger fraction of the free stream kinetic energy, i.e.  $\frac{1}{2}V_\infty^2$ , would be directly consumed by the endothermic dissociation reactions and would thus be prevented from being released at the surface. This can be observed in Fig. 5.14 when comparing the figures in the upper- and lower rows. Finally the heat flux values near the forward stagnation point are listed in Tab. 5.4(c). Due to the surface discretization into 36 panels for the half-circle, these values effectively represent an average over the 10-degree arc surrounding the stagnation point located at  $\theta = 0^\circ$ . Focusing on the higher free-stream Knudsen number first, the stagnation point heat fluxes predicted for the two bin model cases are identical. Compared to this the neighboring values in Tab. 5.4(c) increase by about 70 % for the conventional model with only N3-dissociation enabled and by 40 % for the conventional model with both dissociation reactions enabled. Thus, the lowest stagnation point heat flux is predicted with the conventional models when  $N_2$ - $N_2$  dissociation is taken into account. A similar trend for the stagnation-point heat flux is observed at the lower free-stream Knudsen number. Again, both simulations using the bin model predict practically the same value, which can be entirely attributed to the translational mode. As before, the highest stagnation point heat flux is predicted with the conventional model with only N3-dissociation enabled, being about 15 % higher than the bin model cases. Incidentally, this added 15 % can be attributed to the exchange of internal energy at the stagnation point. The lowest heat flux is again predicted for the conventional model with both dissociation reactions active, with the internal energy modes only contributing about 3 % to the overall heat flux, due to the almost completely dissociated gas reaching the surface.

The differences in the heat transfer rates between the bin model- and the conventional model simulations warrant some closer examination. In order to obtain a clearer picture, it is useful to examine the separate contributions of the individual species and their respective energy modes. These quantities are plotted in Fig. 5.18 for the free stream conditions where  $Kn_D = 0.04$ . For

simplicity, only the two simulations with N3-dissociation enabled and  $x_{N,\infty} = 0.01$  are compared here. Fig. 5.18(a) shows the  $c_h$ -curves for the individual energy modes obtained with the bin model, while Fig. 5.18(b) shows the corresponding profiles for the LB+TCE models. The individual curves in both images are color-coded in a manner similar to the stagnation line profiles of Fig. 5.14: red stands for the translational energy flux of atomic nitrogen and green for that of  $N_2$ . The solid blue lines represent the net flux of internal (rovibrational) energy of  $N_2$ , while the solid black lines represent the sum of all contributions. These last ones correspond to the same curves already plotted in Fig. 5.16(e) for the bin model and for the LB+TCE models, both with 1 % N in the free stream. Notice that the magenta curves representing the formation energy of atomic nitrogen are missing, because in the present cases the net surface flux of  $e_{f,N}$  is always zero. Since the walls are treated as non-catalytic, the possible heterogeneous recombination reaction  $2N \rightarrow N_2$  does not occur on the surface and nitrogen atoms impinging on the wall never release their formation energy when they are reflected back into the flow. In addition to this, two dashed lines (one blue and one black) are shown in Fig. 5.18(a). The meaning of these lines is explained later in this discussion.

Focusing first on the bin model case, one can see that the contribution of the translational mode of N accounts for approximately 2/3 of the overall heat flux, with the translational mode of  $N_2$  constituting the remainder. This is consistent with the number flux profiles for this same case plotted in Fig. 5.18(c), which reveal that the number of N-atoms impinging on the surface per unit time is about 1.5 times greater than that of the  $N_2$ -molecules. When examining the equivalent values for the conventional models, which are shown in Fig. 5.18(b), one can observe that the contributions of the translational modes of N and  $N_2$  are slightly larger when compared to the bin model. However, here too atomic nitrogen has the highest contribution, with the translational mode of  $N_2$  being second. Again, the contributions of the translational modes to the wall heat flux are consistent with the slightly higher observed number fluxes of both species shown in Fig. 5.18(c). Thus, both species transfer roughly the same amount of translational energy per reflected particle to the wall. The remaining contribution to the heat flux is that of the internal modes of  $N_2$ . Here a stark difference between the two simulations is apparent. While in the conventional models the sum of rotational and vibrational energy contributes about 20 % to the overall heat exchange with the wall, this quantity is exactly zero in the bin model simulation. This discrepancy is not caused by the models themselves, but is rather due to the different boundary conditions applied at the wall in each case. Recall from Tab. 5.1(b) that the internal energy accommodation coefficient used with the bin model was  $\alpha_{\text{int}} = 0$ . Thus, according to this condition all nitrogen molecules impinging on the wall are reflected back into the flow without having their internal bin states updated. As a consequence they exchange no internal energy with the wall, resulting in the flat profile shown in Fig. 5.18(a). By contrast, the internal energy accommodation coefficients used with the conventional models, i.e.  $\alpha_{\text{rot}} = 1$  and  $\alpha_{\text{vib}} = 1$ , cause all impinging  $N_2$ -molecules to be reflected back into the flow with rotational and vibrational quantum numbers according to

Boltzmann distributions at the wall temperature  $T_w = 1000$  K. The net effect of this change is that part of the internal energy of the impinging particles is absorbed by the surface.

Rather than being deliberate, these differences in the boundary conditions applied in both simulations were a consequence of the limited ability to make changes to the source code of RGDAS. Recall from Sec. 5.1 that in order to use a state-to-state description within the existing framework of the RGDAS code, each rovibrational bin  $k$  of  $N_2$  was represented by a completely distinct chemical species. Each one of these species is recognized by the code as a separate mixture component possessing only translational degrees of freedom, regardless of the fact that they represent  $N_2$ -molecules. This allows one to co-opt the existing routines for gas-phase TCE chemistry and particle collisions, while completely ignoring the conventional routines for internal energy exchange based on the Larsen-Borgnakke approach. The internal energy content of molecular nitrogen as a whole is then only determined by the relative amounts of each type of bin present in the mixture, i.e. the ratios  $\bar{n}_k/n_{N_2}$ . When applied to the boundary interaction, this means that within its own conventions RGDAS recognizes the impinging  $N_2$  ( $k$ )-particles as only possessing translational degrees of freedom and reflecting them back into the flow with full accommodation of the translational mode, but without altering their respective species labels. Thus, only zero accommodation of the internal energy modes could occur in this procedure. By contrast, the standard boundary behavior hard-coded into RGDAS assumes that all particles possessing internal energy are reflected back into the flow fully accommodated to the surface temperature, which is what occurs in the case of the LB+TCE model simulations. While it is difficult to determine the precise effect on the entire flow field caused by this inconsistency in the boundary conditions, one may still attempt to estimate the hypothetical amount of internal energy that would be reflected back into the flow, if for the bin model case the internal mode of  $N_2$  were fully accommodated to the wall temperature, thus mimicking  $\alpha_{\text{int}} = 1$ . This quantity was estimated by multiplying the number flux of  $N_2$  shown in Fig. 5.18(c), by the average rovibrational energy of particles emitted from the surface according to a Boltzmann distribution of the bins at  $T_w = 1000$ . The net flux of internal energy, which results in this case is no longer zero and is represented by the dashed blue line in Fig. 5.18(a). This quantity is noticeably greater than zero, suggesting that a wall which fully accommodated the internal modes would experience an overall greater heat flux with the bin model. This hypothetical overall flux is indicated by the black dashed curve in the same plot. As can be seen, this raises the stagnation point heat flux by about 35 % with respect to the value for  $\alpha_{\text{int}} = 0$ . Of course, the current estimate fails to take into account how this change in the boundary conditions would feed back into the gas phase and affect the flow field due to the modified distribution of internal energy states of the reflected  $N_2$ -particles. Hence, the two curves just discussed are labeled with an asterisk behind  $\alpha_{\text{int}} = 1$ , to emphasize their hypothetical nature.

Performing the same analysis for the simulations at the higher free-stream density results in the heat transfer coefficients shown in Fig. 5.19. Again, the bin model results are shown on the left, while the conventional model results are shown on the right. Focusing first on Fig. 5.19(c),

## 5. Application of URVC bin model to atmospheric entry flows

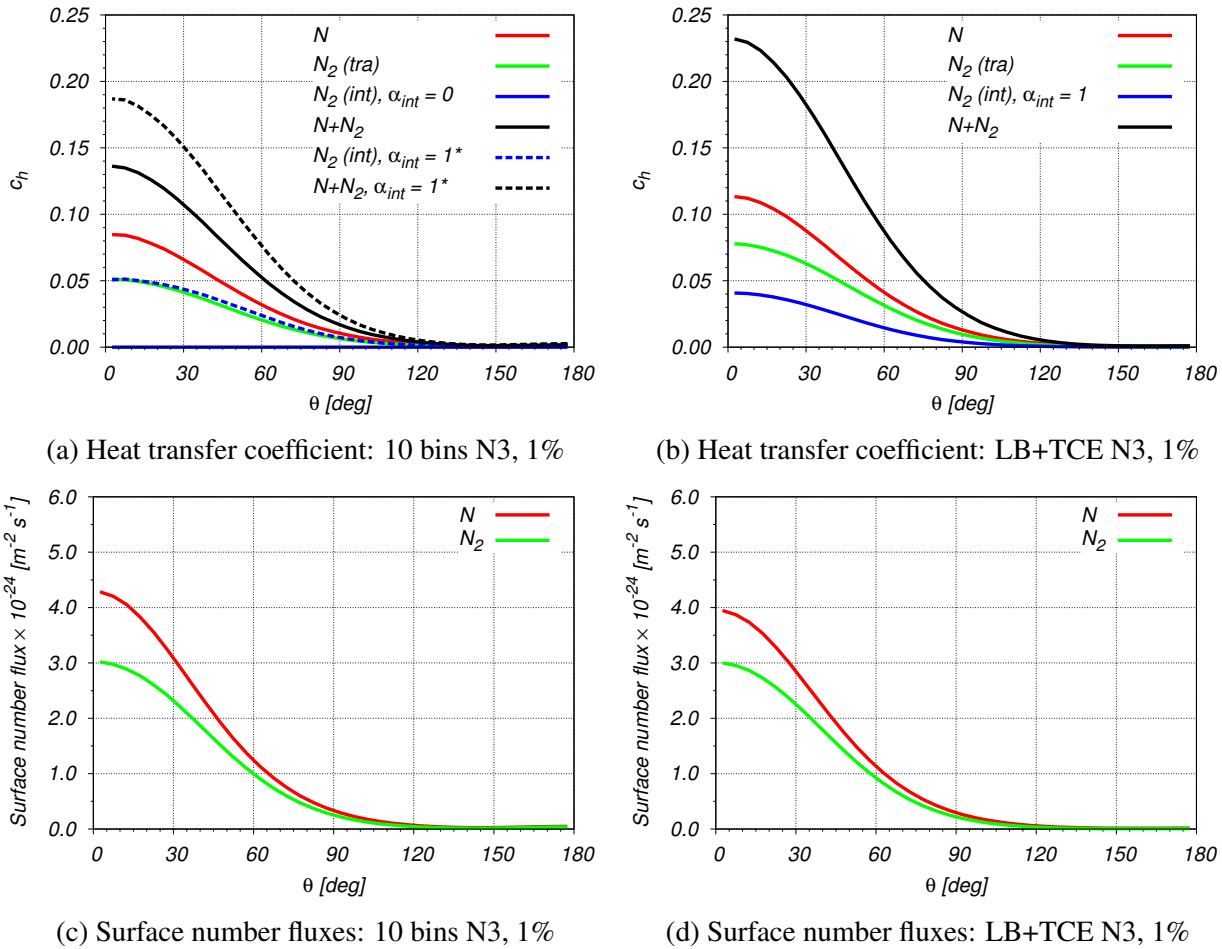


Figure 5.18.: Cylinder in hypersonic cross flow: Detailed contributions to surface heat transfer coefficients (upper row) and surface number fluxes of  $N_2$  and  $N$  (lower row), all at  $Kn_D = 0.04$

one can see that with respect to the lower-density conditions of before the overall number fluxes recorded on the surface are now more than ten times greater. In addition to this the ratio of  $N$ -atoms to molecules of nitrogen is now somewhat different. While in Fig. 5.18(c) about 25 % all of particles impinging on the surface were molecules, now they only amount to about 20 % of the total flux with the bin model, or 10 % in the conventional model case. Certainly this difference can be attributed to the stronger degree of dissociation in the gas phase at these conditions, leaving very few nitrogen molecules in the vicinity of the stagnation point. This is true for the bin model, but the trend is even more pronounced in the comparison calculation done with the conventional models.

This shift towards atomic nitrogen is also reflected in the contributions to the surface heat flux. As can be seen in Fig. 5.19(a), atomic nitrogen is now responsible for about 82 % of the whole heat transferred in the bin model simulations, with the translational mode of  $N_2$  constituting the remainder. Again, due to the particular boundary conditions applied in this case, the internal mode of  $N_2$  does not contribute to the heat transfer at all. However, as was done for the previous case, when estimating the effect a fully accommodating surface would have on the net flux of

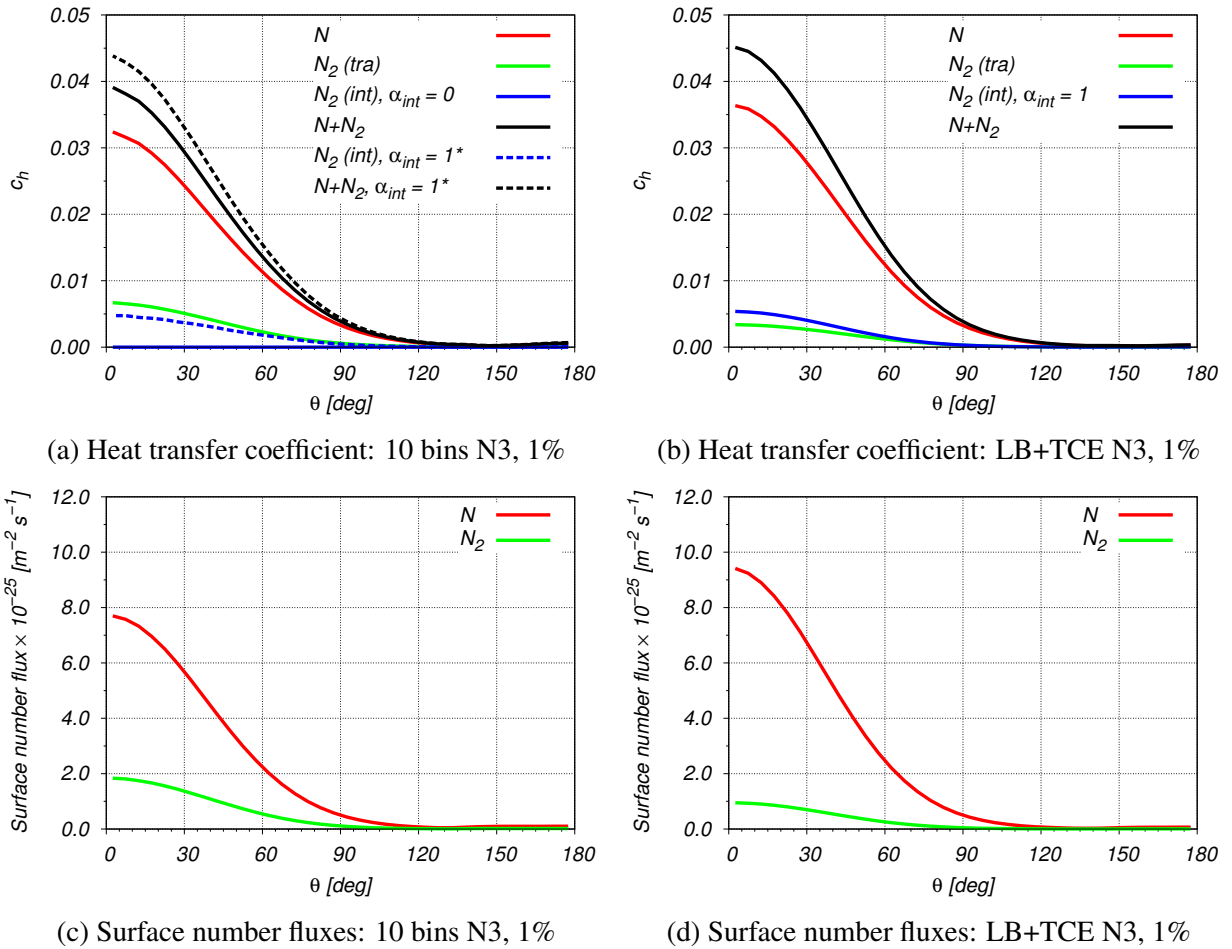


Figure 5.19.: Cylinder in hypersonic cross flow: Detailed contributions to surface heat transfer coefficients (upper row) and surface number fluxes of  $N_2$  and  $N$  (lower row), all at  $Kn_D = 0.004$

internal energy of  $N_2$ , the blue dashed line in Fig. 5.19(a) is obtained. Similar to what was found for the higher free-stream Knudsen number, this hypothetical internal energy flux is comparable to the amount of translational energy of  $N_2$  being exchanged at the wall. However, the overall hypothetical increase in the stagnation point heat flux with respect to the actual results obtained with  $\alpha_{int} = 0$  (dashed vs. solid black line) is only about 13 %. For comparison, in Fig. 5.19(b) the heat flux contributions for the conventional models are shown. In this case the internal modes of  $N_2$  are fully accommodated to the wall temperature, and they contribute an amount to the overall heat flux comparable to that of the translational mode of  $N_2$ . The profiles obtained look fairly close to the hypothetical ones predicted for the bin model in Fig. 5.19(a).

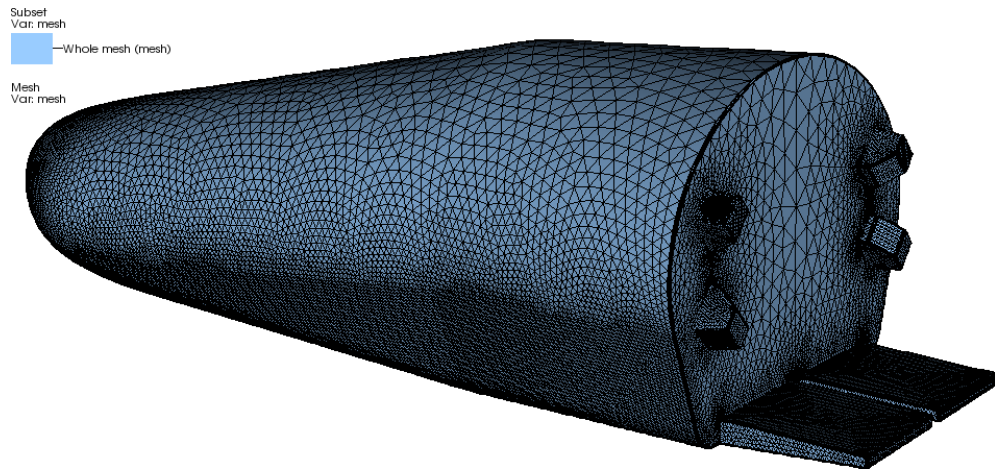
To conclude the discussion of this test case, the main points can be summarized as follows: For the flow conditions simulated in this section one could observe that the bin model predicts both lower degrees of internal energy excitation, as well as slower dissociation of molecular nitrogen when compared the conventional (LB+TCE) models. At the higher free stream Knudsen number considered, this resulted in a delayed generation of atomic nitrogen in the bow shock and only slow excitation of the internal energy modes for the bin model. At the lower Knudsen

number, where the flow conditions approach the continuum regime, stronger chemistry effects are observed in both the bin-model simulations and the equivalent results for the conventional model. However, the slower dissociation rates predicted by the bin model, resulting in an incubation distance along the stagnation stream line, are still apparent.

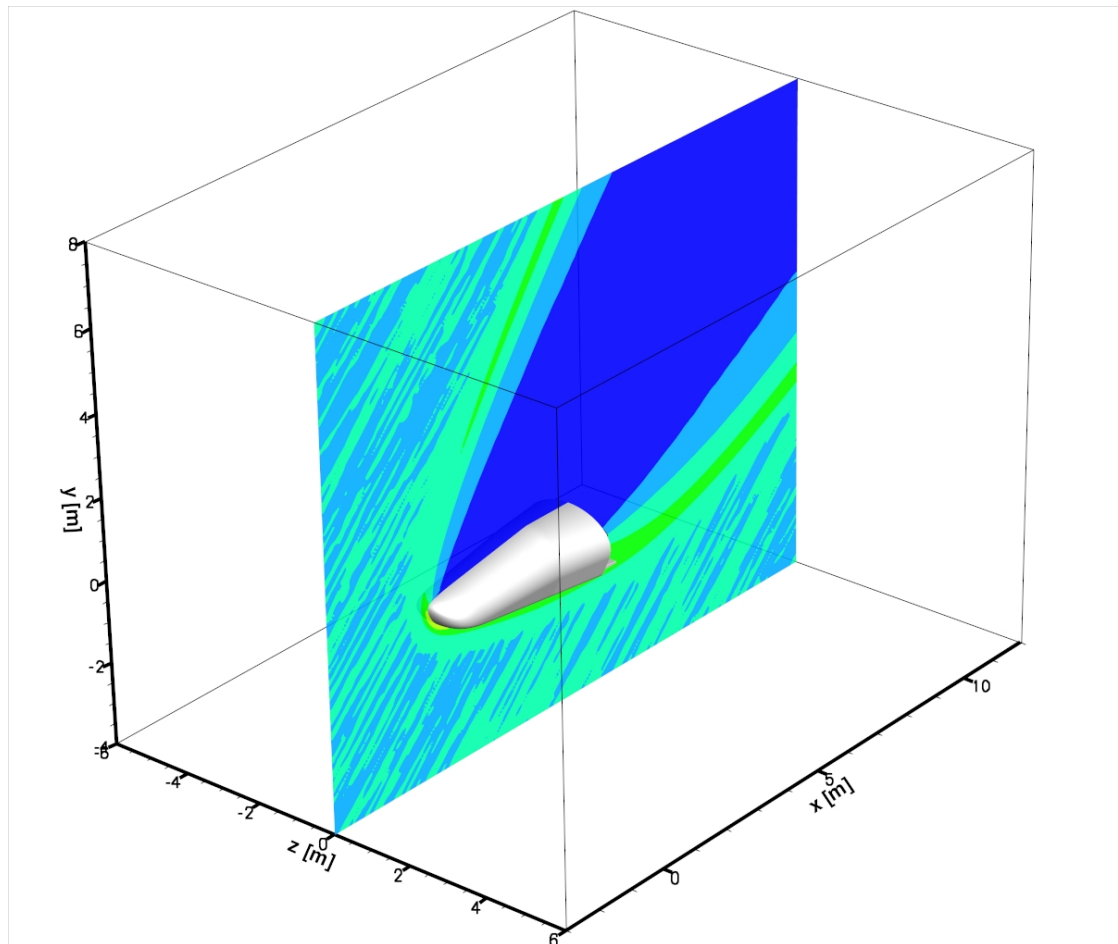
### 5.3. 3D case: IXV in atmospheric entry configuration

After Sec. 5.2, where the behavior of the bin model within RGDAS was studied on a very simple two-dimensional geometry, this section deals with a more realistic flow configuration. In order to demonstrate the viability of the state-to-state bin model in an aerospace engineering application, a flow representative high-altitude re-entry of an existing space craft was simulated. The vehicle in question is called the Intermediate eXperimental Vehicle (IXV). This unmanned vessel was designed for the European Space Agency (ESA) and built by an international consortium led by Thales/Alenia as a technology demonstrator to study several concepts of interest in future orbit return missions: IXV was conceived to study a wingless lifting body configuration, as well as attitude control by aerodynamic control surfaces at high altitudes. Furthermore, several types of reusable and ablative thermal protection systems (TPS) were tested in-flight. It flew successfully on 11 Feb. 2015 and was recovered for analysis after touching down in the Pacific Ocean. The von Karman Institute was involved in pre-flight testing of several reusable TPS materials, in designing the CATalysis Experiment (CATE) [150], as well as in DSMC simulations to assess aerodynamic coefficients in the rarefied and continuum regime [143]. Thus, it was a convenient application for studying the behavior of the URVC bin model.

For the present simulations, the surface mesh, which represents the outer shape of the vehicle, was taken over from this previous work. The mesh is shown in Fig. 5.20(a), with a viewpoint focusing on the stern of the craft. The four small reaction thrusters used for stability control at high altitudes are visible, as are the two separate flaps used for attitude and roll stability at lower altitude. In the 3D version of RGDAS/SMILE, any solid object is represented by such a surface mesh composed of triangular panels. As can be seen here, by using a large number of these panels, the mesh can be made to represent very intricate geometric shapes. This surface mesh is then embedded in a three-dimensional cartesian grid composed of cubic cells. The simulated flow domain with the embedded surface geometry is shown in Fig. 5.20(b). RGDAS/SMILE allows for multiple surface meshes representing separate objects to be loaded simultaneously. This approach allows for a high degree of geometric complexity in the problems to be studied. See, for example, the re-entry simulation involving a whole space station [92]. As was mentioned in Sec. 2.2, RGDAS/SMILE is not the only DSMC package to use this “immersed boundary” approach for geometry representation, and several large-scale DSMC codes in the west were developed using a similar approach.



(a) IXV surface mesh used in RGDAS



(b) Simulation domain with embedded geometry of IXV

Figure 5.20.: IXV surface geometry and simulation domain

The most important simulation parameters are listed in Tab. 5.5. The chosen free stream conditions are meant to approximate Earth's atmosphere at an altitude of  $\approx 100$  km. Of course, these conditions are somewhat artificial, since the gas mixture considered here is entirely composed of nitrogen. The Knudsen number given in Tab. 5.5(a) is calculated based on the free stream mean free path and the reference length,  $L_{\text{ref}}$ , which is close to the vehicle's overall length. The free stream velocity of  $7.45 \text{ km} \cdot \text{s}^{-1}$  is much lower than in Sec. 5.2, and is representative of low earth orbit (LEO) return speeds. This is consistent with the intended mission profile of IXV. For this test case, only a single set of free stream conditions was considered, which is listed in Tab. 5.5(a). Here, the same 10-bin system as in Sec. 5.2 was used, with the free stream containing 1% of atomic nitrogen by molar fraction. Again, this trace amount is added to trigger the inelastic collision processes, which are caused exclusively by  $\text{N}_2(k) + \text{N}$  collisions. Collisions of the type  $\text{N}_2(k) + \text{N}_2(l)$  are assumed as elastic by necessity, and are computed using the VHS model. For comparison purposes, a simulation using the conventional models for inelastic and reactive processes, i.e. LB+TCE, was performed. Unlike Sec. 5.2, the present test case should not be viewed as an exhaustive comparison of the bin- vs. the conventional models. It is rather intended to demonstrate that the bin model can be applied to large-scale 3D DSMC simulations with reasonable computational resources. Therefore, in the only comparison calculation with the conventional models performed for this case, the dissociation reaction due to  $\text{N}_2 + \text{N}_2$ -collisions was kept in, obviating the need of adding atomic nitrogen to the free stream.

The boundary locations of the three-dimensional flow domain are listed in Tab. 5.5(b), and are indicated by the bounding box in Fig. 5.20(b). Even though the side-slip angle of  $0^\circ$  listed in the inflow conditions implies that the steady-state flow field will be symmetric around the mid-plane at  $z = 0$  m, in this test case the full domain was simulated. The vehicle's roll, pitch and yaw axes are aligned with the  $x$ -,  $y$ - and  $z$ -axes used in the domain coordinate system of Fig. 5.20(b), although their orientations differ. The undisturbed free stream enters the domain at an angle of 45 degrees with respect to the  $(x, z)$ -plane. Therefore the windward side with the forward stagnation point is located on the "belly" at the bottom of the vehicle. The domain boundaries were chosen in such a manner as to allow enough space around the vehicle for the bow shock to form at its natural location, as well as to capture most of the rarefaction zone in the vehicle's wake.

The relevant computational parameters are listed in Tab. 5.5(b). As in previous simulations the length of the initial transient phase was estimated by observing the instantaneous particle- and collision counts in the domain over the course of the simulation. In addition to this, unsteady samples of the aerodynamic coefficients were available as a rough indicator of when the steady state had been reached. The number of steady-state sampling steps indicated in Tab. 5.5(b) was constrained by the availability of the high-performance computational resources at the VKI. As can be seen, the domain was sub-divided into 10 million background cells. The resulting background cell size of  $\Delta x^{\text{BG}} = \Delta y^{\text{BG}} = \Delta z^{\text{BG}} = 0.06$  m, although good enough to represent the flow field macroparameters, is not refined enough to resolve the mean free path anywhere in the flow. Thus,

RGDAS's automatic cell refinement routines were necessary to adapt the collision cell sizes all throughout the flow field, including the free-stream region. Since a large number of background cells requires significant amounts of memory to store the flow macroparameter samples, RGDAS allows those background cells which lie on the inside of the surface geometry, to be marked by the indexing algorithm of as "empty". This causes the software to ignore these cells when setting up the cell-based arrays and drastically reduces the overall memory requirements.

Table 5.5.: IXV atmospheric entry: Free stream conditions and simulation parameters

(a) Free stream and boundary conditions

			10 bins <b>N3, 1%</b>	LB+TCE <b>full</b>
$Kn_L$	$\approx 0.008$	$x_{N,\infty}$	0.01	0
$L_{ref}$	4.4 m	$x_{N_2(1),\infty}$	0.99	-
$S_{ref}$	7.26 m <sup>2</sup>	$T_{rot,\infty}$	-	190 K
$V_\infty$	7.45 km/s	$T_{vib,\infty}$	-	190 K
$T_\infty$	190 K	$\alpha_{int}$	0	-
$n_\infty$	$1.0 \times 10^{19} \text{ m}^{-3}$	$\alpha_{rot}$	-	1
Angle of attack	45°	$\alpha_{vib}$	-	1
Slip angle	0°	$T_{wall}$	900 K	900 K

(b) Computational parameters

Time step size	[s]	$1.0 \times 10^{-7}$
Transient steps		100000
Sampling steps		150000
Domain size	[m]	$-3.00 \leq x \leq 12.0$ $-4.0 \leq y \leq 8.0$ $-6.0 \leq z \leq 6.0$
Background cells		$250 \times 200 \times 200$
Simulator particles		$\approx 400 \times 10^6$
Processors		128

Both the simulation using the bin model, as well as the one using the conventional models were run for roughly the same number of time steps. With all particles in the flow domain initialized to the free-stream conditions the flow develops towards its final configuration during the initial transient phase. While the particle count per cell slightly increases due to compression of the gas behind the bow shock and near the stagnation point, the automatic adaptation routines begin to refine the collision grid in those regions. At the final steady state, the number of collision cells had increased to approximately 72 million in both simulations. As would be expected, the majority of these additional collision cells are clustered around the forward stagnation point, where the density rise is most pronounced. After reaching steady state and collecting samples for 150000 consecutive time steps, the time-averaged flow macroparameters and surface fluxes were computed.

Contour plots of the mass density normalized with its free-stream value on the mid-plane are shown in Fig. 5.21. The results for the bin model are shown on the left, in Fig. 5.21(a) and the comparison calculations with the conventional models in Fig. 5.21(b). The color levels in both images represent the same numerical values. As can be seen, the conventional models predict a higher density on the windward side near the stagnation stream point, as well as slightly lower densities in the immediate wake region on the leeward side. It seems that the bow shock is slightly thinner and more closely attached to the body in the simulations with the bin model.

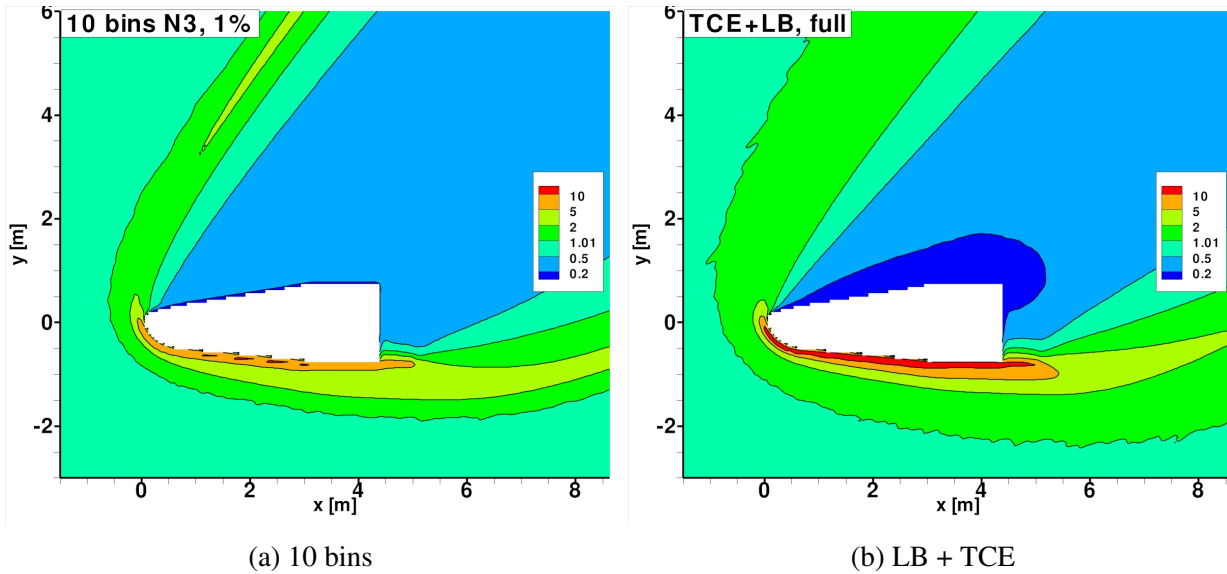


Figure 5.21.: IXV atmospheric entry: density ratio  $\rho/\rho_\infty$  profiles at mid-plane ( $z = 0$ )

Similar behavior is observed when examining the density profiles along successive planes perpendicular to the  $x$ -axis. These are shown in Fig. 5.22. In each case only one-half of the flow domain is shown, since the location  $z = 0$  represents a symmetry plane. All images in the upper row show the density contours extracted from the bin model simulations, while the bottom row shows the equivalent results obtained with the conventional models. The same color legend as in Fig. 5.21(b) is used in all plots, and the position along the  $x$ -axis where each cross section has been extracted, is indicated with each figure. The series of images cover several locations starting near the nose of the vehicle, in Fig. 5.22(a) / Fig. 5.22(e) all the way up to immediately behind the main body in Fig. 5.22(d) / Fig. 5.22(h) respectively. The space occupied by the vehicle itself is shown in white, and in the last two images, one can see a cut through the flaps mounted at the rear of the craft. The general trends observed in Fig. 5.21 are repeated here, with the shock being slightly thinner and more closely attached to the body in the results from the bin model. This is especially noticeable when comparing the last two images, at  $x = 4.00$  and  $x = 4.75$  m.

Moving on to Fig. 5.23, where the translational temperature profiles on the mid-plane are shown, one can observe a behavior consistent with the previous plots for the density. Again, on the left Fig. 5.23(a) shows the results for the bin model, and on the right Fig. 5.23(b) represents the equivalent results for the conventional models. One can see that the region where the translational

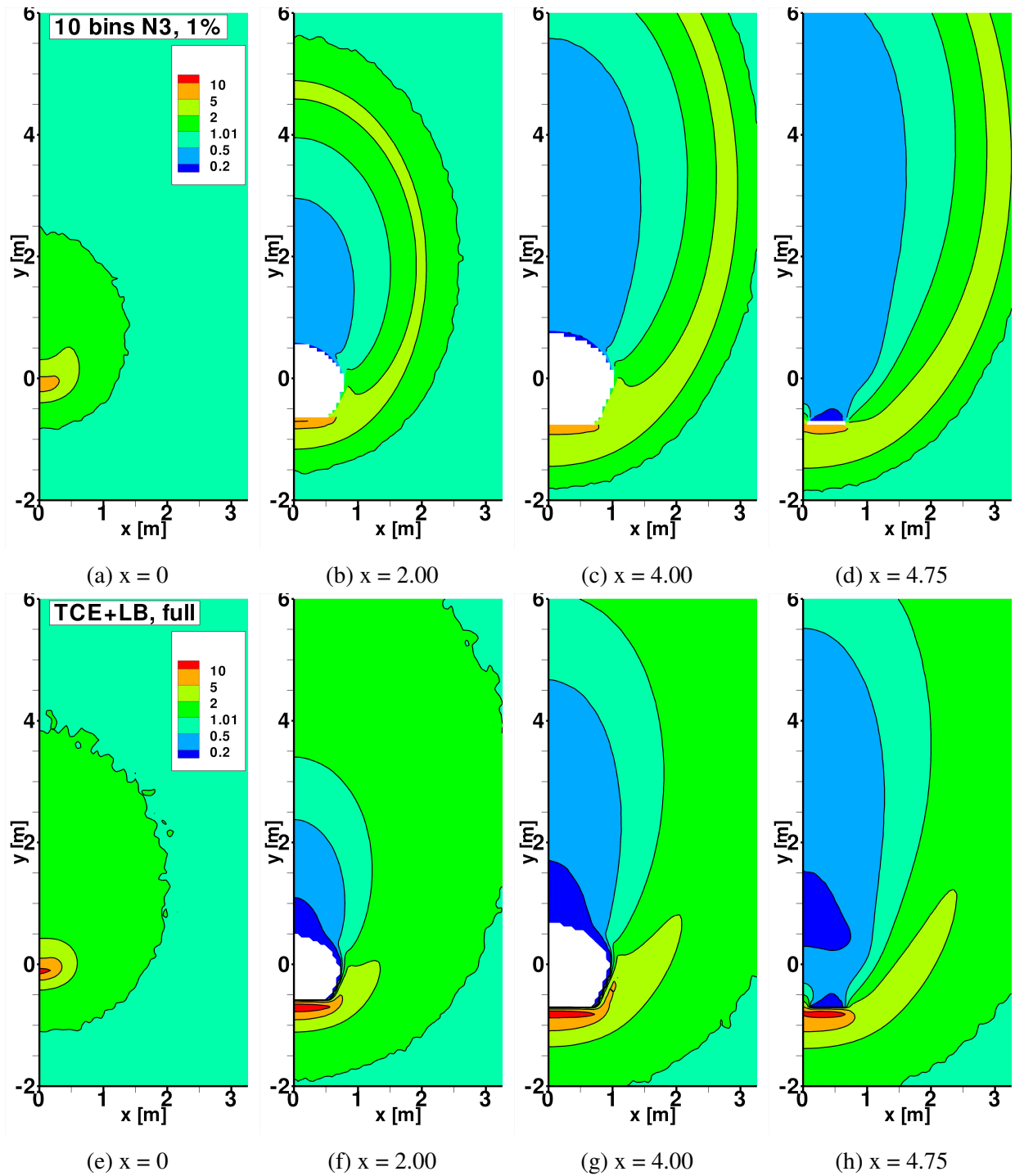


Figure 5.22.: IXV atmospheric entry: density  $[\text{kg} \cdot \text{m}^{-3}]$  profiles perpendicular to longitudinal axis, comparison between bin model (First row) and conventional models (Second row)

temperature surpasses 20000 K on the windward side of the vehicle covers a much wider area in the bin model simulation. The same high temperatures are confined to a much smaller region near the vehicle’s nose in the results with the conventional model.

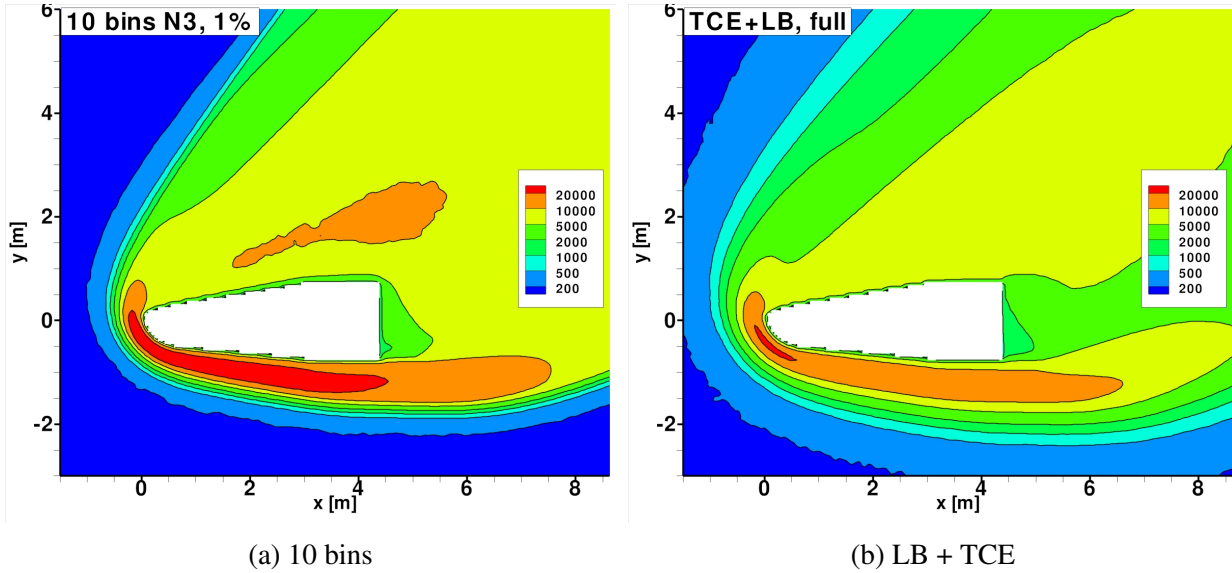


Figure 5.23.: IXV atmospheric entry: translational temperature [K] profiles at mid-plane

The translational temperature fields at the previously shown locations along the  $x$ -axis are shown in Fig. 5.24. The same conventions as before are followed, with the upper row showing half of the temperature field for the bin model, and the lower row showing the equivalent results for the conventional models. As was the case for the plots along the mid-plane, one can observe that  $T$  in the bin model is slightly higher all around the vehicle, but especially in the belly region underneath the body. This higher translational temperature correlates with the lower density observed in Fig. 5.21 and Fig. 5.22 for the bin model, a trend which is consistent with the perfect gas law.

A comparison of the internal mode temperatures of  $N_2$  on the mid-plane is shown in Fig. 5.25. The upper image, i.e. Fig. 5.25(a) shows the internal temperature extracted from the 10 bin populations of  $N_2$ , while Fig. 5.25(b) shows the rotational and Fig. 5.25(c) the vibrational temperature of  $N_2$  obtained with the conventional models. As was the case in Sec. 5.2, direct comparison between the two models is difficult, because the internal temperature of the bin model contains contributions of mixed rovibrational levels, while the rotational and vibrational level contributions are separated in the conventional models.

A curious phenomenon can be observed in Fig. 5.25(a) at the outer edges of the bow shock. There the contours of  $T_{int}$  become highly irregular, and in some areas long “streaks” appear. This is caused by individual simulator particles representing  $N_2$ , which happen to populate higher-than-average bins than the majority of their surrounding counterparts. In the relatively cold regions at the outer edges of the shock, practically all  $N_2$ -particles will populate the lowest-lying bin,

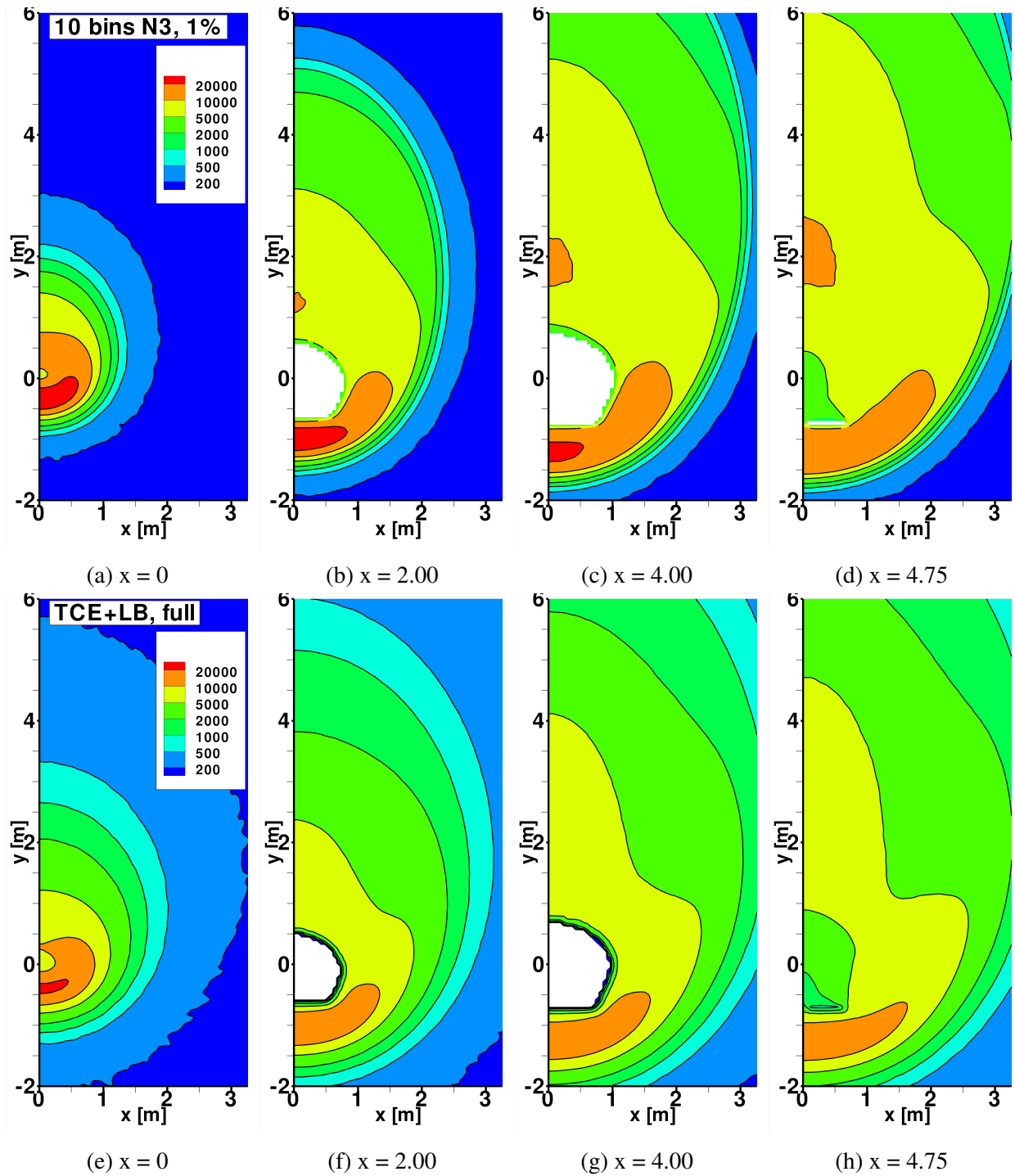


Figure 5.24.: IXV atmospheric entry: translational temperature [K] profiles along longitudinal axis, comparison between bin model (First row) and conventional models (Second row)

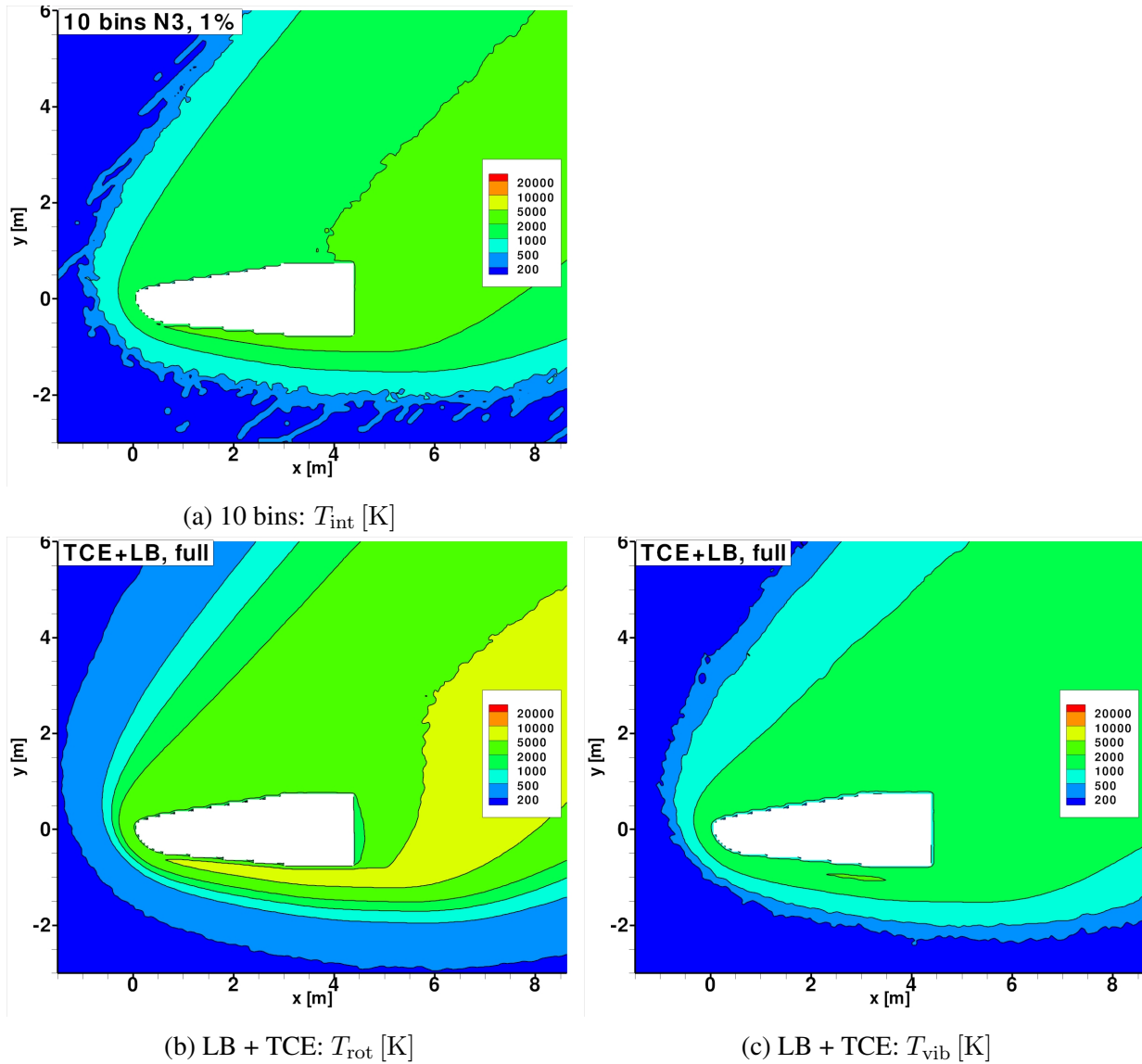


Figure 5.25.: IXV atmospheric entry:  $N_2$  internal mode temperature profiles at mid-plane, Comparison between  $T_{\text{int}}$ , [K] for bin model (First row) vs.  $T_{\text{rot}}$  and  $T_{\text{vib}}$ , [K] for conventional models (Second row)

$k = 1$ , and determination of the internal temperature becomes difficult. Recall from the discussion in Sec. A.3 that  $T_{\text{int}}$  has to be extracted from the local concentrations of  $\text{N}_2(k)$  by solving Eq. (A.35) iteratively. When only one particle in a given cell lies in a higher-energy bin, the internal temperature “jumps” noticeably in that cell. If this particle then moves across several cells without changing its value of  $k$ , it will generate a trace along its path as it moves across the domain. This phenomenon disappears in the higher-temperature regions inside the shock and beyond, because the  $\text{N}_2$ -particles tend to populate a wider range of internal energy bins, allowing for a more accurate representation of the distribution of internal energy states, thus making the determination of  $T_{\text{int}}$  easier. Without any additional changes to the model the only manner to minimize these artifacts would be to continue sampling the flow field for much longer periods, in order to obtain smoother overall temperature profiles. However the sampling phase was constrained by limited accessibility to the computational resources at VKI. In any case, this is a minor detail, which has little influence on the overall results, and is more a matter of aesthetics than anything else. This same issue does not seem to affect the rotational and vibrational temperatures to the same degree, even though they too have been extracted from discrete rotational- and vibrational level populations. Presumably, one reason is that even at the low temperatures at the outer edge of the shock, a greater fraction of the rotational levels, which are based on the rigid rotor approximation, are significantly populated. The vibrational levels of  $\text{N}_2$ , which are based on the anharmonic oscillator approximation, are much more widely spaced than the rotational ones, and below  $\approx 200$  K practically no meaningful temperature signal can be extracted. However, above this threshold the profiles of  $T_{\text{vib}}$  are relatively smooth.

Similar to the previous flow field variables the temperature contours for the internal modes along several transverse planes along the  $x$ -axis are plotted. In Fig. 5.26 profiles of  $T_{\text{int}}$  for the bin model are shown, while Fig. 5.27 shows  $T_{\text{rot}}$  in the upper and  $T_{\text{vib}}$  in the lower row, as extracted from the simulations using the conventional models. As before, the “noisy” contours at the outer edges of the shock are visible in Fig. 5.26(a) to Fig. 5.26(d). Again, it is difficult to make a direct comparison between the two models, because of the differing approaches to partitioning the internal energy modes. In general though, one can observe that the “shock cone” in the bin model results is slightly narrower compared to the conventional model simulations. This is especially noticeable when comparing the figures at the location  $x = 4.75$  m.

Plots of the molar fraction of atomic nitrogen on the mid-plane are shown in Fig. 5.28. The results for the bin model are shown in Fig. 5.28(a) and those obtained with the conventional models in Fig. 5.28(b). Both images make use of the same contour levels, and it is immediately clear that there are significant differences between both results. Contrary to the simulation using the LB+TCE models, the bin model effectively predicts no increase in the concentration of atomic nitrogen anywhere in the flow field. The levels of  $x_{\text{N}}$  remain around the free stream value all throughout the domain. By contrast, the conventional models predict a significant increase in  $x_{\text{N}}$ , reaching nearly 20% in the belly region. Clearly, this rise is caused by the much more vigorous

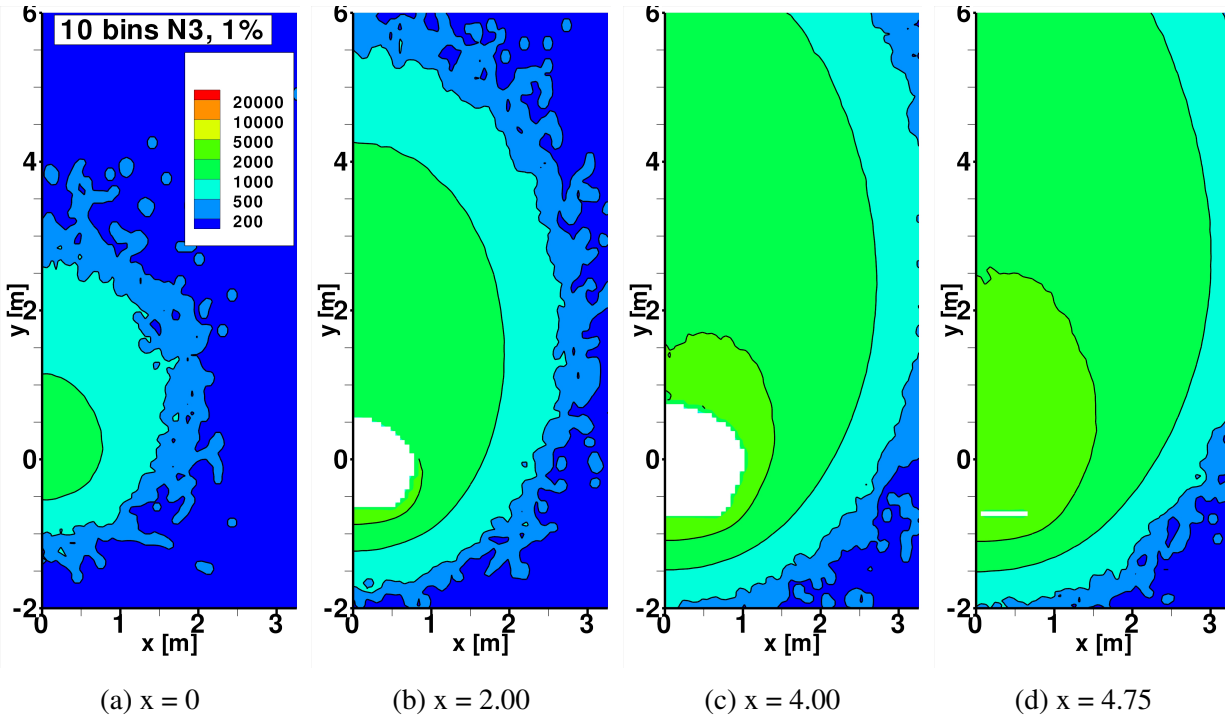


Figure 5.26.: IXV atmospheric entry:  $N_2$  internal mode temperature ( $T_{\text{int}}$  for bin model) profiles perpendicular to longitudinal axis

$N_2$ -dissociation predicted by the TCE reaction rates, which do not consider vibrational favoring. This situation is somewhat similar to what was observed in Sec. 5.2 for the 2D cylinder case with  $\text{Kn}_D = 0.04$ .

At first glance, if one were to only use the Knudsen numbers based on the reference lengths as criterion for characterizing the flow, this result would seem somewhat surprising. For IXV  $\text{Kn}_L \approx 0.008$ , while the Knudsen number based on the cylinder's diameter at the lower-density conditions listed in Tab. 5.1(a) was  $\text{Kn}_D = 0.04$ , which is about an order of magnitude larger. Meanwhile, at the second set of conditions for the 2D cylinder, the Knudsen number was  $\text{Kn}_D = 0.004$  (much closer to the value of this case), and in that situation the bin model predicted a similar degree of dissociation to the LB+TCE models. However, this direct comparison fails to take into account several aspects, which make the present case different from the one discussed in Sec. 5.2. First, with  $7.45 \text{ km/s}$ , the free stream velocity is much lower in this case than the  $10 \text{ km/s}$  used in the cylinder simulations. This means that, on average, the collisions occurring in the bow shock- and stagnation point region tend to be less energetic, and are thus less likely to overcome the dissociation threshold. This would explain why the maximum  $x_N$  near the stagnation point predicted by the LB+TCE models is only  $0.2$ , and not closer to  $0.5$ , as was predicted in the cylinder case. The second aspect again concerns the fact that the Knudsen numbers just quoted are all based on global reference quantities, identifying the test case as a whole, and not on the local gradient lengths and conditions in the flow field. In particular, the characteristic length scale used here was quite arbitrarily chosen to be the overall length of the vehicle, while in Sec. 5.2

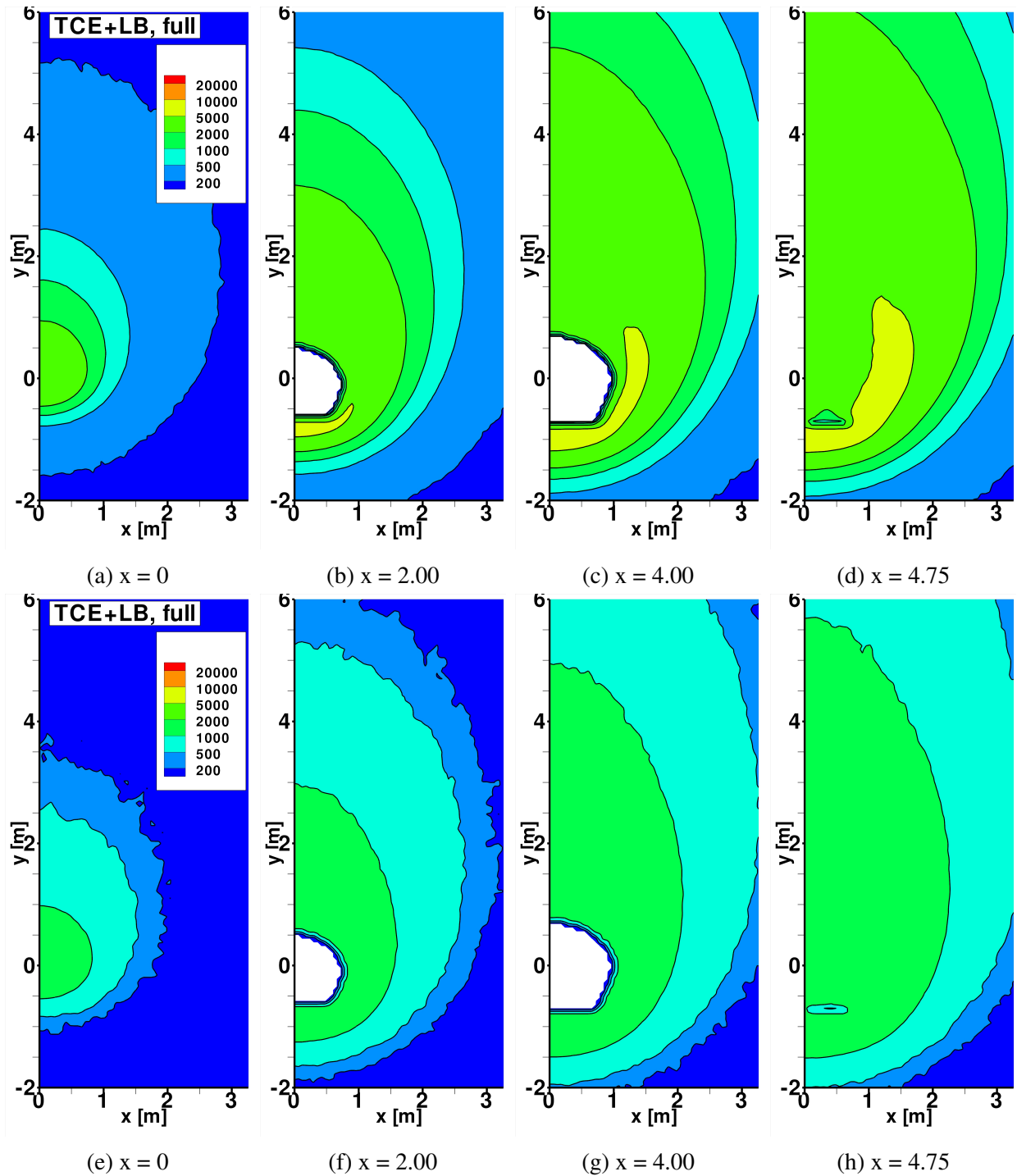


Figure 5.27.: IXV atmospheric entry:  $N_2$  internal mode temperature profiles perpendicular to longitudinal axis, Comparison between  $T_{rot}$  (First row) and  $T_{vib}$ , [K] for conventional models (Second row)

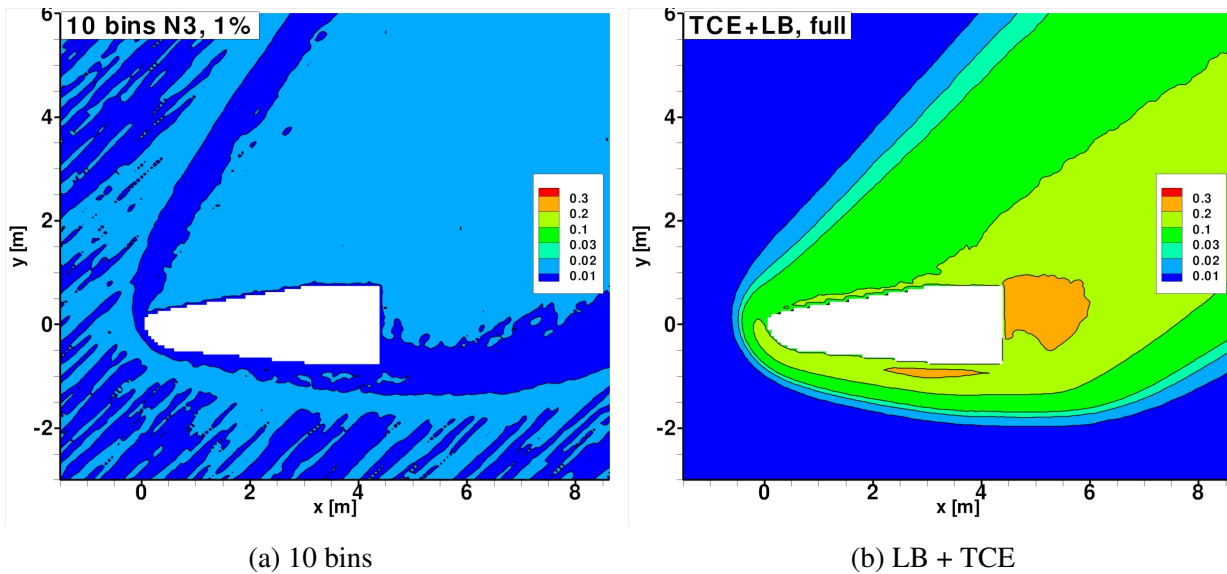


Figure 5.28.: IXV atmospheric entry: mole fraction of atomic nitrogen at mid-plane

the cylinder diameter was used. Using the vehicle’s length can be misleading and cause one to assume that the flow overall is more “continuum-like” than it actually is, since this is practically the largest dimension of relevance in this problem. Recall that this issue was previously examined in Sec. 5.2 while discussing the behavior along the stagnation stream line for the cylinder test case (see Fig. 5.15). There the local density-gradient-based Knudsen numbers suggested departure from continuum conditions for the lower-density free stream conditions, where  $Kn_D = 0.04$ . Further ahead in this section a similar analysis is performed for the present test case (refer to Fig. 5.34), where comparably large values of the local Knudsen number are observed. Finally, a third difference between the 2D cylinder and the present IXV case is the fact that here the flow field is three-dimensional. Therefore, the so-called 3D-relieving effect comes into play, which means that compared to the cylinder of infinite extent along the  $z$ -axis, IXV presents a much smaller cross section to the free stream and therefore has a weaker blocking effect on the incoming flow. As a result, the deceleration of the gas is less severe, and so is the compression of the gas near the forward stagnation point when compared to the 2D cylinder. Thus, the fraction of collisions with high enough energies to cause dissociation will tend to be smaller in the present case.

As with the previous flow field quantities, in Fig. 5.29 the molar fraction of atomic nitrogen is plotted on several transverse planes along the  $x$ -axis. As was seen for the mid-plane in Fig. 5.28(a) the bin model predicts no significant rise in  $x_N$  with respect to the free-stream value. However, the contour plots shown in Fig. 5.29(a) to Fig. 5.29(d) do reveal the rough location of the bow shock by a slight increase in the concentration of atomic nitrogen. The results obtained with the conventional models are shown in Fig. 5.29(e) to Fig. 5.29(h). In general, the molar fraction of atomic nitrogen in the wake behind the vehicle is comparatively high. Peak values of  $x_N > 0.2$  are observed in Fig. 5.29(h) near the vehicle’s stern, immediately above the flaps. Incidentally,

similar diffusion of atomic nitrogen into the low-velocity regions immediately behind the body could also be observed for the cylinder in Sec. 5.2 (see, the lower half of Fig. 5.11(a)). Thus, the effect is opposite to what occurs near the forward stagnation point, where it is  $N_2$  that tends to accumulate.

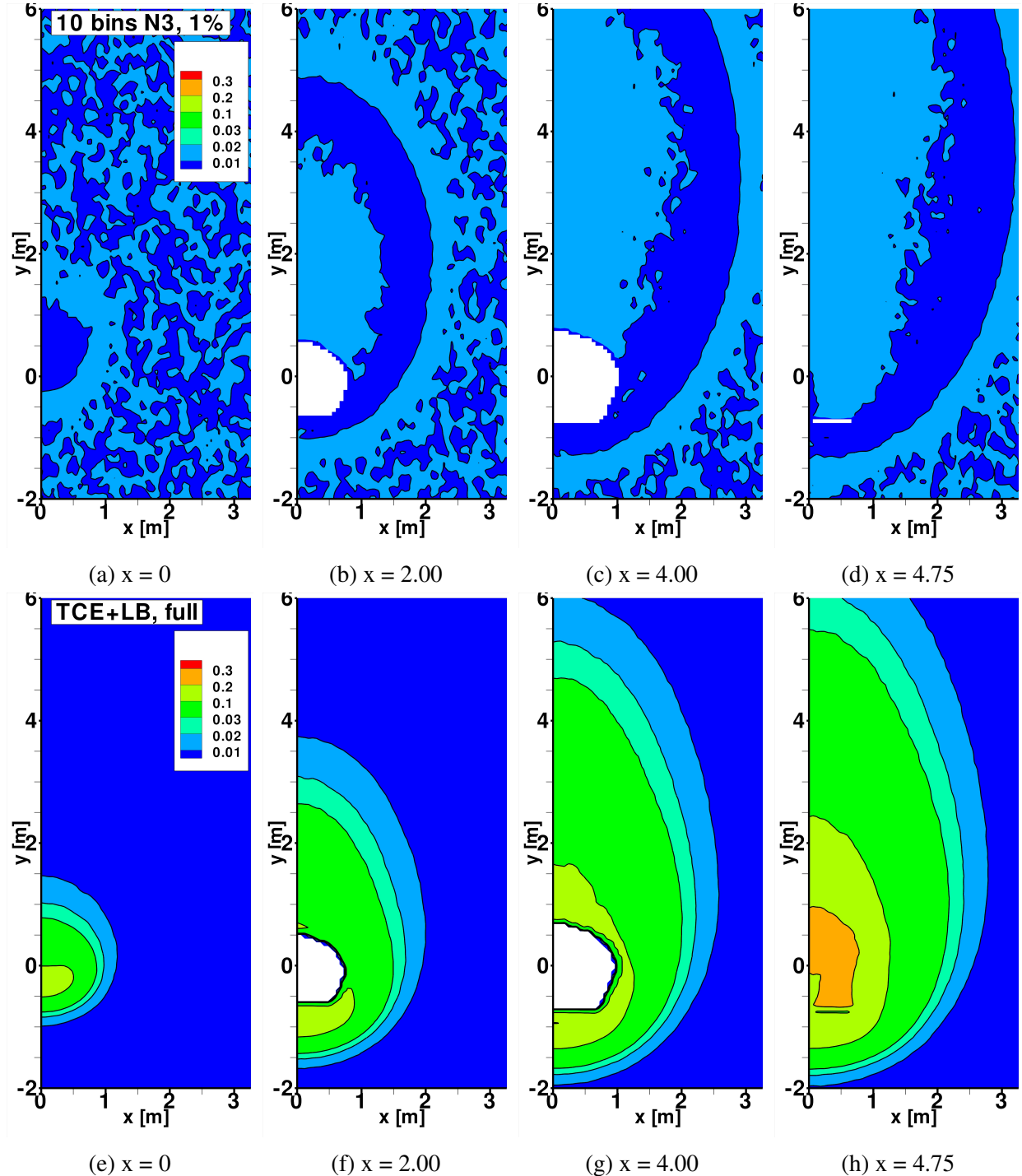


Figure 5.29.: IXV atmospheric entry: mole fraction of atomic nitrogen profiles perpendicular to longitudinal axis, comparison between bin model (First row) and conventional models (Second row)

The magnitude of the velocity on the mid-plane is shown in Fig. 5.30(a) for the bin model, and

the equivalent results for the conventional models are shown in Fig. 5.30(b). At first glance, no major differences between the two results can be noticed. Only after closer examination do small differences in the precise locations and shapes of the velocity contours become apparent. Using the contour at  $7400 \text{ m} \cdot \text{s}^{-1}$  as the arbitrary boundary of the bow shock, one can again determine that the shock cone is slightly “narrower” in the bin model results than with the conventional models. In addition to the velocity magnitude itself, several stream lines on the symmetry plane are shown. These allow to visually narrow down the position of the forward stagnation point stream line. In both simulations this is an approximately straight line extending from the inflow boundary at  $x = -3 \text{ m}$ ,  $y = -3.55 \text{ m}$ , directly towards the stagnation point on the vehicle’s surface. This makes it relatively easy to extract the relevant flow parameters along this line for closer inspection. Again, the precise location of the stagnation stream line does not seem to be severely affected by which of the two models is used.

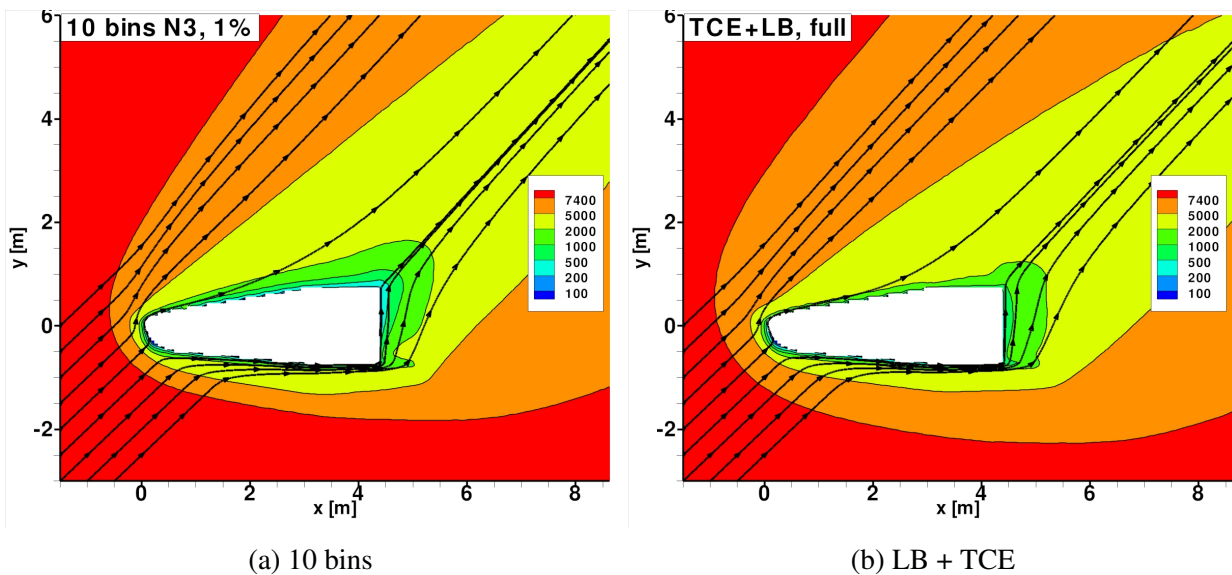


Figure 5.30.: IXV atmospheric entry: velocity magnitude  $[\text{m} \cdot \text{s}^{-1}]$  and stream lines at mid-plane

As with the other flow macroparameters, the velocity magnitude in transverse planes along the  $x$ -axis is plotted in Fig. 5.31. The upper row contains the flow fields for the bin model, while the lower row shows the equivalent plots for the conventional models. Apart from the slightly wider shock cone predicted with the conventional models no major differences can be observed. The high-speed flow across the narrow gap between the two flaps can be seen for both models in Fig. 5.31(d) and Fig. 5.31(h) respectively. Although the stream lines in these planes are not visible, the regions behind the flaps may contain small recirculation zones.

The flow macroparameters along the forward stagnation stream line were extracted from the flow fields and are shown in Fig. 5.32. The abscissa  $s$  in these plots measures the (negative) distance upstream of the stagnation point, which itself is located at  $s \approx 0 \text{ m}$ . It should be noted that due to the immersed-boundary approach used in RGDAS, some of the background cells near the body are partially occupied by the flow, but also by the vehicle’s body. Since flow macroparameters

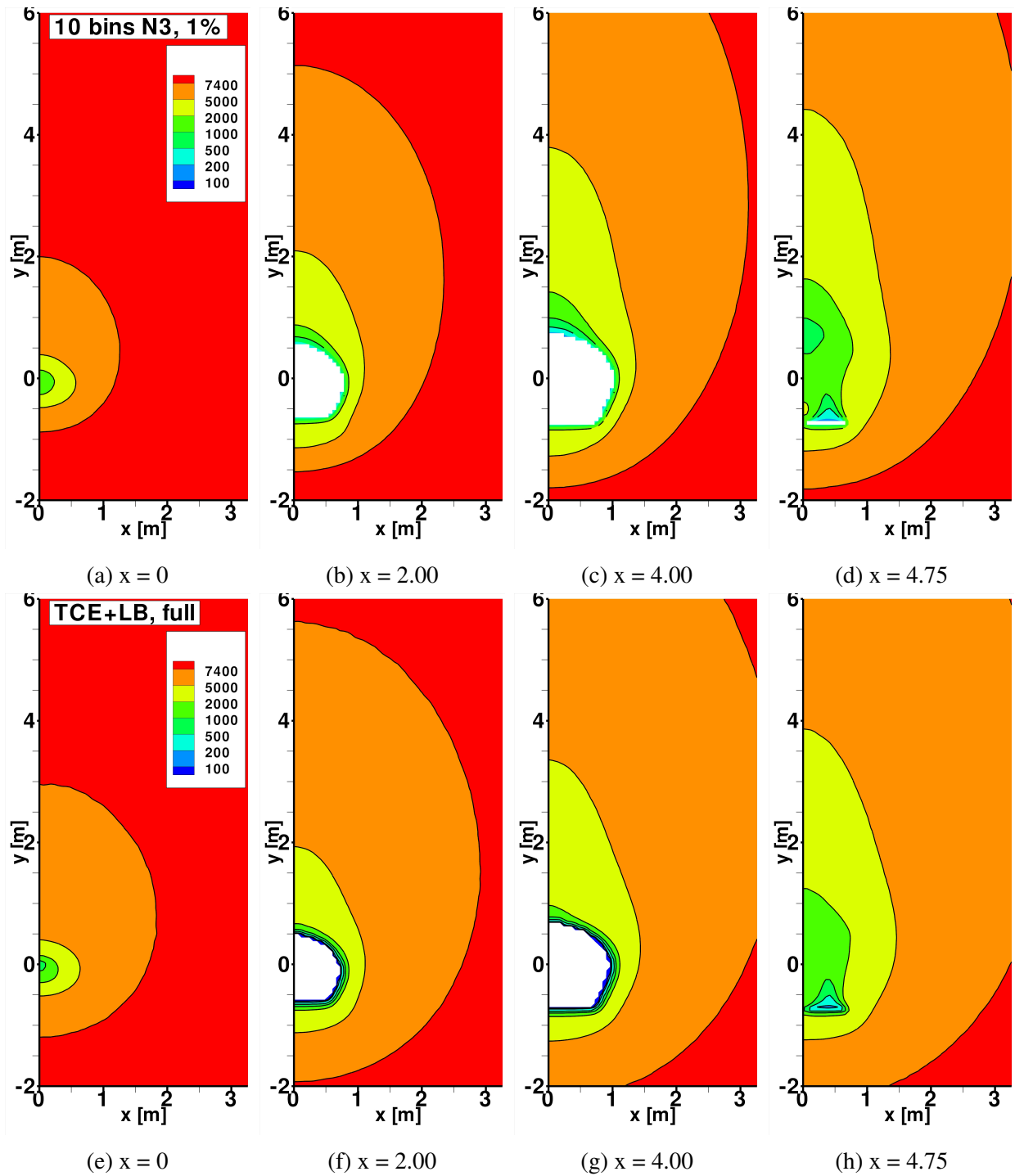


Figure 5.31.: IXV atmospheric entry: velocity magnitude  $[m \cdot s^{-1}]$  profiles perpendicular to longitudinal axis, comparison between bin model (first row) and conventional models (second row)

## 5. Application of URVC bin model to atmospheric entry flows

are always shown as averages over the whole cell, the representation of the flow field in these regions is not fully accurate. Therefore, the exact location of the stagnation point is somewhat ambiguous. Nevertheless, a comparison of the density profiles for both simulations is shown in Fig. 5.32(a). The shapes of these profiles exhibit all the features of a diffuse compression region ahead of the vehicle's surface, which is characteristic of highly rarefied flow. With neither model can a clear distinction between the density rise across the bow shock and the subsequent compression near the stagnation point be made. Globally speaking, the density ratios along the stagnation stream line, as predicted by the bin model, are slightly lower than those predicted by the conventional models. This fact is consistent with the corresponding inverse behavior of the translational temperature.

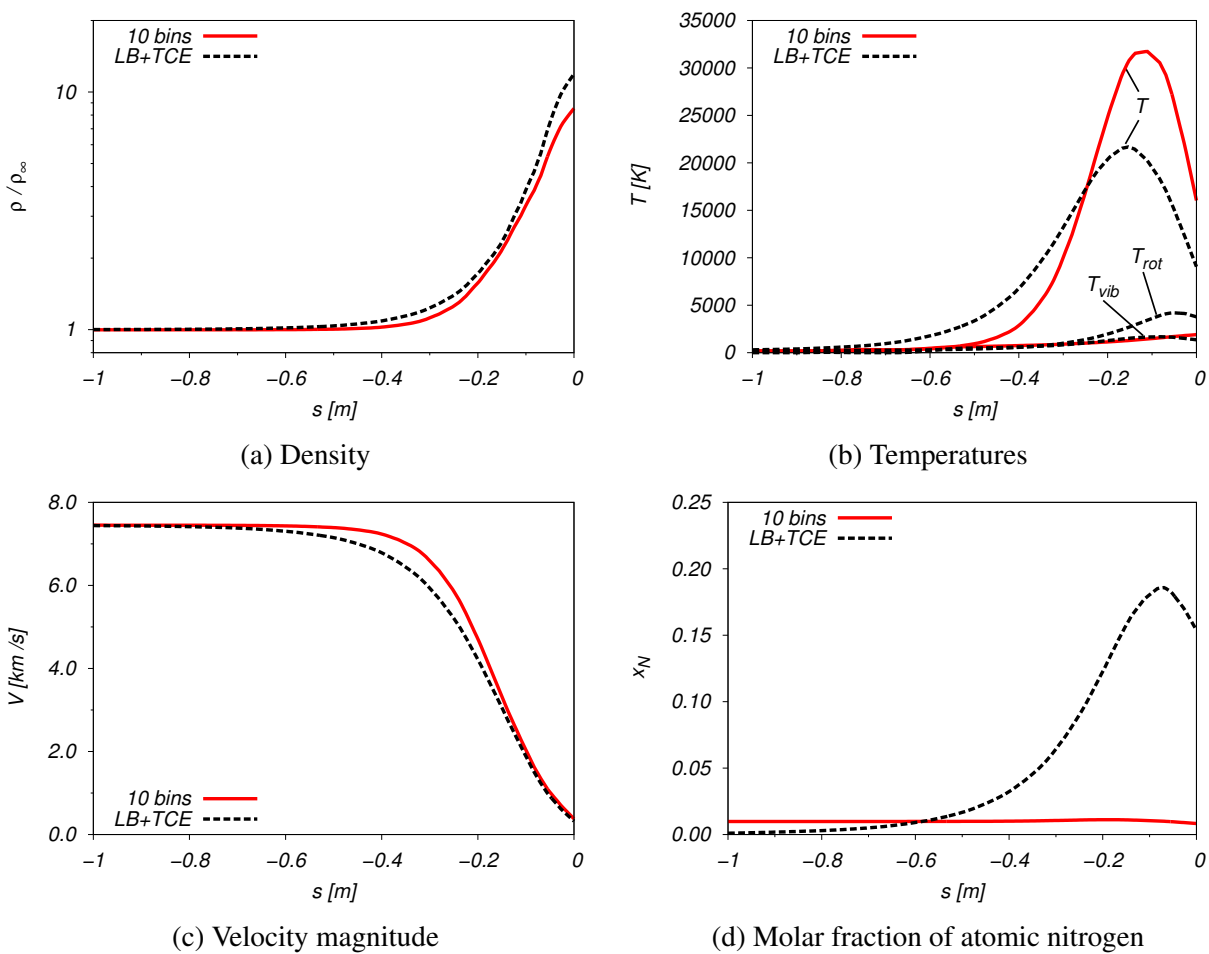


Figure 5.32.: IXV atmospheric entry: flow macroparameters on stagnation stream line. Red solid lines: bin model, black dashed lines: conventional models

The temperature profiles along the stagnation stream line are plotted in Fig. 5.32(b). In addition to the translational temperature, the internal temperature of  $N_2$  is plotted for the bin model, while  $T_{rot}$  and  $T_{vib}$  are plotted for the conventional models. Focusing on the bin model first, one can see that  $T$  and  $T_{int}$  remain separate along the stagnation stream line and do not reach a common value before reaching the stagnation point itself. These profiles reinforce the perception that the flow at

these conditions is highly rarefied, and due the low collision rate in the gas the internal and translational modes do not have enough time to equilibrate. Thus, no clear post-shock equilibrium temperature can be observed. The discrepancies between the translational and internal energy modes seem less severe in the conventional model results. Nevertheless, a high degree of thermal nonequilibrium is still apparent: While the rotational temperature of  $N_2$  begins to approach  $T$  slightly ahead of the stagnation point, the vibrational mode is too slow to relax towards the common temperature over the whole length. The trends observed here are even more extreme than the behavior in Sec. 5.2, where the bin model was also seen to lead to much slower excitation of the internal modes compared to the conventional models. Again, the fact that the rotational and vibrational levels are mixed within the bins, whereas they are treated as separate in the conventional models, partially explains the particularly slow rise in  $T_{\text{int}}$  across the shock. The most striking difference though is probably in the peak values of  $T$  predicted by the two models. With the bin model the highest translational temperature lies around 32000 K, while with the conventional models it is roughly 10000 K lower. Thus, in the bin model a much greater fraction of the energy remains in the translational mode. This difference is most likely caused by the widely differing degrees of dissociation of  $N_2$  predicted by the two models. In Fig. 5.32(d), the concentration of atomic nitrogen along the stagnation stream line is plotted. Whereas no dissociation is predicted with the bin model, the conventional model predicts peak values of  $x_N \approx 0.2$  ahead of the stagnation point. Since the dissociation of  $N_2$  is an endothermic reaction, this would help to explain the lower translational temperatures predicted by the conventional models. This interpretation can be supported by examining the contributions of the different species' energy modes to the overall energy of the flow. Recall that a similar approach was taken in Sec. 5.2. In Fig. 5.33 the specific energies of the two mixture components, along with the flow kinetic energy and the total enthalpy are plotted along the stagnation stream line. Focusing first on the bin model in Fig. 5.33(a), one can see that the translational mode of  $N_2$  absorbs practically all of the initial energy released by the flow, as it is decelerated through the diffuse compression region. By contrast, the contribution of the internal energy mode of  $N_2$  does not increase noticeably along the stagnation stream line. Since dissociation is practically nonexistent in the bin model, the contributions of atomic nitrogen to the total enthalpy remain negligible. For the conventional models shown in Fig. 5.33(b), the behavior is slightly different. Here, a much greater portion of the flow kinetic energy is being diverted directly into the translational mode and formation energy of atomic nitrogen. As a consequence, the relative contribution of the translational energy of  $N_2$  is smaller than in the bin model case. In addition to this, one can observe that with  $h_0 \approx 12$  MJ/kg the total enthalpy at the stagnation point is slightly higher in the bin model case, as compared to  $h_0 \approx 10$  MJ/kg for the conventional model case. This discrepancy can be attributed in part to differences in the flow fields surrounding the vehicle, but may also be caused by the differing internal energy accommodation coefficients used with the two models (see Tab. 5.5(a)).

Overall, one can observe that the compression region ahead of the vehicle predicted with the con-

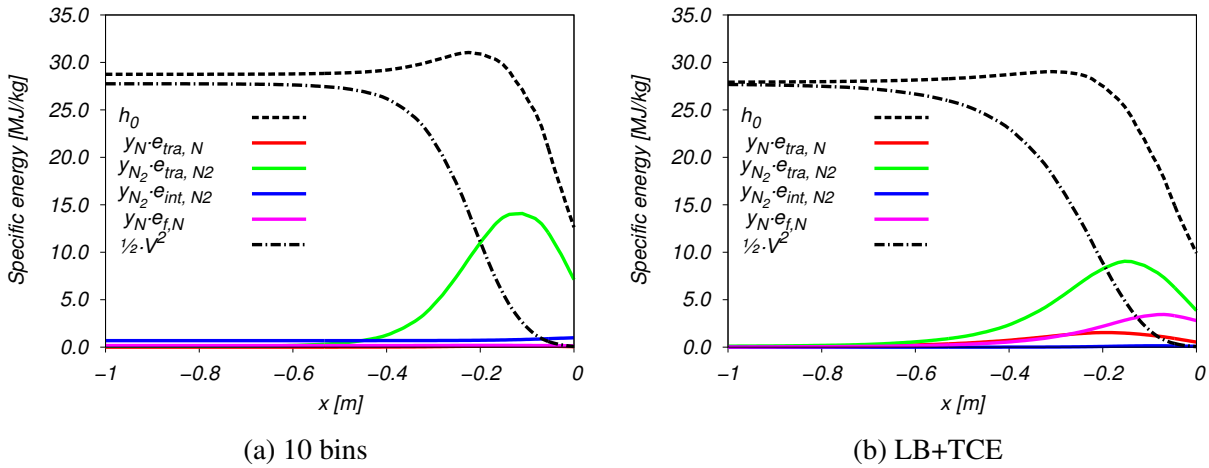


Figure 5.33.: IXV atmospheric entry: contributions to specific energy along stagnation stream line; comparison between bin model (left) and LB+TCE models (right)

ventional models is slightly wider and more diffuse. This can also be appreciated by comparing the velocity magnitude along the stagnation stream line, shown in Fig. 5.32(c). However, with both models the flow is highly rarefied, and the profiles are far from the clearly defined structure that would be expected in the continuum regime (as may be suggested by the global length-based Knudsen number of  $Kn_L = 0.008$ ). As was done in Sec. 5.2, it is thus worthwhile to determine the local Knudsen numbers, evaluated according to Eq. (5.10), along the stagnation stream line. These profiles are shown for both models in Fig. 5.34. Along with the curves of  $Kn_{GLL, \rho}$  the threshold for continuum breakdown suggested by Boyd et al. [149] is shown as a blue dotted line. One can see that especially in the interval  $-0.7 \text{ m} \leq s \leq 0 \text{ m}$  the flow exhibits strong departure from continuum conditions and the local Knudsen numbers even surpass those found for the 2D cylinder case at the lower-density free stream conditions (recall Fig. 5.15(a)). The diffuse shock structure and relative lack of chemical activity thus become less surprising. It should also be noted that the free stream values listed in Tab. 5.5(b) are meant to roughly correspond to Earth atmospheric conditions at approximately 100 km (of course, without oxygen). At such high altitudes, the flow around vehicles of comparable size to IXV is known to be highly rarefied [45].

Finally, in order to better assess the differing influence of the two chemistry models on the aerodynamic forces and heat loads on the vehicle itself, the surface distributions are examined more closely. First, plots of the pressure distribution on the vehicle's surface are shown in Fig. 5.35. All values are reported as normalized pressure coefficients, computed according to Eq. (5.11). In addition to pressure coefficient contours, skin friction lines have been drawn on the surface to help determine the position of separation points. The plot of Fig. 5.35(a) shows the pressure distribution with the bin model on the front and bottom of the vehicle, i.e. the side which faces the incoming free stream, while Fig. 5.35(b) shows the equivalent results for the conventional models.

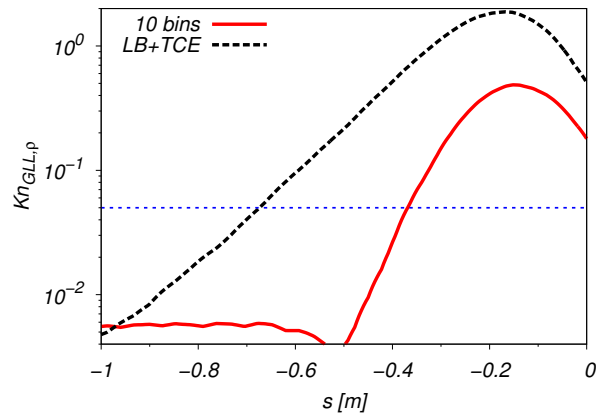


Figure 5.34.: IXV atmospheric entry: comparison of density gradient-based local Knudsen number along stagnation stream line

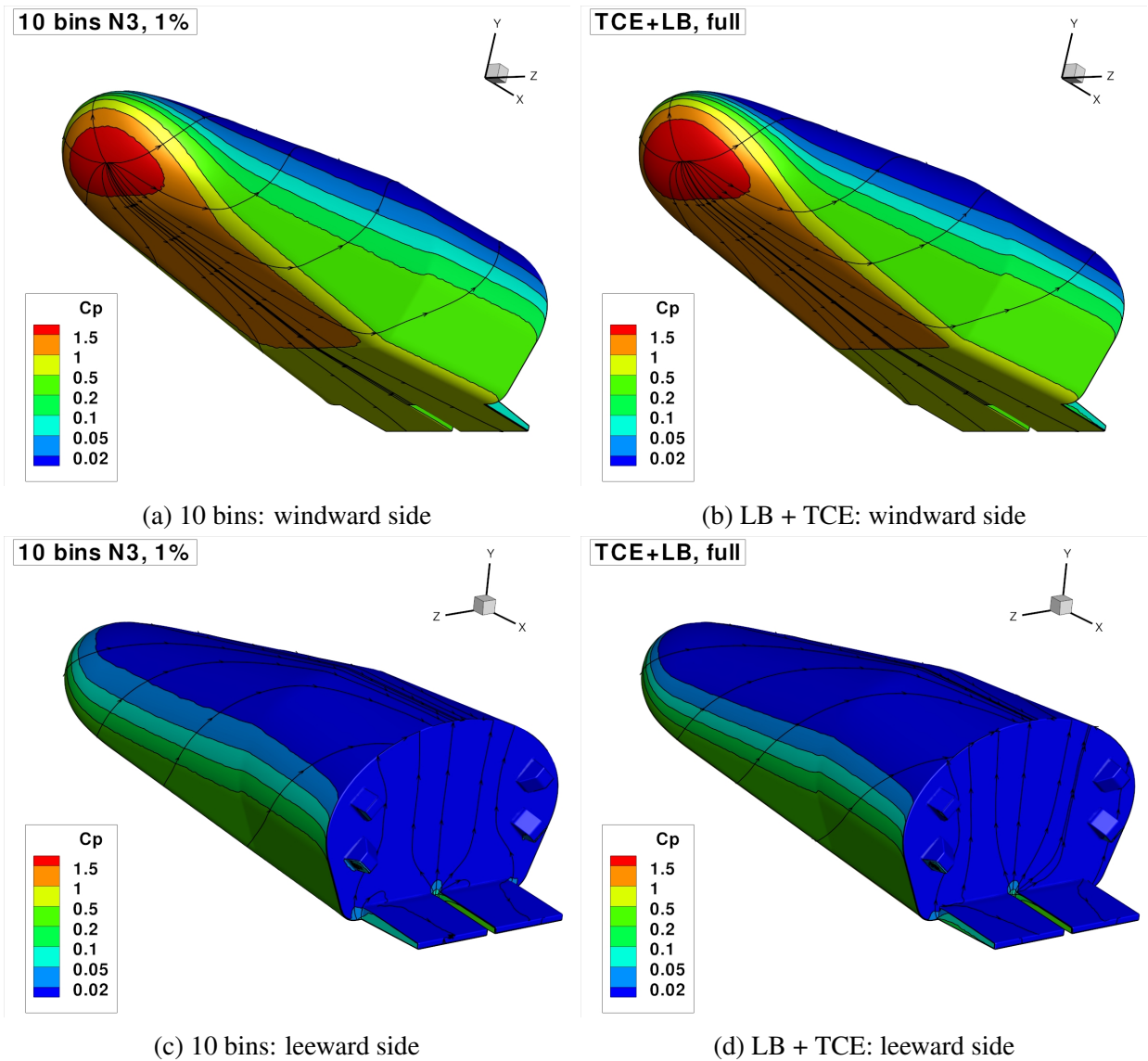


Figure 5.35.: IXV atmospheric entry: profiles of surface pressure coefficient. First row: windward side, second row: leeward side

As can be seen, the skin friction lines show only slight deviations between the two simulations. The forward stagnation point is clearly visible, and its position is not noticeably affected by the choice of the model. Overall, the pressure contours seem to be very similar in both cases, and the only major difference is the slightly higher pressure region  $c_p > 1.5$  surrounding the stagnation point in the conventional model. The pressure distributions on the rear part of the vehicle are shown in Fig. 5.35(c) for the bin model, and Fig. 5.35(d) for the conventional models. Again, there seem to be no major differences between the two models when it comes to the pressure contours. Compared to the values at the front, the pressure acting on the rear is practically negligible. In addition to the density profiles of Fig. 5.21 and Fig. 5.22, this is another indication of the highly rarefied conditions prevalent in the wake. The orientation of the skin friction lines gives an indication of the flow field that develops in this region. The small gap between the two flaps allows for gas to slip through at high speeds and to flow upwards along the rear wall of the vehicle. The sharp edge on the upper rear side of the vehicle serves as a natural point for flow separation. Closer examination of this region reveals two points symmetrically located on the semi-circular edge, where the skin friction lines converge from the rear and upper side of the vehicle, and these constitute separation points. Similarly, additional flow separation points are found on the rear edges of the two flaps. It should be noted that, due to the expansion of the gas in the region shielded by the vehicle, the density drops even below the free stream value. For the DSMC simulations this directly implies a much lower number of simulator particles present in this region. Consequently, their rate of impact on the surface is much lower, and the statistically averaged surface quantities are less certain in this region. This means that surface distributions will be much more “noisy”, and skin friction lines will be less accurate than in the dense regions at the front of the vehicle.

Profiles of the skin friction coefficient, also defined in Eq. (5.11), are shown for the front part of the vehicle, in Fig. 5.36(a) using the bin model, and in Fig. 5.36(b) using the conventional models. Here, the differences between the two models are more noticeable. Whereas the location of the forward stagnation point remains the same, with the conventional models a significantly higher shear stress is predicted along much of the lower part of the vehicle. By contrast, the skin friction contours on the top of the vehicle, shown in Fig. 5.36(c) for the bin model and in Fig. 5.36(d) for the conventional models, reveal that the shear stress is slightly higher with the bin model than with the conventional one. However, the absolute  $c_f$ -values are much smaller than those on the windward side.

Finally, the surface heat flux on the front of the vehicle, normalized as per Eq. (5.11), is shown in Fig. 5.37(a) for the bin model and in Fig. 5.37(b) for the conventional models. As would be expected for the bin model, the highest heat flux into the wall is observed in the region surrounding the forward stagnation point. However, consistent with the observed behavior of the shear stress, the contours on the “belly” reveal that the conventional models predict higher heat fluxes along most of the bottom of the vehicle. The profiles of  $c_h$  for the rear of the vehicle are shown

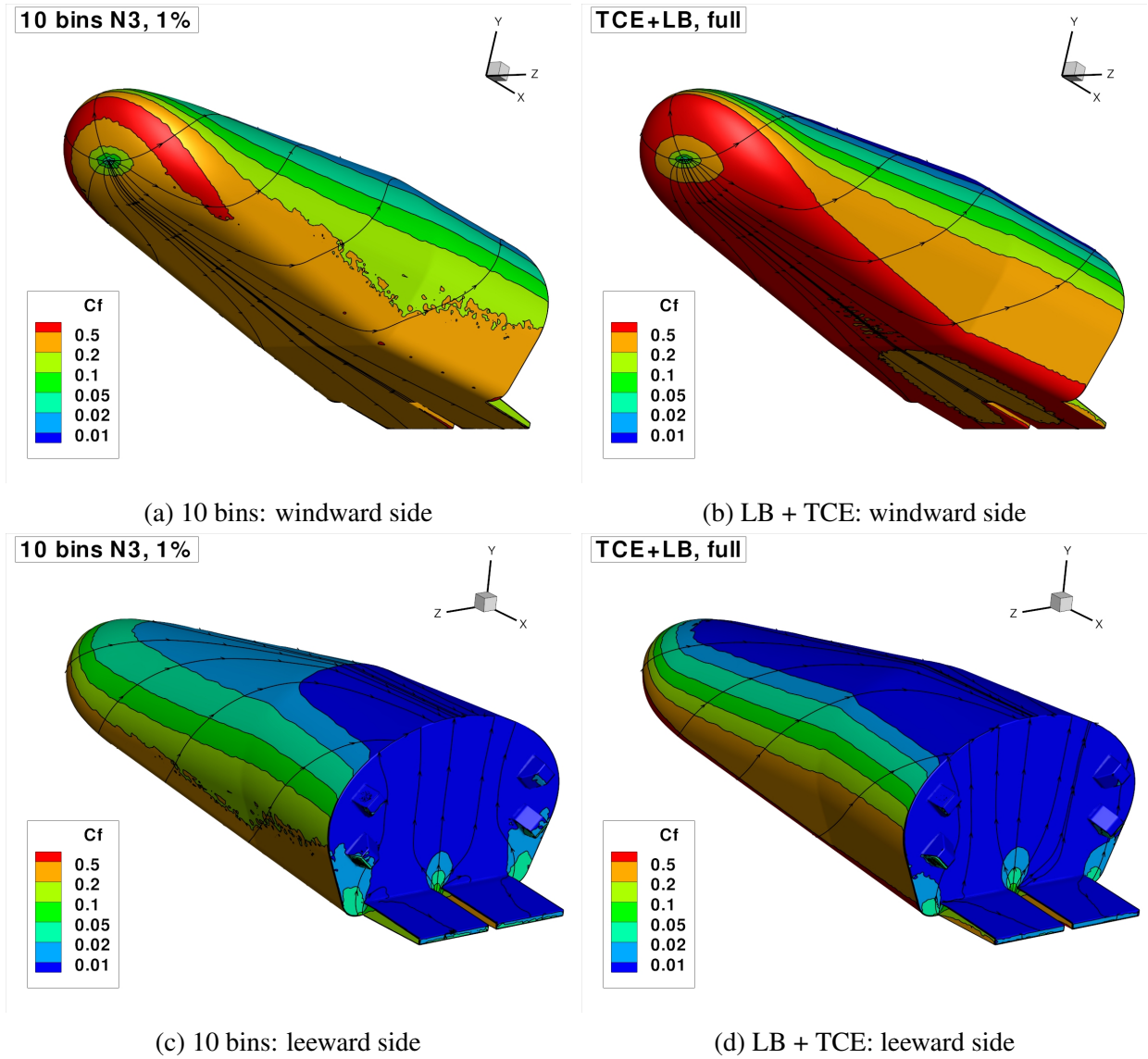


Figure 5.36.: IXV atmospheric entry: profiles of skin friction coefficient. First row: windward side, second row: leeward side

in Fig. 5.37(c) for the bin model and in Fig. 5.37(d) for the conventional models. Unlike for the windward side, only minor differences can be noticed between the two models. Overall, the heat flux on the leeward side are up to 100 times lower than what the bottom part of the vehicle is exposed to. Recall that, based on Fig. 5.23 and Fig. 5.24, with both models the predicted translational and internal mode temperatures in the gas flowing past the rear of the vehicle are fairly high. With 2000-5000 K they are certainly higher than the assumed wall temperature of 900 K. This suggests that the low heat flux in this region is likely due to the low overall flux of impinging particles on the surface, rather than due to the lack of a temperature gradient. In addition to this, one must consider that the highly rarefied conditions in the vehicle’s wake will cause the local velocity distributions to be far from Maxwellian. It is thus possible that the relatively high kinetic temperatures observed in the wake are a result of a combination of particle populations concentrated around vastly different locations in velocity space, rather than because of the width of the velocity distribution itself.

After examining the distributions of pressure, wall shear stress and heat flux over the vehicle’s entire surface, a final comparison of the integrated aerodynamic quantities of lift  $F_L$ , drag  $F_D$  and overall surface heating rate  $\dot{Q}$  can be made. The respective non-dimensional coefficients are defined as:

$$C_L = \frac{F_L}{\frac{1}{2}\rho_\infty V_\infty^2 S_{\text{ref}}}, \quad C_D = \frac{F_D}{\frac{1}{2}\rho_\infty V_\infty^2 S_{\text{ref}}} \quad \text{and} \quad C_h = \frac{\dot{Q}}{\frac{1}{2}\rho_\infty V_\infty^3 S_{\text{ref}}}, \quad (5.12)$$

with  $S_{\text{ref}}$  being the reference surface indicated in Tab. 5.5(a).

The three coefficients are listed in Tab. 5.6, revealing the differences between the two models. Using the conventional model values as reference, the relative discrepancies for the lift- and drag coefficients lie around 15 %. The relatively low sensitivity of the lift- and drag coefficients to the particular chemistry model is not surprising, as other studies have suggested that these quantities are usually not strongly affected by the flow chemistry [45].

Table 5.6.: IXV atmospheric entry: Integrated aerodynamic coefficients

	10 bins <b>N3 1%</b>	LB + TCE <b>full</b>	relative difference %
$C_L$	0.452	0.399	+13.3
$C_D$	1.028	1.218	-15.6
$C_h$	0.219	0.326	-32.8
<i>tra</i>	0.219	0.276	-20.7
<i>int</i>	0	0.050	-100

For the heat transfer coefficient a direct comparison between the two models is somewhat misleading. This is due to differences in the boundary conditions applied for the two respective models. Recall that with the bin model only the translational mode could be treated as fully

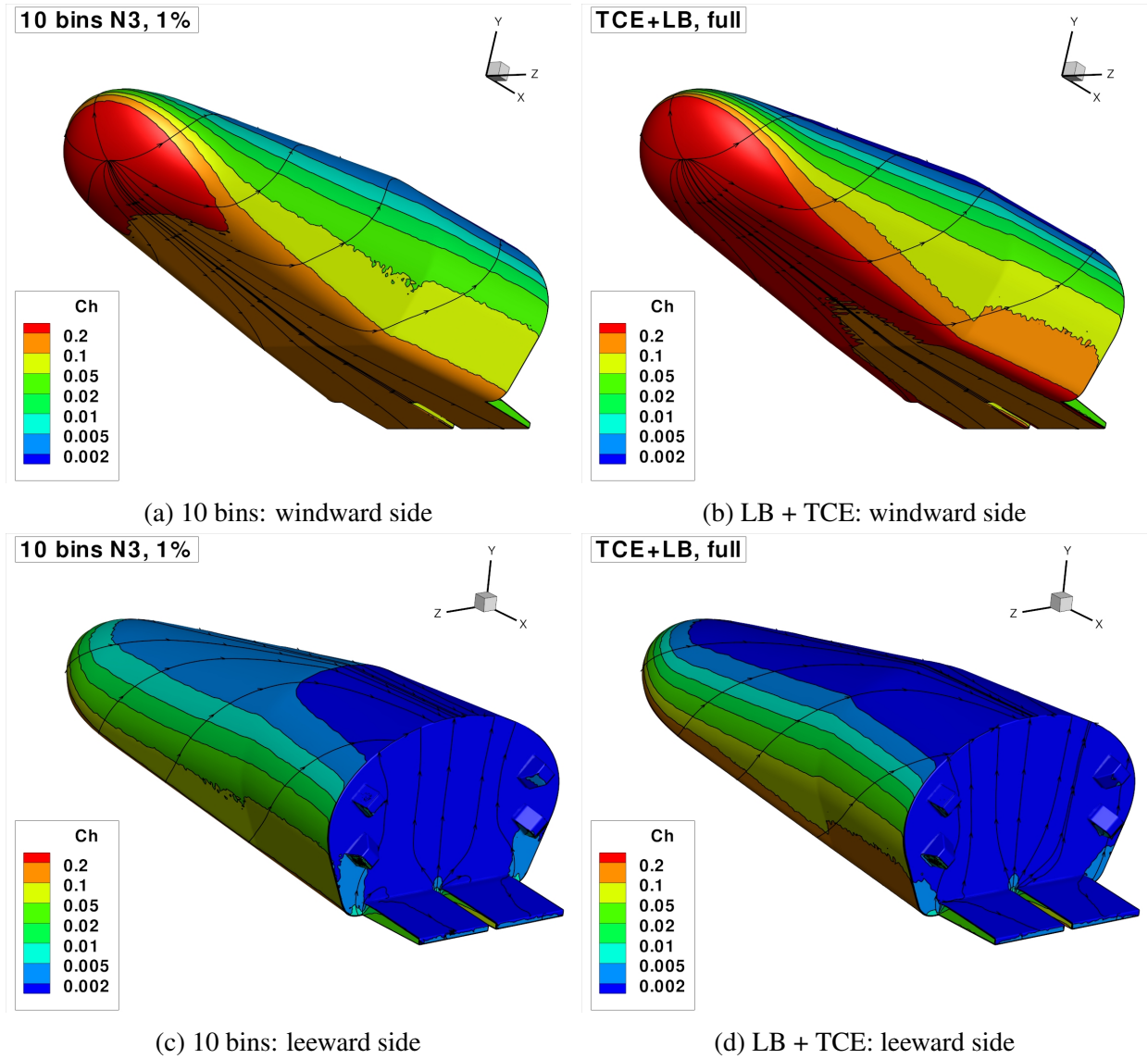


Figure 5.37.: IXV atmospheric entry: profiles of wall heat transfer coefficient. First row: windward side, second row: leeward side

accommodated to the wall temperature. Thus, as listed in Tab. 5.5(a), in the bin model simulations the accommodation coefficient of the internal mode was effectively  $\alpha_{\text{int}} = 0$ . Rather than a conscious choice, this treatment was a consequence of limitations in the possible integration of the bin model into RGDAS: Recall that by using a detailed state-to-state approach, each of the internal energy bins of  $\text{N}_2$  is effectively treated as a separate pseudo-species. While the detailed chemistry model for the gas phase could be integrated into the algorithms already in place in RGDAS without major changes to the source code (recall Sec. 5.1.2), the same is not true for the boundary conditions. The reason is that when a particle of pseudo-species  $\text{N}_2(k)$  collides with the surface, full accommodation to the wall temperature implies that its post-reflection bin,  $k'$  would have to be sampled from a Boltzmann distribution over all  $k \in \mathcal{K}_{\text{N}_2}$  at  $T_{\text{wall}} = 900 \text{ K}$ , before re-releasing it back into the flow. Since imposing  $\alpha_{\text{int}} = 1$  at the surface implies changing the bin index  $k \rightarrow k'$  for each of the reflected  $\text{N}_2$ -particles, this would require the wall reflection algorithm in RGDAS to re-assign a new species label to the particle. However, since RGDAS was originally conceived with a data structure for the conventional models in mind, the indices for the internal energy levels are separate from those for the chemical species. By contrast, with the conventional models, during wall collisions all  $\text{N}_2(v, J)$ -particles are reflected according to Boltzmann rotational and vibrational level distributions at the wall temperature of 900 K, implying  $\alpha_{\text{rot}} = 1$ , and  $\alpha_{\text{vib}} = 1$ . This difference only directly affects the heat transfer coefficient, and when the contributions of the translational- and internal modes to  $C_h$  are listed separately, the difference between the two models is quite noticeable (see the last two rows of Tab. 5.6). The lift- and drag coefficients, on the other hand, are only indirectly affected by the discrepancy in boundary conditions via the differences in the flow fields surrounding the vehicle.

To summarize the two test cases discussed in this chapter, a state-to-state chemistry model for nitrogen based on *ab initio* quantum-chemistry data, which had originally been implemented in a dedicated 1D DSMC solver, has now been integrated successfully with a well-established, high-performance DSMC code. The model has been used to study a hypersonic flow representative of blunt- and lifting body configurations entering Earth's atmosphere. From the results of the simulations, noticeable differences between the state-to-state model and the conventional models for internal energy exchange and dissociation (Larsen-Borgnakke + TCE) were found. At high Knudsen numbers the state-to-state model predicts negligible rates of dissociation, while in near-continuum conditions a noticeable delay in the onset of dissociation behind the bow shock could be observed. This behavior contrasts with the conventional models, which do not include rovibrational favoring of the dissociation reaction. The trends observed in these DSMC simulations are in line with results of previous CFD studies by other authors [117, 7]. At the moment it is premature to claim that the state-to-state model gives more accurate results than the conventional ones, since data on inelastic cross sections for  $\text{N}_2+\text{N}_2$ -interactions are still missing from the detailed chemistry database. However, the method could be adapted to accommodate these additional reactions, once the necessary data become available. Future work should first focus on including

these missing inelastic cross sections for  $N_2+N_2$ -collisions. Another issue not yet fully taken into account is the role played by internal energy accommodation on solid surfaces. While in the conventional model simulations translational, rotational and vibrational energies of reflected molecules were fully accommodated to the wall temperature, in the state-to-state model only accommodation of the translational mode was included. This inconsistency could be resolved rather easily by implementing the equivalent boundary condition in RGDAS for the state-to-state approach.



## 6. Conclusions and perspectives

In this work the DSMC implementation of a coarse-grain model for nitrogen based on a state-to-state description has been presented. The main contribution of the thesis is the development of a methodology by which the detailed reaction mechanism for internal energy exchange and molecular dissociation could be reduced to a manageable size and incorporated into a DSMC code. The feasibility of using this model to simulate problems with realistic 2D/3D geometries and conditions relevant for atmospheric entry applications was demonstrated. In order to integrate the model into DSMC, several intermediate goals had to be achieved.

First, the detailed reaction-kinetic data for internal energy exchange and dissociation in  $N_2+N$ -collisions, which were extracted from an ab initio database developed at NASA Ames Research Center [5], had to be adapted to a form suitable for use by DSMC collision routines. A small sample of the original state-specific cross sections supplied by the Ames database was examined more closely in Sec. 2.5. It was found that these “raw” cross sections were affected by significant statistical noise, due to the relatively coarse sampling of impact parameters employed in the quasi-classical trajectory (QCT) method during their generation. As a consequence, the cross sections in their original form were considered unsuitable for direct use with DSMC. Instead, thermally averaged rate coefficients, obtained by integrating the original cross sections over all collision energies, were used as a starting point. The advantage of these rate coefficients lies in the fact that the aforementioned integration reduces the stochastic noise significantly. Due to the requirements of the detailed chemistry routines in the DSMC method, in a subsequent step these temperature-dependent rate coefficients had to be converted back into collision energy-dependent cross sections. This problem, which is strictly-speaking ill-posed, was tackled in Sec. 3.1 by the use of an analytical inversion technique, inspired by the cross section functional form used in Bird’s classical TCE method [24]. Alternative inversion techniques for obtaining the cross sections numerically, such as Tikhonov regularization [135], or non-linear optimization via the downhill-simplex method [138] were deemed too time-consuming and required too much user supervision to be practical, given the large number of individual cross sections to be processed. In Sec. 3.2, the behavior of the cross sections obtained via analytical inversion was compared to the raw data obtained from the Ames database. The analytical cross sections were found to agree reasonably well with the raw data, both in terms of their magnitudes and shapes. A major advantage of the analytical inversion technique is that it allows one to directly impose the appropriate

activation energy for all endothermic reactions, i.e. those which must overcome a specific energy threshold in order to proceed. This is especially useful, since in the present work the inversion technique was combined with a coarse-grain model to reduce the size of the detailed chemical mechanism. As explained in more detail in Sec. 2.6, this coarse-grain model requires one to lump together many individual state-specific processes, each one with its own activation energy, into a much smaller set. Had the raw cross sections of the Ames database been used directly in this reduction, the resulting average cross sections would have had their activation energies “smeared out” over a finite energy range. However, this would have constituted a problem during actual DSMC simulations, because it meant that in some instances particular state-specific reactions could be triggered, despite the given collision pair not possessing enough total energy to form the reaction products. By first computing the state-specific rate coefficients, then performing the mechanism reduction and finally inverting this reduced set of rate coefficients analytically, this problem could be avoided. In addition to this, the cross sections obtained via analytical inversion were also preferred over the raw cross sections, because for each state-specific process they only require the specification of four of numerical parameters to fully define their behavior. During an actual DSMC simulation this fact allows for considerable savings in computer memory and execution time, because no interpolation of tabulated data is necessary to evaluate the cross section at a given collision energy. Furthermore, since the analytical expressions of the state-to-state cross sections were derived to be consistent with Arrhenius-type rate coefficients, they are automatically easier to adapt and integrate into DSMC codes using the classical total collision energy chemistry models (see Sec. 5.1).

Second, in order to reduce the computational cost of the state-to-state model to reasonable levels, the number of discrete rovibrational states of  $N_2$  (and the associated mechanism for the internal energy exchange and dissociation reactions) had to be reduced considerably. For this purpose, an already existing coarse grain model known as the uniform rovibrational (URVC) bin model [117] was adapted for its use with DSMC. The URVC model was preferred in this implementation over comparable models (e.g. the BRVC [128], or HyBVC models [129]), because unlike these other approaches it does not require the use of additional temperatures in fixing the distribution of rovibrational levels within each bin. Although these temperatures serve as adjustable parameters in the BRVC and HyBVC models to drive the rovibrational levels inside every bin to assume the correct distributions at equilibrium, they are macroscopic quantities, which have no place in a simulation method based on a kinetic description, such as DSMC. In order to determine the most convenient distribution of rovibrational levels among a given number of bins, and to determine the minimum number of bins necessary to reproduce the behavior of the full system by means of the URVC model, a parametric study was conducted in Sec. 3.4. This study helped determine the “binning strategy” to best approximate the thermodynamic behavior of the full set of levels. While no single optimal distribution of levels could be found, the parametric study revealed that significant improvements can be made, if the sizes of the individual bins (i.e. the energy

---

intervals covered by each bin) are roughly scaled with the average energy of the rovibrational levels it contains. Using bins with fewer rovibrational levels at lower energies allows for a much better representation of the internal energy content in the gas at low temperatures. This is a desirable feature in atmospheric-entry flows, where the undisturbed free stream gas is usually cold. The final choice used 10 variably-sized bins, which were able to reproduce the thermodynamic properties of the full set of levels over a wide range of temperatures.

For purposes of model testing, a dedicated DSMC code capable of simulating the detailed chemical dynamics of the state-to-state mechanism in unsteady 0D- and steady 1D flows was written by the author at the von Karman Institute. With the help of this code, the DSMC implementation of the URVC bin model was verified in Sec. 4.1 against equivalent master equation calculations in adiabatic reservoir-type simulations. The sensitivity of the internal energy relaxation- and dissociation rates to the choice of bins was examined, and the 10 variably-sized bins were again found to produce results which closely approximate those of the full set of levels. Subsequently, in Sec. 4.2 the URVC bin model was used to study internal energy excitation and dissociation in nitrogen as it is compressed across a normal shock. This test case revealed that the bin model based on the NASA Ames N3 cross sections predicts extremely high kinetic temperatures in the shock, with relatively slow excitation of the rovibrational energy modes and a delay in the onset of dissociation. These findings are consistent with results obtained by other authors, who performed CFD simulations based on a hydrodynamic description [117].

Finally, the bin model was adapted further for its use with an external production-level DSMC tool. In this case, the RGDAS code developed at ITAM was used. This integration was done in order to demonstrate the feasibility of using the state-to-state model in large-scale 2D and 3D DSMC simulations. As examples, two test cases roughly representative of Earth atmospheric entry conditions were used. The behavior of the bin model was studied by comparing it to calculations, which used the conventional Larsen-Borgnakke and total collision energy models for internal energy exchange and dissociation. It was found that the bin model predicts a much lower degree of internal energy excitation and slower dissociation across the bow shock than the conventional models. These differences were attributed to the vibrationally-favored dissociation included in the bin model and the different dynamics of rotational excitation at high temperatures.

While integration of the bin model in RGDAS was largely successful, several limitations still exist, and a number of compromises had to be made: 1) In every simulation with the bin model an arbitrary amount of atomic nitrogen had to be initially present in order to trigger internal energy exchange and further dissociation of  $N_2$ . 2) The simulations performed to test the bin model had to be restricted to relatively high-temperature conditions, where at least some minimal dissociation would be expected. Otherwise, at lower temperatures where  $N_2+N_2$ -collisions dominate the inelastic collision kinetics, the results obtained with the current version of the bin model would not be meaningful. This is because the inelastic processes contained in the N3 database only

cover those due to  $N_2+N$ -collisions, which can only take place with at least some atomic nitrogen present in the mixture. 3) As discussed in Sec. 5.1, some ad hoc changes to the RGDAS collision routines had to be made to allow for the correct reproduction of the inelastic process rates of the bin model. 4) During the analysis of the surface heat flux in Sec. 5.2 and Sec. 5.3, it was remarked that the boundary conditions applied at the body's surface during the bin model simulations were slightly different to those used with the conventional models. While in the bin model simulations the internal energy modes of particles reflected from the surface were frozen, in the conventional model simulations they were assumed to be fully accommodated to the surface temperature. This inconsistency makes direct comparison of the surface heat fluxes obtained via the two different models difficult, as it is not clear whether the observed differences are due to the different gas-phase chemistry behavior, or due to the boundary condition itself.

Problems 1) and 2) can be attributed to the fact that the current bin model, as it was used in this thesis, does not contain any of the inelastic cross sections for  $N_2+N_2$ -collisions. Thus, these shortcomings could be fixed if the relevant rate data could be obtained. Future developments should thus concentrate on completing the nitrogen model with the missing N4-data, which would include excitation and dissociation reactions by  $N_2+N_2$ -collisions. Only with these data will a realistic assessment of the behavior of the state-to-state model, as compared to the current conventional models, be possible. Furthermore, inclusion of the N4-reactions is necessary for comparisons with experiments to be meaningful. This is an important remaining task, and although the QCT-based rates are assumed to have been obtained from first-principles, comparison with experiments would be a necessary validation step. It should be noted that the NASA Ames quantum chemistry group has already generated a potential energy surface for the N4-system, and recent publications hint at the availability of QCT-based rate data [151, 152]. Alternatively, the N4 PES of the Truhlar group [123] has been recently published online [153] and has been used to perform QCT-calculations [6]. This alternative source of ab initio data is of interest, since it would allow to cross-check the results obtained with the NASA database.

The issues raised in 3) and 4) were mainly a by-product of the incomplete integration of the state-to-state model into the RGDAS code, and ultimately arose due to the desire to avoid modifying the source code of this external DSMC tool. The first problem could easily be solved by fully implementing within RGDAS the state-to-state model, as described in Ch. 3. This would allow one to determine the total cross section in whichever functional form would be most convenient, without being restricted to the VHS cross section form dictated by the conventional collision routines. Since the present work represents only a proof-of-concept, where the intent was merely to demonstrate the feasibility of applying the bin model to large-scale DSMC simulations, the necessary extensive changes to the RGDAS source code were not attempted. The same is true for adapting the wall reflection boundary conditions within RGDAS, in order to make the bin-, and conventional models behave in a consistent manner with one another. However, both tasks could be accomplished with relative ease given the support of the developers of RGDAS.

---

Although not of crucial importance in highly rarefied atmospheric-entry flows, the fact that recombination reactions are not included in the present model prevent it from attaining the correct chemical equilibrium state. This deficiency was remarked in Sec. 4.1. Also, the particular upstream conditions in the normal shock of Sec. 4.2 were chosen deliberately, so as to cause the gas to fully dissociate behind the shock. Thus, the problem of not being able to attain a mixed  $N_2$ - $N$  post-shock equilibrium composition was avoided. However, if the upstream Mach number had been chosen to be slightly lower, one would have been confronted with a situation where the lack of recombination far downstream of the shock would prevent the gas from reaching the correct equilibrium composition. More generally, while recombination may not be important in the shock layer of rarefied reentry flows, it does play a role in expanding flows, such as in nozzles and in the boundary layers formed around a reentry vehicle's surface. While some researchers have included recombination in DSMC calculations with phenomenological models (i.e. TCE, QK), the correct implementation for a state-to-state description has yet to be found. As a starting point, consider the works of Kuščer [154], Alexeev [155] and Giovangigli [156], who discuss the necessary detailed balance relations for reversible dissociation-recombination-reactions in the context of the generalized Boltzmann equation. The remaining challenge lies in interpreting their formulations and apply them to the particle-based routines of DSMC. Apart from enforcing detailed balance, another challenge in implementing recombination reactions is that DSMC collision schemes are formulated almost exclusively with binary collisions in mind. This is historically justified, since practically all of the theory for rarefied gas dynamics is limited to binary collisions. However, it poses a problem for modeling recombination, since a certain amount of three-body collisions in the gas are likely necessary for recombination to occur. Although some DSMC implementations model these three-body collisions in an ad hoc manner, in the opinion of the author a rigorous formulation of the three-body collision algorithm has yet to be proposed. On the other hand, it is not entirely clear how recombination actually occurs in reality. While certainly some three-body collisions result in atoms instantaneously recombining to form molecules, probably most recombination happens as a series of two-body collisions, where an unstable  $N_2$ -molecule is initially formed by two N-atoms colliding and (maybe several) subsequent collisions with other particles to stabilize the new molecule. This mechanism has been mentioned by Smith [157] and could be difficult to implement within a DSMC framework. The relative importance of true three-body collisions vs. series of binary collisions could be assessed using the MD method used by Valentini and Schwartzentruber, since they would be able to track individual N-atoms deterministically.

A final point about the feasibility of using of the bin model, or in fact any state-to-state-based model in more realistic test cases has to be made. One should realize that even with a reduction from about 10000 to only about 10 internal states, the  $N_3/N_4$ -systems are still too large for most engineering applications. Consider even the most basic gas mixture of relevance in Earth atmospheric entry, i.e. 5-species air, which consists of  $N_2$ ,  $O_2$ ,  $NO$ ,  $N$  and  $O$ . Assuming that for each of the three molecular species in this mixture the internal energy states are represented by

10 bins respectively, the number of individual cross sections necessary to account for all possible transitions involving these collision partners is already on the order of tens of thousands. This is clearly too large a number of pseudo-species to be handled in practical situations. Without an even further reduction in the number of bins, in the foreseeable future the state-to-state approach is thus likely to remain an academic subject. Nevertheless, there are several ways in which continued research into such high-fidelity models can still provide beneficial for future applications. One of its main uses will be to verify, or challenge some of the core assumptions inherent to the much less costly models currently in general use (i.e. Larsen-Borgnakke+TCE models in DSMC, or multi-temperature models in CFD), and help to propose improvements, or alternatives to these conventional models. Furthermore, since the QCT-derived chemistry data are essentially parameter-free, they could be used to study the detailed chemical behavior of the gas in situations where experimental data is scarce, or nonexistent. Finally, another situation where a state-to-state approach is probably more easily applied, is that of single-species monoatomic gas flows, where the electronic excited states are important, e.g. Argon plasma [158].

# Bibliography

- [1] G.A. Bird. *Molecular Gas Dynamics and the Direct Simulation of Gas Flows*. Oxford University Press, 1994.
- [2] J.D. Anderson. *Hypersonic and high-temperature gas dynamics*. AIAA Education. American Institute of Aeronautics and Astronautics, 2 edition, 2006.
- [3] J.H. Ferziger and H.G. Kaper. *Mathematical Theory of Transport Processes in Gases*. Elsevier Science Publishing, 1972.
- [4] F. Esposito and M. Capitelli. Quasiclassical Molecular Dynamic Calculations of Vibrationally and Rotationally State Selected Dissociation Cross-Sections:  $N + N_2(v, j) \rightarrow 3N$ . *Chemical Physics Letters*, 302:49–54, 1999.
- [5] R. Jaffe, D. Schwenke, G. Chaban, and W. Huo. Vibrational and Rotational Excitation and Relaxation of Nitrogen from Accurate Theoretical Calculations. In *46th AIAA Aerospace Sciences Meeting and Exhibit, Reno, Nevada*, 2008.
- [6] J.D. Bender, P. Valentini, I. Nompelis, Y. Paukku, Z. Varga, D.G. Truhlar, T.E. Schwartzentruber, and G.V. Candler. An improved potential energy surface and multi-temperature quasiclassical trajectory calculations of  $N_2 + N_2$  dissociation reactions. *Journal of Chemical Physics*, 145:054304, 2015.
- [7] M. Panesi, R.L. Jaffe, D.W. Schwenke, and T.E. Magin. Rovibrational internal energy transfer and dissociation of  $N_2^1(\Sigma_g^+) - N(^4S_u)$  system in hypersonic flows. *The Journal of Chemical Physics*, 138 (4):044312, 2013.
- [8] B.J. Alder and T.E. Wainwright. Studies in molecular dynamics. I. General method. *The Journal of Chemical Physics*, 31(2):459–466, 1959.
- [9] B.J. Alder and T.E. Wainwright. Studies in Molecular Dynamics. II. Behavior of a Small Number of Elastic Spheres. *Journal of Chemical Physics*, 33(5):1439–1451, 1960.
- [10] A. Nordsieck and B.L. Hicks. Monte Carlo Evaluation of the Boltzmann Collision Integral. In *5th International Symposium on Rarefied Gas Dynamics, Oxford*, 1966.
- [11] F.G. Tcheremissine. A method for direct numerical integration of the Boltzmann equation. Technical report, NASA, 1972. Numerical Method in the Theory of Gases, Comput Cent., USSR Acad. Sci., Moscow, 1969, pp. 43–63. Transl. in NASA TT F-638.
- [12] A.V. Bobylev. The theory of the nonlinear spatially uniform Boltzmann equation for

- Maxwell molecules. *Soviet Scientific Reviews Section C Mathematical Physics Reviews*, 7:111–233, 1988.
- [13] I.M. Gamba and S.H. Tharkabhushanam. Spectral-Lagrangian methods for Collisional Models of Non-Equilibrium Statistical States. *Journal of Computational Physics*, 228(6):2012–2036, 2009.
- [14] C.P.T. Groth and J.G. McDonald. Towards Physically-Realizable and Hyperbolic Moment Closures for Kinetic Theory. *Continuum Mechanics and Thermodynamics*, 21:467–493, 2009.
- [15] J.G. McDonald and C.P.T. Groth. Towards realizable hyperbolic moment closures for viscous heat-conducting gas flows. *Journal of Continuum Mechanics and Thermodynamics*, 25:573–603, 2013.
- [16] H. Struchtrup and M. Torrilhon. Regularization of Grad’s 13-moment-equations: Derivation and linear analysis. *Physics of Fluids*, 15:2668–2680, 2003.
- [17] M. Torrilhon and H. Struchtrup. Regularized 13-moment-equations: Shock structure calculations and comparison to Burnett models. *Journal of Fluid Mechanics*, 513:171–198, 2004.
- [18] G.A. Bird. *Molecular Gas Dynamics*. Clarendon Press, 1976.
- [19] C. Cercignani, A. Frezotti, and S. Sibilla. Hypersonic Rarefied Flows DSMC Analysis by a Simplified Chemical Model. *Meccanica*, 30:93–104, 1995.
- [20] D. Bruno, A. Frezotti, and G.P. Ghiroldi. Oxygen transport Properties estimation by CT-DSMC simulations. *Physics of Fluids*, 27(5):057101, 2015.
- [21] A.L. Garcia. Hydrodynamic fluctuations in a dilute gas under shear. *Physical Review A*, 36(9):4348–4355, 1987.
- [22] A.L. Garcia, J.B. Bell, W.C. Crutchfield, and B.J. Alder. Adaptive Mesh and Algorithm Refinement Using Direct Simulation Monte Carlo. *Journal of Computational Physics*, 154:134–155, 1999.
- [23] A.L. Garcia and W. Wagner. Time step truncation error in direct simulation Monte Carlo. *Physics of Fluids*, 12(10):2621–2633, 2000.
- [24] G.A. Bird. Simulation of Multi-Dimensional and Chemically Reacting Flows. In *11th International Symposium on Rarefied Gas Dynamics*, 1978.
- [25] G.A. Bird. Monte-Carlo simulation in an engineering context. In *12th International Symposium on rarefied gas dynamics*, 1980.
- [26] G.A. Bird. Direct simulation of typical AOTV entry flows. In *4th AIAA/ASME Joint Thermophysics and Heat Transfer Conference*, 1986.
- [27] G.A. Bird. Perception of numerical methods in rarefied gasdynamics. In *16th International*

---

*Symposium on rarefied gas dynamics*, 1988.

- [28] A.B. Carlson and G.A. Bird. Implementation of a vibrationally linked chemical reaction model for DSMC. In J. Harvey and G. Lord, editors, *Rarefied Gas Dynamics 19*, page 906. Oxford University Press, 1995.
- [29] G.A. Bird. A Comparison of Collision Energy-based and Temperature-based Procedures in DSMC. In *26th International Symposium on Rarefied Gas Dynamics*, 2008.
- [30] G.A. Bird. The Q-K model for gas-phase chemical reaction rates. *Physics of Fluids*, 23:106101, 2011.
- [31] G.A. Bird. Chemical Reactions in DSMC. In *27th International Symposium on Rarefied Gas Dynamics*, 2011.
- [32] H.A. Hassan and D.B. Hash. A generalized hard-sphere model for Monte Carlo simulation. *Physics of Fluids*, 5(3):738–744, 1993.
- [33] D.B. Hash, J.N. Moss, and H.A. Hassan. Direct Simulation of Diatomic Gases Using the Generalized Hard Sphere Model. *Journal of Thermophysics and Heat Transfer*, 8(4):758–764, 1994.
- [34] D.B. Hash and H.A. Hassan. Direct Simulation with Vibration-Dissociation Coupling. *Journal of Thermophysics and Heat Transfer*, 7(4):680–686, 1993.
- [35] F.E. Lumpkin III. *Development and evaluation of continuum models for translational-rotational nonequilibrium*. PhD thesis, Stanford University, 1990.
- [36] C. Borgnakke and P.S. Larsen. Statistical Collision Model for Monte Carlo Simulation of Polyatomic Gas Mixture. *Journal of Computational Physics*, 18:405–420, 1975.
- [37] F.E. Lumpkin III, B.L. Haas, and I.D. Boyd. Resolution of differences between collision number definitions in particle and continuum simulations. *Physics of Fluids A*, 3(9):2282–2284, 1991.
- [38] B.L. Haas, D.B. Hash, G.A. Bird, F.E. Lumpkin III, and H.A. Hassan. Rates of thermal relaxation in direct simulation Monte Carlo methods. *Physics of Fluids*, 6(6):2191–2201, 1994.
- [39] G.J. LeBeau. A parallel implementation of the direct simulation Monte Carlo method. *Computer methods in applied mechanics and engineering*, 174:319–337, 1999.
- [40] G.J. LeBeau and F.E. Lumpkin III. Application highlights of the DSMC Analysis Code (DAC) software for simulating rarefied flows. *Computer methods in applied mechanics and engineering*, 191:595–609, 2001.
- [41] G.J. LeBeau, K.A. Boyles, and F.E. Lumpkin III. Virtual sub-cells for the Direct Simulation Monte Carlo method. In *41st AIAA Aerospace Sciences Meeting and Exhibit*, 2003.
- [42] R.G. Wilmoth, A.B. Carlson, and G.J. LeBeau. DSMC grid methodologies for computing

- low-density hypersonic flows about reusable launch vehicles. In *31st AIAA Thermophysics Conference*, 1996.
- [43] J.N. Moss, R.G. Wilmoth, and J.M. Price. DSMC simulations of blunt body flows for Mars entries: Mars pathfinder and Mars microprobe capsules. In *32nd AIAA Thermophysics Conference*, 1997.
- [44] J.N. Moss, R.C. Blanchard, R.G. Wilmoth, and R.D. Braun. Mars Pathfinder Rarefied Aerodynamics: Computations and Measurements. *Journal of Spacecraft and Rockets*, 36(3):330–339, 1999.
- [45] J.N. Moss, C.E. Glass, and F.A. Greene. DSMC Simulations of Apollo Capsule Aerodynamics for Hypersonic Rarefied Conditions. In *9th AIAA/ASME Joint Thermophysics and Heat Transfer Conference*, 2006.
- [46] J.N. Moss, K.A. Boyles, and F.A. Greene. Orion Aerodynamics for Hypersonic Free Molecular to Continuum Conditions. In *14th AIAA/AHI International Space Planes and Hypersonic Systems and Technologies Conference*, 2006.
- [47] R. Prakash, S.L. Gai, and S. O’Byrne. DSMC Computations of Hypersonic Flow Separation and Re-attachment in the Transition to Continuum Regime. In *30th International Symposium on Rarefied Gas Dynamics*, 2016.
- [48] C. Zhang and T.E. Schwartzentruber. Robust cut-cell algorithms for DSMC implementations employing multi-level Cartesian grids. *Computers & Fluids*, 69:122 – 135, 2012.
- [49] D.J. Rader, M.A. Gallis, J.R. Torczynski, and W. Wagner. Direct simulation Monte Carlo convergence behavior of the hard-sphere-gas thermal conductivity for Fourier heat flow. *Physics of Fluids*, 18:077102–1 – 077105–16, 2006.
- [50] G.A. Bird, M.A. Gallis, J.R. Torczynski, and D.J. Rader. Accuracy and efficiency of the sophisticated direct simulation Monte Carlo algorithm for simulating noncontinuum gas flows. *Physics of Fluids*, 21:017103, 2009.
- [51] M.A. Gallis, R.B. Bond, and J.R. Tarczynski. A kinetic-theory approach for computing chemical-reaction rates in upper-atmosphere hypersonic flows. *Journal of Chemical Physics*, 131:124311, 2009.
- [52] I.A. Boyd. Analysis of Rotational Nonequilibrium in Standing Shock Waves of Nitrogen. *AIAA Journal*, 28(11):1997–1999, 1990.
- [53] I.D. Boyd. Rotational-translational energy transfer in rarefied nonequilibrium flows. *Physics of Fluids A*, 2(3):447–452, 1990.
- [54] I.D. Boyd. Rotational and Vibrational Nonequilibrium Effects in Rarefied Hypersonic Flow. *Journal of Thermophysics and Heat Transfer*, 4(4):478–484, 1990.
- [55] I.D. Boyd and J.P.W. Stark. Direct Simulation of Chemical Reactions. *Journal of Thermophysics and Heat Transfer*, 4(3):391–393, 1990.

- 
- [56] I.D. Boyd. Analysis of vibrational-translational energy transfer using the direct simulation Monte Carlo method. *Physics of Fluids A*, 3(7):1785–1791, 1991.
- [57] I.D. Boyd. Temperature dependence of rotational relaxation in shock waves of nitrogen. *Journal of Fluid Mechanics*, 246:343–360, 1993.
- [58] I.D. Boyd. Relaxation of discrete rotational energy distributions using a Monte Carlo method. *Physics of Fluids A*, 5(9):2278–2286, 1993.
- [59] I.D. Boyd and T. Gokcen. Evaluation of Thermochemical Models for Particle and Continuum Simulations of Hypersonic Flow. *Journal of Thermophysics and Heat Transfer*, 7(3):406–411, 1993.
- [60] I.D. Boyd. Analysis of vibration-dissociation-recombination processes behind strong shock waves of nitrogen. *Physics of Fluids A*, 4(1):178–185, 1992.
- [61] I.D. Boyd. Modeling backward chemical rate processes in the direct simulation Monte Carlo method. *Physics of Fluids*, 19:126103, 2007.
- [62] I.D. Boyd. A threshold line dissociation model for the direct simulation Monte Carlo method. *Physics of Fluids*, 8:1293–1300, 1996.
- [63] P Vijayakumar, Q. Sun, and I.D. Boyd. Vibrational-translational energy exchange models for the direct simulation Monte Carlo method. *Physics of Fluids*, 11(8):2117–2126, 1999.
- [64] S. Dietrich and I.D. Boyd. Scalar and Parallel Optimized Implementation of the Direct Simulation Monte Carlo. *Journal of Computational Physics*, 126:328–342, 1996.
- [65] A.J. Lofthouse, I.D. Boyd, and M.J. Wright. Effects of Continuum Breakdown on Hypersonic Aerothermodynamics. *Physics of Fluids*, 19:Article 027105, 2007.
- [66] A.J. Lofthouse, L.C. Scalabrin, and I.D. Boyd. Velocity Slip and Temperature Jump in Hypersonic Aerothermodynamics. *Journal of Thermophysics and Heat Transfer*, 22:38–49, 2008.
- [67] T.E. Schwartzenuber and I.D. Boyd. A hybrid particle-continuum method applied to shock waves. *Journal of Computational Physics*, 215:402–416, 2006.
- [68] Q Sun and I.D. Boyd. Evaluation of macroscopic properties in the direct simulation Monte Carlo method. *Journal of Thermophysics and Heat Transfer*, 19(3):329–335, 2005.
- [69] T.E. Schwartzenuber, L.C. Scalabrin, and I.D. Boyd. A modular particle-continuum numerical method for hypersonic non-equilibrium gas flows. *Journal of Computational Physics*, 225:1159–1174, 2007.
- [70] T.E. Schwartzenuber, L.C. Scalabrin, and I.D. Boyd. Hybrid Particle-Continuum Simulations of Nonequilibrium Hypersonic Blunt-Body Flowfields. *Journal of Thermophysics and Heat Transfer*, 22:29–37, 2008.
- [71] J.M. Burt and I.D. Boyd. A low diffusion particle method for simulating compressible

- inviscid flows. *Journal of Computational Physics*, 227:4653–4670, 2008.
- [72] J.M. Burt and I.D. Boyd. Extension of a Multiscale Particle Scheme to Near-Equilibrium Viscous Flows. *AIAA Journal*, 47(6):1507–1517, 2009.
- [73] J.M. Burt and I.D. Boyd. A hybrid particle approach for continuum and rarefied flow simulation. *Journal of Computational Physics*, 228:460–475, 2009.
- [74] I.D. Boyd and E. Josyula. State Resolved Vibrational Relaxation Modeling for Strongly Nonequilibrium Flows. In *49th AIAA Aerospace Sciences Meeting including the New Horizons Forum and Aerospace Exhibition*, 2011.
- [75] I.V. Adamovich, S.O. Macheret, J.W. Rich, and C.E. Treanor. Vibrational Relaxation and Dissociation Behind Shock Waves Part 1: Kinetic Rate Models. *AIAA Journal*, 33(6):1064–1069, 1995.
- [76] I.V. Adamovich, S.O. Macheret, J.W. Rich, and C.E. Treanor. Vibrational Relaxation and Dissociation Behind Shock Waves Part 2: Master Equation Modeling. *AIAA Journal*, 33(6):1070–1075, 1995.
- [77] J.G. Kim and I.D. Boyd. Monte Carlo simulation of nitrogen dissociation based on state-resolved cross sections. *Physics of Fluids*, 26:012006, 2014.
- [78] D. Gao and T.E. Schwartzentruber. Optimizations and OpenMP implementation for the direct simulation Monte Carlo method. *Computers & Fluids*, 42:73–81, 2011.
- [79] D. Gao, C. Zhang, and T.E. Schwartzentruber. A Three-Level Cartesian Geometry Based Implementation of the DSMC Method. In *48th AIAA Aerospace Sciences Meeting, Orlando, Florida*, 2010.
- [80] D. Gao, C. Zhang, and T.E. Schwartzentruber. Particle Simulations of Planetary Probe Flows Employing Automated Mesh Refinement. *Journal of Spacecraft and Rockets*, 48(3):397–405, 2011.
- [81] P. Valentini and T.E. Schwartzentruber. Large-scale Molecular Dynamics Simulations of Normal Shock Waves in Dilute Argon. *Physics of Fluids*, 21(066101):1–9, 2009.
- [82] P. Valentini and T.E. Schwartzentruber. A Combined Event-Driven/Time-Driven Molecular Dynamics Algorithm for the Simulation of Shock Waves in Rarefied Gases. *Journal of Computational Physics*, 228:8766–8778, 2009.
- [83] P. Norman, P. Valentini, and T.E. Schwartzentruber. GPU-Accelerated Classical Trajectory Calculation Direct Simulation Monte Carlo Applied to Shock Waves. *Journal of Computational Physics*, 247:153–167, 2013.
- [84] J.V. Austin and D.B. Goldstein. Rarefied Gas Model of Io’s Sublimation-Driven Atmosphere. *Icarus*, 148:370–383, 2000.
- [85] C.H. Moore, D.B. Goldstein, P.L. Varghese, L.M. Trafton, and B. Stewart. 1-D DSMC simulation of Io’s atmospheric collapse and reformation during and after eclipse. *Icarus*,

- 201(2):585–597, 2009.
- [86] K.A. Stephani, D.B. Goldstein, and P.L. Varghese. Development of a Hybrid DSMC/Navier-Stokes Solver with Application to the STS-119 Boundary Layer Transition Flight Experiments. In *49th AIAA Aerospace Sciences Meeting including the New Horizons Forum and Aerospace Exposition, Orlando, Florida*, 2011.
- [87] K.A. Stephani, D.B. Goldstein, and P. L. Varghese. Consistent treatment of transport properties for five-species air direct simulation Monte Carlo/Navier-Stokes applications. *Physics of Fluids*, 24:077101, 2012.
- [88] K.A. Stephani, D.B. Goldstein, and P.L. Varghese. A non-equilibrium surface reservoir approach for hybrid DSMC/Navier–Stokes particle generation. *Journal of Computational Physics*, 232(1):468–481, 2013.
- [89] M.S. Ivanov and S.V. Rogasinsky. Analysis of the numerical techniques of the direct simulation Monte Carlo method in the rarefied gas dynamics. *Soviet Journal of Numerical Analysis and Mathematical Modelling*, 3(6):453–465, 1988.
- [90] M.S. Ivanov and S.F. Gimelshein. Computational Hypersonic Rarefied Flows. *Annual Review of Fluid Mechanics*, 30:469–505, 1998.
- [91] M.S. Ivanov, A.V. Kashkovsky, S.F. Gimelshein, G.N. Markelov, A.A. Alexeenko, Y.A. Bondar, G.A. Zhukova, S.B. Nikiforov, and P.V. Vaschenkov. SMILE System for 2D/3D DSMC Computations. In *25th International Symposium on Rarefied Gas Dynamics*, 2006.
- [92] G.N. Markelov, A.V. Kashkovsky, and M.S. Ivanov. Space Station Mir Aerodynamics Along the Descent Trajectory. *Journal of Spacecraft and Rockets*, 38(1):43–50, January - February 2001.
- [93] N.E. Gimelshein, S.F. Gimelshein, and D.A. Levin. Vibrational relaxation rates in the direct simulation Monte Carlo method. *Physics of Fluids*, 14(12):4452–4455, 2002.
- [94] S.F. Gimelshein, N.E. Gimelshein, D.A. Levin, M.S. Ivanov, and I.J. Wysong. On the use of chemical reaction rates with discrete internal energies in the direct simulation Monte Carlo method. *Physics of Fluids*, 16(7):2442–2451, 2004.
- [95] Z. Li, I. Sohn, and D.A. Levin. State Specific Vibrational Relaxation and Dissociation Models for Nitrogen in Shock Regions. In *28th International Symposium on Rarefied Gas Dynamics, Zaragoza, Spain*, 2012.
- [96] N. Parsons, D.A. Levin, A.C. van Duin, and T. Zhu. Modeling of molecular nitrogen collisions and dissociation processes for direct simulation Monte Carlo. *The Journal of Chemical Physics*, 141(23):234307, 2014.
- [97] A. Venkattraman, A.A. Alexeenko, M.A. Gallis, and M.S. Ivanov. A Comparative Study of No-Time-Counter and Majorant Collision Frequency Numerical Schemes in DSMC. In *28th International Symposium on Rarefied Gas Dynamics*, volume 1501, pages 489–495, 2012.

- [98] K. Koura. Transient Couette Flow of Rarefied Binary Gas Mixtures. *The Physics of Fluids*, 13(6):1457–1466, 1970.
- [99] K. Nanbu. Theoretical basis of the direct simulation Monte Carlo method. In *15th International Symposium on Rarefied Gas Dynamics*, 1986.
- [100] K. Koura and H. Matsumoto. Variable soft sphere molecular model for inverse-power-law or Lennard-Jones potential. *Physics of Fluids A*, 3(10):2459–2465, 1991.
- [101] K. Koura, H. Matsumoto, and T. Shimada. A test of equivalence of the variable-hard-sphere and inverse-power-law models in the direct-simulation Monte Carlo method. *Physics of Fluids A*, 3:1835–1837, 1991.
- [102] K. Koura. Statistical Inelastic cross-section model for the Monte Carlo simulation of molecules with discrete internal energy. *Physics of Fluids A*, 4(8):1782–1788, 1992.
- [103] K. Koura. Direct simulation Monte Carlo study of rotational nonequilibrium in shock wave and spherical expansion of nitrogen using classical trajectory calculations. *Physics of Fluids*, 14(5):1689–1695, 2002.
- [104] J. Fan. A Generalized Soft-Sphere Model for Monte Carlo Simulation. *Physics of Fluids*, 14(12):4399, 2002.
- [105] J.G. Kim, O.J. Kwon, and C. Park. Modification and expansion of the generalized soft-sphere model to high temperature based on collision integrals. *Physics of Fluids*, 20:017105, 2008.
- [106] F. Bergemann and I.D. Boyd. *Rarefied Gas Dynamics: Experimental Techniques and Physical Systems (Progress in Aeronautics and Astronautics)*, chapter 3: New Discrete Vibrational Energy Model for the Direct Simulation Monte Carlo Method, pages 174–183. American Institute of Aeronautics and Astronautics, 1994.
- [107] M. Laux, S. Fasoulas, and E. W. Messerschmid. Development of a DSMC Code on Planar Unstructured Grids with Automatic Grid Adaptation. In *30th AIAA Thermophysics Conference*, 1995.
- [108] M. Laux, S. Fasoulas, and E. W. Messerschmid. DSMC simulation of flow fields with adaptive boundary conditions. In *31st AIAA Thermophysics Conference*, 1996.
- [109] M. Laux. Optimization and Parallelization of the DSMC Method in Unstructured Grids. In *32nd AIAA Thermophysics Conference*, 1997.
- [110] M. Laux. Local Time Stepping with Automatic Adaptation for the DSMC Method. In *7th AIAA/ASME Joint Thermophysics and Heat Transfer Conference*, 1998.
- [111] P. Ortwein, T.B. Binder, Copplestone S., A. Mirza, P. Nizenkov, M. Pfeiffer, S. Stindl, T. Fasoulas, and C.D. Munz. *High Performance Computing in Science and Engineering 2014*, volume VI, chapter Parallel Performance of a Discontinuous Galerkin Spectral Element Method Based PIC-DSMC Solver, pages 671–681. Springer International Publishing,

2015.

- [112] T.J. Scanlon, E. Roohi, C. White, M. Darbandi, and J.M. Reese. An open source, parallel DSMC code for rarefied gas flows in arbitrary geometries. *Computers & Fluids*, 39:2078–2089, 2010.
- [113] J.B. Anderson, J.D. Foch, M.J. Shaw, R.C. Stem, and B.J. Wu. Statistical Theory of Electronic Energy Relaxation. In *Proceedings of the 15th International Symposium on Rarefied Gas Dynamics*, 1986.
- [114] D. Bruno, M. Capitelli, Esposito F., S. Longo, and P. Minelli. Direct simulation of non-equilibrium kinetics under shock conditions in nitrogen. *Chemical Physics Letters*, 360:31–37, 2002.
- [115] F. Esposito, M. Capitelli, and C. Gorse. Quasi-classical dynamics and vibrational kinetics of  $N + N_2(v)$  system. *Chemical Physics*, 257:193–202, 2000.
- [116] J.G. Kim and I.D. Boyd. State Resolved Thermochemical Modeling of Nitrogen Using DSMC. In *43rd AIAA Thermophysics Conference*, 2012.
- [117] T. Magin, M. Panesi, A. Bourdon, R.L. Jaffe, and D.W. Schwenke. Coarse-grain model for internal energy excitation and dissociation of molecular nitrogen. *Chemical Physics*, 398:90–95, 2012.
- [118] R. Le Roy, Y. Huang, and C. Jary. An accurate analytic potential function for ground-state  $N_2$  from a direct-potential-fit analysis of spectroscopic data. *Journal of Chemical Physics*, 125(16):164310, 2006.
- [119] D.W. Schwenke. Dissociation Cross Sections and Rates for Nitrogen. In *Non-Equilibrium Gas Dynamics - From Physical Models to Hypersonic Flights*, number RTO-EN-AVT-162, 2009.
- [120] R.L. Jaffe, D.W. Schwenke, and M. Panesi. *Hypersonic Nonequilibrium Flows: Fundamentals and Recent Advances*, volume 247, chapter 3: First principles calculation of heavy particle rate coefficients, pages 103–158. American Institute of Aeronautics and Astronautics, 2015.
- [121] C Park. Review of Chemical-Kinetic Problems of Future NASA Missions, I: Earth Entries. *Journal of Thermophysics and Heat Transfer*, 7(3):385–398, 1993.
- [122] J.N. Moss, G.A. Bird, and V.K. Dogra. Nonequilibrium thermal radiation for an aeroassist flight experiment vehicle. In *AIAA 26th Aerospace Sciences Meeting*, 1988.
- [123] Y. Paukku, K.R. Yang, Z. Varga, and D.G. Truhlar. Global ab initio ground-state potential energy surface of  $N_4$ . *The Journal of Chemical Physics*, 139:044309, 2013.
- [124] Y. Paukku, K.R. Yang, Z. Varga, and D.G. Truhlar. Erratum: “Global ab initio ground-state potential energy surface of  $N_4$ ” [J. Chem. Phys. 139, 044309 (2013)]. *The Journal of Chemical Physics*, 140:019903, 2014.

- [125] T.E. Magin, M. Panesi, A. Bourdon, R. Jaffe, and D. Schwenke. Rovibrational internal energy excitation and dissociation of molecular nitrogen in hypersonic flows. In *10th AIAA/ASME Joint Thermophysics and Heat Transfer Conference, Chicago, Illinois*, 2010.
- [126] A. Munafo, M. Panesi, R.L Jaffe, G. Colonna, A. Bourdon, and T.E. Magin. QCT-based vibrational collisional models applied to nonequilibrium nozzle flows. *The European Physical Journal D*, 66(7)::188, 2012.
- [127] M. Panesi, A. Munafo, T.E. Magin, and R.L. Jaffe. Nonequilibrium shock-heated nitrogen flows using a rovibrational state-to-state method. *Physical Review E*, 90:013009, 2014.
- [128] A. Munafo, M. Panesi, and T.E. Magin. Boltzmann rovibrational collisional coarse-grained model for internal energy excitation and dissociation in hypersonic flows. *Physical Review E*, 89:023001, 2014.
- [129] A. Munafo, Y. Liu, and M. Panesi. Modeling of dissociation and energy transfer in shock-heated nitrogen flows. *Physics of Fluids*, 27:127101, 2015.
- [130] E. Torres and T.E. Magin. State-to-state model for DSMC simulation of internal energy exchange in hypersonic flows. In *51st AIAA Aerospace Sciences Meeting including the New Horizons Forum and Aerospace Exposition*, 2013.
- [131] T. Zhu, Z. Li, and D.A. Levin. Development of a two-dimensional binning model for N<sub>2</sub>-N relaxation in hypersonic shock conditions. *Journal of Chemical Physics*, 145:064302, 2016.
- [132] A. Munafo. *Multi-Scale Models and Computational Methods for Aerothermodynamics*. PhD thesis, Ecole Centrale Paris, 2014.
- [133] E. Nagnibeda and E. Kustova. *Non-Equilibrium Reacting Gas Flows*. Heat and Mass Transfer. Springer, 2009.
- [134] B.S. Baykov, D.K. Bayalina, and Kustova E.V. Inverse Laplace transformation for evaluation of state-specific cross sections for dissociation reaction and vibrational energy transitions. *Vestnik St. Petersburg University: Mathematics*, 49(4):389–397, October 2016.
- [135] A.N. Tikhonov and V.A. Arsenin. *Solution of Ill-posed Problems*. Winston & Sons, Washington, 1977.
- [136] Y.A. Bondar and M.S. Ivanov. DSMC Dissociation Model Based on Two-Temperature Chemical Rate Constant. In *45th AIAA Aerospace Sciences Meeting and Exhibit, Reno, Nevada*, 2007.
- [137] P. Minelli, Esposito F., D. Bruno, M. Capitelli, and S. Longo. Extracting Cross Sections from Rate Coefficients: Application to Molecular Gas Dissociation. *Journal of Thermophysics and Heat Transfer*, 25(3):374–377, 2011.
- [138] J.A. Nelder and R. Mead. A Simplex Method for Function Minimization. *The Computer Journal*, 7(4):308–313, 1965.

- [139] F Bariselli. Development of gas-surface interaction models for DSMC methods. Research Master project report VKI PR 2015-05, von Karman Institute for Fluid Dynamics, 2015. [Supervisors: T.E. Magin & E. Torres].
- [140] E. Torres and T.E. Magin. Statistical simulation of internal energy exchange in shock waves using explicit transition probabilities. In *28th International Symposium on Rarefied Gas Dynamics: RGD28, Zaragoza, Spain, 2012*.
- [141] A. Munafò, J.R. Haack, I.M. Gamba, and T.E. Magin. A Spectral-Lagrangian Boltzmann Solver for a Multi-Energy Level Gas. *Journal of Computational Physics*, 264:152–176, 2014.
- [142] E. Torres and T.E. Magin. Implementation of state-to-state rovibrational bin model for molecular nitrogen in DSMC. In *8th European Symposium on Aerothermodynamics for Space Vehicles, Lisbon Portugal, 2015*.
- [143] T. Banyai, E. Torres, T.E. Magin, A.V. Kashkovsky, P.V. Vashchenkov, M.S. Ivanov, and P. Rambaud. Evaluation of the aerodynamic properties of the intermediate experimental vehicle in the rarefied and transitional regime. In *Progress in Flight Physics*, volume 5, pages 425–440, 2013.
- [144] E. Torres, Y.A. Bondar, and T. E. Magin. Uniform rovibrational collisional N<sub>2</sub> bin model for DSMC, with application to atmospheric entry flows. In *30th International Symposium on Rarefied Gas Dynamics: RGD 30, Victoria, BC, Canada, 2016*.
- [145] M.S. Ivanov, G.N. Markelov, and S.F. Gimelshein. Statistical simulation of reactive rarefied flows: numerical approach and applications. In *7th AIAA/ASME Joint Thermophysics and Heat Transfer Conference*, 1998.
- [146] J.G. Parker. Rotational and Vibrational Relaxation in Diatomic Gases. *Physics of Fluids*, 2(4):449–462, 1959.
- [147] R.C. Millikan and D.R. White. Systematics of Vibrational Relaxation. *Journal of Chemical Physics*, 39(12):3209–3214, 1963.
- [148] C. Park. *Problems of Rate Chemistry in the Flight Regimes of Aeroassisted Orbital Transfer Vehicles*, volume 96, pages 511–537. AIAA, New York, 1985.
- [149] I.D. Boyd, G. Chen, and G.V. Candler. Predicting failure of the continuum fluid equations in transitional hypersonic flows. *Physics of Fluids*, 7(1):210–219, 1995.
- [150] F. Panerai, O. Chazot, B. Helber, I. Sakraker, T. Pinchon, and R. Barreteau. Aerothermochemistry Testing of a Ceramic Matrix Composite TPS for a Lifting Reentry Vehicle. In *4th European Conference for Aerospace Sciences, EUCASS, 2011*.
- [151] M. Panesi, R.L. Jaffe, and D.W. Schwenke. Energy transfer study of N<sub>2</sub>-N<sub>2</sub> and N<sub>2</sub>-N interactions by using rovibrational state-to-state model. In *44th AIAA Thermophysics Conference, San Diego, California, 2013*. AIAA 2013-3147.

- [152] A. Munafo, R.L. Jaffe, D.W. Schwenke, and M. Panesi. Dissociation and Energy transfer study of N<sub>2</sub>-N and N<sub>2</sub>-N<sub>2</sub> interactions by using rovibrational and coarse-grained state-to-state models. In *53rd AIAA Aerospace Sciences Meeting, Kissimmee, Florida, 2015*. AIAA 2015-0480.
- [153] R.J. Duchovic, Y.L. Volobuev, G.C. Lynch, A.W. Jasper, D.G. Truhlar, T.C. Allison, A.F. Wagner, B.C. Garrett, J. Espinosa García, and J.C. Corchado. POTLIB library. <http://comp.chem.umn.edu/potlib>.
- [154] I. Kuscer. Dissociation and recombination in an inhomogeneous gas. *Physica A: Statistical Mechanics and its Applications*, 176(3):542–556, 1991.
- [155] B.V. Alexeev, A. Chikhaoui, and I.T. Grushin. Application of the generalized Chapman-Enskog method to the transport-coefficient calculation in a reacting gas mixture. *Physical Review E*, 49(4):2809–2825, 1994.
- [156] V. Giovangigli. *Multicomponent Flow Modeling*. Birkhäuser Boston, 1999.
- [157] Felix T. Smith. *Kinetic Processes in Gases and Plasmas*, chapter IX: Triple Collisions and Termolecular Reaction Rates, pages 321–380. Academic Press, 1969.
- [158] M.G. Kapper and J.-L. Cambier. Ionizing Shocks in Argon. Part 1: Collisional-Radiative Model and Steady-State Structure. *Journal of Applied Physics*, 109:113308, 2011.

# A. Bin model-related definitions

## A.1. Generalized Boltzmann equation for $N_2(k)$ +N-mixture

The Boltzmann equation is written for a mixture of molecular- and atomic nitrogen. It is assumed that every  $N_2$ -molecule populates one of the particular internal energy bins labeled with an index  $k \in \mathcal{K}_{N_2}$ , and the set  $\mathcal{K}_{N_2} = \{1, 2, \dots, n_{\text{bins}}\}$  contains all indices pointing to these  $n_{\text{bins}}$  internal energy states. For simplicity, it is assumed that atomic nitrogen only occupies a single internal energy state, and thus requires no special index. For such a mixture, the generalized Boltzmann equation in fact becomes a system of  $n_{\text{bins}} + 1$  equations, which must be solved simultaneously:

$$\begin{aligned} \frac{\partial f_k}{\partial t} + \mathbf{c} \cdot \nabla_{\mathbf{x}} f_k &= Q_k^{\text{scat}} + Q_k^{\text{re}}, & k \in \mathcal{K}_{N_2} \\ \frac{\partial f_N}{\partial t} + \mathbf{c} \cdot \nabla_{\mathbf{x}} f_N &= Q_N^{\text{scat}} + Q_N^{\text{re}} \end{aligned} \quad (\text{A.1})$$

The terms on the left hand side are collectively known as the streaming operator, which governs the time evolution and advection of the  $N_2(k)$ - and N-velocity distributions in physical space. The effect of external forces (i.e. gravitational, electromagnetic) has been neglected in this formulation. The terms on the right hand side are collectively called the collision operators. These are responsible for changes in the distributions occurring in velocity space. For clarity, they can be sub-divided into “non-reactive”, i.e. scattering and “reactive” terms, as done by Giovangigli [156]. The scattering terms constitute a sum over partial collision operators describing all types of collisions, which result in no change of the chemical species of the colliding particles. These types of collisions can be written as follows:

$$N_2(k, \mathbf{c}_1) + N_2(l, \mathbf{c}_2) \rightleftharpoons N_2(k', \mathbf{c}'_1) + N_2(l', \mathbf{c}'_2), \quad k, l, k', l' \in \mathcal{K}_{N_2} \quad (\text{A.2})$$

$$N_2(k, \mathbf{c}_1) + N(\mathbf{c}_2) \rightleftharpoons N_2(k', \mathbf{c}'_1) + N(\mathbf{c}'_2), \quad k, k' \in \mathcal{K}_{N_2} \quad (\text{A.3})$$

$$N(\mathbf{c}_1) + N(\mathbf{c}_2) \rightleftharpoons N(\mathbf{c}'_1) + N(\mathbf{c}'_2) \quad (\text{A.4})$$

These processes take into account all possible transitions between internal energy states available to the colliding particles, including elastic collisions. In a state-to-state description, they can be thought of as pseudo-reactions. Recall of course, that in addition to the internal energy states, collisions may also modify the velocities of the particles involved. For example, Eq. (A.4) implies that in the present model a collision between two nitrogen atoms is always elastic. Collecting all

of the collision types represented by Eq. (A.2) through Eq. (A.4), the respective non-reactive collision terms of Eq. (A.1) take on the following forms:

$$Q_k^{\text{scat}} = \sum_{\substack{l, k', l' \\ \in \mathcal{K}_{N_2}}} Q_{k, l}^{k', l'} + \sum_{k' \in \mathcal{K}_{N_2}} Q_{k, N}^{k', N}, \quad k \in \mathcal{K}_{N_2} \quad (\text{A.5})$$

$$Q_N^{\text{scat}} = \sum_{\substack{l, l' \\ \in \mathcal{K}_{N_2}}} Q_{N, l}^{N, l'} + Q_{N, N}^{N, N} \quad (\text{A.6})$$

The particular type of non-reactive collision covered by the NASA Ames N3 database is the one described by Eq. (A.3). Its partial collision operator can be written as follows:

$$Q_{k, N}^{k', N} = \iiint_{\substack{\mathcal{R}^3 \times \mathcal{R}^3 \\ \times \mathcal{R}^3}} \left( f'_{k'} f'_N \frac{\bar{a}_k}{\bar{a}_{k'}} - f_k f_N \right) W_{k, N}^{k', N} d\mathbf{c}'_1 d\mathbf{c}'_2 d\mathbf{c}_2, \quad k, k' \in \mathcal{K}_{N_2} \quad (\text{A.7})$$

where the distributions of the species on the right hand side of Eq. (A.3) are ‘‘primed’’ in order to distinguish them from those on the left hand side. The factors  $\bar{a}_k$  and  $\bar{a}_{k'}$  are the degeneracies of the pre- and post-collision bins of  $N_2$ , and  $W_{k, N}^{k', N}$  is called the ‘‘transition probability’’ by some authors [155, 156], even though it has dimensions of  $\text{length}^{-3} \times \text{time}^5$ . It is related to the differential cross section via the expression:

$$W_{k, N}^{k', N}(\mathbf{c}_1, \mathbf{c}_2, \mathbf{c}'_1, \mathbf{c}'_2) d\mathbf{c}'_1 d\mathbf{c}'_2 = g \bar{\sigma}_{k, N}^{k', N}(g, \boldsymbol{\Omega}) d\boldsymbol{\Omega}, \quad (\text{A.8})$$

where  $g = |\mathbf{c}_1 - \mathbf{c}_2|$  is the relative velocity magnitude of the pre-collision pair,  $\boldsymbol{\Omega}$  represents the post-collision deflection (solid) angle, and  $\bar{\sigma}_{k, N}^{k', N}(g, \boldsymbol{\Omega})$  itself is the differential cross section for the given process. Analogous to Eq. (A.8), a transition probability exists for the reverse paths, and a corresponding differential cross section can be defined.

$$W_{k', N}^{k, N}(\mathbf{c}'_1, \mathbf{c}'_2, \mathbf{c}_1, \mathbf{c}_2) d\mathbf{c}_1 d\mathbf{c}_2 = g' \bar{\sigma}_{k', N}^{k, N}(g', \boldsymbol{\Omega}') d\boldsymbol{\Omega}'. \quad (\text{A.9})$$

This is essentially the mirror image of Eq. (A.8) with all the pre-and post-collision indices swapped. The corresponding integrated cross sections<sup>1</sup> are obtained by integrating over all deflection angles:

$$\bar{\sigma}_{k, N}^{I, k', N}(g) = \int_0^{4\pi} \bar{\sigma}_{k, N}^{k', N}(g, \boldsymbol{\Omega}) d\boldsymbol{\Omega} \quad \text{and} \quad \bar{\sigma}_{k', N}^{I, k, N}(g') = \int_0^{4\pi} \bar{\sigma}_{k', N}^{k, N}(g', \boldsymbol{\Omega}') d\boldsymbol{\Omega}'. \quad (\text{A.10})$$

All of the cross sections, which are the subject of Sec. 3.1 and Sec. 3.2, are such integrated cross sections. The micro-reversibility relations, which exist between the forward- and reverse collisions implied by the two-way arrows in Eq. (A.3), can be formulated concisely in terms of

---

<sup>1</sup>Theses are called the ‘‘total’’ cross section by some authors [1], although this term is somewhat misleading when multiple reaction paths are available to the collision pair (see the discussion in Sec. 3.3.1)

the reaction probabilities [155]:

$$W_{k,N}^{k',N}(\mathbf{c}_1, \mathbf{c}_2, \mathbf{c}'_1, \mathbf{c}'_2) \bar{a}_k = W_{k',N}^{k,N}(\mathbf{c}'_1, \mathbf{c}'_2, \mathbf{c}_1, \mathbf{c}_2) \bar{a}_{k'}. \quad (\text{A.11})$$

By substituting Eq. (A.8) and Eq. (A.9) for the respective forward- and reverse reactions, this relation can be re-written in terms of the differential cross sections. The resulting expression may be simplified with the help of the differential relations  $d\mathbf{c}_1 d\mathbf{c}_2 = d\mathbf{G} g^2 dg d\Omega'$  and  $d\mathbf{c}'_1 d\mathbf{c}'_2 = d\mathbf{G} g'^2 dg' d\Omega$  to yield:

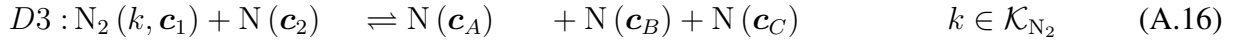
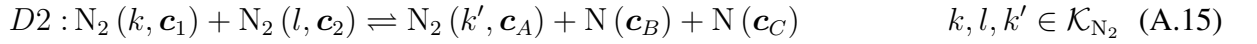
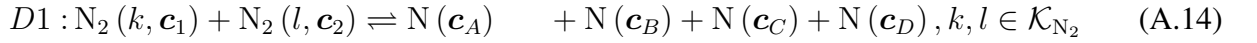
$$\bar{a}_k g^2 dg^2 \bar{\sigma}_{k,N}^{k',N}(g, \Omega) d\Omega d\Omega' = \bar{a}_{k'} g'^2 dg'^2 \bar{\sigma}_{k',N}^{k,N}(g', \Omega') d\Omega d\Omega' \quad (\text{A.12})$$

Integrating both sides over the two sets of deflection angles, and taking into account that  $dg^2 = dg'^2$ , makes it possible to simplify the detailed balance relation and to write it in terms of the integrated cross sections:

$$\bar{a}_k g^2 \bar{\sigma}_{k,N}^{I,k',N}(g) = \bar{a}_{k'} g'^2 \bar{\sigma}_{k',N}^{I,k,N}(g') \quad (\text{A.13})$$

Notice that this relation is equivalent to Eq. (3.7), except for the fact that here it has been expressed in terms of the relative velocities  $g$  and  $g'$ , instead of the relative translational energies  $E = \frac{\mu_{N_2,N}}{2} g^2$  and  $E' = \frac{\mu_{N_2,N}}{2} g'^2$ .

Moving on to the reactive collision terms, one can notice that the types of chemical reactions possible in an  $N_2(k)$ ,  $N$ -mixture are all dissociation reactions:



The corresponding reactive collision terms represent the sum over the contributions of all three reactions:

$$Q_k^{\text{re}} = Q_k^{(D1)} + Q_k^{(D2)} + Q_k^{(D3)} \quad k \in \mathcal{K}_{N_2}, \quad (\text{A.17})$$

$$Q_N^{\text{re}} = Q_N^{(D1)} + Q_N^{(D2)} + Q_N^{(D3)} \quad (\text{A.18})$$

Out of the three dissociation reaction types, Eq. (A.16) is the only one for which cross section data were available in the Ames N3 database. The partial collision operators for all  $N_2(k)$  corresponding to reaction (D3) take on the form:

$$Q_k^{(D3)} = \iiint_{\mathcal{R}^3 \times \mathcal{R}^3 \times \mathcal{R}^3 \times \mathcal{R}^3} \left( f_N^A f_N^B f_N^C \frac{\beta_N^2}{\beta_k} - f_k f_N \right) \mathcal{W}_{k,N}^{N,N,N} d\mathbf{c}_A d\mathbf{c}_B d\mathbf{c}_C d\mathbf{c}_2 \quad k \in \mathcal{K}_{N_2} \quad (\text{A.19})$$

Here, the distribution functions of the species prior to dissociation are represented by:  $f_k = f_k(\mathbf{c}_1)$  and  $f_N = f_N(\mathbf{c}_2)$ . In order to distinguish the distribution functions of the three nitrogen atoms on the right hand side from the one on the left, arbitrary indices have been assign to them:  $f_N^A = f_N(\mathbf{c}_A)$ ,  $f_N^B = f_N(\mathbf{c}_B)$  and  $f_N^C = f_N(\mathbf{c}_C)$ .

For atomic nitrogen, the reactive collision term is composed of two separate contributions, because N appears both as a reactant and as a product in Eq. (A.16):

$$Q_N^{(D3)} = \sum_{k \in \mathcal{K}_{N_2}} \left\{ \int_{\mathcal{R}^3 \times \mathcal{R}^3 \times \mathcal{R}^3 \times \mathcal{R}^3} \left( f_N^A f_N^B f_N^C \frac{\beta_N^2}{\beta_k} - f_k f_N \right) \mathcal{W}_{k,N}^{N,N,N} d\mathbf{c}_A d\mathbf{c}_B d\mathbf{c}_C d\mathbf{c}_1 \right. \\ \left. - 3 \int_{\mathcal{R}^3 \times \mathcal{R}^3 \times \mathcal{R}^3 \times \mathcal{R}^3} \left( f_N f_N^B f_N^C \frac{\beta_N^2}{\beta_k} - f_k f_N^A \right) \mathcal{W}_{k,N}^{N,N,N} d\mathbf{c}_A d\mathbf{c}_B d\mathbf{c}_C d\mathbf{c}_1 \right\} \quad (\text{A.20})$$

The terms  $\beta_k$  and  $\beta_N$  that appear as factors multiplying the distribution functions in Eq. (A.19) and Eq. (A.20) are called the statistical weights:

$$\beta_k = \frac{h_P^3}{\bar{a}_k m_{N_2}^3}, \quad k \in \mathcal{K}_{N_2}, \quad \text{and} \quad \beta_N = \frac{h_P^3}{a_N m_N^3}, \quad (\text{A.21})$$

wherein  $h_P$ , i.e. Planck's constant appears, as well as the particle masses of molecular- and atomic nitrogen. Notice that in the second term of Eq. (A.20), two of the indices distinguishing the four distribution functions of atomic nitrogen have been swapped with respect to those appearing in the first integral. This second term is responsible for describing the effects of dissociation on atomic nitrogen as a “product” species, rather than as a “reactant”. This is why the integral is multiplied by the stoichiometric coefficient  $\nu_N^{\text{back}} = 3$ .

Similar to the non-reactive collisions discussed before, detailed balance relations for this dissociation-recombination reaction can be formulated in terms of the forward- and backward reaction probabilities [156]:

$$\mathcal{W}_{k,N}^{N,N,N}(\mathbf{c}_1, \mathbf{c}_2, \mathbf{c}_A, \mathbf{c}_B, \mathbf{c}_C) \beta_N^2 = \mathcal{W}_{N,N,N}^{k,N}(\mathbf{c}_A, \mathbf{c}_B, \mathbf{c}_C, \mathbf{c}_1, \mathbf{c}_2) \beta_k. \quad (\text{A.22})$$

where now the statistical weights of Eq. (A.21) appear as factors. However, transforming Eq. (A.22) into a relationship between “dissociation” and “recombination” cross sections is not as straightforward as it was in the case of the binary collisions discussed before [133]. The increased complexity is due to the larger set of degrees of freedom involved, and instead of being able to parametrize the differential reaction cross sections in terms of just one relative velocity magnitude  $g$  and a single deflection angle  $\Omega$ , the creation of an additional particle during the dissociation results in a much more cumbersome notation. Alexeev et al [155] derived an expression linking the forward reaction probability  $\mathcal{W}_{k,N}^{N,N,N}$  to the differential dissociation cross section:

$$\mathcal{W}_{k,N}^{N,N,N}(\mathbf{c}_1, \mathbf{c}_2, \mathbf{c}'_1, \mathbf{c}'_2, \mathbf{c}'_3) d\mathbf{c}'_1 d\mathbf{c}'_2 d\mathbf{c}'_3 = \\ g_{12} \frac{\bar{\sigma}_{k,N}^{N,N,N}(g_{12}, g'_{1(23)}, \Omega_{1(23)}, \Omega_{23})}{\frac{(4\pi)^2}{3} [g'_{1(23)}]_{\text{max}}^3} g_{1(23)}'^2 dg'_{1(23)} d\Omega_{1(23)} d\Omega_{23}, \quad (\text{A.23})$$

where the sub-indices correspond to the diagram in Fig. 3.6(b) and  $[g'_{1(23)}]_{\max}$  results from energy conservation (see Sec. 3.3.4). This expression now depends on the two pre- and post-collision relative speeds  $g_{12}$ ,  $g'_{1(23)}$  and the two post-collision angles  $\Omega_{1(23)}$  and  $\Omega_{23}$ . However, this choice of parameters is not unique, and other combinations of velocities and angles could have been selected. The definition of a cross section for the recombination process appears to be even more problematic, since it involves three particles simultaneously, and it seems that to this day no rigorous derivation has been attempted. Regarding the state-specific integrated dissociation cross section  $\bar{\sigma}_k^D$  appearing throughout Ch. 3, it was tacitly assumed that this quantity could be parametrized in terms of only the relative pre-collision energy  $E = \frac{1}{2}\mu_{\text{N}_2,\text{N}} g^2$ . Therefore, it would be reasonable to assume that it is obtained by integrating the differential cross section  $\bar{\sigma}_{k,\text{N}}^{\text{N},\text{N},\text{N}}$  appearing in Eq. (A.23) over all  $g'_{1(23)}$ ,  $\Omega_{1(23)}$  and  $\Omega_{23}$ . However, this link has not been demonstrated so far. It is because of these difficulties that a rigorous treatment of the dissociation-recombination process in the context of the Boltzmann equation has not yet been presented in literature. Fortunately, in many cases of practical interest, such as the rarefied atmospheric entry flows discussed in Ch. 5 of this thesis, recombination is known to have a minor influence on the flow and can be neglected.

The (set of) generalized Boltzmann equation(s) represented by Eq. (A.1), can be solved (usually numerically) assuming that suitable initial- and boundary conditions are specified. From the mathematical viewpoint, the solution is complete, once the set of distribution functions can be determined everywhere in the domain, at any time of interest. However, from a physical (or engineering) point of view, the solution becomes only really useful, after it has been post-processed to yield the macroscopic moments. These moments correspond to the classical flow field variables, more familiar to a fluid dynamicist.

By integration of the velocity distribution functions for all (pseudo-) species, the macroscopic number densities may be obtained:

$$\bar{n}_k = \int_{\mathcal{R}^3} f_k d\mathbf{c}, \quad k \in \mathcal{K}_{\text{N}_2} \quad \text{and} \quad n_{\text{N}} = \int_{\mathcal{R}^3} f_{\text{N}} d\mathbf{c} \quad (\text{A.24})$$

Obviously,  $n_{\text{N}_2} = \sum_{k \in \mathcal{K}_{\text{N}_2}} \bar{n}_k$  and  $n = n_{\text{N}_2} + n_{\text{N}}$ . The mass densities follow by multiplication by the respective particle masses  $m_{\text{N}_2}$  and  $m_{\text{N}}$ :

$$\bar{\rho}_k = m_{\text{N}_2} \bar{n}_k, \quad \mathcal{K}_{\text{N}_2}, \quad \text{and} \quad \rho_{\text{N}} = m_{\text{N}} n_{\text{N}}. \quad (\text{A.25})$$

The hydrodynamic velocity is the mass-average over all (pseudo-) species:

$$\mathbf{v} = \frac{1}{\rho} \left\{ m_{\text{N}_2} \sum_{k \in \mathcal{K}_{\text{N}_2}} \int_{\mathcal{R}^3} \mathbf{c} f_k d\mathbf{c} + m_{\text{N}} \int_{\mathcal{R}^3} \mathbf{c} f_{\text{N}} d\mathbf{c} \right\}, \quad (\text{A.26})$$

where  $\rho = \bar{\rho}_{\text{N}_2} + \rho_{\text{N}}$  is the overall mass density. The mixture temperature is determined based on

the kinetic energies in the hydrodynamic frame of reference of all (pseudo-) species involved:

$$T = \frac{1}{3 n_{\text{KB}}} \left\{ m_{\text{N}_2} \sum_{k \in \mathcal{K}_{\text{N}_2}} \int_{\mathcal{R}^3} |\mathbf{C}|^2 f_k d\mathbf{C} + m_{\text{N}} \int_{\mathcal{R}^3} |\mathbf{C}|^2 f_{\text{N}} d\mathbf{C} \right\}, \quad (\text{A.27})$$

where  $\mathbf{C} = \mathbf{c} - \mathbf{v}$  is the peculiar velocity. A separate temperature  $T_{\text{int}}$  can be defined for characterizing the internal energy content of  $\text{N}_2$ . It is determined based on the populations of the internal energy states, i.e. the  $\bar{n}_k$ , as explained in Sec. A.3.

## A.2. Mass production terms for macroscopic balance equations in bin model

In Sec. 4.1 the set of balance equations for the URVC bin model is used as a means to verify the DSMC implementation. This system of equations makes use of the bin-specific source terms listed here: The mass production term of bin  $k$  due to inelastic collisions of the type  $\text{N}_2(k) + \text{N} \rightleftharpoons \text{N}_2(k') + \text{N}$  is given by:

$$\bar{\omega}_k^{\text{in}} = m_{\text{N}_2} \sum_{\substack{k' \in \mathcal{K}_{\text{N}_2} \\ (k \neq k')}} \{ -\bar{k}_{k \rightarrow k'}^E \bar{n}_k n_{\text{N}} \} + m_{\text{N}_2} \sum_{\substack{k' \in \mathcal{K}_{\text{N}_2} \\ (k \neq k')}} \{ \bar{k}_{k' \rightarrow k}^E \bar{n}_{k'} n_{\text{N}} \}, \quad k \in \mathcal{K}_{\text{N}_2}, \quad (\text{A.28})$$

where the  $\bar{k}_{k \rightarrow k'}^E$  in the depletion term are determined from Eq. (2.14) when  $k' > k$  and from Eq. (2.15) when  $k' < k$ . The coefficients  $\bar{k}_{k' \rightarrow k}^E$  in the replenishing term are determined analogously by exchanging  $k$  with  $k'$ . The mass production term of bin  $k$  due to the dissociation reaction  $\text{N}_2(k) + \text{N} \rightleftharpoons 3\text{N}$  is given by:

$$\bar{\omega}_k^{\text{re}} = m_{\text{N}_2} \left( -\bar{k}_k^D \bar{n}_k n_{\text{N}} + \bar{k}_k^R n_{\text{N}}^3 \right), \quad k \in \mathcal{K}_{\text{N}_2}, \quad (\text{A.29})$$

where the bin-specific dissociation rate coefficient was defined by Eq. (2.18) and the bin-specific recombination rate coefficient was given by Eq. (2.19). Correspondingly, the mass production term of atomic nitrogen due to the same dissociation reaction is given by:

$$\omega_{\text{N}} = 2 m_{\text{N}} \sum_{k \in \mathcal{K}_{\text{N}_2}} \left( \bar{k}_k^D \bar{n}_k n_{\text{N}} - \bar{k}_k^R n_{\text{N}}^3 \right). \quad (\text{A.30})$$

### A.3. Definition of the state-to-state internal temperature out of thermal equilibrium

In the simulations presented in Ch. 4 and Ch. 5, use is made of the internal temperature as a means to quantify the energy content of the internal mode of  $N_2$ . At thermal equilibrium the translational and internal temperatures are equal, i.e.  $T = T_{\text{int}} = T_{\text{eq}}$ , but this is not the case when the gas is exposed to sudden compression, or expansion. The amount by which the translational and internal temperatures differ from one another is an indicator of the degree of internal energy nonequilibrium. The specific thermal energy contributed by the internal mode of  $N_2$  for an arbitrary distribution of the internal energy bins is given by:

$$e_{N_2}^{\text{int}} = \frac{1}{m_{N_2}} \sum_{k \in \mathcal{K}_{N_2}} \frac{\bar{n}_k}{n_{N_2}} \bar{E}_k \quad (\text{A.31})$$

Assuming that these bin populations were to follow a hypothetical Boltzmann distribution at  $T_{\text{int}}$ , their populations would be expressed as:

$$\left[ \frac{\bar{n}_k}{n_{N_2}} \right]_{T_{\text{int}}} = \frac{\bar{a}_k}{\bar{Z}_{N_2}^{\text{int}}(T_{\text{int}})} \exp\left(-\frac{\bar{E}_k}{k_B T_{\text{int}}}\right), \quad k \in \mathcal{K}_{N_2} \quad (\text{A.32})$$

where the partition function of the internal energy mode was given by:

$$\bar{Z}_{N_2}^{\text{int}}(T_{\text{int}}) = \sum_{k \in \mathcal{K}_{N_2}} \bar{a}_k \exp\left(-\frac{\bar{E}_k}{k_B T_{\text{int}}}\right) \quad (\text{A.33})$$

Substituting the hypothetical Boltzmann distribution of Eq. (A.32) into Eq. (A.31), one would obtain:

$$e_{N_2}^{\text{int}}(T_{\text{int}}) = \frac{1}{m_{N_2}} \sum_{k \in \mathcal{K}_{N_2}} \frac{\bar{a}_k \bar{E}_k}{\bar{Z}_{N_2}^{\text{int}}(T_{\text{int}})} \exp\left(-\frac{\bar{E}_k}{k_B T_{\text{int}}}\right) \quad (\text{A.34})$$

However, when out of equilibrium the actual populations  $\bar{n}_k/n_{N_2}$  do not conform to Eq. (A.32), and the average energy would have to be calculated from Eq. (A.31) directly. By equating Eq. (A.34) with the general expression using the actual populations, one obtains:

$$\sum_{k \in \mathcal{K}_{N_2}} \left\{ \frac{\bar{n}_k}{n_{N_2}} \bar{E}_k \right\} = \sum_{k \in \mathcal{K}_{N_2}} \left\{ \frac{\bar{a}_k \bar{E}_k}{\bar{Z}_{N_2}^{\text{int}}(T_{\text{int}})} \exp\left(-\frac{\bar{E}_k}{k_B T_{\text{int}}}\right) \right\} \quad (\text{A.35})$$

Notice that by adjusting the value of  $T_{\text{int}}$  to satisfy this equation, given the particular distribution of bins  $\bar{n}_k/n_{N_2}$ , the correct energy content of the internal mode is maintained. Thus, when out of equilibrium the internal temperature is found as an implicit solution to this non-linear equation.

